The pressure-driven fragmentation of clouds at high redshift.

Harpreet Dhanoa

Thesis submitted for the Degree of Doctor of Philosophy
of the University of London

Department of Physics & Astronomy
UNIVERSITY COLLEGE LONDON

August 2013

I, Harpreet Dhanoa, confirm that the work presented in this thesis is my own. Where information has been derived from other sources, I confirm that this has been indicated in the thesis.

To all those special people who made this possible.

”Fall seven times, stand up eight.”

— Japanese Proverb

ABSTRACT

Understanding the role of star formation and its feedback effects at high redshift is extremely important, as this greatly influences the nature of the first galaxies. This knowledge will also allow us to resolve the formation conditions of hyper-metal poor stars such as SDSS J102915+172927 (Caffau *et al.* 2011). This star is thought to be the first 'truly' low metallicity star, as it possesses a total metallicity between $10^{-5} - 10^{-7}\,Z_{\odot}$ (Caffau *et al.* 2012). Hence it's formation was probably triggered by a single primordial supernova (SN) event. Fragmentation studies that only include metal-line cooling, cannot reproduce the conditions in which such a star could form (Klessen *et al.* 2012). Therefore it is critical to simulate the physical processes that occur on the small scale as reliably as possible, as they impact large scale dynamics. At present early universe supernova shock models only include non-equilibrium chemistry and its associated cooling for temperatures below 10^4 K (Machida *et al.* 2005; Kitayama & Yoshida 2005; Nagakura *et al.* 2009; Chiaki *et al.* 2013). The metal-line cooling is often calculated separately assuming the collisional equilibrium. If we want to obtain realistic results, it is important to incorporate a complete chemistry (which includes metals, molecules and dust) and therefore evaluate the non-equilibrium cooling that occurs at all temperatures.

In Chapter 2, we first try to understand the chemistry that would occur in a low metallicity gas. We investigate the chemical evolution of a metal-free cloud that has been mixed with ejecta from a single supernova. The very first stars would have been massive and simulations predict a range of masses (Bromm & Yoshida 2011). The initial mass of the star dictates the type of supernova explosion it will undergo. As each type of SN produces a different elemental yield, we would like to ascertain if it is possible to constrain molecular tracers of progenitor mass from a primordial cloud that interacted with that particular SN ejecta.

A metal-free chemical network with its associated cooling is coupled to a hydrodynamics code in Chapter 3. Previous studies (Machida *et al.* 2005; Kitayama & Yoshida 2005; Nagakura *et al.* 2009; Chiaki *et al.* 2013) have focused on the fragmentation of the shell that forms as early universe supernova remnant interacts with an interstellar medium of a uniform density. Our model has improved upon these studies by modelling a multiphase medium with multidimensional simulations, with the goal to investigate the shock-driven fragmentation of a metal-free clump. We also investigate the effect of cosmic rays, CMB ionisation and deuterium chemistry on clumping and fragmentation of a neutral clump.

Vasiliev *et al.* (2008) highlighted an important link between the formation of extremely metal poor stars and the radial distribution of primordial gas within a first galaxy, prior to the supernova explosion. This distribution is heavily dependent on the size of the metal-free star and its HII region prior the explosion. Hence in Chapter 4 we extend our metal-free model by simulating the formation of a HII region around a 40 $M_{\odot}$ star in a number of gas clouds with differing density profiles. As the explosion mechanism for this star is not well understood, we explore a range of explosion energies and their impact on compression and fragmentation of the clump.

The impact of metal and dust cooling on the fragmentation of low metallicity gas has been highlighted by a number os studies (e.g. Bromm & Loeb 2003; Santoro & Shull 2006; Omukai *et al.* 2005; Schneider *et al.* 2012). In Chapter 5 we consider the effect of cooling from metals, metal bearing molecules and dust. The nature and production of high redshift dust is not well constrained. Assuming dust-to-gas ratio can be scaled with metallicity, a simple dust model is implemented which includes cooling induced by gas-grain collisions is evaluated at all temperatures.

The observational properties of dust and the physical consequences of its presence in the interstellar medium are extremely well-known and well-documented (Draine 2003). However its composition, structure and size-distribution are still subjects of much discussion. In Chapter 6 we have carried out an investigation of the chemical evolution of gas in different carbon-rich circumstellar environments. We pay careful attention to the accurate calculation of the molecular photoreaction rate coefficients to ascertain whether there is a universal formation mechanism for carbon dust in strongly irradiated astrophysical environments.

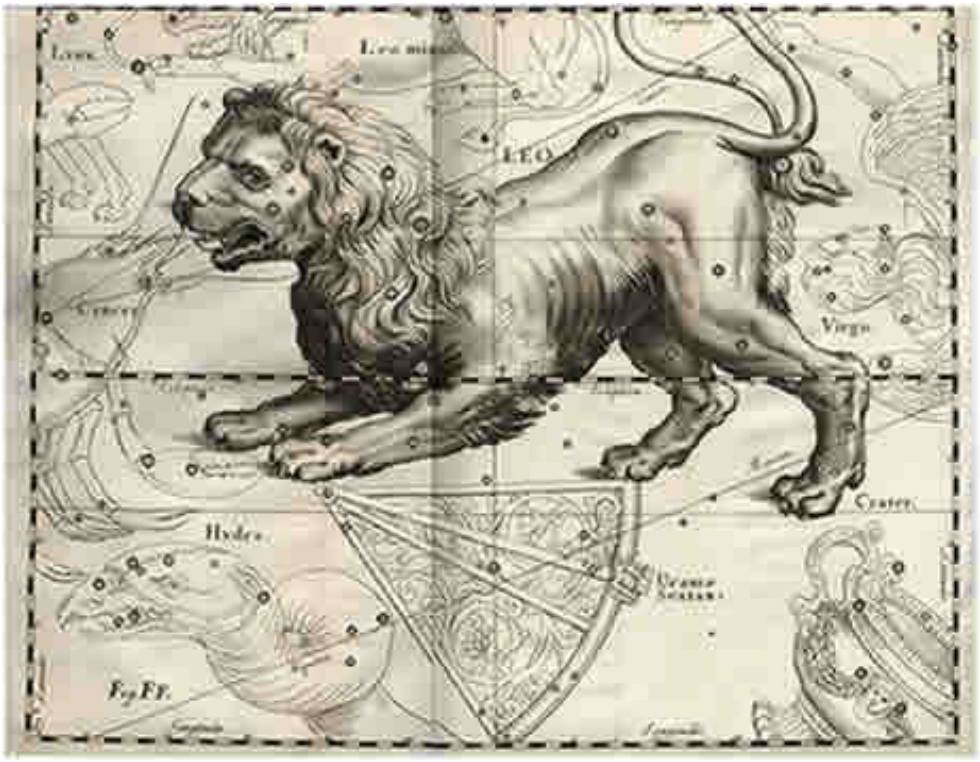

The Constellation of Leo

CONTENTS

List of Figures

LIST OF TABLES

CHAPTER 1

INTRODUCTION

1.1 Low-mass star formation in the first galaxies

The first galaxies are expected to form when the universe was less than 500 Myrs old. These building blocks of galaxy formation are intriguing for theorists to investigate as they were very different from the galaxies observed today. They were formed in low-mass dark matter haloes ($M \geq 10^7$ M$_\odot$) with low metallicity gas, at a time in the universe when matter was 1000 times denser than today. They have been recognised as key drivers of early cosmic evolution, truly marking the end of the cosmic dark ages and the beginning of cosmic reionisation. Another important reason to investigate these unobservable environments is that they are thought to be the key sites where the transition from Population III (metal-free stars) to Population II (low-metallicity, second generation) stars took place.

The galaxies today are differentiated from globular star clusters by the fact they are contained within a dark matter halo. Current models suggest that the first stars had masses in the range $10 - 100$ M$_\odot$ and could form in binaries or clusters within dark matter haloes of mass 10^6 M$_\odot$ at redshifts z $30 - 20$ (Stacy *et al.* 2010). So at which point are they considered galaxies? A universally accepted definition has not yet been established but a working definition that has been used by a number of theoretical groups is: an object which is able to retain photoheated gas and can sustain continuous star formation. Depending on the numerical model this object has a total mass between $10^7 - 10^8$ M$_\odot$. For a review of the subject see Bromm & Yoshida (2011).

Though we cannot observe these systems yet, due the increasing complexity and resolution of numerical simulations we have a much improved picture of the environment before the onset of

the second generation star formation. The assembly of the first galaxies and the evolution of the first stars were intrinsically linked, feedback from their radiation and supernovae injected energy and metals into the intergalactic medium (IGM). This in turn affected the cooling of the gas in the dark matter halos. Assuming a ΛCDM cosmology, means that these dark matter haloes will hierarchically merge to form these first galaxies.

Using 3D simulations with cosmological initial conditions Greif *et al.* (2010) followed the evolution of mini haloes that merge to form a dark matter halo $\sim 10^8$ $M_\odot$ at redshift $z = 10$. They traced the transport of metals and radiative feedback that would occur during the merging process and found that a cold dense gas ($\sim 10^5\, M\odot$) formed in the center of the newly formed galaxy. This gas was uniformly enriched by a pair instability supernova that occurred in a progenitor mini halo, to form gas with a metallicity of $\sim 10^{-3}$ $Z_\odot$ at the centre of the halo which is in a state of collapse. This could be a potential formation site for a cluster of Population II stars.

The modelling of star formation in such environments is much more complicated than star formation in mini-halos at redshift $z \geq 20$. The impact of radiation field from stars or the build up of a background radiation have been shown to regulate the formation of molecular gas clouds (Ahn & Shapiro 2007; Johnson *et al.* 2007; Susa 2008). Recent cosmological hydrodynamical simulations confirmed that strong turbulence develops within large, protogalactic halos from SN explosions or dark matter halo merger (Wise & Abel 2007). Simulations by Greif *et al.* (2008) show that the turbulence which occurs within a dark matter halo of mass 10^8 $M_\odot$ is typically supersonic, and is created by cold-flow accretion streams that feed gas into the galactic centre.

Some theories predict the majority of the first galaxies will contain both low-mass Population III and Population II stars (Bromm & Yoshida 2011). This expectation is based on the theory of a critical metallicity, $Z_{crit} \sim 10^{-4} - 10^{-3}$ $Z_\odot$**, above which the mode of star formation is thought to change from top-heavy to normal, i.e., bottom-heavy (Santoro & Shull 2006; Schneider *et al.* 2002). Due to the pre-enrichment the first galaxies are thought to be supercritical and therefore would definitely experience Population II star formation (Haiman *et al.* 1996; Tegmark *et al.* 1997; Yoshida *et al.* 2003). If a subset of the first Population II stars could be formed with sub-solar masses, they would survive to the present. These stars would be fossils of the cosmic dark ages, that are located in our immediate cosmic neighbourhood. Hence, these stars could act as observational probes. This is the basis of stellar archaeology, i.e. the hyper metal poor stars (and extremely metal poor stars) observed in our galactic halo are thought to be formed in gas enriched with ejecta of a

single (or few) supernova, which provide constraints on the environment in which they were formed and the yields of primordial SN (Christlieb *et al.* 2002; Frebel 2010) .

SDSS J102915+172927 is a hyper metal poor star found in the galactic halo by Caffau *et al.* (2011). It is about 13 billion years old, making it one of the oldest stars in the Galaxy. The discovery of this star has created a lot of interest, as it has total metallicity $10^{-5} - 10^{-7}$ $Z_{\odot}$ and mass of 0.8 $M_{\odot}$ (Caffau *et al.* 2012). This is below the critical metallicity predicted by theorists, which means that metallicity alone does not determine the formation of this star. If we want to better understand how such hyper metal poor stars can form, we need a comprehensive study into the microphysics that affect the thermal state of low-metallicity gas and hence its fragmentation. Astrophysical shocks are known to compress and fragment gas into dense possible star forming cores. It is important to study the chemistry and shock induced fragmentation of low-metallicity gas as a viable formation route for these sub-solar population II stars. Supernovae are the best candidates for shocks at high redshift.

1.2 Primordial Supernovae

Figure 1.1 presents the results from a study by Heger & Woosley (2002), the graph displays the final mass (black line) and type of supernova remnant expected from the initial mass of a non-rotating metal-free star. The graph has been separated into four regimes according to initial mass: low-mass stars below$\sim$10$M_{\odot}$ that end as white dwarfs; massive stars between $\sim$10 and $\sim$100 $M_{\odot}$; very massive stars between $\sim$100 and $\sim$1000 and supermassive stars (arbitrarily) above $\sim$1000 $M_{\odot}$. All stars above 10 $M_{\odot}$ are expected to explode via a supernova explosion. The compact remnant expected for star with an initial mass between $10 - 28$ $M_{\odot}$ is a neutron star; metal-free stars with an initial mass above this are expected to form black holes, except stars with an initial mass between 140 - 260 $M_{\odot}$ which undergo a pair instability supernova (PISN). It is postulated that the PISN explosion mechanism (energy of 10^{53} erg) would completely destroy the star, not leaving behind any remnant. These are thought to be the most energetic and brightest thermonuclear explosions in the universe. The grey line represents the mass of the star before the remnant producing event, assuming that there is no mass loss during the star's lifetime. The dashed lines refer to cases where the mass loss is uncertain.

The difference between solar metallicity and metal free supernovae is due to the difference in the pre-supernova structure of the star. This alters the way mixing of layers due to Rayleigh

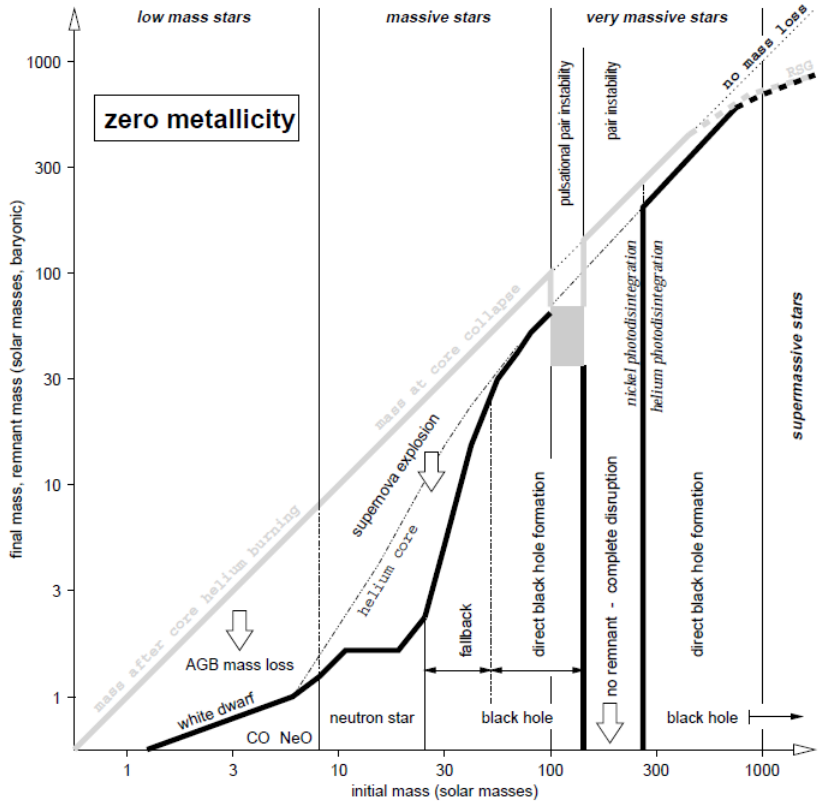

Figure 1.1: Results from Heger & Woosley (2002) displaying the initial-final mass function of non-rotating primordial stars (Z=0). The x-axis gives the initial stellar mass. The y-axis gives both the final mass of the collapsed remnant (thick black curve) and the mass of the star when the event begins that produces that remnant (e.g., mass loss in AGB stars, supernova explosion for those stars that make a neutron star, etc.; thick grey curve). Mass of helium core (dashed-double-dotted curve) which is ejected during the supernova explosion

Taylor instabilities and the fallback process occurs during the SN explosion Joggerst *et al.* (2009). Metal-free stars are predicted to be more compact than solar metallicity stars (Heger & Woosley 2010). They also have a lower opacity and lack the initial seed nuclei for carbon-nitrogen-oxygen (CNO) cycle. This leads to inefficient hydrogen burning and the formation of a very dense hydrogen shell of low entropy in the pre-SN structure.

Zhang *et al.* (2008) predict via simulations that zero-metallicity SNe have more material fall back on the compact SN remnant during the explosion and therefore form more compact remnants than solar metallicity stars of the same mass. However all of this depends on the accuracy of the stellar evolution models that predict the pre-SN structure. There are many uncertainties in modelling low-metallicity and metal-free stars, especially above 30 $M_{\odot}$. The most important unknown factors

are i) the wind metallicity dependence and hence mass loss that occurs via stellar winds during the stars lifetime ((Fryer *et al.* 2012) and ii) the mixing and fallback that occurs during the explosion process (Joggerst *et al.* 2010). This leaves the explosion mechanism that operates within the first generation of stars very poorly understood.

1.3 Star formation at high redshift: Fragmentation and chemistry

1.3.1 Theory of Fragmentation

Before assessing fragmentation at high redshift, it is worthwhile considering the physical processes that influence the fragmentation of solar metallicity gas. Within prestellar clouds, the self-gravity of star forming gas must oppose pressure gradients, magnetic fields, and turbulence (Mac Low & Klessen 2004; McKee & Ostriker 2007; Ballesteros-Paredes *et al.* 2007), resulting in a delicate balance between these competing effects. Although this is a complex system, the process of collapse, and hence the characteristic mass of the stars that will form within the cloud, is determined by the thermodynamic state of the gas (e.g. Klessen & Burkert 2000; Jappsen *et al.* 2005; Hennebelle & Chabrier 2009). It is of the utmost importance, therefore, to be aware of the balance between heating and cooling processes in the gas if we want to have a proper understanding of star formation at high redshift.

Li *et al.* (2003) demonstrated that turbulent gas having an equation of state with P proportional to n^{γ} (P is the pressure, n is number density of the gas and γ is the polytropic index of the gas) fragments efficiently when $\gamma < 1$, resulting in a cluster of low mass stars. They showed that in a gas for which gamma > 1, very few objects were formed. Therefore this gas is biased towards forming massive stars. Larson (1985, 2005) suggested that the gas may fragment at the point of transition from a cooling dominated regime (where γ <1 equates to a decreasing temperature when the density increases) to a heating dominated regime (where γ >1 equates to an increasing temperature with increasing density).

The work of Jappsen *et al.* (2006) supports Larson's proposal. The authors perform a set of numerical simulations using piece-wise polytropic equations of state and found that the transition from γ <1 to γ >1 does indeed define a characteristic mass scale for fragmentation. This behaviour is physically relevant to the fragmentation occurring in filaments, where gas is turbulent and self-gravitating. As a result, filaments with γ <1 are unstable to fragmentation (Larson 1985, 2005), while filaments with $\gamma > 1$ do not fragment.

By studying the similarity solution, Kawachi & Hanawa (1998) demonstrated that self-gravitating, gaseous filaments will easily fragment into clumps during their evolution. This is due to the fact that the timescale for fragmentation becomes shorter than the timescale for contraction toward the axis of the filament. Simulations of present day star formation confirm that most stars do form within filaments (e.g. Smith *et al.* 2011), and there is observational evidence to support this (e.g. Arzoumanian *et al.* 2011).

1.3.2 Metal-free stars: Primordial chemistry and fragmentation

The first generation of stars were metal-free stars (Pop III) formed from the pristine primordial gas. In this gas, atomic hydrogen is the dominant coolant above 10^4 K. Below this temperature, H_2 is the main coolant. Once the gas has been ionised the HD molecule also becomes important, and thus it plays a crucial role in the formation of lower mass metal-free stars known as Pop III.5 stars. The initial mass function (IMF) describes how masses are distributed within a population of newly formed stars. Until fairly recently, studies (Abel *et al.* 2002; Bromm *et al.* 2002; Yoshida *et al.* 2006) suggested that IMF of the first stars was 'top-heavy', indicating a bias towards forming large/massive stars. These studies predicted a single extremely massive star would form in a mini halo (10^6 $M_\odot$), with a typical mass greater than 100 $M_\odot$.

However, recent simulations suggest that, instead the primordial gas will fragment into binary systems (Turk *et al.* 2009; Stacy *et al.* 2010) or clusters (Smith *et al.* 2011; Greif *et al.* 2011). The IMFs calculated by these studies suggest that these stars will be primarily higher-mass objects (typically several tens of solar masses) but stars can form with masses as low as 0.5 $M_\odot$. These models include the primordial chemistry and associated cooling for temperatures below 10^4 K. For example Greif *et al.* (2011) include a chemical network that consisted of 45 reactions with 12 chemical species: H, H^+, H^-, H_2^+ , H_2, He, He^+, He^{++}, D, D^+, HD, and free electrons. The cooling from molecular hydrogen is given by Glover & Abel (2008), and accounts for the tranisition to local thermodynamic equilibrium level populations that occurs for gas with number densities $n \gg 10^4$ cm^{-3}.

These IMFs appear to be more consistent with analysis of abundance patterns of extremely metal-poor stars in the Galactic Halo, e.g (Beers & Christlieb 2005), which point to their enrichment being due to core collapse supernovae from stars of $20 - 40\,M_\odot$, and not to pair instability supernovae (which have progenitors of 120 – 260 $M_\odot$ Heger & Woosley (2002, 2010)). Subsequent to the

formation of one Pop III star, the formation of other metal-free stars nearby is repressed due to radiative feedback and metal enrichment of the IGM (Greif *et al.* 2010; Wise *et al.* 2012).

1.3.3 Metal-enriched stars: Low-metallicity chemistry and fragmentation

Population II.5 (Pop II.5) are the first low-metallicity stars to form from the gas enriched by metals from the supernovae of Pop III stars. There are two competing models underlining different origins of the physical processes that determine the fragmentation behaviour of low- metallicity gas: cooling dominated by atomic lines and cooling dominated by dust. Both models predict different critical metallicities for the transition between primordial star formation to the present day mode of star formation, which is biased towards the formation of low mass stars $< 1\,\mathrm{M}_{\odot}$. Both models are described below.

1.3.3.1 Metal-line cooling model

In this model, the fragmentation in low metallicity gas is influenced by cooling due to atomic fine-structure lines from elements such as carbon or oxygen for densities $\geq 10^4 cm^{-3}$. Santoro & Shull (2006) calculate a critical metallicity of $\mathrm{Z}_{crit} \sim 10^{-3}\,\mathrm{M}_{\odot}$ by analytically estimating the cooling rate needed to equal the heating from adiabatic compression for given halo properties. This method was improved upon by Frebel *et al.* (2007), who combined the carbon and oxygen abundances to theorise the transition criteria for low-mass star formation as $D_{trans} > -3.5$, where $D_{trans} = log_{10}(10^{[\mathrm{C/H}]} + 0.3 \times 10^{[\mathrm{O/H}]})$.

1.3.3.2 Dust cooling model

This model considers dust cooling as the dominant process that influences fragmentation (Omukai *et al.* 2005; Omukai 2010; Schneider *et al.* 2002, 2012). These studies predict a much lower critical metallicity between $10^{-5} - 10^{-6}\,\mathrm{Z}_{\odot}$. However, there are many unknown factors that contribute to this calculation, such as dust composition and gas-phase depletion at high redshift. Cherchneff & Dwek (2010) predict that primordial supernovae will produce a high amount of dust in its first stage of evolution but its survival through reverse shock is undetermined. Numerical studies by Tsuribe & Omukai (2006, 2008) show that an IMF which peaks below 1 solar mass can occur for gas with a metallicity between $10^{-5} - 10^{-6}\,\mathrm{M}_{\odot}$ and densities above $n = 10^{12}\,\mathrm{cm}^{-3}$. Dopcke *et al.* (2011) refined this approach to include time dependent chemistry and found similar results.

1.4 What can we learn from extremely metal poor stars?

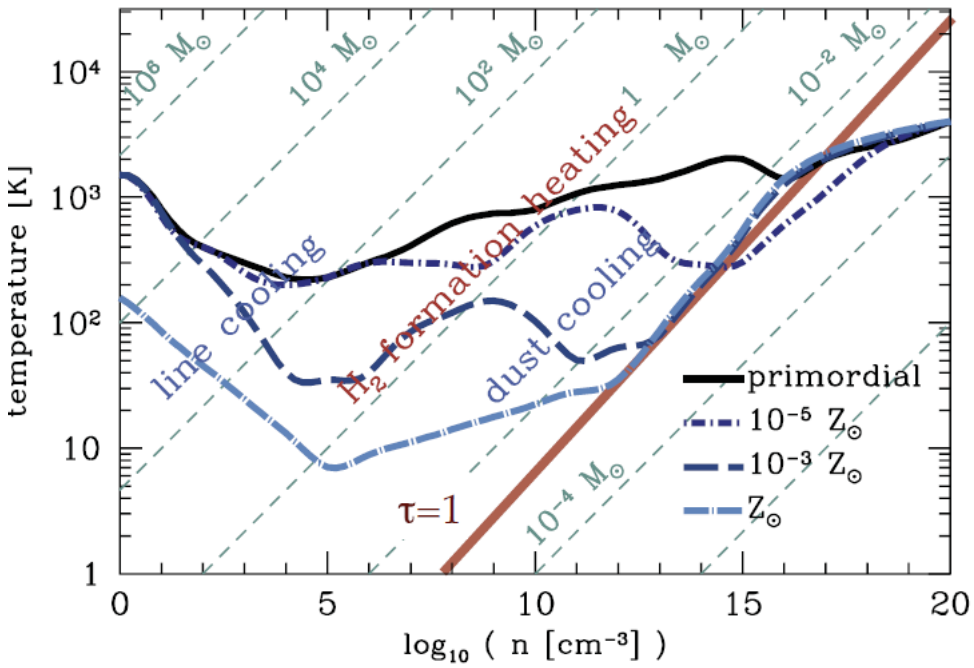

Figure 1.2: A schematic diagram given by Klessen et al. (2012) which shows the relation between the expected equilibrium temperature T and the density n for different metallicities: $Z/Z_{\odot}$ = 0, 10^{-5}, 10^{-3} and 1. The three low metallicity lines reflect the one-zone calculations by Omukai *et al.* (2005); Omukai (2010). The 'dip' in the T-n relation at low densities is due to metal-line cooling followed by H_2 formation heating. While the 'dip' at high densities and sub-solar metallicities is due to dust cooling followed by the transition to the optically thick regime for continuum radiation (solid red line).

1.4.1 SDSS J1029+1729

Very low metallicity stars have been detected in Galactic halo in large-scaled surveys such as Beers *et al.* (1992). Extremely metal-poor (EMP) stars are defined to have a metallicity [Fe/H] < -2.5, where metallicity is defines as follows

$$\left[\frac{\mathrm{A}}{\mathrm{B}}\right] = \log_{10}\left(\frac{\mathrm{N_A}}{\mathrm{N_B}}\right) - \log_{10}\left(\frac{\mathrm{N_A}}{\mathrm{N_B}}\right)_{\odot} \tag{1.1}$$

where $\mathrm{N_A}$ and $\mathrm{N_B}$ are the abundances of elements A and B respectively. Hyper metal-poor (HMP) stars are defined to possess metallcity [Fe/H] < -4. Previous HMP stars e.g. HE0107-5240 (Christlieb *et al.* 2002) and HE1327-2326 (Frebel *et al.* 2005), have a metallicity [Fe/H] < -5 but

show an excess in CNO elements e.g. [C/Fe] $\simeq 4$ (Aoki *et al.* 2006). Caffau *et al.* (2011) found the first 'true' HMP star SDSS J1029+1729, as it does not show the enhancement of CNO like the previous HMP stars, their analysis shows that it has a total metallicity between $10^{-5} - 10^{-7}$ $Z_{\odot}$ (Caffau *et al.* 2012). As this is the first star to have elemental abundances in range $< 10^{-5}$ to 10^{-4}, it challenges the metal-line only cooling model discussed in §1.3.3.

Klessen *et al.* (2012) considered the characteristic mass scale for fragmentation relating to the formation a star of this metallicity. Their aim was to determine the conditions for which the effective equation of state of the gas changed from $\gamma < 1$ to $\gamma > 1$. Figure 1.2 depicts the results of this study, and shows the temperature-density (T - n) relation for gas of varying metallicities. In the case of an ideal gas with a barotropic EOS (where $P \propto n^{\gamma}$) and the chemical composition is constant, the relation $\gamma = d(\ln \mathrm{T})/d(\ln \mathrm{n}) + 1$ holds and the effective index is obtained from the slope of the T - n relation. Wherever there are 'dips' in the T - n relation the gas may fragment. The first dip visible is a result of metal line cooling, which is effective in low density regions. For a gas of metalllicity 10^{-5} $Z_{\odot}$ this corresponds to a Jeans mass notably larger than $10 M_{\odot}$. The results of numerical simulations by Bromm *et al.* (2001) and Jappsen *et al.* (2009) support this conclusion. The authors argue that the fragmentation needed to form SDSS J1029+1729 can only be induced by dust cooling shown by the second dip. However there are objections to this theory, for example Silvia *et al.* (2010) contends that dust production may not be effective at such a high redshift. Dust formation and associated characteristics at high redshift are, however, badly constrained making it difficult to draw this type of conclusion. If such fragmentation cannot be caused by dust then there is a need to properly investigate all possible fragmentation scenarios in metal-free or extremely low-metallicity environments.

1.4.2 EMP & HMP stars and the link to SN explosion energies

The explosion mechanism of the metal free and low metallicity stars is not very well understood. Therefore the explosion energy is further unconstrained. If EMP and HMP stars are truly formed from gas polluted by a single (or a few) SN, then these stars contain key information on yield of the particular SN that formed from its ejecta. Hence recreating these observed yields through numeric modelling gives a strong indication of the explosion energy of the SN that created these low mass, very low metallicity stars. In this section we give a quick overview of the work that has been done in this area, with a focus on 40 $M_{\odot}$ stars as these are the stars we will investigate in this thesis.

Tominaga (2009) investigated the jet-induced explosion mechanism for a 40 $M_{\odot}$ primordial star. This mechanism is associated with Gamma-ray bursts and hypernovae. The author modelled an aspherical stellar explosion (2D) with special relativistic hydrodynamics and importantly included gravity to calculate the nucleosynthetic yield. He predicted a lower explosion energy, leads to larger fall back and therefore higher [C/Fe] yields. This is consistent with observations of HMP stars (Beers & Christlieb 2005).

Joggerst *et al.* (2009) modelled 15 and 25 $M_{\odot}$ non-rotating stars, which ended their lives as blue giants and not red giants. This causes the star to experience less mixing and therefore more fallback during the explosion, causing greater [C+O/Fe] yields than HMP stars and does not match any EMP stars. This highlights the need to include rotation, for more accurate results. As Ekström *et al.* (2008) have shown that rotating models have larger outer envelops, allowing mixing to occur on larger time scales and the star to become a red giant. The rotationally-induced mixing that occurs during the explosion, produces more nitrogen. This produces yields which are more comparable to EMP and HMP stars.

Hence Joggerst *et al.* (2010) studied the SN yields from 15, 25 & 40 $M_{\odot}$ stars of metallicity Z= 0 & 10^{-4} $Z_{\odot}$, using a rotating model. As the explosion mechanism is uncertain for these stars, the progenitors were artificially exploded using the piston mechanism. The following explosion energies were investigated: 0.6×10^{51} ergs, 1.2×10^{51} ergs and 2.4×10^{51} ergs. Where 1.2×10^{51} ergs is the median explosion energy for observed core-collapse SNe. They found that rotation of the star had more effect on the yield than explosion energy, i.e the redness or blueness of the progenitor star. The low-metallicity stars were more compact than the metal-free stars and therefore experienced more fallback during the explosion. Overall, they found good agreement between EMP stars and one HMP star (15 $M_{\odot}$ metal free star with 2.4×10^{51} ergs). This implies EMP stars were produced in the vicinity of metal-free or low metallicity stars undergoing conventional core collapse SNe.

Fryer *et al.* (2012) modelled the SN explosion of metal free stars using the neutrino-driven explosion mechanism associated with core collapse SNe. They incorporated the most up-to-date stellar models, without including rotation. They predict that a 40 $M_{\odot}$ metal free star would undergo a 'failed' explosion, i.e. direct collapse into a black hole. They promote other models such as a collapsar or magnetar explosion mechanism for low-metallicity stars above 35 $M_{\odot}$. These models produce a large range of explosion energies.

1.5 Astrophysical Shocks

Shock waves occur in many different astrophysical environments and supernova remnants interacting with the ISM are an example of this.

The sound speed of a gas, v_{sound}, is defined by the speed at which small perturbations propagate within the gas. Assuming the pressure p and density ρ of the gas are related by the following relationship

$$p = K\rho^{\gamma}, \tag{1.2}$$

where K is a constant and γ is the polytropic index of the gas given by the ratio of principle specific heats. The sound speed of the unperturbed gas is given by

$$v_{sound} = \sqrt{\gamma \frac{p}{\rho}}. \tag{1.3}$$

Shock waves are produced when the speed of the gas increases greater than its sound speed, i.e supersonic flow. At the point where this occurs, the sound waves reach a point where they cannot travel anymore upstream and the pressure progressively builds in that region. A compression wave or high pressure shock wave is rapidly created. This shock wave takes the form of a sharp change in gas properties on the order of a few mean paths of the fluid particles in thickness. This discontinuity of fluid properties is known as the shock front.

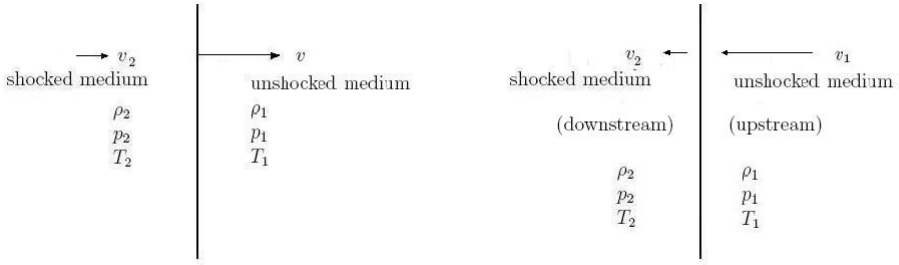

(a) Reference frame of unshocked medium, v = velocity of the shock front v_{shock}

(b) Reference frame of shock, i.e shock front $v_{shock} = 0$

Figure 1.3: The shock front in different reference frames

The following is a mathematical description of a non-magnetised adiabatic shock wave. The sharp change in fluid properties (density, velocity, pressure) at the shock front is called a 'jump'.

We begin with investigating the quantities that are conserved across the shock, these are therefore known as 'jump conditions'. For a steady one dimensional flow within the reference frame of the shock (see figure 1.3(b)), these are known as the Rankine-Hugoniot conditions:

$$\rho_1 v_1 = \rho_2 v_2, \tag{1.4}$$

$$\rho_1 v_1^2 + p_1 = \rho_2 v_2^2 + p_2, \tag{1.5}$$

$$\frac{1}{2}v_1^2 + E_1 + \frac{p_1}{\rho_1} = \frac{1}{2}v_2^2 + E_2 + \frac{p_2}{\rho_2} \tag{1.6}$$

where v is the velocity and E is the specific internal energy. The pre-shock material is denoted by subscript 1, i.e. the ambient interstellar material ahead of the expanding shock wave and subscript 2 denotes the post-shock gas. As we are in the reference frame of the shock, v_1 is not zero but $v_1 = -v_{shock}$. Equations (1.4)-(1.6) each respectively corresponds to the conservation of the following quantities across the shock front: mass, momentum and total energy (i.e. kinetic, internal and thermal). The second condition also describes the conservation of pressure, i.e. the ram pressure ρv^2 and thermal pressure p must be equal across the shock.

The specific volume of the gas is given by $V = 1/\rho$ and has the following adiabatic relationship $pV^\gamma = constant$. Thus using equation 1.2 the change in internal energy becomes

$$dE = -pdV = -K\rho^\gamma d\frac{1}{\rho}, \tag{1.7}$$

note that K is not constant across the shock. The polytropic index of the gas, γ, varies depending on the properties of the fluid and is given by:

$\gamma = 5/3$ for non-relativistic monoatomic gas (generally found in the ISM),
$\gamma = 4/3$ for relativistic monoatomic gas,
$\gamma = 7/5$ for non-relativistic diatomic gas.

1.6 Supernova Remnants

A supernova remnant (SNR) is defined as the structure formed by the explosion of the supernova interacting with the ambient medium. It consists of the ejected metal-rich material formed by supernova nucleosynthesis and the ambient medium that has been shocked and swept up along its path. The SNRs created by the death of metal poor stars within the first galaxies have not been observed. However they have been numerically modelled and have the same four stages of evolution that is observed of SNRs in our universe today.

1.6.1 Free Expansion Phase

Immediately following the explosion, the SN explosion ejects mass M_{ej} with a kinetic energy of $E_0 \equiv 10^{51}$ erg ($= E_{51}$). There are some unusual core collapse (CC) SNe that may have energies of $\sim 10^{52}$ erg (known as hypernovae) but typical SNe have $E_{51} \approx 1$. The rms velocity is

$$\langle v_{ej}^2 \rangle^{1/2} = \left(\frac{2E_0}{M_{ej}} \right)^{1/2} = 1.0 \times 10^4 \text{km s}^{-1} E_{51}^{1/2} \left(\frac{M_\odot}{M_{ej}} \right)^{1/2} \tag{1.8}$$

the ejecta has typical speed of $\sim$ 10, 000 km s^{-1}, driving a strong shock at the leading edge. Since the ejected mass is significantly greater than the mass of the circumstellar medium it encounters, there is no appreciable slowing of the ejecta and it continues to expand at a nearly constant velocity. Therefore it is called the free expansion phase. At this point there is only one shock front.

1.6.2 Reverse-Shock Phase

The density of the expanding ejecta decreases as function of time as t^{-3}, and the pressure of the shocked ambient medium becomes greater than the thermal pressure of the supernova ejecta. This creates a second shock wave called the 'reverse shock', which propagates back into the ejecta. When the ejecta is in the free-expansion phase, cooling is almost entirely adiabatic. While this adiabatic cooling is effective in lowering the temperature of the ejecta, energy is conserved in the system, as it is not radiated away. When the expanding ejecta encounters the reverse shock it is heated and its velocity reduced. Just like the forward shock or blast wave, the reverse shock heats the ejecta to very high temperatures, thus it radiates strongly in X-rays.

This radiative cooling is still relatively inefficient, and most of the energy of the system is still conserved. The reverse shock becomes important when the mass of the swept up material is

comparable to the mass of the ejecta. The radius of the blast wave when this occurs is

$$R = \left(\frac{3M_{ej}}{4\pi\rho_1}\right)^{1/3} = 5.88 \times 10^{18}\mathrm{cm}\left(\frac{\mathrm{M_{ej}}}{\mathrm{M_\odot}}\right)^{1/3} \mathrm{n_0}^{-1/3}. \tag{1.9}$$

Before this point the expansion of the SNR is uniform at a constant initial velocity. The above relation holds for uniform ambient density. However, the progenitors for core collapse SN go through a final red supergiant phase before the SN explosion, leaving a dense circumstellar medium with a $\sim r^{-2}$ density profile.

1.6.3 Sedov-Taylor Phase

Once the mass swept-up by the forward shock greatly exceeds the ejecta mass, the remnant enters the Sedov-Taylor phase. The reverse shock has propagated all the way back through the ejecta and dissipated. The SNR can be approximated as a idealised point explosion expanding in a uniform density and therefore can be described by a self-similar solution known as the Sedov-Taylor solution (Taylor 1950; Sedov 1946). The similarity variable can be derived by dimensional analysis, and is given by

$$\xi = R(\rho/E_0t^2)^{1/5} \tag{1.10}$$

where R is the distance the blast wave has traveled from the supernova, E_0 is the explosion energy of the initial event, ρ is the density of the ISM, and t is time. ξ is dimensionless, and equation 1.10 can be used to show that the distance traveled by the blast wave (for γ = 5/3) as a function of E, ρ, and t, is given by

$$R \propto (\frac{E}{\rho})^{\frac{1}{5}}t^{\frac{2}{5}}. \tag{1.11}$$

It can be seen from this that the shock velocity decreases by

$$v_{shock} = \frac{dR}{dt} \propto t^{-\frac{3}{5}}. \tag{1.12}$$

1.6.4 Radiative phase

As the shock velocity decreases, the temperature of the post-shock gas decreases. This causes an increase in radiative cooling. At the point where radiative cooling becomes more dominant than adiabatic cooling, the SNR leaves the Sedov-Taylor phase and enters the radiative phase. The speed

of the forward shock is only a few hundred km s^{-1} and the gas temperature falls below 10^6 K. The cooler gas is compressed by hotter interior gas, leading to higher densities and further increasing its cooling rate. This causes the formation of a thin shell behind the shock front. Cooling of the gas is a runaway process, the more it cools, the more the cooling rate increases. The shell increases its mass by sweeping up matter in such a way that its momentum is conserved.

If the internal pressure from the hot interior gas is ignored, the SNR can be approximated by the snowplough model. Conservation of momentum gives

$$\frac{4}{3}\pi R_{sh}^3 \rho_1 v_{sh} = \text{constant}, \tag{1.13}$$

where R_{sh} is the radius of the shell and v_{sh} $(= \frac{dR_{sh}}{dt})$ is the velocity of the shell. If the shell is formed at time t_0, when $R_{sh} = R_0$ and $v_{sh} = v_0$, the above relation can be integrated to give the following evolution equations:

$$R_{sh} = R_0 \left(1 + 4\frac{v_0}{R_0}(t - t_0)\right)^{\frac{1}{4}}, \tag{1.14}$$

$$v_{sh} = v_0 \left(1 + 4\frac{v_0}{R_0}(t - t_0)\right)^{-\frac{3}{4}}. \tag{1.15}$$

When the SNR is in the adiabatic stage ($t < t_0$) the gas temperature is T$\geq 10^6$ K. Once the shell has formed the gas within it has a temperature of $< 10^5$ K and becomes optically visible. The shell is dominated by collisionally excited lines such as O^{++}. Eventually the shell will become subsonic and dissipate into the ISM.

1.7 SNR radiation mechanisms

In this section we describe the radiation emitted by observed SNRs, which radiate throughout the electronic spectrum. These mechanisms will also be present for supernovae at high redshift.

In radio waves, the emission results from synchrotron radiation. This is when relativistic and ultra relativistic electrons gyrate in a magnetic field. When these electrons interact with the magnetic field they are accelerated by increased speed or change in direction, hence radio waves are emitted. The radiation is termed to be 'non-thermal' in origin, as the spectrum cannot be described by blackbody radiation. Synchrotron emission is characterised by a featureless power-law spectrum, where the radio flux, S_ν is given by $S_\nu \propto \nu^{-\alpha}$, where ν is the frequency and α is the spectral index, which depends on the energy distribution of the electron population.

The infrared (IR) continuum is due to dust grains that are collisionally heated in the post-shock gas. Also there are observed IR line emission in the radiative phase, originating from low to moderately ionised states of abundant heavy elements such as O, Ne, S, Si, Ar and Fe.

Optical radiation prior to the radiative phase comes mainly from hydrogen Balmer lines. For this, we need neutral hydrogen to be present ahead of the shock which is more likely for a type Ia SN than a CC SN. This is because CC SNe ionise their surrounding medium by producing a flash of ultraviolet (UV) radiation at the moment of explosion and by prior ionising radiation from the progenitor star. There is a broad Hα line generated by the charge exchange between slow neutral atoms and fast protons behind the shock producing fast moving neutral atoms. Due to collisional excitation, strong optical lines are observed from a variety of atomic species in the radiative phase, predominantly from Hα and singly-ionised sulfur ([S II]). Ultraviolet (UV) emission is also produced from higher ionisation states.

Soft X-rays (0.1-2 keV) produced in SNRs are generally thermal in origin, this is where the material is in local thermal equilibrium. The line emission comes from highly ionised elements. Lines from species known as “hydrogen-like” or “helium-like” are easily measurable. These elements have been stripped of nearly all their electrons, leaving only one or two bound to the nucleus. As is the case with optical and infrared lines, the transition of the bound electron down to lower energy levels causes the emission of a photon. The energy of this photon is equal to the transition energy between the two states. It is a more complicated scenario for atomic species with multiple electrons. Due to more complex transitions between energy states, multiple lines are produced. Using current X-ray spectroscopic technology these lines are difficult to distinguish from each other. There is also continuum emission observed in soft X-rays which is described below.

Hard X-rays (2-50 keV) in SNRs can be either thermal or non-thermal in origin. Thermal X-rays are generally due to electrons in a hot gas colliding with nuclei due to their random thermal motions. This radiation is called ”thermal bremsstrahlung” and originates from the acceleration of electrons in coulomb collisions with other electrons and with ions and nuclei. Bremsstrahlung can also occur when electrons decelerate when they encounter electrons from atoms. Thermal bremsstrahlung produces a characteristic spectrum. Each collision event produces a photon, and the energy of the photon corresponds approximately to the change in energy that occurred during the collision. This radiation is also known as free-free emission as the electron is free before the interaction and free afterwards. Free-bound emission (or radiative recombination) can also take

place. This is when a proton or ion captures a free electron, emitting a photon in the process. The energy of the photon depends on both the kinetic energy of the electron and the orbital in which it is captured.

Non-thermal emission from particles is not related to the thermal motions of particles. Instead it is associated with synchrotron emission, i.e. the acceleration of electrons as they spiral around a magnetic field. This is the dominant non-thermal emission in SNRs, which is identical to the mechanism that produces radio waves, but is produced by much more energetic electrons. The maximum photon energy in keV of an electron with energy E is given by

$$h\nu = 1.93(E/100 \text{ Tev})^2(B/10/\mu G)\text{kev} \tag{1.16}$$

Gamma-rays can be produced by Bremsstrahlung, as both the thermal and non-thermal emission can account for photons of all energies. The highest energy Bremsstrahlung emission can be up to TeV. Another origin of gamma-ray radiation is the inverse-Compton scattering caused by the interaction relativistic electrons with cosmic microwave background or far-infrared photons, which can upscatter the photons to very high energies. There is one more source of gamma-ray emission, which is the decay of neutral pions, or π^0 particles, into two gamma-ray photons. This process occurs 98.7% of the time for π^0 decay. The π^0 particles are produced in collisions between cosmic-ray protons and thermal protons, as well as protons and alpha particles in the pre-shock gas.

1.8 Cosmic-rays

Cosmic-rays are highly energetic particles streaming through space at relativistic speeds. In actual fact about 89% of cosmic rays are protons, 10% are alpha particles, and 1% are the nuclei of heavier elements. These nuclei constitute 99% of the cosmic rays, the remaining 1% are mainly electrons (Swordy 2001). The measured cosmic ray spectrum ranges from 1 MeV to 10^{11} GeV. The large range of cosmic-ray energies reflects a wide variety of sources.

Supernovae are known to accelerate electrons to produce cosmic rays (Morlino & Caprioli 2012). The explosion mechanism is not understood for metal-free stars and hence the spectrum of cosmic rays that are produced by these high redshift stars is unknown. When Stacy *et al.* (2010) theorised the cosmic ray energy spectrum produced by a PISN, they chose values which produced a spectrum close to the spectrum observed in the Milky Way.

Cosmic-rays interact with the interstellar medium in two ways: spallation and ionisation. High energy cosmic rays cause spallation by colliding with matter which results in the expulsion of a large number of nucleons from the target object. Low energy cosmic-rays (< 1 Gev) are responsible for ionising matter, producing electrons with a spectrum of energies. These electrons may cause secondary ionisations. Therefore low energy cosmic rays are known to be important drivers of chemistry in the local ISM, especially within molecular clouds.

The low-energy cosmic ray flux measured near the Earth requires correcting for the effects of the solar wind and therefore cosmic ray rate determined from this value is uncertain. Observed abundances of $H_3{}^+$ in diffuse molecular clouds indicates the average interstellar cosmic-ray ionisation rate is 2×10^{-16} s^{-1} (Indriolo *et al.* 2007). This ionisation rate within molecular clouds is derived from the $H_3{}^+$: H_2 ratio. As $H_3{}^+$ is produced by the products from CR reactions and H & H_2, for example:

$$\begin{aligned} H_2 + CR &\rightarrow H_2^+ + e^-, \\ H_2^+ + H_2 &\rightarrow H_3^+ + H. \end{aligned}$$

1.9 SN triggered star formation

There is observational evidence that SN can trigger star formation within our Galaxy, for example in Upper Scorpios (Preibisch *et al.* 2002) and the Cygnus Loop (Patnaude *et al.* 2002). Even our own Sun is thought to be formed by the interaction of a cloud with a SN shock. This has been confirmed by the discovery of short lived radio isotope ^{60}Fe within meteorites, whose abundance can only be explained by the impact of a distant Core Collapse SN shell (Boss & Keiser 2010).

One of the first studies into the link between SN shocks and star formation was by Woodward (1976). Boss (1995) showed isothermal shocks from a nearby AGB or distant SN can successfully trigger the collapse of a cloud and inject shock material into it. Foster & Boss (1996, 1997) furthered this work, by simulating a 2D cloud hit by an isothermal shock and confirmed the previous results. Therefore SN triggered star formation could only take place when SNR has become radiative. When the cooling within the shell becomes so rapid that the shell has the same temperature as the ambient medium, it can be modelled as an isothermal shock. Several AMR studies have confirmed this (Nakamura *et al.* 2006; Melioli *et al.* 2006) and found the formation of 'Rayliegh-Taylor fingers' by shock front instabilities are the physical mechanisms by which shock-material is injected into

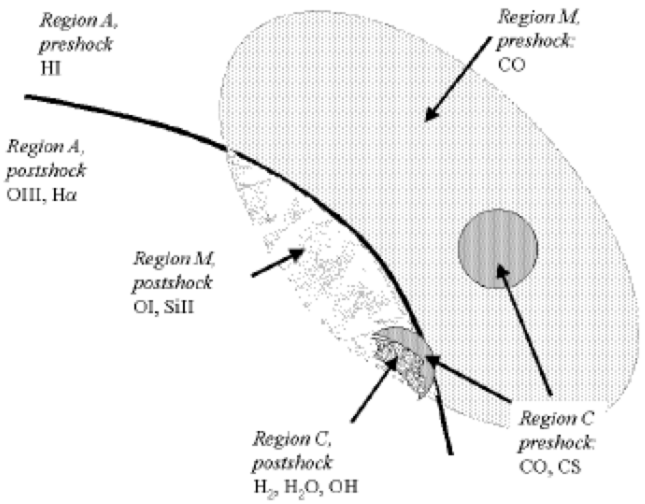

Figure 1.4: Schematic by Rho & Reach (2003) displaying a SN shock interacting with a neutral multi-phase cloud i.e. a cloud that contains dense cores

the collapsing cloud.

It is not physically accurate to model a SN as isothermal, one cannot always neglect the heating caused by compression of the shocked material. Vanhala & Cameron (1998) studied non-isothermal shocks and found that the shock could either trigger collapse or inject particles. However, these results have been debated as the authors used an SPH model, which was unable to properly simulate instabilities that occur. In contrast, Kaufman & Neufeld (1996), also studied non-isothermal shocks using a gridcode and found that shocks with velocity 5 -40 km s^{-1} could cause a clouds to collapse and inject material. To further validate their work, they successfully modelled the shock emission from Kleinmann-Low nebula in the Orion molecular cloud. Modern studies such Boss & Keiser (2010) stipulate that SN shocks start at velocities 10^3 km s^{-1} can only trigger collapse of a cloud once they have slowed down to 5 -70 km s^{-1}.

The previous studies all investigate a single density cloud. Molecular clouds are known to contain dense cores and considered to be 'clumpy', so to model a uniform density is an over simplification. Chevalier (1999) was the first to consider the two density regime for the preshock material, i.e. the cloud/core was placed in a inter-core material. They were able to model the IR emission from interaction of SNR IC 443 with a molecular cloud, with clump having a high density of 10^4 cm^{-3} surrounded by a moderate density of 10^2 cm^{-3}, with a shock velocity of 65-100 km

s^{-1} . This results in a ensemble of different shocks that develop on the small scale due to the high contrast in density. This model resolves the observation of SN shock velocities causing triggered star formation, which are higher than the predicted values from previous uniform density studies (Phillips & Marquez-Lugo 2010). This is due to the fact the shock velocity within the clump is much lower than the ambient medium (Reach *et al.* 2005).

This multiphase regime has been effective in modelling the IR emission from many other SNRs (Reach *et al.* 2002; Hewitt *et al.* 2009). The cores found within the pre-shock cloud are termed as 'prestellar cores', as they do not contain stars but after being perturbed by the SN shock are very likely to be formation sites for protostars (Reach *et al.* 2002). The outer layers of dense cores are stripped by the ram pressure of the shock. The stripping radius R_{st} is found by balancing the ram pressure force $p_{ram}\pi R^2$ with the gravitational force binding a thick layer with radius R from the centre $\frac{GM^2}{R^2}$, which is approximately

$$R_{st}\ 10^{17} \left(\frac{r_{10}^3}{EN_{51}}\right)^{\frac{1}{4}} \left(\frac{M}{M_\odot}\right)^{\frac{1}{2}} \text{cm}, \tag{1.17}$$

where EN_{51} is the supernova energy in units of 10^{51} erg, r_{10} is the radius of the (assumed adiabatic) remnant in units of 10 pc, and M is the mass of the clump. Reach *et al.* (2002) observed SNR 31 391 and found that the size of the clumps they observed in post shock clouds were comparable to the stripped radius given above. These clumps also had smaller radii than unshocked prestellar cores, thus confirming that the clumps are gravitationally bound cores stripped of their outer layers. Any clumps that encountered the SNR at an earlier stage would become a shocked filament rather than retaining a core structure. They comment that the surviving clumps would accrete matter slowly compared to other protostellar cores, due to the stripping of their outer layers.

The main aim of this work is to investigate the method of SN triggered star formation at high redshift. We first begin by understanding the chemistry that occurs in low-metallicity gas via a simple one zone model in Chapter 2. To explore this method at high redshift, we begin by developing a chemico-dynamic code, where a metal-free chemistry and cooling is coupled to a hydrodynamic code (Chapter 3). A toy model is set up, where a 15 $M_\odot$ cloud is shocked by a SN shell and the compression and fragmentation of the cloud is followed. We examine a range of microphysical processes that may affect the clumping and fragmentation. In Chapter 4 we extend our metal-free model by simulating the formation of a HII region around a 40 $M_\odot$ star in a number of gas clouds with differing density profiles and we explore a range of explosion energies. In

Chapter 5 we extend the toy model to study the effect of metal line cooling and molecular cooling on fragmentation of the clumps. We consider the effect of dust cooling on the formation of the SN shell. The nature and production of dust is not well understood at high redshift. Within the local ISM dust and its properties have been well observed but the formation mechanisms of carbon dust are not well constrained. In Chapter 6 we have carried out an investigation of the chemical evolution of gas in different carbon-rich circumstellar environments to ascertain whether there is a universal formation mechanism for carbon dust in strongly irradiated astrophysical environments.

CHAPTER 2

CHEMISTRY IN LOW-METALLICITY CLOUDS

2.1 Introduction

The first stars, known as Population III (Pop III) stars, played a pivotal role in the evolutionary history of the Universe. Their formation marked the end of the cosmic dark ages and began the introduction of heavy elements into the Universe (Bromm & Larson 2004). This chemical enrichment process introduced more effective coolants, which promoted thermal instabilities and smaller fragmentation scales. The hierarchical formation of dark matter haloes and the increasing metal fraction has led to the structures we see in the Universe today. Understanding the environment in which Pop III stars formed and died is an important open question in modern astrophysics. This therefore drives the science goals for many of the next generation of probes, such as the James Webb Space Telescope (Gardner *et al.* 2006) and the Square Kilometer Array (Johnston *et al.* 2008). These instruments may not be able to directly observe Pop III stars (without strong lensing) but will be able to probe the first galaxies. Due to the lack of direct observational evidence, there have been many studies that try to understand the Pop III formation process through computational modelling.

According to standard big bang nucleosynthesis, Pop III stars formed from a metal-free gas consisting of only hydrogen, helium and trace amounts of lithium (Coc *et al.* 2005). Simulations predict that Pop III stars started forming in dark matter haloes of mass $\sim 10^6$ $M_\odot$ (known as mini-haloes) between redshift $20 < z < 30$ (Bromm *et al.* 2009). Due to the limited amount of coolants available, these stars would have been much larger and more luminous than those observed in our local universe (Schaerer 2002). Presently the masses of these stars are still under investigation (Hasegawa *et al.* 2009), but are thought to be between 30 to 300 $M_\odot$ (Glover 2005;

Bromm & Yoshida 2011). The large range of masses is due to the fact that simulations of the formation of Pop III stars are computationally expensive which leads to approximations being made in the microphysics, and different studies include different feedback effects include from protostellar accretion.

There is also a strong dependence between initial mass of metal free stars and the redshift in which it is formed. As the lowest temperature to which the gas can be cooled is coupled to the CMB temperature. At later times ($z \approx 10$) it is found that lower mass Pop III stars can form. Once Pop III stars are formed, there is a radiative feedback effect i.e., the ionising radiation causes an increase in electron fraction. This catalyses the formation of molecules, which causes an increase in cooling and therefore it is possible to form smaller mass metal-free stars, known as Pop III.5 stars. So Pop III stars can have different initial masses depending on the time of formation and proximity to other stars.

The mass of the star corresponds directly to how they end their lives. Stars in the mass range 10-100 $M_\odot$ explode in a core collapse supernovae leaving behind a neutron star or black hole. Above 100 $M_\odot$, the progenitor star would experience a hypernova, which is an explosion with a much higher energy than a standard SN ($\sim 10^{52}$ erg). A progenitor with a mass within the range of 140-260 $M_\odot$ undergo a pair instability supernova (PISN) with an even higher explosion energy of 10^{53} erg (Heger & Woosley 2002). Each type of supernova would have different chemical yields, as different relative abundances of elements are produced due to the dependence on the energy of the explosion and the mass of star (Umeda & Nomoto 2002). At the moment there are two ways to observationally probe gas that may possibly have been polluted by a single supernova; stellar archaeology and Gamma Ray Burst studies.

Lower mass stars are formed from the material enriched by Pop III supernovae, and these are known as Population II stars. If these stars have a mass $\leq 0.8M_\odot$, their life span exceeds the current lifetime of the universe and therefore they would still be present today. Stellar archeology is based on the premise that the most metal poor stars observed in the Galactic Halo belong to the stellar generation that was formed from low metallicity gas left behind by the first stars. The atmospheres of these stars preserve the details of the chemical composition of their birth gas cloud and hence provide observational constraints on the nature of first stars, initial mass function and chemical yields of early supernovae. However, the extremely metal poor stars that provide this information are rare and hard to identify (Schörck *et al.* 2009).

The next generation of telescopes give us hope that we may be able to directly observe molecular clouds seeded by a single supernova, that have not been further processed by star formation or chemical enrichment. As each type of supernova produces a different chemical yield, it is safe to say there would be differences in abundances of different chemical species. It would be instructive to chemically model a cloud mixed with the ejecta from different types of supernova. This forms the main motivation of this work.

Cherchneff & Lilly (2008) were the first to carry out a detailed investigation of the chemical evolution of the ejecta from a massive primordial supernova. The ejecta from a single 170 $M_{\odot}$ PISN, was modelled for 1000 days after the initial explosion. The chemical network consisted of 79 species and 500 reactions. Photochemistry was not included, and the dynamics were not coupled with the chemistry. Two cases were explored: full mixing of the ejecta with the hydrogen envelope, and an unmixed case where the ejecta is stratified. They concluded that Pop III SNe are efficient sites for dust and molecule production. The abundances formed are dependent on the amount of atomic hydrogen present.

Cherchneff (2009) extended this work to include the fully mixed SN ejecta from 20$M_{\odot}$ and 270 $M_{\odot}$ progenitors. Neutral-neutral and radiative association reactions were found to be the main chemical pathways to molecule formation. Lower-mass progenitors were less efficient at forming molecular and dust components, whereas the higher mass progenitors had a delayed start to molecule formation due to their higher energy explosions. The author also comments on the unlikely nature of the molecules surviving the reverse shock that forms when the SN shock interacts with surrounding neutral medium. Cherchneff & Dwek (2009, 2010) investigate the same scenario as Cherchneff (2009) using a comprehensive chemistry network. They confirmed previous results, including the importance of a molecular formation model, as it is a bottleneck to dust formation and so studies that ignore it result in an overestimation of dust mass.

As each type of SN produces a different elemental yield, we would like to ascertain if it is possible to constrain molecular tracers of progenitor mass from a gas cloud that interacted with the SN ejecta. So when it is possible to observe molecular abundances in very low-metallicity gas by future observational probes, we can estimate the mass of the progenitor star. This is only possible if a gas cloud has been polluted by metals produced from a single SN, so the unique chemical yield of the SN is retained. In this work we follow the chemical evolution of a cloud mixed with ejecta from a single SN over 10^7 years. We investigate the chemical evolution from three different SN yields, in both a stable cloud (section 2.2.1) and a cloud undergoing gravitational collapse (section 2.2.2).

H^+	H_2	H_2^+	H_3^+	H^-	C^+	N^+	O^+
He^+	Na^+	CH	CH^+	CH_2^+	CH_3^+	CO	CO^+
O^+	O_2^+	C_2	C_2^+	C_2H	C_2H^+	OH	OH^+
H_2O	H_2O^+	HCO^+	H_3O^+	CN	CN^+	NH	HCN
HCN^+	C_2N^+	$HCNH^+$	$C_2H_2^+$	CH_2	CH_3	CH_4	CH_4^+
CH_5^+	C_2H_2	$C_2H_3^+$	C_3^+	C_3H	C_3H^+	C_3H_2	$C_3H_3^+$
CO_2	HCO_2^+	O_2H^+	NO	N_2	NH^+	NH_2	NH_2^+
NH_3	NH_3^+	NH_4^+	S^+	HS	HS^+	H_2S	H_2S^+
H_3S^+	CS	CS^+	HCS	HCS^+	SO	SO^+	SO_2
SO_2^+	OCS	H_2CS^+					

Table 2.1: 75 Chemical Species

2.2 The Chemical model

We are trying to determine which molecular tracers will be abundant at high redshift and whether they can constrain progenitor mass. Cherchneff (2009) commented that molecules are likely to be destroyed by reverse shocks, so molecules formed once the ejecta is introduced to the ambient medium will survive for a longer period of time. We model the chemical evolution that occurs when the ejecta from a Pop III SN has been well mixed with a primordial cloud at redshift $z \sim 17$. At this redshift, assuming ΛCDM, the SN occur in a dark matter halo of mass $\sim 10^6$ $M_\odot$, and we expect the ejecta to be expelled into the intergalactic medium (IGM) (Wise & Abel 2008) or stay within the dark matter halo.

The three different progenitor masses investigated are $80M_\odot$, $150M_\odot$ and $200M_\odot$. The chemical yields for each progenitor mass have been taken from the following studies: Chieffi & Limongi (2002, hereafter CL02), Umeda & Nomoto (2002, hereafter UN02) and Heger & Woosley (2002, hereafter HW02) corresponding to the cases of $80M_\odot$, $150M_\odot$ and $200M_\odot$ respectively.

The following molecules are studied: CO, H_2O, HCO^+, HCN, NO, NH_3 and CS. These molecules are known tracers of star forming regions in our Galaxy. Bayet *et al.* (2008) also investigated these molecules as tracers of star forming regions at high redshift. To explore different environments, we investigate both the case of a cloud in hydrostatic equilibrium and a cloud undergoing gravitational collapse. The chemical model incorporates 1071 gas phase chemical reactions with 7 elements (H, C, N, O, S, He and Na) and 75 molecular species (Table 2.1).

	$80M_{\odot}$	$150M_{\odot}$	$200M_{\odot}$
C/H	1.40×10^{-7}	1.40×10^{-7}	1.40×10^{-7}
O/H	4.54×10^{-7}	1.18×10^{-6}	1.53×10^{-6}
N/H	5.99×10^{-14}	3.24×10^{-10}	1.58×10^{-12}
S/H	7.59×10^{-9}	4.06×10^{-8}	1.54×10^{-7}
He/H	7.50×10^{-5}	7.50×10^{-5}	7.50×10^{-5}
Na/H	2.28×10^{-10}	2.07×10^{-10}	9.76×10^{-11}

Table 2.2: Table containing the initial elemental fractional abundances used for the three different progenitor masses

2.2.1 Stable Cloud

A gas parcel within a cloud in the IGM is allowed to chemically evolve for 10^7 years, so the species will gain equilibrium abundances. It is assumed that the cloud is not further affected dynamically, and is therefore in hydrostatic equilibrium. It is also assumed that the gas parcel is in local thermal equilibrium , and that the cloud is uniformly mixed with the supernova ejecta at time $t = 0$ s. Following Panagia (2005) and Wise & Abel (2008) we set the metallicity of the gas as 10^{-3} $Z_{\odot}$, as this is the predicted metallicity of gas found in a mini-halo enriched by a single Pop III star SN. The fractional abundance of carbon observed in diffuse interstellar clouds seeded by supergiants is $\left[\frac{C}{H}\right] = 1.4 \times 10^{-4}$, where H is the abundance of atomic hydrogen. This value can be scaled by metallicity of our cloud, to give us the mixing ratio for carbon of $[\frac{C}{H}]$=1.4×10^{-7}. The rest of the elements from the different chemical yields can be scaled relative to this value in the following manner; for an element X, the fractional abundance is

$$\left[\frac{X}{H}\right] = \frac{X}{C} \times 1.4 \times 10^{-7}. \tag{2.1}$$

The fractional abundances used in our model for the three different progenitor masses are presented in Table 2.2.

In the following subsection we will investigate the effect of various environmental factors that may influence the formation of molecules. This will illustrate the reasoning behind our choice of initial conditions for the model, which we will call the ‘standard model’. It is important to find which molecular tracers are least affected by the environmental conditions, as these will be the best indicators of progenitor mass. We investigate the effect of the following parameters on the chemical evolution of the cloud: density, gas temperature, cosmic ray ionisation rate, background

UV fields, and dust fraction. It is important to identify which molecular tracers are most 'stable', i.e their equilibrium values are least affected by different initial conditions.

2.2.1.1 Initial conditions

In our Galaxy the study of dense molecular clouds (or other areas which are shielded from UV radiation) have shown the importance of including cosmic ray (CR) ionisation in chemical modelling (Dalgarno 2006*a*). Cosmic rays can penetrate into these shielded areas ionising neutral material, producing electrons and positive ions which then drive the evolution of the chemistry. Cosmic rays are expected to be generated by supernova explosions, and at high redshift a weak Cosmic Ray Background is expected to have built up from the first SNe. If a Pop III star is formed at redshift 20, then it will undergo a supernova around redshift 17 (Schaerer 2002). We calculated the background CR ionisation rate in the dark matter halo at redshift z≈17, using the relation given by Stacy & Bromm (2007):

$$\zeta \approx 10^{-19}\mathrm{s}^{-1}\frac{\mathrm{U_{cr}}}{2\times10^{-15}\mathrm{erg\ cm}^{-3}}\left(\frac{\epsilon_{\mathrm{min}}}{10^{7}\mathrm{eV}}\right)^{-1.3}, \tag{2.2}$$

where U_{cr} is the redshift-dependent energy density of the CR, and ϵ_{min} ($= 10^6$ eV) is the minimum energy of the CRs. Using the normalised constants given by Stacy & Bromm (2007) for calculating the redshift-dependent energy density of the CR; we get a background CR ionisation rate of $\approx 10^{-18}$ s^{-1} for redshift z = 17. Observations show that molecular clouds near or in the vicinity of a SN remnant can encounter a CR ionisation rate one hundred times greater than the galactic CR background rate (Ceccarelli *et al.* 2011). In Figure 2.1(a) we investigate the effect of varying the CR ionisation rate on the equilibrium abundance of molecular tracers in the 80 $M_\odot$ case. Increasing the CR rate has a mixed effect on molecular abundances, depending on whether the formation and/or destruction rate is affected by the increase of electrons and ions. Nitrogen oxide (NO) and Carbon monoxide (CO) are the least influenced, maintaining a constant fractional abundance. The other molecules have such low abundances that in terms of observation (minimum required fractional abundance is 10^{-12}) the change of abundance can be considered negligible. For our standard model, the cosmic ray ionisation rate is taken from the equation above to be $10^{-18}\mathrm{s}^{-1}$.

Molecular clouds in our Galaxy are subject to a diffuse interstellar radiation field (Draine 1978), which is in the UV and formed mainly from the contribution of massive stars. The radiation field at high redshift for molecular clouds in the IGM is poorly constrained. In Figure 2.1(b) we model a gas cloud subjected to a flux, measured as a percentage of the Galactic interstellar radiation field.

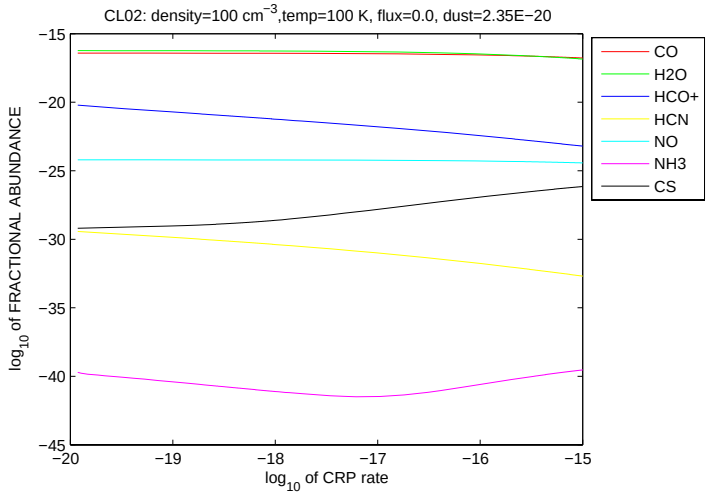

(a) Cosmic ray ionisation rate

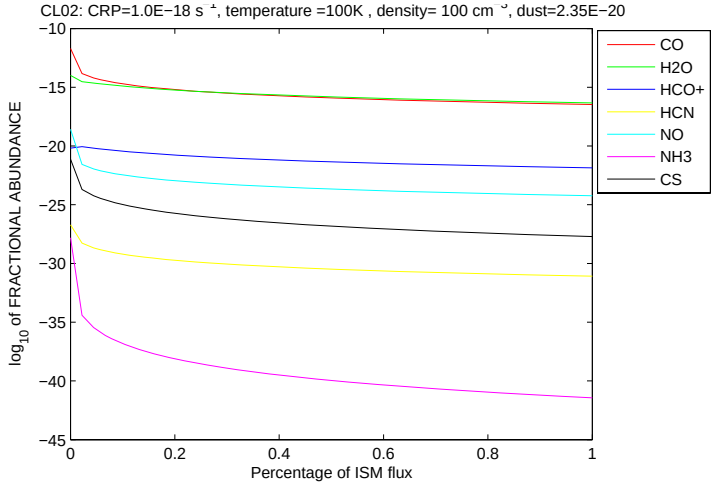

(b) Flux

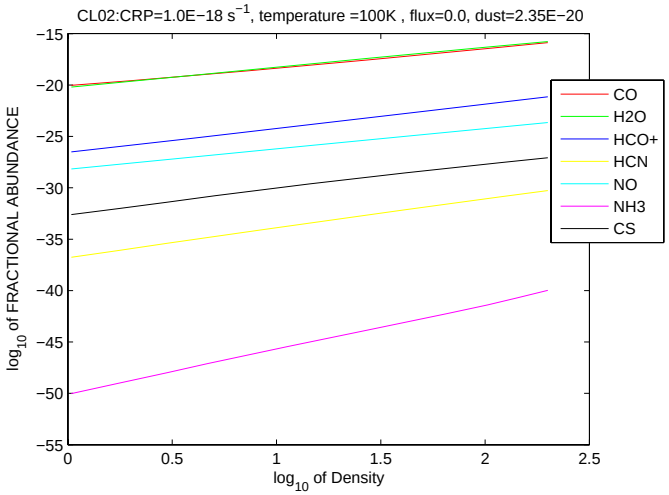

(c) Density

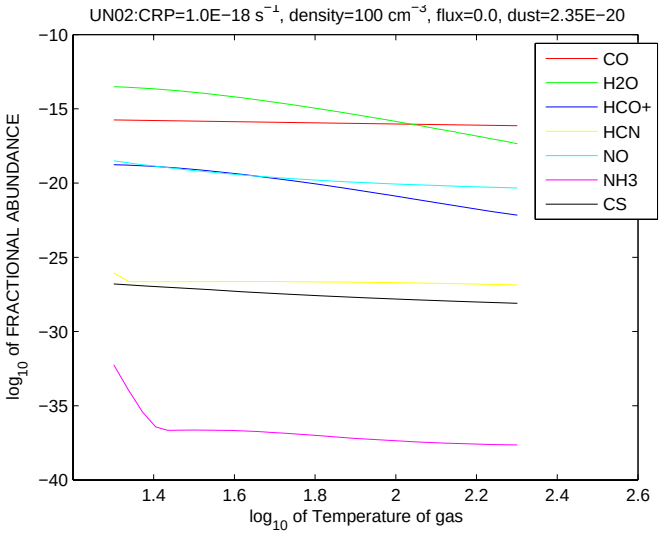

(d) Temperature

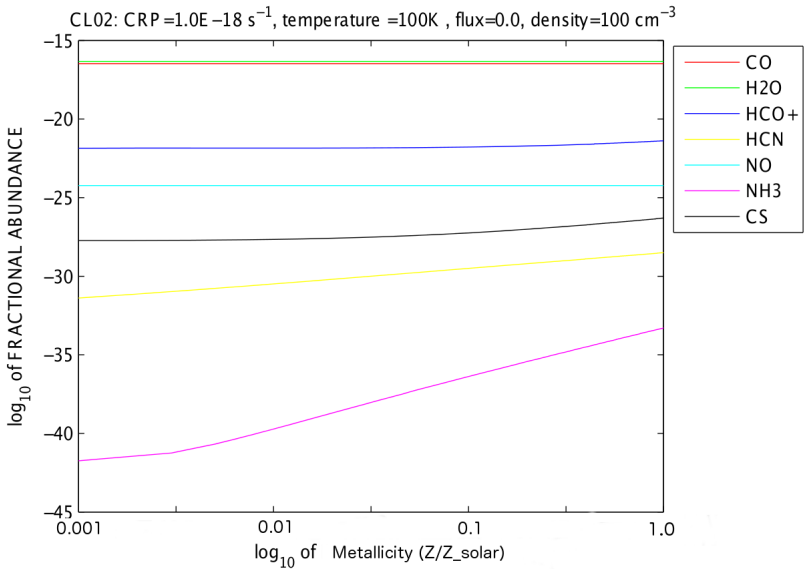

(e) dust fractional abundance

Figure 2.1: Initial conditions parameter investigation for the standard model. Molecular abundance for varying density, temperature, dust fractional abundance, flux and cosmic ray ionisation rate, for the 80 $M_{\odot}$ case are displayed.

The largest change in the molecular equilibrium abundances is between a completely shielded area (0% flux) and 10% flux. The effect of UV radiation on all the molecules is negative. The gas with the most abundant molecular fractions is formed in a completely shielded area, and so this is the scenario we will consider in the standard model.

In a ΛCDM universe, the density of neutral hydrogen in a mini halo cooled to the lowest possible temperature (CMB temperature) is 1cm^{-3} at z=20 and 100cm^{-3} at z=15. This density range is examined and the results are shown in Figure 2.1(c). Density affects all the molecular tracers in the same way, i.e., the abundances below 100 cm^{-3} drop significantly. In our standard model we model the gas density of the cloud to be 50cm^{-3}. This is the density of the gas around a star 10 pc away from the progenitor star but still within the dark matter Halo (Yoshida et al. 2007) and this is the neutral stationary gas that is expected to be injected with metals from the SN.

We also investigated the effect of temperature on the gas cloud and on the equilibrium abundances for the 80 $M_{\odot}$ case, which is shown in Figure 2.1(d). At z=20 the virialised temperature of a primordial gas cloud in a mini halo is 200K (Stacy & Bromm 2007) and so this was taken as an upper limit. We found that the most of the molecular tracers abundances of most molecules do not vary greatly with temperature. However there is a significant effect on water, which is close to the observable range below 50 K and then drops significantly. The change in abundance for water (i.e. 10^{-13} to 10^{-17}) is much more significant than the decrease in abundance for HCO^{+}(10^{-19} to 10^{-23}). Ammonia (NH_3) is the only molecule to show a significant decrease in abundance at temperatures above 15K, however this abundance is too low to be observed and the temperature is not achievable at z = 17 as the CMB temperature is ~ 50 K. At redshift $z = 17$, it is reasonable to assume the gas is at a temperature of 100K as this is the lower end of the temperature range that the low- density gas (n $\sim 10^4$ cm^{-3}) can cool in a metal free environment (Glover & Abel 2008). Therefore this is the temperature adopted for the gas in the standard model.

The amount of dust produced by Pop III SNe and high mass stars at large redshift is under considerable debate (Gall *et al.* 2011), as observations of high redshift galaxies and QSOs show large amounts of dust present. Dust is an important constituent of SN ejecta, as the grain surfaces provide a formation site for molecules such as H_2 (Watson & Salpeter 1972). The effect of dust (fractional abundance) within our model is incorporated directly via the surface dust grain formation rate of molecular hydrogen (Rawlings *et al.* 1992). The fractional abundance of dust in a solar metallicity cloud is 10^{-12} (Herbst 1993); we vary the fractional abundance of dust below this value

to observe its effects on the molecular abundances. The only effect of dust that we include in this model is that the grain surface acts as a catalyst to form molecular hydrogen, therefore we scale the reaction rate by metallicity. The results are shown in figure 2.1(e). The presence of dust only influences abundances of molecules whose formation network is dependent on H_2 abundances. This is mainly NH_3, HCN and CS, which are all below the observable limit. As dust is such a unconstrained parameter we will simply scale the fractional abundance of dust with metallicity, ($Z/Z_\odot$=10^{-3}) i.e. $\frac{\text{dust}}{\text{H}} = 10^{-15}$ (by number).

2.2.2 Infalling Cloud

The gas from Pop III SN explosion can be ejected into the IGM where it may then accrete into another dark matter halo. An interesting situation arises for dark matter halos $< 10^{11}\,M_\odot$: if the velocity of the neutral gas is low, it may accrete without being shock heated; this is known as 'cold flow' (Dekel & Birnboim 2006). If the ejecta does not leave its host dark matter halo, the gas can recombine to form cool neutral gas. In both these cases the gas is likely to undergo gravitational collapse. Therefore we consider the concept of an infalling parcel of gas. Due to the increase in density, we expect the molecular abundances for the infalling gas to increase. This may amplify the tracers of progenitor mass to an observable level. The estimates for time of recollapse of the gas within a mini halo after a SN, range from 10 million years (O'Shea *et al.* 2005) to 100 million years (Yoshida *et al.* 2007).

We explore a simplistic model in which the neutral gas is located within a large enough potential well to undergo gravitational collapse. We assume the gas has a uniform metallicity (where the metals originate from a single SN) and is not undergoing any thermal shocks etc. We look at two infall cases: i) the temperature remains constant as the density increases and ii) gas which increases in temperature as the density increases. The second model is analogous to cores which may become hot cores, which is the first stage of pre-stellar formation. It is assumed that gas in both infall models has the same metallicity ($10^{-3}\,M_\odot$) described for the stable cloud model. The elemental fractional abundances are outlined in Table 2.2 for three different SN yields. The dust fraction is scaled with metallicity, so w assume the fractional abundance by number is $\frac{\text{dust}}{\text{H}} = 10^{-15}$. We assume there is no UV radiation present. The cosmic ray ionisation rate is $10^{-18}\,s^{-1}$. The scenario where there are no cosmic rays present is also considered. This is because the cosmic rays from SNR die away after a few million years, and it gives us the opportunity to observe the effect of cosmic rays on the system.

Simulations by Greif *et al.* (2010) study the formation of an dark matter halo ($\sim 10^8\,\mathrm{M}_\odot$) at redshift $z = 10$ and the evolution of the gas that it contains. They found dense pockets of gas with a density of 100 cm^{-3} and a temperature of 100 K. This gas has a fractional abundance of $\mathrm{H}_2 = 10^{-3}$, which indicates a high molecular fraction for this redshift. We take these values of temperature and density as our initial conditions for both infall models. We first allow the gas to chemically evolve at a constant density for 10^6 years. This is to achieve equilibrium values of the chemical species, the gas is then allowed to undergo collapse, which is followed in performing a single point calculation. This includes a semi-analytic model written by Prof JMC Rawlings implementing the self-similar solution to gravitational isothermal collapse described by Shu (1977). As the density of the collapsing cloud increases the chemical evolution of a gas parcel is followed.

The initial conditions and dynamic evolution corresponding to the two different infall models are summarised below.

2.2.2.1 Infall with constant temperature

The time-dependent fractional abundances of molecules in a gas parcel undergoing collapse are followed. To acquire equilibrium abundances a cloud of density $100\,\mathrm{cm}^{-3}$ and temperature 100 K is allowed to chemically evolve for 10^6 years. Then free fall collapse is initiated. A single point calculation is performed, the density is allowed to increase. The density increases from 100 cm^{-3} to $10^7\,\mathrm{cm}^{-3}$. The density is terminated here as the gas can be approximated as isothermal. This assumption holds as long as the gas is more or less optically thin and the energy exchange by radiation is efficient.

2.2.2.2 Infall with increasing temperature

The initial conditions are the same as the previous infall model, i.e. the density is 100 cm^{-3} and the temperature is 100 K. Before collapse the cloud is allowed to chemically evolve for 10^6 years. Once collapse is initiated, the density increases to $10^5\,\mathrm{cm}^{-3}$ without any change to the temperature. When the density increases further (above 10^5 cm^{-3}) the gas start to become optically thick, and the heat from the compression cannot be radiated away. Therefore the temperature increases between the densities of $10^5\,\mathrm{cm}^{-3}$ and $10^{10}\,\mathrm{cm}^{-3}$, and finally reaches 1000 K. We keep the dust model simple and therefore only include H_2 surface chemistry. Therefore freeze-out or mantle desorption are not included, as we are not focussing on complex molecule formation.

2.3 Results and discussion

2.3.1 Stable cloud

The results of the standard model are displayed in Figure 2.2, where one can see the chemical evolution of the cloud for the three different cases investigated. The final abundances for all three cases are shown in Table 2.3. The initial abundances for all the molecular species is set to 10^{-20}, hence the initial conditions represent a neutral atomic cloud. An important molecule which has not been included in this figure is H_2, which has a fractional abundance of $H_2/H \simeq 10^{-3}$ after 10^7 years for all three cases. Even though the gas has a finite metallicity and therefore contains dust, the main formation pathway is

$$H^- + H \rightarrow H_2 + e^-,$$

which is the favoured route at high redshift, and its main destruction pathway is with cosmic rays

$$H_2 + \mathrm{crp} \rightarrow H_2^+ + e^-.$$

The OH formation and destruction routes are quite different from the ISM at $z = 0$ (and not dependent on H_2). In this case OH is predominantly formed and destroyed by the following reactions:

$$\begin{aligned} H + O &\rightarrow OH + \text{photon}, \\ H^+ + OH &\rightarrow OH^+ + H. \end{aligned}$$

The abundance of OH peaks at around 10^5 years, after which point the ionisation level is significant ($\frac{H^+}{H} > 10^{-5}$) and so the destruction rate starts to dominate. The molecule nitrous oxide (NO) is produced and destroyed by two neutral-neutral reactions, as follows:

$$\begin{aligned} N + OH &\rightarrow NO + H, \\ C + NO &\rightarrow CO + N \end{aligned}$$

NO is thus dependent on the abundance of OH, and therefore the production of NO also decreases after 10^5 years. A secondary formation route takes over, which is

$$NH + O \rightarrow NO + H,$$

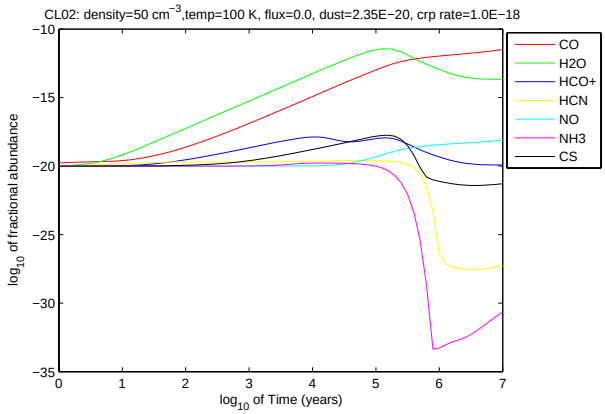

(a) 80 $M_{\odot}$

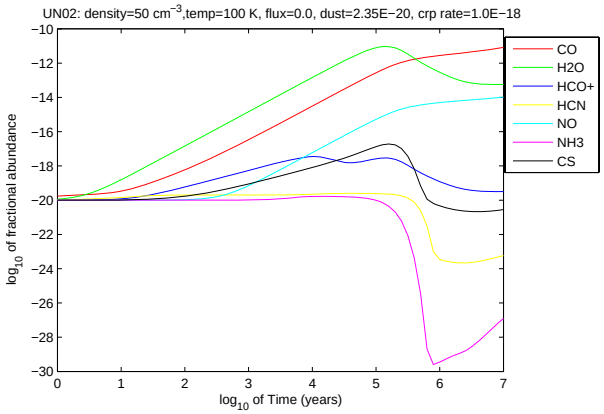

(b) 150 $M_{\odot}$

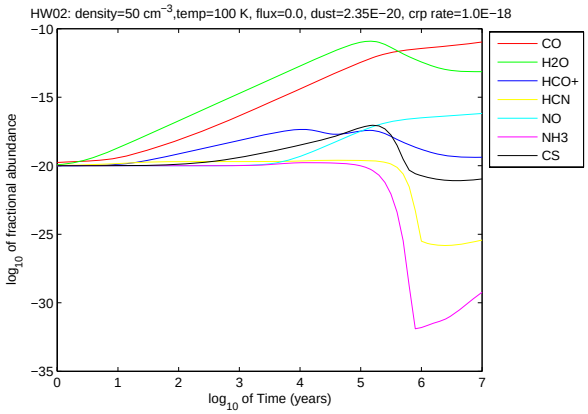

(c) 200 $M_{\odot}$

Figure 2.2: Standard Model - time dependent chemical evolution of a stable gas parcel for the three progenitor masses: 80 $M_{\odot}$ 150 $M_{\odot}$ and 200 $M_{\odot}$

which can form NO using the freed oxygen from OH destruction. The NH is formed predominately by the reaction

$$\mathrm{NH_3^+} + e^- \rightarrow \mathrm{NH} + \mathrm{H} + \mathrm{H}.$$

The molecule $\mathrm{NH_3^+}$, is formed via the main destruction of ammonia ($\mathrm{NH_3}$), when it interacts with electrons. The formation path of ammonia is the same as in the ISM of our Galaxy:

$$\mathrm{N^+} \overset{\mathrm{H_2}}{\rightarrow} \mathrm{NH^+} \overset{\mathrm{H_2}}{\rightarrow} \mathrm{NH_2^+} \overset{\mathrm{H_2}}{\rightarrow} \mathrm{NH_3^+} \overset{\mathrm{H_2}}{\rightarrow} \mathrm{NH_4^+}$$
$$\mathrm{NH_4^+} + \mathrm{e^-} \rightarrow \mathrm{NH_3} + \mathrm{H}.$$

There is a strong drop in the abundance of ammonia at $\sim 10^6$ years, as the gas has recombined and so eliminating free electrons. Therefore all the nitrogen molecules are more likely to form NO as it is formed by neutral-neutral reactions. The main destruction pathway of NO is a reaction with neutral carbon, which is very abundant and remains almost constant throughout the chemical evolution of the cloud.

The abundance of CO increases to an asymptotic value for all three cases and is the most abundant tracer. The production of this molecule is is also dependent on OH:

$$\mathrm{C} + \mathrm{OH} \rightarrow \mathrm{CO} + \mathrm{H}.$$

The destruction pathways is the same as the ISM at $z = 0$, i.e

$$\mathrm{CO} + \mathrm{He^+} \rightarrow \mathrm{C^+} + \mathrm{O} + \mathrm{He}.$$

For $\mathrm{He^+}$ to be abundant requires a high level of ionisation. As there is only a weak ionising field present due to the cosmic ray flux, the abundance of CO steadily increases.

The water molecule is the second most abundant molecular tracer, though at earlier times (i.e., before 10^5 years) it is more abundant than CO. Water has the following formation and destruction pathways:

$$\begin{aligned} \mathrm{H_3O^+} + e^- &\rightarrow \mathrm{H_2O} + \mathrm{H}, \\ \mathrm{H^+} + \mathrm{H_2O} &\rightarrow \mathrm{H_2O^+} + \mathrm{H}. \end{aligned}$$

	80 $M_\odot$	150 $M_\odot$	200 $M_\odot$
CO	3.12×10^{-12}	8.34×10^{-12}	1.08×10^{-11}
H_2O	2.19×10^{-14}	5.69×10^{-14}	7.37×10^{-14}
HCO^+	1.22×10^{-20}	3.19×10^{-20}	4.16×10^{-20}
HCN	5.50×10^{-28}	5.78×10^{-24}	3.73×10^{-26}
NO	7.49×10^{-19}	1.04×10^{-14}	6.58×10^{-17}
NH_3	2.33×10^{-31}	1.25×10^{-27}	5.87×10^{-30}
CS	5.18×10^{-22}	2.82×10^{-21}	1.08×10^{-21}

Table 2.3: Standard Model: fractional abundances of molecular tracers after 10^7 years

H_3O^+ is formed from H_2O^+, but this is not a cyclic pathway as H_2O^+ is neutralised via the following reaction:

$$H_2O^+ + e^- \rightarrow O + H + H.$$

which has a rate ($= 10^{-7} \times (T/300)^{0.5}$), this is an order of magnitude higher than the rate for reaction H_2O^+ +e^- $\rightarrow$ OH +H. The formation of H_3O^+ is via the same pathway as in the ISM at $z = 0$:

$$OH^+ \overset{H_2}{\rightarrow} H_2O^+ \overset{H_2}{\rightarrow} H_3O^+.$$

Hence the formation of H_2O is strongly driven by the OH^+molecule. This molecule is primarily formed from a proton reacting with OH. Therefore water exhibits a similar peak in formation at 10^5 years, due to its dependence on the OH abundance and sensitivity to the ionisation fraction.

The molecule HCN is controlled by the following reaction:

$$HCN^+ + H \quad \leftrightarrow \quad HCN + H^+.$$

However it also has formation reactions which have very small reaction rates

$$H^- + CN \quad \rightarrow \quad HCN + e^-,$$
$$H_2 + CN \quad \rightarrow \quad HCN + H.$$

As the ionisation of the gas decreases with time due to recombination, the destruction reaction becomes dominant and hence the abundance of HCN becomes negligible. Another tracer with a

very low abundance is CS, which is formed via the reactions

$$\begin{aligned} CH + S^+ &\rightarrow CS^+ + H, \\ H_2 + CS^+ &\rightarrow HCS^+ + H, \\ HCS^+ + e^- &\rightarrow CS + H \end{aligned}$$

and is destroyed only by the reaction

$$CS + H^+ \rightarrow CS^+ + H,$$

which dominates as the cloud becomes more ionised.

From Table 2.3, we can see that after 10^7 years the main difference in the final abundances is between molecules containing nitrogen. The nitrogen-bearing species are low in abundance compared to CO and H_2O. Both HCN and NH_3 are sensitive to environmental parameters, as shown in Figure 2.1. The best candidate for a molecular tracer of progenitor mass in a shielded environment is NO. It is least affected by ionisation levels as both formation and destruction routes are neutral-neutral reactions (Figures 2.1(a) & 2.1(b)). Dust does not effect its formation or destruction as both processes are not influenced by the abundance of H_2. It also has a very stable abundance across the temperature range investigated in Figure 2.1(d).

At high redshifts ($z \sim 10$) it will be quite difficult to observe most of the molecules being investigated. As carbon monoxide is the most abundant molecule out of all the tracers and reaches an abundances that are more likely to be observed. As the parameters that govern the chemistry at such high redshift are still undetermined, we investigated a range of parameters in which CO could be produced. For example, there may be a region where there is more UV flux. So the values of gas temperature, dust abundance, UV flux and CR rate were varied with density. The results for column density of CO, were calculated assuming a pathlength of 183 pc and are shown in Figure 2.3. This value was chosen from large clouds formed in simulations of atomic cooling haloes at redshift $z = 10$ (Greif et al. 2010). The results are showing the equilibrium abundances for the 80 $M_\odot$ model.

Figure 2.3(a) displays the sensitivity of the results due to cosmic ray ionisation rate and density. It is assumed that there is no UV radiation present. The following parameters are kept constant: gas temperature =100 K, metallicity of the gas is Z= $10^{-3}Z_\odot$ and dust fractional abundance is scaled

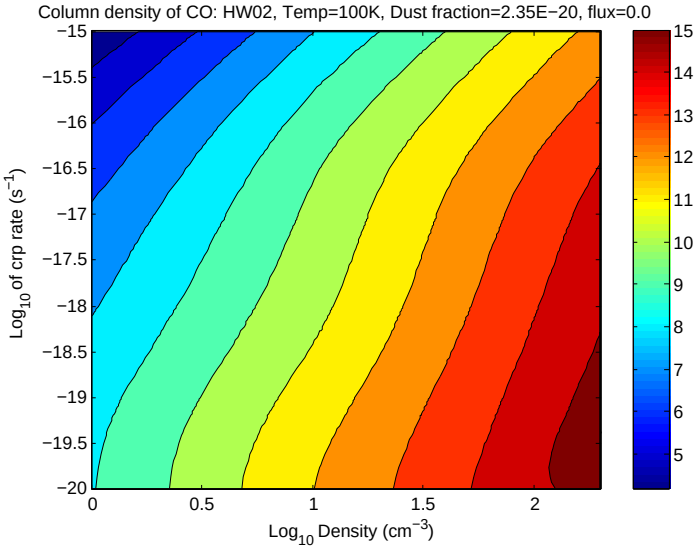

(a) CR ionisation rate

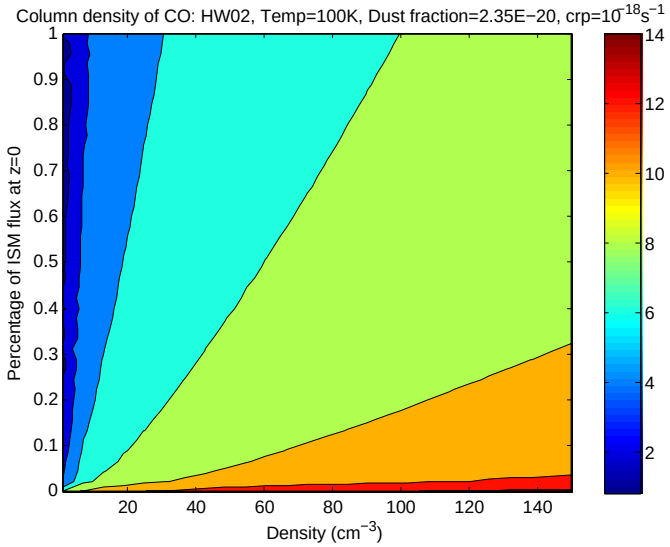

(b) Flux

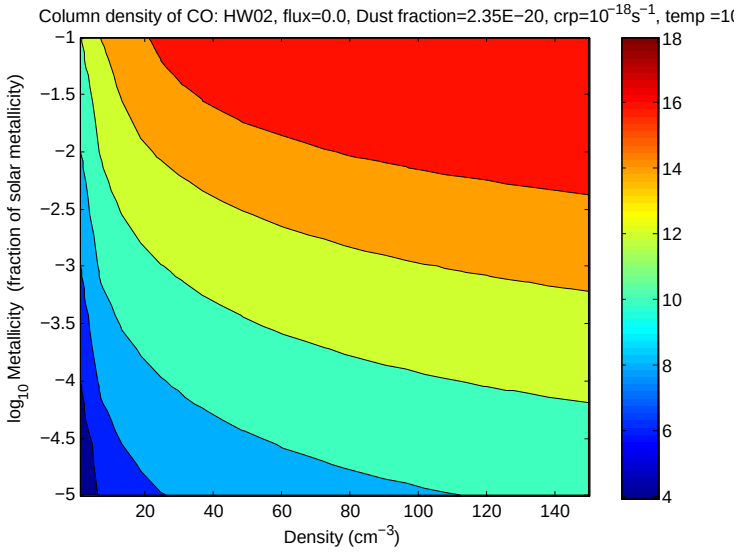

(c) Metallicity

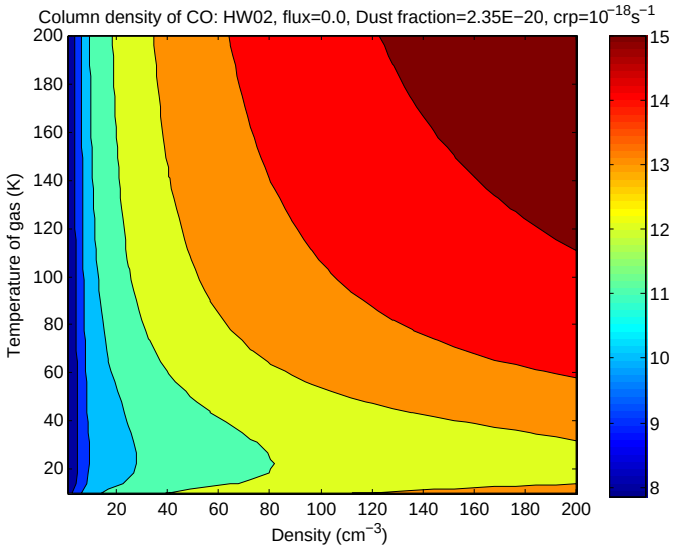

(d) Temperature

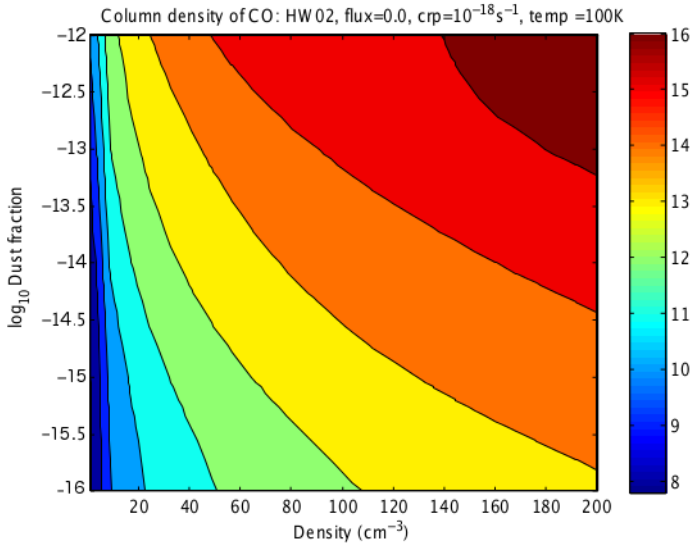

(e) Dust fractional abundance

Figure 2.3: Investigating how the column density ($\log_{10}$) of CO varies with the following parameters: density, temperature, dust fractional abundance, metallicity, flux and cosmic ray ionisation rate for the 80 $M_{\odot}$ case

with metallicity (2.35×10^{-20}). It is evident that a low background cosmic ray ionisation rate ($< 10^{-18}\,\mathrm{s}^{-1}$) and high density ($n > 10^{1.5}\,\mathrm{cm}^{-3}$) provides an environment where CO production is at its greatest.

Figure 2.3(b), the UV radiation is varied as a percentage of the Galactic interstellar radiation field. The following parameters are kept constant: gas temperature =100 K, cosmic ray ionisation rate $= 10^{-18}\,\mathrm{s}^{-1}$, the metallicity of the gas is Z$= 10^{-3}$Z$_\odot$ and dust fractional abundance is scaled with metallicity (10^{-15}). As expected the highest amount of CO is produced when there is no UV radiation present. The increase in density makes very little difference to the CO column density.

The metallicity in the gas can vary due to mixing and diffusion, so we have investigated metallicity (=Z/Z$_\odot$) against density. We do not expect metallicity to ever be higher than Z$= 10^{-2}$ (Grief et al, 2010), however it is included for the purpose of comparison. The following parameters are kept constant: gas temperature =100 K, cosmic ray ionisation rate $= 10^{-18}\,\mathrm{s}^{-1}$ and it is assumed that there is no UV flux present. From Figure 2.3(c), we can see that only gas with metallicity Z$\geq 10^{-3}$Z$_\odot$ will have CO column density which is greater than 10^{13}. We assume below this value that it will not be possible to observe CO at all.

In Figure 2.3(d), we vary the temperature of the gas against density. The following parameters are kept constant: cosmic ray ionisation rate $= 10^{-18}\,\mathrm{s}^{-1}$, the metallicity of the gas is $Z = 10^{-3}$Z$_\odot$ and dust fractional abundance is scaled with metallicity and it is assumed that there is no UV flux present. The temperature of the gas has a great effect on the abundance of CO if the temperature is above 60 K and the density above $n = 50\,\mathrm{cm}^{-3}$.

Finally we investigate the amount of dust present in the gas. As this is an uncertain value, there is much debate over the dust-to-gas ratio and the size of the dust grains at high redshift (Dwek & Cherchneff 2010). We investigate a range of fractional abundances for dust with a set constant metallicity of $Z = 10^{-3}\,\mathrm{Z}_\odot$. The upper limit is set to the value found in the ISM at redshift zero $z = 0$. The following parameters are kept constant: cosmic ray ionisation rate $= 10^{-18}\,\mathrm{s}^{-1}$, the metallicity of the gas is $Z = 10^{-3}$Z$_\odot$, the temperature of the gas is 100 K and it is assumed that there is no UV flux present. The dust fraction must be higher than 1.0×10^{-19} within a gas cloud of density $n \geq 60\,\mathrm{cm}^{-3}$, for the column density of CO to be high enough that observations maybe considered.

So in summary the most advantageous physical environment for the production of CO would be: high density ($n > 100\,\mathrm{cm}^{-3}$), high temperature (T$>$ 100 K), a high abundance of dust grains

($> 3 \times 10^{-15}$), a low ionisation rate from cosmic rays ($\leq 10^{-16}\,\mathrm{s}^{-1}$) and shielded from UV radiation. This makes physical sense as a high dust fraction would allow the gas to cool to form neutral gas at high redshift.

2.3.2 Infalling cloud

2.3.2.1 Infall with constant temperature

	80 $M_\odot$		150 $M_\odot$		200 $M_\odot$	
	CRI rate = $0\,\mathrm{s}^{-1}$	CRI rate = $10^{-18}\,\mathrm{s}^{-1}$	CRI rate = $0\,\mathrm{s}^{-1}$	CRI rate = $10^{-18}\,\mathrm{s}^{-1}$	CRI rate = $0\,\mathrm{s}^{-1}$	CRI rate = $10^{-18}\,\mathrm{s}^{-1}$
CO	3.09×10^{-8}	5.50×10^{-8}	1.15×10^{-7}	1.38×10^{-7}	1.38×10^{-7}	1.41×10^{-7}
H_2O	4.27×10^{-7}	3.98×10^{-7}	1.07×10^{-6}	1.02×10^{-6}	1.32×10^{-6}	1.23×10^{-6}
HCO^+	4.79×10^{-20}	1.23×10^{-13}	1.91×10^{-20}	3.89×10^{-14}	1.26×10^{-24}	4.79×10^{-14}
HCN	1.82×10^{-15}	3.09×10^{-15}	1.26×10^{-11}	1.34×10^{-11}	3.89×10^{-14}	1.32×10^{-14}
NO	3.09×10^{-19}	2.34×10^{-17}	3.81×10^{-14}	1.34×10^{-11}	1.02×10^{-13}	2.45×10^{-13}
NH3	3.89×10^{-29}	4.46×10^{-21}	1.51×10^{-28}	2.45×10^{-17}	8.91×10^{-26}	1.05×10^{-18}
CS	5.37×10^{-11}	9.12×10^{-11}	2.69×10^{-9}	2.63×10^{-9}	9.33×10^{-10}	2.69×10^{-10}

Table 2.4: Final fractional abundance of molecular tracers for the case of infalling cloud with constant temperature. Two cases are investigated with the cosmic ray ionisation rate (CRI) of $0\,\mathrm{s}^{-1}$ and $10^{-18}\,\mathrm{s}^{-1}$

The results for the case of infalling gas with constant temperature, are displayed in Table 2.4. All three cases are investigated (i) with a cosmic ray ionisation rate of $10^{-18}\,\mathrm{s}^{-1}$ and (ii) without cosmic rays present. Figures 2.4 – 2.6 display the results for the scenario with the cosmic rays present. The figures are displayed in two ways: part (a) displays the chemical evolution of the infalling cloud against time (the infall begins at a million years), and part (b) displays the chemical evolution as a function of density. Even though molecular hydrogen is not displayed on the graph, its formation path is the same as the stable cloud but its fractional abundance has increased to ~ 0.14 at 10^7 years for both cases.

In the stable cloud model carbon monoxide (CO) was the most abundant tracer. But in the infalling model with constant temperature, the increase in density causes CO to be the second most abundant tracer. At the maximum density the two main formation reactions are

$$\mathrm{C} + \mathrm{SO} \rightarrow \mathrm{CO} + \mathrm{S},$$

$$\mathrm{C} + \mathrm{O_2} \rightarrow \mathrm{CO} + \mathrm{O}.$$

The destruction pathways are dependent on the cosmic ray rates; when there are no comic rays the

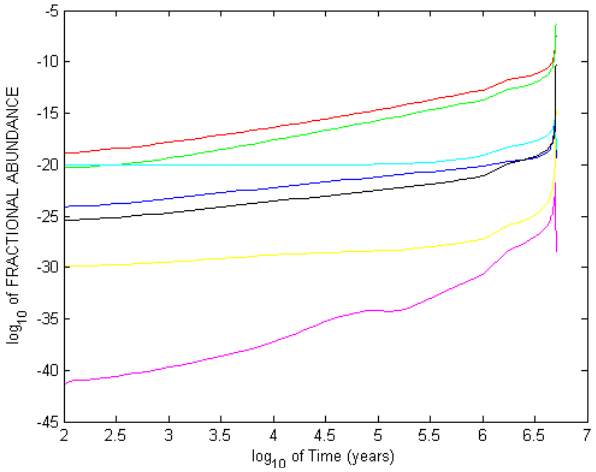

(a)

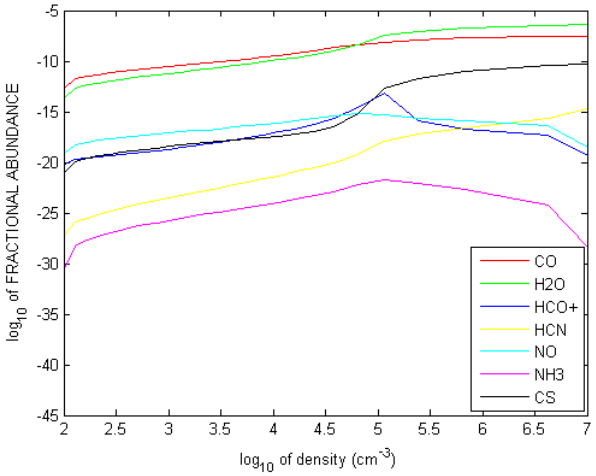

(b)

Figure 2.4: Infall model with constant temperature: 80 $M_\odot$ progenitor mass

dominant reaction is

$$CO + OH \rightarrow CO_2 + H$$

which has a rate $\sim 10^{-18}\,s^{-1}$ and with cosmic ray ionisation rate present the dominant reaction is

$$CO + H_3^+ \rightarrow HCO^+ + H_2.$$

which has a higher rate of $\sim 10^{-14}\,s^{-1}$. There is an overall increase in CO when cosmic rays are present, (for a cosmic ray ionisation rate is $10^{-18}\,s^{-1}$) the formation rate is $10^{-5}\,s^{-1}$, compared to $\sim 10^{-7}\,s^{-1}$ when there are no cosmic rays present.

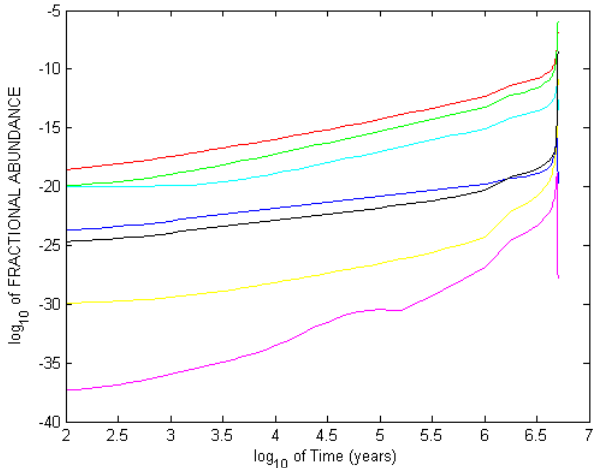

(a)

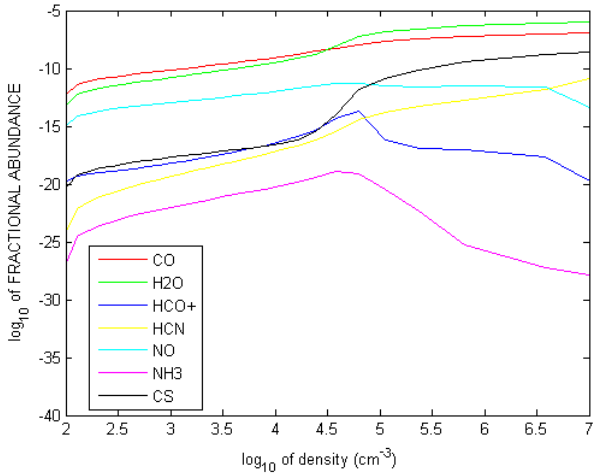

(b)

Figure 2.5: Infall model with constant temperature: 150 $M_{\odot}$ progenitor mass

At the end of the simulation water has become the most abundant molecular tracer in this scenario for all the cases. The abundance has increased greatly compared to the stable cloud model, where the fractional abundance was only around 10^{-14}. This is because unlike the stable cloud case, H_2O formation route for an infalling cloud for both cosmic ray scenarios is via a neutral-neutral reaction:

$$H + OH \rightarrow H_2O + \text{photon}.$$

However there are two different dominant destruction reactions depending on the cosmic ray ionisation rate. H_2O is destroyed with protons in the presence of cosmic rays with an ionisation

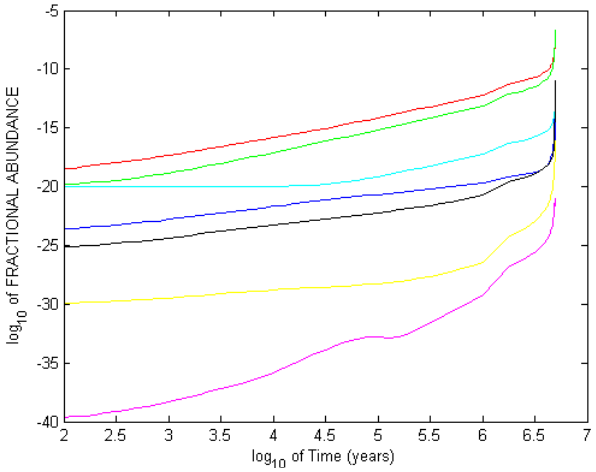

(a)

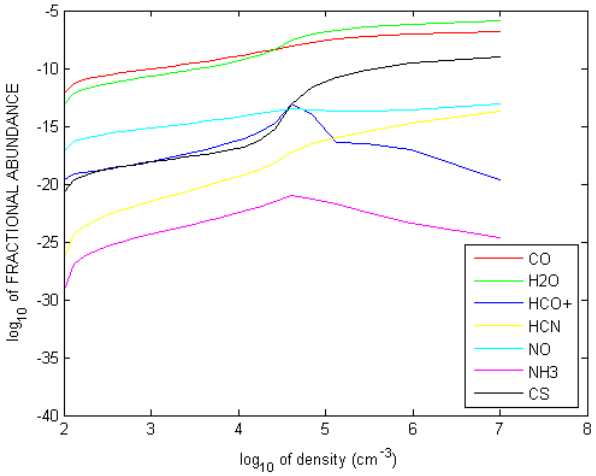

(b)

Figure 2.6: Infall model with constant temperature: 200 $M_{\odot}$ progenitor mass

rate of $10^{-18}\,\mathrm{s}^{-1}$, i.e.

$$H^+ + H_2O \rightarrow H_2O^+ + H$$

and without cosmic rays the destruction pathway is

$$HS^+ + H_2O \rightarrow S + H_3O^+.$$

Slightly more H_2O molecules are produced when no cosmic rays are present. The formation rates are similar for the two scenarios but the destruction rate ($\sim 10^{-12}\,\mathrm{s}^{-1}$) is much higher in the presence of cosmic rays than compared to the no cosmic ray case ($\sim 10^{-17}\,\mathrm{s}^{-1}$).

Both the formation and destruction path way for the molecule HCO^+ is via reactions with carbon atoms:

$$\begin{aligned} C + H_3O^+ &\rightarrow HCO^+ + H_2, \\ C + HCO^+ &\rightarrow CO + CH^+. \end{aligned}$$

In all three cases we see a peak in the formation of this molecule when the density is $\sim 10^5\,\mathrm{cm}^{-3}$and then a decline in its formation. This is because H_3O^+ starts to be destroyed by the reaction above ($\sim 10^{-8}\,\mathrm{s}^{-1}$) much more quickly than it is formed ($\sim 10^{-12}\,\mathrm{s}^{-1}$), i.e.,

$$H_2 + H_2O^+ \rightarrow H_3O^+ + H.$$

We would expect the higher density gas ($10^7\,\mathrm{cm}^{-3}$) of the infall model to produce higher abundances of HCO^+ than the stable cloud model (50 cm^{-3}). However, the infall model without cosmic rays produces a similar amount of HCO^+. In the case of a SN yield from a 200 $M_\odot$ progenitor star, H_3O^+ is less abundant than the stable cloud model. When a cosmic ray background is included, there is a significant increase in the abundance of HCO^+. This is because the increase in ionisation fraction ($\frac{H^+}{H}$) causes an increase in the amount of H_3O^+ produced.

The main formation and destruction pathways for HCN in the infalling model are the same cycle of reactions stated for the stable cloud, with the addition of a secondary destruction reaction which favours the formation of larger molecules:

$$HCN + H_3O^+ \rightarrow HCNH^+ + H_2O.$$

Unlike the stable cloud, as the density increases it causes the formation rate ($\sim 10^{-10}\,\mathrm{s}^{-1}$) to increase several magnitudes larger than the destruction rate ($\sim 10^{-16}\,\mathrm{s}^{-1}$) when cosmic rays are present. This is because the ionisation fraction decreases as the density increases; from Figures 2.5(b) - 2.6(b) it can be seen that this causes a constant increase in the formation of HCN. This results in a much larger abundance of HCN in the infall model compared to the stable model. Similar HCN abundances are produced regardless of the presence of cosmic rays. When cosmic rays are not included the dominant formation reaction becomes

$$H_2 + CN \rightarrow HCN + H.$$

The formation and destruction path ways for NO for this infalling case are the same as the stable cloud model, i.e.

$$\begin{aligned} \mathrm{N} + \mathrm{OH} &\rightarrow \mathrm{NO} + \mathrm{H}, \\ \mathrm{C} + \mathrm{NO} &\rightarrow \mathrm{CO} + \mathrm{N}. \end{aligned}$$

This does not change when cosmic rays are excluded. There is difference in abundances when cosmic rays are excluded, as the destruction rate is increased ($\sim 10^{-7}\,\mathrm{s}^{-1}$ compared to $\sim 10^{-10}\,\mathrm{s}^{-1}$). This is due to the decrease in the ionisation fraction, allowing more carbon atoms to be present. At the beginning of the simulation the ionisation fraction is 0.08 and at the end the value becomes $\sim 10^{-26}$ when the cosmic rays are not present and with a cosmic ray present (ionisation rate of $10^{-18}\,\mathrm{s}^{-1}$) the ionisation fraction has a higher value of $\sim 10^{-11}$. When we investigated the sensitivity of the molecular tracers to initial conditions of the stable cloud, the equilibrium abundance of NO was unaffected to range of cosmic ray ionisation rates considered for a gas density of 100 cm^{-3} (Figure 2.1(a)). However, for the high densities considered in the infalling model, there is a large difference between NO abundances when cosmic rays are excluded.

When examining the formation of ammonia, there is a deviation from the formation path of the stable cloud model. At the density $\sim 10^5\,\mathrm{cm}^{-3}$, the dominant formation reaction becomes:

$$\mathrm{NH}_3^+ + \mathrm{Na} \rightarrow \mathrm{NH}_3 + \mathrm{Na}^+.$$

The rate for this reaction is higher when cosmic rays are included ($\sim 10^{-19}\,\mathrm{s}^{-1}$ compared to $\sim 10^{-30}$), as more NH_3^+ is produced. This formation reaction is not dominant at redshift z=0, due to elements such as Na, Mg & Fe being locked in dust grains. The destruction reaction is the same for both cases:

$$\mathrm{NH}_3 + \mathrm{S}^+ \rightarrow \mathrm{NH}_3^+ + \mathrm{S}.$$

Ammonia is still the least abundant of all the tracers we consider. The formation of NH_3 peaks around $10^5\,\mathrm{cm}^{-3}$, just like HCO^+, as it is dependent on ionised species which become less abundant at higher densities. Without the inclusion of cosmic rays the value of NH_3 at $10^7\,\mathrm{cm}^{-3}$ is comparable to values of the stable cloud model.

For the infalling model the formation and destruction of CS is due to the following reactions:

$$\begin{aligned} \mathrm{C} + \mathrm{SO} &\rightarrow \mathrm{CS} + \mathrm{O}, \\ \mathrm{H}^{+} + \mathrm{CS} &\rightarrow \mathrm{CS}^{+} + \mathrm{H}. \end{aligned}$$

These formation reactions no longer depend on ionised species, as they were for the stable cloud model. As with all molecules that are formed by neutral-neutral reactions (e.g. HCN), there is a huge increase in abundance as compared to the stable cloud model. As the destruction is via protons, which decrease as the ionisation fraction decreases, CS becomes the third most abundant molecular tracer. Due to the difference of sulphur produced in each SN yield, there is an appreciable difference in the fractional abundance of CS produced in the three progenitor mass models we consider, making this the best tracer for progenitor mass for this infall model. However, there is an unclear dependence on the presence of cosmic rays. For the two larger progenitor masses there is more CS produced when there are no cosmic rays present, but the opposite occurs for the 80 $M_{\odot}$ case. The formation rate of CS is always greater when cosmic rays are present in all three cases, but the dependence of cosmic rays on the destruction pathof SO is different in all three cases. Hence there this a mixed overall effect.

2.3.2.2 Infall with temperature increase

	80 $M_{\odot}$		150 $M_{\odot}$		200 $M_{\odot}$	
	CR rate = $0\ s^{-1}$	CR rate = $10^{-18}\ s^{-1}$	CR rate = $0\ s^{-1}$	CR rate = $10^{-18}\ s^{-1}$	CR rate = $0\ s^{-1}$	CR rate = $10^{-18}\ s^{-1}$
CO	1.40×10^{-7}	1.40×10^{-7}	1.40×10^{-7}	1.40×10^{-7}	1.40×10^{-7}	1.40×10^{-7}
H_2O	2.81×10^{-8}	3.02×10^{-8}	9.33×10^{-8}	9.55×10^{-8}	1.28×10^{-7}	1.35×10^{-7}
HCO^+	3.71×10^{-26}	2.45×10^{-16}	3.16×10^{-29}	2.45×10^{-17}	1.23×10^{-28}	1.55×10^{-17}
HCN	2.57×10^{-24}	4.79×10^{-20}	4.67×10^{-24}	1.95×10^{-17}	2.63×10^{-21}	5.75×10^{-20}
NO	6.03×10^{-14}	6.03×10^{-14}	3.16×10^{-10}	3.16×10^{-10}	1.58×10^{-12}	1.58×10^{-12}
NH3	2.29×10^{-38}	3.02×10^{-28}	2.45×10^{-35}	1.58×10^{-24}	1.66×10^{-37}	7.94×10^{-27}
CS	6.03×10^{-25}	5.89×10^{-20}	2.19×10^{-27}	2.95×10^{-20}	5.01×10^{-27}	7.08×10^{-21}

Table 2.5: Table of fractional abundances of molecular tracers for the infall model with increasing temperature

In this model the gas temperature increases to 1000K above density of $n = 10^5\,\mathrm{cm}^{-3}$. This is because the gas is assumed to become optically thick and cannot effectively radiate energy. If such an environment could be observed it would be advantageous, since we have seen in Figures 2.1(c) and 2.3(d) that the increase in density and temperature create a propitious environment for molecules. This is evident as the fractional abundance of molecular hydrogen reaches ~ 0.01.

The two cosmic ionisation rates have a significant effect on the the ionisation fraction ($= \frac{H^+}{H}$): when there are no cosmic rays present the ionisation fraction is $\sim 10^{-44}$ at 10^7 years, when there is a cosmic ionisation rate of $10^{-18}\,s^{-1}$ the ionisation fraction increases to 10^{-12}. The results displaying the fractional abundance of the other molecular tracers are presented in Figures 2.7 - 2.9.

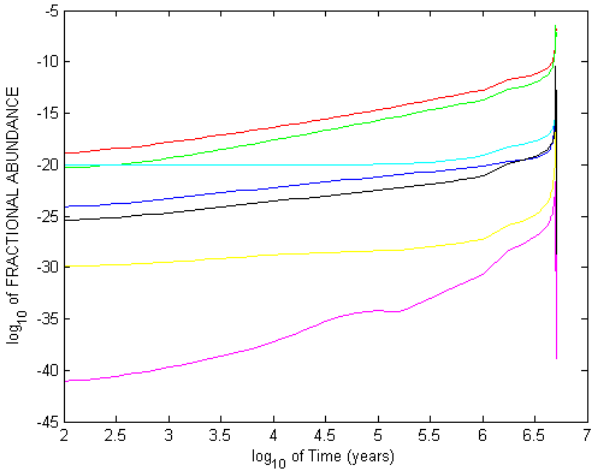

(a)

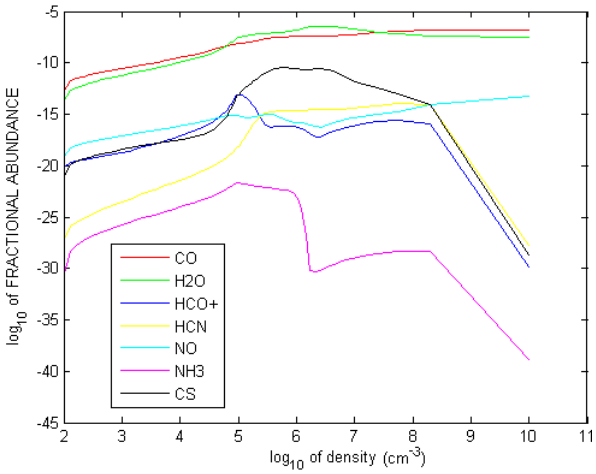

(b)

Figure 2.7: Infall model with increasing temperature: 80 $M_\odot$ progenitor mass

Carbon monoxide (CO) has the same abundance for all three progenitor cases and both cosmic ray ionisation rates, as nearly all the carbon atoms are 'locked up' in this molecule. The formation and destruction pathways are cyclic:

$$H + CO_2 \rightarrow CO + OH$$

$$OH + CO \rightarrow CO_2 + H$$

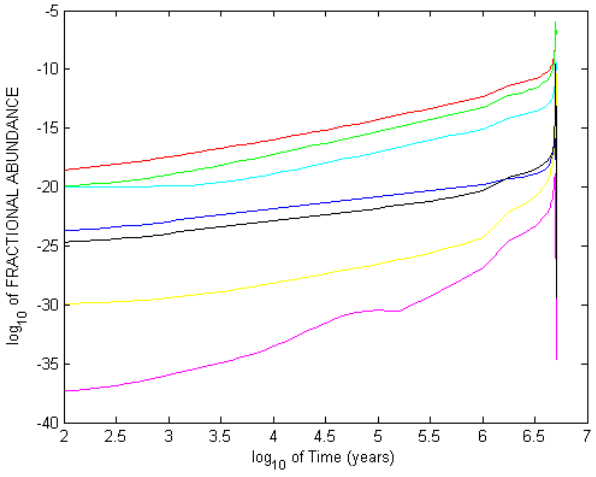

(a)

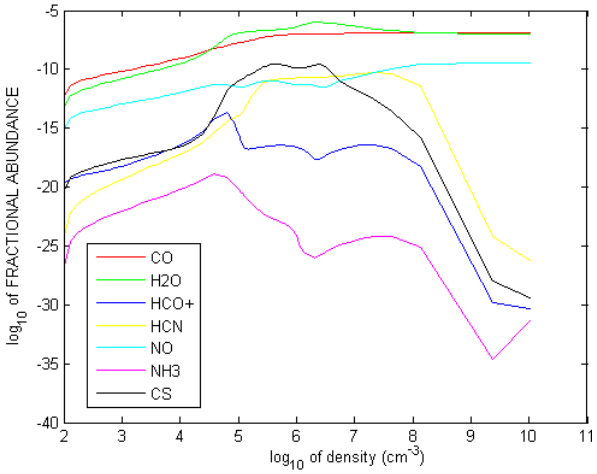

(b)

Figure 2.8: Infall model with increasing temperature: 150 $M_\odot$ progenitor mass

With the high temperature and densities, the formation reaction has a rate of $\sim 10^2\,\mathrm{s}^{-1}$ and the destruction rate is $\sim 10^{-8}\,\mathrm{s}^{-1}$. So unlike the infall model with constant temperature CO is the most abundant molecule.

Water has become the second most abundant tracer. It forms via a neutral reaction

$$\begin{aligned} \mathrm{H} + \mathrm{OH} &\rightarrow \mathrm{H_2O} + \mathrm{photon}, \\ \mathrm{H} + \mathrm{H_2O} &\rightarrow \mathrm{OH} + \mathrm{H_2} \end{aligned}$$

There is a small difference between the results obtained for the two cosmic ray ionisation rates, because there is more OH present when the cosmic ray ionisation is included. This is because the

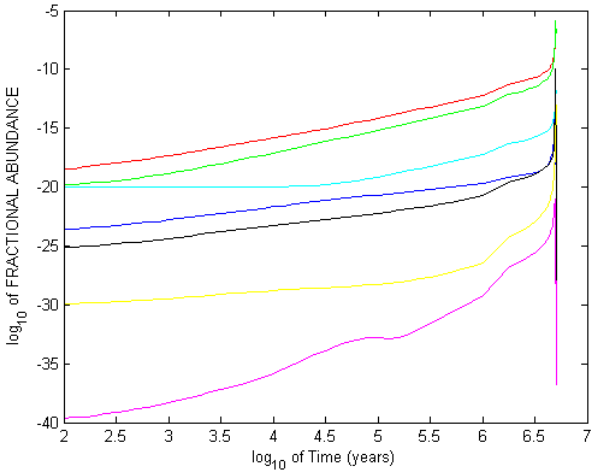

(a)

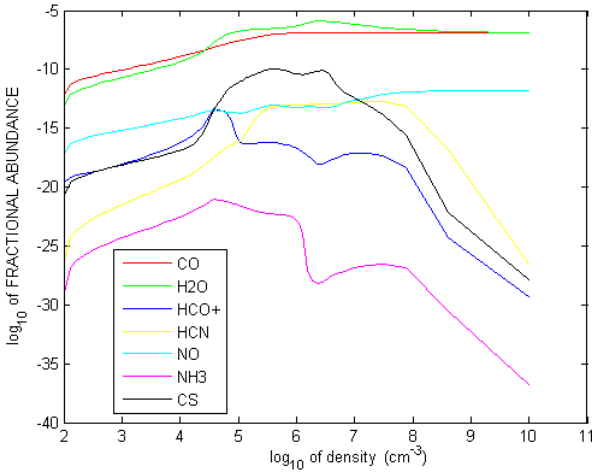

(b)

Figure 2.9: Infall model with increasing temperature: 200 $M_\odot$ progenitor mass

OH destruction pathway is

$$H + OH \rightarrow O + H_2$$

and more OH is destroyed when there is no cosmic rays present due to the low ionisation fraction. For the 200 $M_\odot$ progenitor case the abundance of water is very close to the abundance of CO, while the other two cases have a magnitude difference between the fractional abundance of CO and H_2O.

The molecule NO is formed by the same pathways as in the previous infall model. At this high density ($10^{10}\,\mathrm{cm}^{-3}$) and temperature (1000 K), the cosmic ray rate does not affect the abundance of NO. This is because nearly all the nitrogen atoms become 'locked up' in this molecule. However,

due to the decrease in other tracers, NO has become the third most abundant tracer. As there is a significant difference in the amount nitrogen produced in each SN yield, at late times it NO shows itself to be the best tracer of progenitor mass.

This environment promotes the formation of CO and NO, which leaves very few nitrogen and carbon atoms to form other molecules. This is why other molecular tracers have very small fractional abundances compared to the constant temperature infall model.

The molecule HCO^+ has the same formation and destruction pathways as in the infall model with constant temperature, i.e., reactions with carbon atoms. The ionisation fraction is a major influence on the formation of HCO^+, as the primary reactant is H_3O^+. This explains the large difference in the HCO^+ abundance between the models with two cosmic ionisation rates. All three progenitor cases have similar values, the 80 $M_\odot$ progenitor case has slightly higher values because there are fewer oxygen atoms locked up in water molecules.

There is a big difference in the HCN values when cosmic ray ionisation rates are included; the formation pathway is also different. Without cosmic rays the neutral-neutral formation and destruction reactions are cyclic:

$$\begin{aligned} \mathrm{H_2 + CN} &\rightarrow \mathrm{HCN + H}, \\ \mathrm{H + HCN} &\rightarrow \mathrm{CN + H_2} \end{aligned}$$

This changes when cosmic rays are included:

$$\begin{aligned} \mathrm{H + HCN^+} &\rightarrow \mathrm{HCN + H^+}, \\ \mathrm{H + HCN} &\rightarrow \mathrm{CN + H_2} \end{aligned}$$

Neutral-neutral reactions are much slower than ion transfer reactions, therefore the formation rate when cosmic rays are present is higher than when cosmic rays are not included (i.e.$\sim 10^{-11}\,\mathrm{s}^{-1}$ compared to $\sim 10^{-21}\,\mathrm{s}^{-1}$). Hence cosmic rays increase the ion fraction and cause an increase in HCN formation.

The formation and destruction route for ammonia is no longer the same as the previous infall

model when cosmic rays are excluded, the H_2 molecule becomes the dominant reactant:

$$\begin{aligned} H_2 + NH_2 &\rightarrow NH_3 + H, \\ H + NH_3 &\rightarrow NH_2 + H_2. \end{aligned}$$

The formation rate and destruction rate is $\sim 10^{-22}$ when the gas has the highest temperature and density. The increase in temperature at higher densities causes a high abundance of H_2 to be formed. When cosmic rays are included the formation pathway changes:

$$\begin{aligned} NH_3^+ + Na &\rightarrow Na^+ + NH_3, \\ H + NH_3 &\rightarrow NH_2 + H_2. \end{aligned}$$

The previous dominant pathways of neutral-neutral reactions are much slower ($\sim 10^{-32}$) than this ion exchange formation rate ($\sim 10^{-19}$). Hence ammonia is more abundant when cosmic rays are present.

Finally the tracer CS has the same formation reaction as in the previous infall model, and the destruction reaction is the same for both cosmic ray rates

$$C + CS \rightarrow C_2 + S.$$

However, the rate for this reaction is much lower when cosmic rays are not included (i.e., $10^{-28}\,\mathrm{s}^{-1}$ compared to $10^{-19}\,\mathrm{s}^{-1}$).

2.4 Conclusions

For the range of initial conditions we investigated for a stable cloud, it has been shown that if the cloud density is n$< 100\,\mathrm{cm}^{-3}$, CO and H_2O are the most abundant tracers. When it is possible to observe molecules at redshift $z > 10$, these would be most observable as they can reach fractional abundances above 10^{-12}. If the cloud being observed has only been seeded by a single supernova, these molecular tracers would not be useful to constrain the progenitor mass of the star that underwent the supernova explosion. The chemistry occurring in low-metallicity clouds is not dependent on H_2 and is driven by atomic reactions. The molecular tracer that could constrain the progenitor mass is NO, though it is does not reach abundances that could be observable. Nitrogen is an element that differs significantly in the SN yield from the three different progenitor masses.

This is subject to the accuracy of these computational SN yields. The other molecular tracers have abundances that are very low and so have very little chance of being observed. For the formation of the molecule CO the most advantageous environment is: high density, high temperature, a high abundance of dust grains, a low ionisation rate from cosmic rays and shielded from UV radiation.

We also considered gas that may undergo collapse, which reached a maximum density of $10^7\,\mathrm{cm}^{-3}$ and the temperature remained constant at 100 K. The increase in density causes all the molecular tracers to increase in abundance. The molecules CO and H_2O have a significant increase in their abundances and would be the most likely to be observed. The inclusion of cosmic rays has a small effect on molecules that rely on neutral-neutral reactions but a significant effect on NH_3 and HCO^+, which depend on the ionisation fraction of the cloud. Neither of these molecules could be observed. The best molecular tracer of progenitor mass in this case is CS which has a fractional abundance above 10^{-12} for all three cases, and the difference in sulphur abundance between the three SN yields is significant.

The second infall model we consider reaches a maximum density of $10^{10}\,\mathrm{cm}^{-3}$ and has the associated temperature increase to 1000 K to represent the environment of a hot core. The ionisation fraction becomes very small and the molecular fraction of the gas increases greatly. The fractional abundance of H_2 becomes 0.01 and the nearly all of the carbon and nitrogen atoms are 'locked up' in CO and NO. The cosmic ray ionisation rate has very little effect on these molecules. In conclusion CO and H_2O have large enough abundances in high density gas ($n > 10^7$ cm^{-3}) to be observed. Theoretically, at late times NO is the best tracer of progenitor mass as for two cases (150 & 200 $M_\odot$) the abundances are observable. However for the 80 M$\odot$ case is the abundance of NO only reaches $\sim 10^{-14}$. Other molecules have very small abundances in this environment. Hence cooler dense gas such as described in the previous infall case with constant temperature is a favourable environment to distinguish the molecular tracers of progenitor mass.

CHAPTER 3

THE PRESSURE-DRIVEN FRAGMENTATION OF METAL-FREE CLUMPS

Based on paper by Dhanoa, Mackey & Yates (2014)

3.1 Introduction

The first stellar objects (Population III stars) are expected to form around redshift $z \sim 20$ (Bromm *et al.* 2002; Stacy *et al.* 2010). An initial mass function (IMF) describes the distribution of initial masses for a population of stars. Without any efficient metal cooling, the most effective coolant available is molecular hydrogen (H_2). A top heavy IMF has been inferred for the primordial environment in which these stars formed. This means that these stars will have been massive, luminous and short-lived. Their feedback strongly affects the surrounding medium, hence affecting the initial conditions of the gas which spawns the next generation of stars. Hence at lower redshifts increased ionisation levels, larger dark matter haloes and lower cosmic microwave background (CMB) temperatures all contribute to the subsequent formation of lower-mass primordial stars (Yoshida *et al.* 2007).

The supernova (SN) explosions of these metal-free stars can induce the formation of lower mass stars via several important feedback mechanisms: ionising radiation, shock waves and chemical enrichment. The abundance of H_2 is enhanced significantly in the wake of a strong shock wave

(Shapiro & Kang 1987). This and the introduction of metals allows the gas to cool to lower temperatures. As the expanding SN shell interacts with the surrounding interstellar medium (ISM), hydrodynamic instabilities occur within the shocked gas (Wang & Chevalier 2001). The SN shock also amplifies density gradients found in the ISM, promoting thermal instability in the gas, causing it to fragment and clump. Therefore, star formation is thought to occur in two ways; i) fragmentation of the SN shell itself or ii) pressure-induced collapse of clumps found in the ISM (Elmegreen 1998).

One of the first numerical studies to investigate the induced low-mass star formation of Population II.5 (Pop II.5) was by Mackey *et al.* (2003). Pop II.5 stars are defined as the first generation of low metallicity stars. They implement a one-zone model, solving for the thermal and chemical evolution of post-shock gas. They assume isobaric conditions to increase the gas density in the cooling cloud, ignoring a possible time-dependence of the external pressure, and of course not taking account of any potential hydrodynamical effects. Mackey *et al.* (2003) argued that an equilibrium primordial gas cloud that is shocked by a supernova would be heated to a higher entropy state, then cool isobarically back to its original equilibrium temperature, but now at a much higher density than before. In this way the Jeans mass of the gas could be reduced by a large factor, allowing much lower-mass stars to form. In reality, however, pressure is a decreasing function of time in a supernova remnant, because the explosion is (by definition) vastly over-pressurised compared to its surroundings. However, they did find that the likelihood of forming these extremely metal-poor (EMP) stars depended on the radial distribution of the metal-free gas prior to SN explosion.

Salvaterra *et al.* (2004) investigated the formation of low-mass stars within the fragmenting primordial SN shell. They implemented a semi-analytic model and found that, if the explosion energy is above $\mathrm{E}_{SN} \geq 10^{51}$ ergs, low-mass star formation can be triggered. However they found a minimum ambient density ($n_0 > 300\mathrm{cm}^{-3}$) is needed for Type II SN, whereas PISN require lower ambient densities. The main issue with this work is that chemical evolution is not taken into account, and so the cooling was not determined by the evolving abundances of the chemical species.

The first primordial SN model to couple chemical and thermal evolution was by Machida *et al.* (2005), where they investigated low-mass star formation triggered by supernovae in primordial clouds. A semi-analytic 1D model was implemented to follow the evolution of a gas shell produced by a supernova explosion of energy $10^{51} - 10^{52}$ ergs, over a range of redshifts ($z = 10 - 50$). A metal-free chemistry was included and the cooling from H_2 and HD molecules was taken into

account. They concluded that SN explosions can induce the fragmentation of the shell and form low-mass stars in dark matter halos of only a few times 10^6 $M_\odot$. The typical mass of the fragments is ~ 1.0 $M_\odot$, which is similar to the mass of extremely metal poor stars observed in the Galactic Halo (Christlieb *et al.* 2002).

Vasiliev *et al.* (2008, henceforth VVS08) went a step further by performing an axially-symmetric 2D numerical simulation of high-energy supernova explosions (10^{53} erg) in a dwarf galaxy of total mass 1.7×10^7 $M_\odot$ at redshift $z = 12$. They investigated the effect of galactic rotation on the dynamical and chemical evolution of a supernova-driven shell, and included the heating and cooling processes and chemical evolution of a metal-free gas. They follow the H_2 and HD chemistry using a limited network of only 17 reactions, thereby neglecting intermediate species and overestimating the abundances of H_2 and HD. The cooling rates were computed separately for temperatures above and below 2×10^4K. For temperatures below T$< 2 \times 10^4$ K, non-equilbrium molecular line cooling was calculated from the abundances of chemical species. However, for T$> 2 \times 10^4$ K the cooling rates were computed from the cooling function calculated by Sutherland & Dopita (1993). The results highlight the importance of the initial conditions for SN model, as including rotation of the dark matter halo changes the density profile of the gas. They concluded that low mass star formation cannot occur in such conditions as suggested by Mackey *et al.* (2003) and Salvaterra *et al.* (2004).

Studies that model the observed chemical abundances of EMP and HMP stars found in the Galaxy, have found that these stars are most probably formed from SNe with explosion energies much less than 10^{52} erg (Joggerst *et al.* 2010). Therefore, these stars are not formed in the vicinity of a PISN (10^{53} erg) or a hypernova (10^{52} erg) but instead via the influence of a core collapse SN with a progenitor star of mass ≤ 40 $M_\odot$. This means that VVS08 investigated a scenario which is not indicative of the physical environment in which these stars were formed. They do however make an important point stating the further need for sophisticated numerical models including chemistry driven by cosmic rays, UV radiation and X-rays. As the chemical and dynamical evolution of the shocked gas is intrinsically linked through thermal processes, it is critical to simulate processes that occur on the small scale as reliably as possible, as they impact large scale dynamics.

Shigeyama & Tsujimoto (1998) argue that the EMP stars observed in our Galaxy today were not formed from a well mixed gas. Instead they propose a model in which EMP stars formed from the SN shell formed of the swept up interstellar gas. Hence metals would only be accreted from the

surrounding medium in the subsequent evolution. However, instabilities are likely to form which will cause the ejecta and swept material to mix. Hence this model had been previously disputed. However, the discovery of the HMP star SDSS J102915+172927, which has a total metallicity of $10^{-5} - 10^{-7}$ $Z_{\odot}$ (Caffau *et al.* 2012) highlights the importance of reassessing the fragmentation and collapse of metal-free gas at high redshift.

So far, early universe SN models have focused on the fragmentation of the SN shell itself. It is also important to investigate the collapse and fragmentation of clumps within the ISM of the first galaxies. It has been observed in our Galaxy that SNe can induce the collapse of smaller gas clumps found in the ISM that otherwise may not undergo star formation (Reach *et al.* 2005). These clumps are stripped of their outer layers and compressed. These clumps will accrete less of the surrounding material, when they undergo protostellar evolution (Reach *et al.* 2002). Therefore this is a possible formation route for the HMP stars such as SDSS J102915+172927.

We intend to investigate the shock-driven fragmentation of a metal-free clump via a core collapse supernova shock, with multidimensional hydrodynamic simulations. This study will improve upon previous SN models by following the non-equilibrium cooling that occurs at all temperatures and will include a comprehensive chemistry. We will investigate the effect of cosmic rays, CMB ionisation and deuterium chemistry on clumping and compression.

3.2 The Model

We model the evolution of a SN shell produced by the explosion of a metal-free star and its subsequent collision with a metal-free clump (40 pc from the progenitor star) at redshift $z = 10$. We assume that this takes place in the centre of a dark matter halo, in which the SNR is well contained. Therefore, we do not need to take into account the density decrease of the ISM which occurs at the halo edge. It is also assumed that the SN remnant (SNR) is created by a core-collapse SN with an explosion energy of 10^{51} erg and that the system we model is not affected by any nearby radiation sources.

The model is simulated using a fixed grid radiative-hydrodynamics code written by Mackey & Lim (2010). This uses a numerical method to solve the fluid dynamic equations which is described by Falle *et al.* (1998) and can model gas dynamics in 1D, 2D and 3D. In contrast with smooth particle hydrodynamics (SPH) code, this grid-based code can successfully follow the instabilities that develop. The code does not include the effects of gravity.

We are investigating the shock driven fragmentation of clouds, the dynamics of which are pressure-dominated. As we do not follow the collapse of the fragments we ignore the effects of gravity at this stage. Special attention is given to the microphysics involved, as the cooling that takes place at all temperatures is non-equilibrium. Therefore the only accurate way to model this is to include the non-equilibrium chemistry. We have developed a microphysics module which links non-equilibrium chemistry and the thermal model, the full details are given in the section below (§3.3).

3.3 Microphysics Module

For each timestep the microphysics module solves the following ordinary differential equation (ODE) for internal energy density E (in erg cm^{-3}):

$$\frac{\partial E}{\partial t} = -\Lambda + \Gamma, \tag{3.1}$$

where Λ is the cooling function of the gas (in erg cm^{-3} s^{-1}) and Γ is the heating function of the gas (in erg cm^{-3} s^{-1}). Both the heating and cooling functions are dependent on the abundances of the molecular and the atomic species of the gas. Hence the need to follow the chemical evolution of the gas. This is done by solving the following set of equations

$$\frac{\partial x_i}{\partial t} = C_i\left(x_j, \mathrm{T}\right) - D_i\left(x_j, \mathrm{T}\right) x_i, \tag{3.2}$$

where x_i is the fractional abundance (relative to the number density of hydrogen nuclei i.e., $n_{\mathrm{H}} + 2n_{\mathrm{H_2}} + n_{\mathrm{H^+}}$) of chemical species i, for a total number of chemical species N_{s}, T is the temperature of the gas, C is the formation rate of the species and D is the destruction rate of the species.

Hence a set of coupled ODEs (Eqns 3.1 & 3.2) are solved by the integrating package `CVODES`. The right hand side of Eqn (3.1) is treated in the following way to take into account heating from the CMB,

$$\frac{\partial E}{\partial t} = -\Lambda(\mathrm{T}) + \Lambda(\mathrm{T_{CMB}}), \tag{3.3}$$

where $\mathrm{T_{CMB}}$ is the temperature of CMB photons. The initial values for internal energy density, mass density and fractional abundances of the species are passed to the microphysics module from

the hydrodynamics part of the code. Assuming the gas is ideal, the temperature is determined by the following relation

$$E = \frac{3}{2} n k_B \mathrm{T}, \tag{3.4}$$

where n is the total number density and k_B is Boltzmann's constant. The fractional abundances of the atomic species and electrons are calculated from conservation equations which are set to values relative to the total number of hydrogen nuclei: x_{H}=1.0, $x_{\mathrm{He}} = 0.08$ and $x_{e^-} = 0.0$. The primordial number ratio of helium atoms to hydrogen atoms was obtained from Flower (2007). We assume the atomic, ionic and molecular species are collisionaly coupled to each other and are subject to a common velocity field, which eliminates the need for solving separate equations of motion for each species.

At the end of each timestep the microphysics module returns: i) a new value for internal energy to be used within the hydrodynamic part of the code for the next timestep, and ii) the new chemical abundances which defines the initial abundances for the next timestep. The length of each timestep for both the hydrodynamics code and the microphysics module is the same, as this is a more stable method than allowing many smaller timesteps for the chemistry. The time step is determined by the fastest changing chemical quantity within the microphysics module.

3.3.1 The Chemical Network

The chemical evolution of the gas is modelled using a chemical network consisting of 11 species and 36 reactions (see Table 3.1). The species include: H, He, H_2, H^+, $H_2{}^+$, $H_3{}^+$, HeH^+, He^+, He^{++}, H^- and e^-. For simplicity we do not include lithium, as Glover & Savin (2009) have shown that the low abundances present in primordial environments have minimal influence on the cooling of intermediate to low density gas. Dust is not present in metal-free environments and therefore is not included. Glover & Abel (2008) do not include $H_3{}^+$ and HeH^+ as their contribution to cooling within their model was negligible. However, for completeness we include both species in the chemistry network, to ensure that H_2 is not over-produced.

We restrict the chemical species to three atoms or fewer. It is possible to produce H_5^+ but the abundances would be so small that it is safe to exclude it (Glover & Savin 2009). As well as neglecting photoreactions, the reactions that include electronically excited hydrogen (H^*) have been ignored as we do not expect the densities to be become large enough for H^* to affect H_2

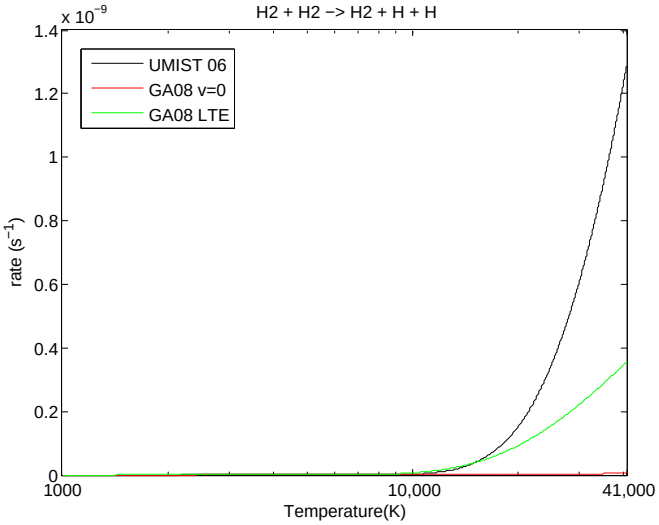

Figure 3.1: A comparison of reaction rates for reaction R10 above 10,000 K. Where UMIST 06 = UMIST database for Astrochemistry 2006 (Woodall *et al.* 2007*a*) and GA08= Glover & Abel (2008)

formation (Rawlings *et al.* 1993). To cover the whole temperature range of our model ($10 - 10^9$ K), reaction rates are either extended, extrapolated outside of their temperature range or switched off appropriately. It is understood that SNRs observed in the Galaxy do not reach temperatures above 10^9 K (Dwek & Arendt 1992), but as the SN is modelled by the injection of thermal energy (and not kinetic energy), there is an increase in temperature at earlier times (for further details see section § 3.3.2).

The rates for reactions which only include atomic species and their related ionic species are split into radiative recombination rates (R1 – R3) and collisional ionisation rates (R4 – R6). The radiative recombination of Hydrogen is treated by Hummer (1994) in the Case B approximation. This is a valid assumption for the lower densities we expect in our simulation and the rate is valid until 10^7 K. The helium radiative recombination rates (R2 – R3) are given by Verner & Ferland (1996). They give analytic fits of reaction rates which are valid from 3 K to 10^9 K. The collisional ionisation rates by electron impact are given by Voronov (1997), which are valid between 1 eV and 20 KeV. For the sake of simplicity we make an assumption that the electron and gas temperatures are equal, so these rates are valid up to 2.3×10^8 K. The maximum value for all these rates are then extended as a constant value for temperatures above the temperature range of the individual rates.

We did not adopt the primordial chemistry network by Abel *et al.* (1997), which is valid from $10 - 10^8$ K, consisting of 9 chemical species and 28 reactions. These rates are now outdated and

the importance of using accurate chemical rates in metal free-environments was highlighted by Glover *et al.* (2005). This led to the work by Glover & Abel (2008, henceforth GA08) which collated fits of metal-free chemical reaction rates from a number of sources. All the fits are smooth for computational ease and valid for temperatures below 10,000 K. However, where possible we chose to utilise the reaction rates from the UMIST database for astrochemistry 2006 (Woodall *et al.* 2007*a*, henceforth UMIST 06), which are generally valid for a higher maximum temperature of 41,000 K. These rates are primarily determined experimentally.

Some UMIST 06 rates are not smooth functions (e.g. Figure 3.5); as the overall rate is given by a collection of rates valid at different temperature ranges, which do not match at the boundaries. The GA08 rate network are numeric fits for reaction rates from a number of sources and are valid until $10 - 10,000$ K. When the GA08 rates are extrapolated to higher temperatures ($> 10^4$ K), they become inaccurate compared to the UMIST 06 rates which are valid up to $41,000$ K. For example, both rates for reaction R10 are displayed in Figure 3.1, one can see that above $10,000$ K the fit by GA08 underestimates the value of the reaction rate. The UMIST06 rates are valid for a larger temperature range and therefore we use them even though they might not be smooth functions. Hence we have adapted the UMIST 06 rates to solve the boundary matching issue (this is is discussed below). Although we do not model the thermal contribution due to molecules above 10,000 K, there is still a need to accurately model the chemical evolution above this temperature range. This is because reliable modelling of the molecular cooling at 10,000K is only possible if we have the correct abundances of molecular species when the gas is cooled down to this temperature. As the cooling and chemical processes involved in the SN shock are non-equilibrium, the abundances of the chemical species at 10,000K cannot be set as precalculated equilibrium abundances or assumed to be in a purely ionic state (i.e H^+, He^+ & He^{++}). We assume molecular species cannot exist above 10^5 K, and at this temperature the gas is fully ionised.

To try to correctly model the chemical evolution of the gas between 10^4 K and 10^5 K, we have adapted the reaction rates to cover the whole temperature range of the model. In general the molecular reactions are separated into sets: destruction or formation. The first set of reactions are either extrapolated or extended to the maximum temperature 10^{12} K and the second set are switched off above 41,000K (using a exponential function) to make sure molecules are not formed at higher temperatures. This exponential cut-off of the formation rates makes sure that there are no molecules such as H^- present at T$\geq 10^5$ K. A general treatment of each type of molecular reaction is given below. The exact details of how each molecular reaction is adapted is given in the

Appendix.

	Reaction	References for rate coefficients
R01	$H^+ + e^- \rightarrow H + \gamma$	H
R02	$He^+ + e^- \rightarrow He + \gamma$	VF
R03	$He^{++} + e^- \rightarrow He^+ + \gamma$	VF
R04	$H + e^- \rightarrow H^+ + e^- + e^-$	V
R05	$He + e^- \rightarrow He^+ + e^- + e^-$	V
R06	$He^+ + e^- \rightarrow He^{++} + e^- + e^-$	V
R07	$H_2 + H \rightarrow H + H + H$	GA08
R08	$H^- + H \rightarrow H + H + e^-$	GA08
R09	$H^- + He \rightarrow He + H + e^-$	GA08
R10	$H_2 + H_2 \rightarrow H_2 + H + H$	UM06
R11	$H^- + e^- \rightarrow H + e^- + e^-$	JR
R12	$H_2 + He^+ \rightarrow He + H^+ + H$	UMO6
R13	$H_2 + e^- \rightarrow H + e^- + H$	UM06
R14	$H_2^+ + e^- \rightarrow H^+ + e^- + H$	hd*
R15	$HeH^+ + e^- \rightarrow He^+ + e^- + H$	hd*
R16	$H^+ + H \rightarrow H_2^+ + \gamma$	UM06, GA08
R17	$H^+ + He \rightarrow HeH^+ + \gamma$	UM06
R18	$H + e^- \rightarrow H^- + \gamma$	UM06, GA08
R19	$HeH^+ + e^- \rightarrow He + H$	UM06
R20	$H_2^+ + e^- \rightarrow H + H$	UM06
R21	$H_3^+ + e^- \rightarrow H + H + H$	UM06
R22	$H_3^+ + e^- \rightarrow H_2 + H$	UM06
R23	$H^- + H_2^+ \rightarrow H + H + H$	GA08
R24	$H + He^+ \rightarrow He + H^+$	UM06,hd
R25	$H_2 + He^+ \rightarrow He + H_2^+$	UM06
R26	$H^+ + H^- \rightarrow H + H$	UM06
R27	$H^- + H_2^+ \rightarrow H_2 + H$	UM06
R28	$H^- + He^+ \rightarrow He + H$	UM06
R29	$H + H_2^+ \rightarrow H_2 + H^+$	UM06
R30	$H_2^+ + H_2 \rightarrow H_3^+ + H$	UM06

	Reaction	References for rate coefficients
R31	$H^- + H_3^+ \rightarrow H_2 + H_2$	UM06
R32	$H + HeH^+ \rightarrow He + H_2^+$	UM06
R33	$H_2 + HeH^+ \rightarrow He + H_3^+$	UM06
R34	$H_2^+ + He \rightarrow HeH^+ + H$	UM06
R35	$H^- + H^+ \rightarrow H_2^+ + e^-$	SK87
R36	$H^- + H \rightarrow H_2 + e^-$	UM06

Table 3.1: Chemistry network for metal-free case:
Notes- UM06 =UMIST database for astrochemistry [rate 06, non-dipole enhanced] (Woodall *et al.* 2007*a*); GA08 = Glover & Abel (2008); H =Hummer (1994); GP98 = Galli & Palla (1998); SK87= Shapiro & Kang (1987); hd = matching scheme (see section 3.3.1); hd*= same value as R14; JR= private communication with Jonathan Rawlings; V=Voronov (1997);VF= Verner & Ferland (1996)

3.3.1.1 Collisional Dissociation: XY + M → X + Y + M

These reactions are dependent on both temperature and density. At high temperatures collisional dissociation reactions become important, as they are the main destruction route for molecules (in a non-radiation (UV) dominated regions). The molecule H_2 is dissociated by atomic collisions above T$\geq$ 5000 K and at temperatures above 10,000 K collisions with electrons become dominant. The collisional dissociation reactions included in the network are reactions R07 - R11 (Table 3.1).

Reaction R07 is sensitive to densities below $n \sim 10^4$ cm^{-3}, as above this density the rate reaches its LTE value. Therefore there is a reaction rate valid for H_2 that is all in the vibrational ground state (this applies for low-density gas $n \approx 1\,\mathrm{cm}^{-3}$), and a rate which applies for H_2 with LTE level populations. For the intermediate densities the following relation applies:

$$\log \mathrm{k_{R07}} = \left(\frac{\mathrm{n/n_{cr}}}{1+\mathrm{n/n_{cr}}}\right) \log \mathrm{k_{R07,LTE}} + \left(\frac{1}{1+\mathrm{n/n_{cr}}}\right) \log \mathrm{k_{R07,v=0}}$$

where $k_{\mathrm{R07,LTE}}$ is the LTE collisional dissociation reaction rate and $k_{\mathrm{R07,v=0}}$ is collisional dissociation rate in the low density limit (both rates are taken from Glover & Abel (2008)). The critical

density is given by

$$\frac{1}{n_{cr}} = \frac{x_{\rm H}}{n_{cr,{\rm H}}} + \frac{x_{\rm H_2}}{n_{cr,{\rm H_2}}} + \frac{x_{\rm He}}{n_{cr,{\rm He}}}$$

where

$$\begin{aligned} n_{cr,{\rm H}} &= {\rm dex}[3.0 - 0.416\log({\rm T}/10000) - 0.327\log({\rm T}/10000)^2] \\ n_{cr,{\rm H_2}} &= {\rm dex}[4.845 - 1.3\log({\rm T}/10000) + 1.62\log({\rm T}/10000)^2] \\ n_{cr,{\rm He}} &= {\rm dex}[5.0792(1.0 - 1.23\times10^{-5}({\rm T} - 2000))] \end{aligned}$$

The value for $n_{cr,{\rm H}}$ is taken from Martin *et al.* (1996), the value for $n_{cr,{\rm H_2}}$ is obtained from Shapiro & Kang (1987) and the value for $n_{cr,{\rm He}}$ is taken from Dove *et al.* (1987). All other collisional dissociation rates are taken in their LTE form. As the rate for intermediate densities is accurate for all the densities we consider, it is the value we evaluate in our model.

To illustrate how these rates have been adapted to cover the high temperature range we will consider the UMIST 06 rate for reaction R07, which is shown in Figure 3.2. The UMIST 06 database gives a fit to the reaction rates in the general Langevin form

$$k_{R07} = a\left(\frac{T}{300}\right)^b \exp\left(\frac{-c}{T}\right), \tag{3.5}$$

where T is the temperature of the gas and $a, b,$ & c are constants. The rate for reaction R07 is valid for temperatures 1833−41,000 K. If the rate is extrapolated above this temperature range shown as the dashed line in Figure 3.2(a), it reaches a maximum value at 55000 K. Above this temperature the maximum value is kept constant, so the destruction rate remains high for temperatures above T$>$ 55000 K. This ensures that when the SN shell encounters molecules in gas, the molecules are destroyed quickly for temperatures above $> 10^5$ K. This is the expected behaviour for hot shocked gas within a SNR. Below the valid temperature range (Figure 3.2(b)) instead of keeping the minimum value constant, the rate was extrapolated. When compared to the GA08 rate, the fit gave correct values at T$<$ 1000 K. As the rate is so small ($\sim 10^{-20}$) at it minimum temperature of 1833 K, extrapolation may not change the overall accuracy of the chemical abundance compared to keeping the minimum value constant, but it does ensure a smoother function for the integrator to solve. Reactions R07-R15 are all treated with this in a similar way.

For the high temperatures that this module covers, there are some collisional dissociation

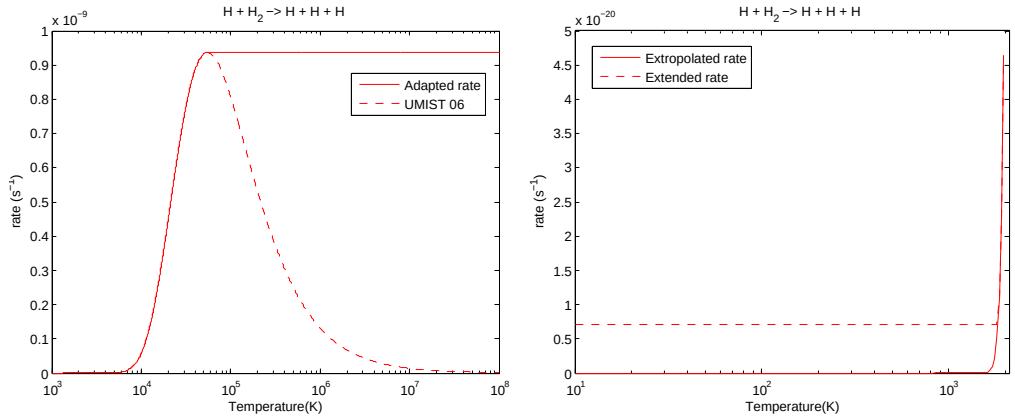

(a) (b)

Figure 3.2: Example of how collisional dissociation rates are adapted above and below their temperature range to cover full temperature range of model. The figures show UMIST 06 rate for reaction R07 which is valid for the temperature range 1833−41,000 K. On the left the displays how the rate is extrapolated above 41,000 K until its maximum value. The maximum value is then extended for all temperatures $> 55,000$ K. On the right displays how the rate is extrapolated below the temperature range, instead of the minimum value at 1833 K being extended as a constant.

reactions that were important but were not found in literature. Reaction R14 and R15 are examples of these. If we take the case of R14, a rate can be determined using a method of approximation used by Pontefract & Rawlings (2004); here the rate coefficient takes the form of $k = a \times e^{(-b/T)}$, where b is the bond strength of the molecule, and a is a constant. The reaction rate becomes

$$k_{R14} = a \times e^{\frac{-2.648eV}{T(\mathrm{eV})}}, \tag{3.6}$$

where T is the temperature of the gas in eV. The value of coefficient a was determined by using this method to approximate the rate for reaction R13 and equating it to the UMIST 06 rate at 5000 K. Molecular hydrogen has a bond strength of 4.46 eV. All three rates are shown in Figure 3.3), i.e. both the estimated rates for R13 and R14 plus the UMIST 06 rate for reaction R13. It is clear that the approximation given by Pontefract & Rawlings (2004) overestimates the destruction rate of H_2 above 3000 K. In light of this, we have opted to use the same reaction rate given by UMIST 06 for R13, for both reactions R14 and R15. This is a reasonable assumption for reaction R15, as the molecule HeH+ has a bond strength similar to H_2. However H_2^+ has a lower bond strength, so may dissociate more easily. As there are too many unknowns in using the approximation method it was considered better to use the same destruction rate as for H_2, than to over-estimate the rate, especially at lower temperatures (T$<$ 10,000 K).

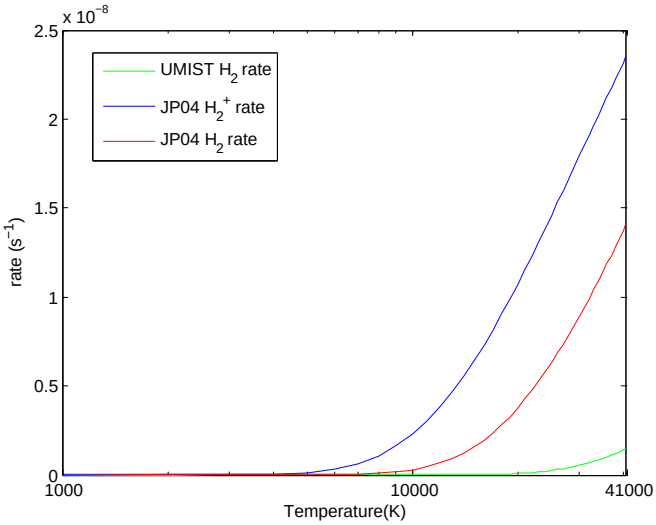

Figure 3.3: The reaction rate for R13 ($H_2 + e^- \rightarrow H + H + e^-$) given by UMIST 06 is compared to the approximation given by Pontefract & Rawlings (2004) for this reaction (JP04 H_2 rate). The approximation given by Pontefract & Rawlings (2004) for the reaction rate for $H_2^+ + e^- \rightarrow H^+ + H + e^-$ is also displayed for comparison (JP04 H_2^+ rate).

3.3.1.2 Dissociative Recombination: $XY^+ + e^- \rightarrow X + Y$

These reactions are important at lower temperatures (T $<$ 1000 K), as low electron temperatures promote recombination with ions. This is in contrast to high temperature dissociations where electrons tend to transfer energy to the molecule/ion, causing it to fragment. The dissociative recombination reactions included are R19 – R22 in Table 3.1. All the rates are from the UMIST 06 database and are obtained from experiments. The temperatures at which these rates are valid are between 300 –1000 K (see Appendix table A.2), instead of extending the maximum value the rates were extrapolated to cover the whole temperature range. When compared with rates from GA08 which are valid to 10000K, the fits have similar trends which confirms an accurate representation of the reaction rate at higher temperatures, see Figure 3.4. Reaction R23 is a dissociative charge transfer reaction which is of the form $XY^+ + Z^- \rightarrow X + Y + Z$. The reactant may not be an electron but the nature of the reaction is the same and is dominant at lower temperatures i.e T $<$ 1000 K.

3.3.1.3 Radiative Association: $X^+ + Y \rightarrow XY^+ + \gamma$

Radiative association reactions (R16-R18) form molecular bonds and generally have slow rates which increase with higher temperatures. If they are extrapolated or extended, these reaction rates would result in efficient production of molecules at all temperatures. Hence it is important to switch

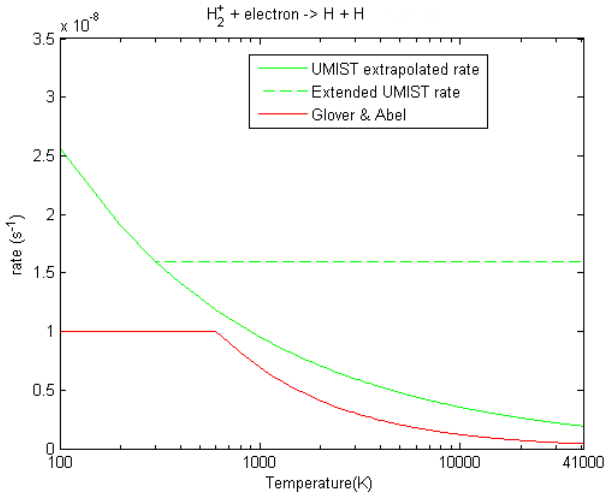

Figure 3.4: The graph displays two reaction rates for dissociative recombination reaction R20. The red line is the rate given by Glover & Abel (2008) and the green line is the rate given by UMIST 06 (valid for the temperature range 300 - 1000 K). The green dashed line represents UMIST 06 rate when the maximum value of the rate at 1000 K is extended as a constant value for higher temperatures. The solid green line displays the UMIST 06 rate extrapolated for higher temperatures. (The rate is extrapolated for temperatures T $<$ 300 K for both UMIST 06 rates displayed).

off the rates appropriately, as we do not expect molecules present in gas at temperature $\geq 10^5$ K. For all formation reactions the rates above 41,000 K have been switched off in the following manner

$$k = k_0 \times \exp\left(1.0 - \frac{\mathrm{T}}{4.1 \times 10^4\, K}\right), \tag{3.7}$$

where k is the reaction rate and k_0 is the value of the reaction rate at 41,000 K. This ensures the rate is a smooth function at the temperature boundary and the rate has a feasible shape above 41,000 K.

For reactions R16 & R18 the UMIST 06 database provides a number of rates which are valid for different temperature ranges. Unfortunately the values do not match at the temperature boundaries (see Figures 3.5(a) and 3.5(b)). Therefore the rates have been matched with GA08 rates, at the point where both rates have the same value. When switching rates like this, the UMIST rate was always taken as the correct upper value. Both these rates have to be switched off above 41,000K using a more extreme form of the previous cut-off:

$$k = k_0 \times \exp\left(10 \times \left(1.0 - \frac{T}{4.1 \times 10^4}\right)\right). \tag{3.8}$$

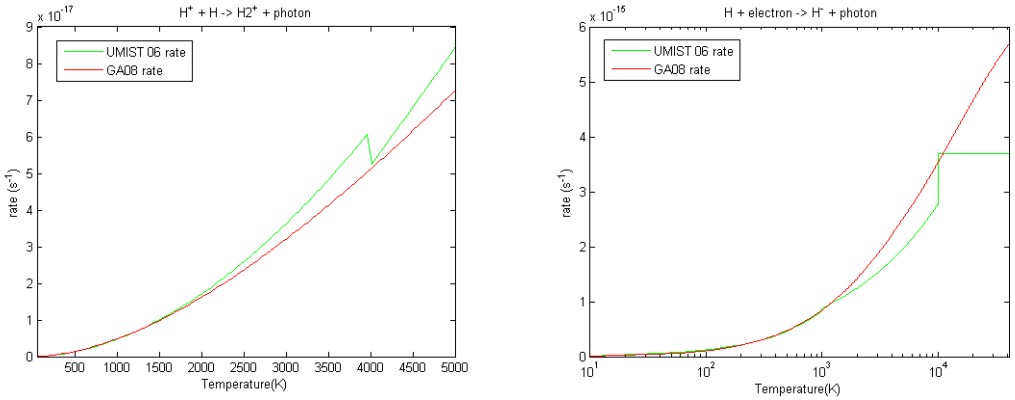

(a) R16 (b) R18

Figure 3.5: Both the rates for reactions R16 and R18 provided by UMIST 06 are given by a number of rates valid at different temperature ranges. It can be seen they do not match at the temperature boundaries (sharp jumps) and therefore have been matched with the GA08 rates.

Otherwise, the production rates for H^- and H_2^+ were greater than the destruction rates at temperatures above 10^5 K.

3.3.1.4 Non neutral-neutral reactions

The chemistry set does not include any neutral-neutral reactions but we have charge transfer (R24-R29), proton transfer (R30- R34) and associative detachment (R35 -R36) reactions. The associative detachment reactions form molecules from atomic ions or neutrals and therefore are exponentially cut-off at 41,000K using the form in Equation (3.7). The other reactions do not break bonds, if a reaction contains molecules in its products it is also exponentially cut-off to prevent the formation of molecules above 41,000 K. Please see the Appendix for individual details.

Reaction R24 also has a number of reaction rates to cover the temperature range 10 – 41,000K. At 10,000K the rates do not match (see Figure 3.6). In this case we could not match with the GA08 rate as it uses the same value of rate given by UMIST 06 below 10,000K. Therefore we had to develop our own matching scheme between $10^3 - 10^4$ K:

$$k_{24} = k_{low} + (\mathrm{T}/10^4\ \mathrm{K}) * (k_{upper} - k_{low}) \tag{3.9}$$

where k_{low} is the UMIST 06 rate for R24 valid below 10^4 K and k_{upper} is the UMIST 06 rate for reaction R24 valid above 10^4 K.

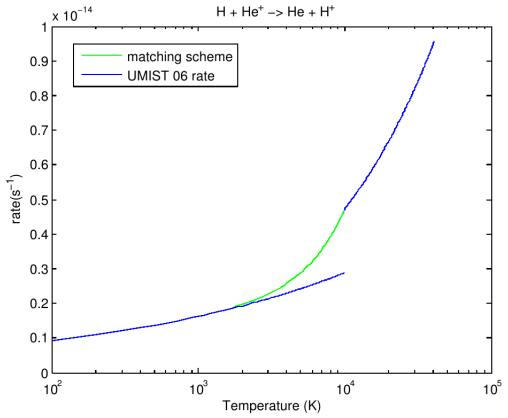

Figure 3.6: The two rates provided by UMIST 06 for reaction R24 shown in blue, do not match at the 10^4 K boundary. Therefore a matching scheme was devised between the temperatures $10^3 - 10^4$ K (shown in green).

3.3.2 The Thermal Model

The SN is modelled by injecting thermal energy, not kinetic (i.e. we ignore the free-expansion phase). To avoid artificial overcooling at early times, we only switch on the cooling when the gas adiabatically cooled down to 10^8 K. The energy density is passed by the hydrodynamic code and is converted into gas temperature using Equation (3.4). The cooling processes included in the thermal model are listed within Table 5.5.

The molecular line cooling is valid below 10^4 K and becomes dominant at lower temperatures (further details below). Above this temperature the atomic line cooling is dominant, the processes are listed in Table 5.5. Most of the atomic cooling functions provided by Fukugita & Kawasaki (1994) and Hummer (1994) are valid for T$\leq 10^7$ K and are extended at a constant value to 10^8 K. Bremsstrahlung cooling provided by Shapiro & Kang (1987) is valid up to 10^8 K and therefore does not need extending.

3.3.2.1 Molecular Cooling

The thermal model includes the rovibrational cooling of $H_2{}^+$and H_2. Within the low density limit (ld), the gas is optically thin, and the cooling per molecule is given by the sum of the cooling rates due to collisions with a number of different partners. For example, the cooling per molecule of hydrogen would be

$$\Lambda_{\mathrm{H_2,ld}} = \sum_i \Lambda_{\mathrm{H_2},i}\, n_i \text{ erg s}^{-1}, \tag{3.10}$$

where i= H, H_2, H^+, He & electrons and n_i is the respective number densities of the species. This value is multiplied by the number density of H_2 to obtain the overall cooling rate (ergs $\mathrm{cm}^{-3}\,\mathrm{s}^{-1}$). We use the Glover & Abel (2008) H_2 cooling function instead of other cooling functions such as Galli & Palla (1998) which only include collisions with H_2 and H. Atomic hydrogen is most abundant and hence its collisions with H_2 is the most effective cooling mechanism in neutral gas. Low temperature gas at solar metallicity becomes molecular ($n_{\mathrm{H_2}}/n_{\mathrm{H}} \sim 0.5$), hence H_2 – H_2 collisions become very important. Within primordial gas, the highest fractional abundance of H_2 can be 10^{-3} at densities $n < 10^{10}$ cm^{-3} (Greif *et al.* 2010; Glover & Savin 2009). It is more likely that a H_2 molecule collides with helium atoms than another H_2 molecule at T$<$ 2000 K, plus the cooling due to collisions with protons and electrons is significant for ionised gas (Glover & Abel 2008). Therefore it is important to include all these cooling rates. The ortho-para hydrogen ratio is kept constant at 3:1. This is a robust approximation within the temperature range in which H_2 cooling is important (Glover & Abel 2008).

At high densities, the gas become optically thick and so the level populations within molecules are assumed to be in local thermodynamic equilibrium. At these densities the cooling rate per molecule is independent of the chemical composition and is given by

$$\Lambda_{\mathrm{LTE}} = \sum_{i,j>i} A_{ji} E_{ij} f_j \tag{3.11}$$

where A_{ji} is the radiative de-excitation rate for transition from level j to i, E_{ij} is the corresponding energy and f_j is the fraction of that molecule in level j, which are computed assuming LTE. For molecular hydrogen this occurs at densities $n \sim 10^4 - 10^5$ cm^{-3} and the analytic fit for this rate is obtained from Hollenbach & McKee (1979) . The LTE rate for H_2^+ cooling is obtained from Glover & Abel (2008).

The gas within our simulations will have densities between these two regimes i.e. intermediate densities, Galli & Palla (1998) provide the following expression for the cooling rate per molecule

$$\Lambda = \frac{\Lambda_{\mathrm{LTE}}}{1 + \frac{\Lambda_{\mathrm{LTE}}}{\Lambda_{ld}}}. \tag{3.12}$$

This is the expression we use for all the molecular cooling functions as it provides the correct value of cooling rate per molecule as the density approaches critical density and the low density regime. However, to save computing time we use the low density function for $n < 1$ cm^{-3}.

Cooling Process	Collisional Partner	Reference
Atomic line cooling:		
H I	e^-	Fukugita & Kawasaki (1994)
He I	e^-	Fukugita & Kawasaki (1994)
He I(2^3 S)	e^-	Fukugita & Kawasaki (1994)
He II	e^-	Fukugita & Kawasaki (1994)
Collisional ionisation:		
HI	e^-	Fukugita & Kawasaki (1994)
HeI	e^-	Fukugita & Kawasaki (1994)
HeII	e^-	Fukugita & Kawasaki (1994)
Recombination:		
HII		Hummer (1994)
HeII		Fukugita & Kawasaki (1994)
HeII (dielectric recombination)		Fukugita & Kawasaki (1994)
HeIII		Fukugita & Kawasaki (1994)
Bremsstrahlung:		
H II		Hummer (1994)
He II		Shapiro & Kang (1987)
He III		Shapiro & Kang (1987)
Compton scattering:	CMB photons	Peebles (1971)
Molecular line cooling:		
H_2	H, He, H^+, H_2, e^-	Glover & Abel (2008)
		Hollenbach & McKee (1979)
H_2^+	H, e^-	Glover & Abel (2008)

Table 3.2: Cooling processes

3.3.3 Testing the Module

To test the microphysics module, we compared the network and cooling functions with those used by GA08. The chemistry network used by GA08 included 32 reactions that involve species that contain helium and hydrogen only. They include three body reactions and the density dependent rates for reactions R10 and the reaction $H_2 + He \rightarrow H + H + He$. The GA08 network does not include H_3^+ and HeH^+.

We set up a one-zone isobaric model, i.e. a point calculation in which the density remains constant but the temperature and chemical species evolve with time. Initially, the gas has a temperature of 10,000 K and is completely ionised (i.e. x_{H^+}=1.0 and $x_{He^{++}}$=0.08) for three different densities (n = 1, 100, 10^4 cm^{-3}). The results after the gas has cooled for 50×10^6 years

are shown in Figure 3.7.

For the low density test (i.e. $n = 1$ cm^{-3}) both microphysics modules reach the same temperature of 244 K. In the test for $n = 10^4$ cm^{-3} the temperatures are very close; our module cools down to 6115 K and the GA08 module cools to 6090 K. At this density the H_2 cooling is within the LTE regime. The temperatures are very close, the difference is due to the rates we have included and not because the three body reactions were excluded. Three body reactions are dominant for densities $n \geq 10^5\,\mathrm{cm}^{-3}$, and can be neglected as we do not expect the densities in the module to reach this value. In the test for $n = 100$ cm^{-3} we obtain 69 K whilest the GA08 module obtains 90 K. When we include the reactions that are missing from our module, we still obtain 69 K. This highlights that the differences in temperature are due to the differences between the rates used in UMIST 06 database and the GA08 module.

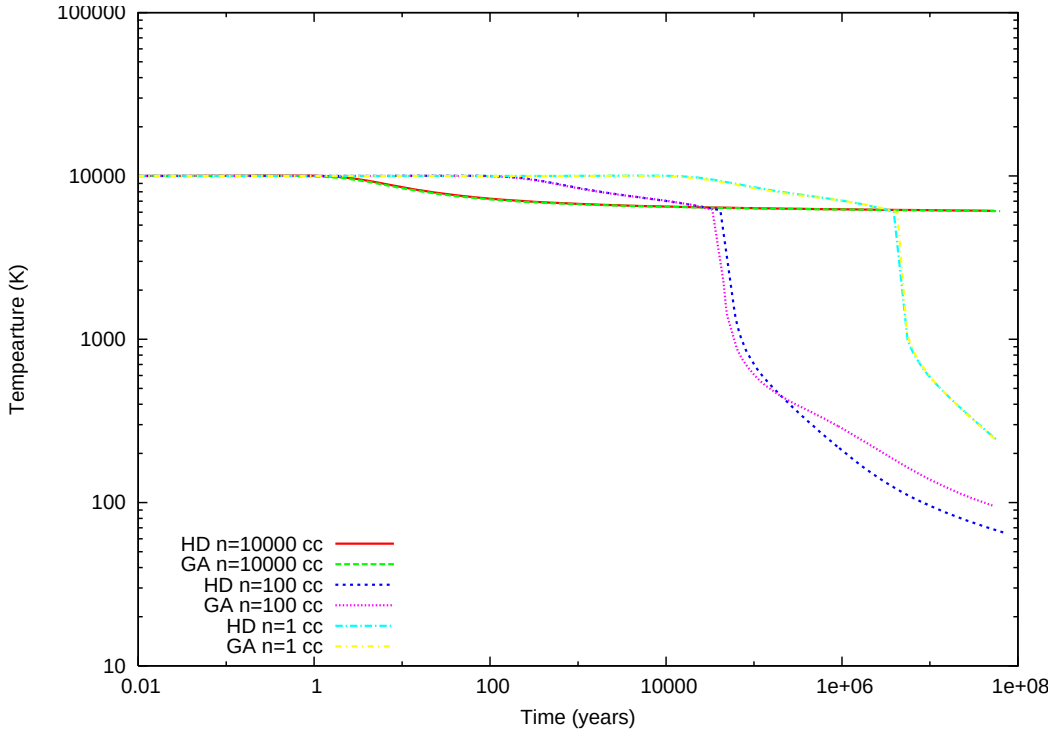

Figure 3.7: One-zone test to compare the microphysics module (HD) against the chemistry and cooling presented by Glover & Abel (2008) (GA). The gas is initially fully ionised and has a temperature of 10^4 K. Three different densities are investigated: $n = 1$ cm^{-3}, $n = 100$ cm^{-3} and $n = 10^4$ cm^{-3}

Fig. 3.8 shows the results of a 1D test, in which the expansion of a blastwave is followed using different chemistry/cooling assumptions: adiabatic with no chemistry, including chemistry but only atomic coolants, and including chemisty with atomic and molecular coolants. The radius of the

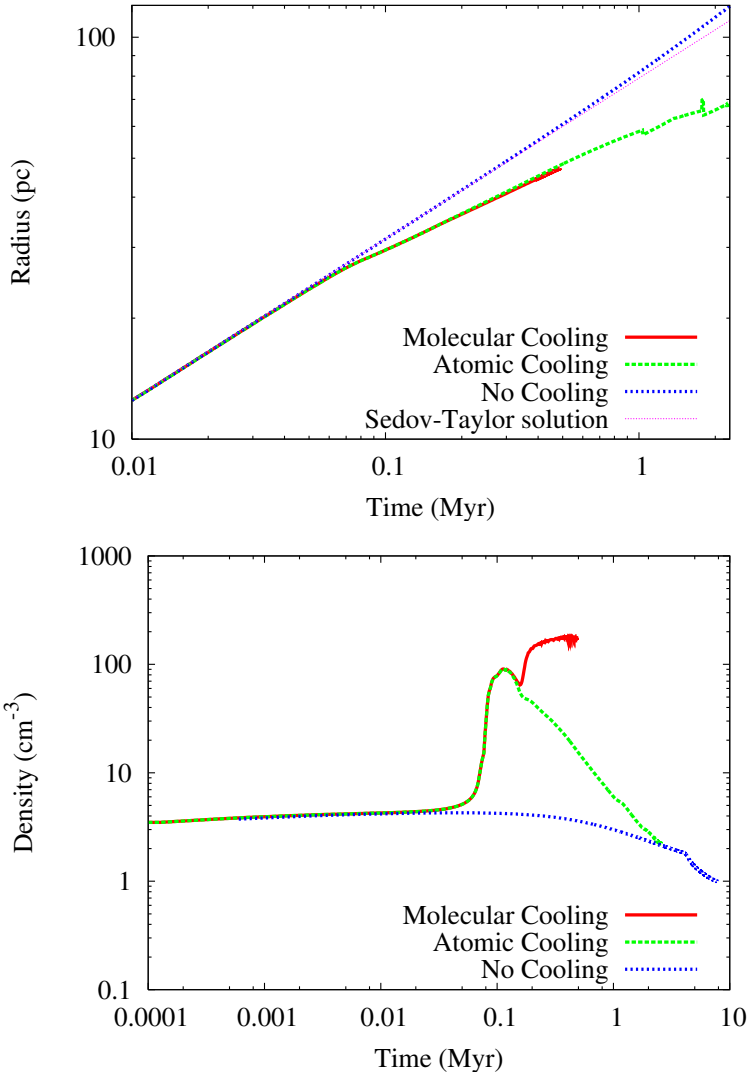

Figure 3.8: Supernova shell expansion as a function of time for an adiabatic calculation, a calculation with atomic line cooling only, and a calculation with atomic and molecular cooling switched on. The expansion radius is compared to the analytic Sedov-Taylor solution in the upper plot. The lower plot shows the maximum gas number density in the shell as a function of time for the same three models.

SN forward shock (upper panel) and maximum density in the shell (lower panel) are plotted as a function of time since explosion. We used uniform radial grid with 5120 grid zones between $r = 0$ and $r = 130\,\mathrm{pc}$, and input 10^{51} ergs of thermal energy in the 8 grid zones closest to the origin. The ISM is a constant density medium with $\rho = 2.44 \times 10^{-24}\,\mathrm{g\,cm^{-3}}$ at a redshift of 20. The initial ISM temperature is $T = 10^4\,\mathrm{K}$ (corresponding to a pressure of $p \approx 1.5 \times 10^{-12}\,\mathrm{dyne\,cm^{-2}}$). Without any cooling this can be compared to the Sedov-Taylor solution, and when cooling and chemistry are included we compare to the results of Machida *et al.* (2005).

The adiabatic calculation matches the Sedov-Taylor solution until about 0.8 Myr, after which the shock runs ahead of this solution. The explanation for this is that the shock weakens as it slows down at late times, and the ISM ambient pressure is no longer negligible. This breaks the scale-free nature of the analytic solution, and the result is that the shock radius advances faster than predicted at late times (cf. Raga *et al.* 2012).

At about 0.05 Myr the simulations with cooling start to decelerate and deviate from the adiabatic solution. The expansion rate changes from the Sedov-Taylor value $R_{\mathrm{sh}} \propto t^{2/5}$ to the momentum-conserving value $R_{\mathrm{sh}} \propto t^{1/4}$. Atomic cooling is initially much stronger than molecular cooling, so both of these runs match each other until the molecular cooling begins to affect the shell and the ISM at $t \approx 0.2\,\mathrm{Myr}$. At later times the shell density in the cooling model decreases steadily because it can no longer cool, and the weak forward shock keeps adding lower entropy gas to the shell. The molecular cooling model has a higher density shell once molecular cooling becomes important at $t \approx 0.2\,\mathrm{Myr}$, because it can cool to much lower temperatures. This has the further effect that the shell remains at a high density for much longer.

The molecular cooling calculation shows that we get compression factors of $> 100\times$ in the shell at $t \geq 0.2\,\mathrm{Myr}$. This model disagrees strongly with Machida *et al.* (2005) (see their fig. 4), who found only weak density increase in the supernova shell for times up to 10^7 years. The density in their analytic model was set by the imposed pressure-confining boundary conditions on the shell, so we suspect that one of the boundary conditions was incorrect.

3.4 1D Toy Model: Evolution of SNR

The initial conditions of a SN model are heavily dependent on the properties of the progenitor star, the mass of the halo and where the cloud is situated. A Population III star within a mini halo at redshift $z = 20$ creates a HII region thats extends to 100 pc, whereas the same star will produce a HII region of radius $\sim 10 - 20$ pc within a dark matter halo of mass 10^7 $M_\odot$ at $z = 12$ (Whalen & Norman 2008). When a cloud or clump is situated at the edge of a HII region, the presence of a UV radiation field causes the photoionisation and photodissociation of the chemical species within it. This changes the chemistry and hence the thermal state of the cloud. If the cloud is situated within the HII region, it is further affected by interacting with the stellar wind and the strong ionising radiation may evaporate the cloud completely.

Most of the previous SN models have assumed a constant density of 1 cm^{-3} for the surrounding ambient medium of the SN blast (Machida *et al.* 2005; Salvaterra *et al.* 2004). As a starting point we will adopt the same properties for the ambient ISM and place a dense neutral cloud at 40 pc from the progenitor star. At redshift $z = 10$ the HII region within such a halo would be around 10 pc, this will ensure the cloud does not interact with any FUV radiation from the progenitor star. In reality the cloud would be embedded within a denser medium than $1\,\mathrm{cm}^{-3}$, this density approximates gas found within a HII region. As we are modelling the gas between the progenitor star and the cloud as a single low density gas, we are treating this as a toy model.

In this toy model we assume a neutral cloud of density $n = 115\,\mathrm{cm}^{-3}$ and temperature T= 200 K, and is located 40pc away from the pre-supernova star and that it has survived the life of the star without being affected by any radiation. The ambient medium is ionised gas with a temperature of 10^4 K and density $n = 1$ cm^{-3}. It is assumed there is no other clumpy material between the cloud and the SN. The SN explosion energy is 10^{51} ergs, which is the average explosion energy of a core collapse SN observed in the Universe today. It is understood that both the effects of the HII region and uncertainty in explosion energy need to be investigated. This will be done in the next chapter.

The initial abundances for the chemical species were treated as follows. The ambient medium was assumed to be fully ionised, with only two chemical species present: $n_{\mathrm{H}^+}/n_{\mathrm{H}} = 1.0$ and $n_{\mathrm{He}^+}/n_{\mathrm{H}} = 0.08$. The cloud is assumed to be neutral. Free electrons to catalyse the formation of molecules are needed, hence the fractional abundance of H^+ is set to $\mathrm{x}_{\mathrm{H}^+} = 10^{-4}$, which is the predicted abundance for gas at redshift $z = 10$ left over from the Big Bang (Galli & Palla 1998).

The results from the 1D model (512 mid points) are shown in Figures 3.9 – 3.13; which display both the dynamic and chemical evolution of the gas during the development of the SNR and its subsequent collision with the gas cloud, at various timesteps. The initial conditions are displayed in Figure 3.9, where the time is set at $t = 0$ s. The cloud which starts at 40 pc is modelled as a hollow sphere. This is because the pre-collision output will be used as the initial conditions of the 2D model.

Around $t \sim$ 12,000 years the shock front is travelling at a velocity of 300 km s^{-1} and has reached 13.5 pc (Figure 3.10). The SNR is expanding adiabatically and the post-shock temperature is T$\sim 10^7$ K. Most of the hot gas situated close to the explosion site is still much hotter than the post-shock temperature. Mainly fully ionised hydrogen and helium is present in the post shock medium, singly ionised helium has survived due to low densities and therefore fewer possible collisions. The ambient ISM no longer consists of only ionised hydrogen and helium; due to the absence of an UV radiation field, ions and atoms have recombined to form molecules. From Figure 3.9(b), one can see that the initially ionised gas produces abundances of $x_{HeH^+} \simeq 5 \times 10^{-13}$, $x_{H_2^+} \simeq 10^{-8}$, $x_{H^-} \simeq 10^{-8}$ and $x_{H_3^+} \simeq 10^{-16}$ in the ISM compared to the neutral cloud. Although there is slightly more molecular hydrogen present in the cloud ($x_{H_2} = 10^{-6}$) than the ISM ($x_{H_2} = 10^{-7}$) due to its cooler temperature.

Figure 3.11 shows the SNR after $t \sim$ 86,700 years. At this point the shock front has reached about 28.5 pc and the SN shell has fully formed. The SNR starts to sweep up material and a shell begins to form at 27pc after 72,800 years. The shell has a density of 27 cm^{-3}, a minimum central temperature of 1.1×10^4 K and velocity 88 km s^{-1}. The post-shock temperature is $\sim 10^6$ K. The outer edges of the cloud have started slowly flowing outwards due to diffusion ($\sim$ 0.4 km s^{-1}), becoming less dense at the edges. Within this outflow there is an increase of H_2 formation, due to the increase of electrons available.

Overall, the abundances of the chemical species within the ISM have continued to increase at different rates. The molecules $H_3{}^+$ and HeH^+show the greatest increase due to the availability of free electrons and ions. The gas within the cloud also continues to chemically evolve; there is an increase in molecular hydrogen reaching a fractional abundance of 5×10^{-5}, whereas the other species have found their equilibrium values by 86,700 years. Although the SN shell and ISM have a similar temperature, the increase in pressure inside the shell causes a slight increase in the formation of $H_2{}^+$and $HeH^+$and destruction of H_2 and $H_3{}^+$, as the collisional destruction rate for

H_2 becomes dominant above 5000 K. The loss of this primary coolant is reflected in the slightly higher temperature within the SN shell.

Figure 3.12 displays the SN shock at $\sim$ 39pc just before it collides with the cloud at time t $\sim$258,000 years. The pressure from the hot gas behind the shock has greatly decreased. The SN shell has swept up more material, although the maximum density has decreased to 60 cm^{-3} due to the decrease in pressure, the shell has increased in width. This loss in density and ionisation fraction caused an increase in the amount of molecular hydrogen and $H_2{}^+$within the center of the shell so that its minimum temperature is equal to that of the ISM. As the post-shock temperature is T$\geq 5 \times 10^5$ K, all the chemical species are destroyed by collisions in the hot gas.

Figure 3.13 displays the system at $t \sim$ 408,000 years. This is after the SN shell has collided with the cloud at 40 pc, and a reverse shock has formed. The cooler gas from the shell and cloud start to flow back into the post-shock region, increasing the abundances of chemical species present.

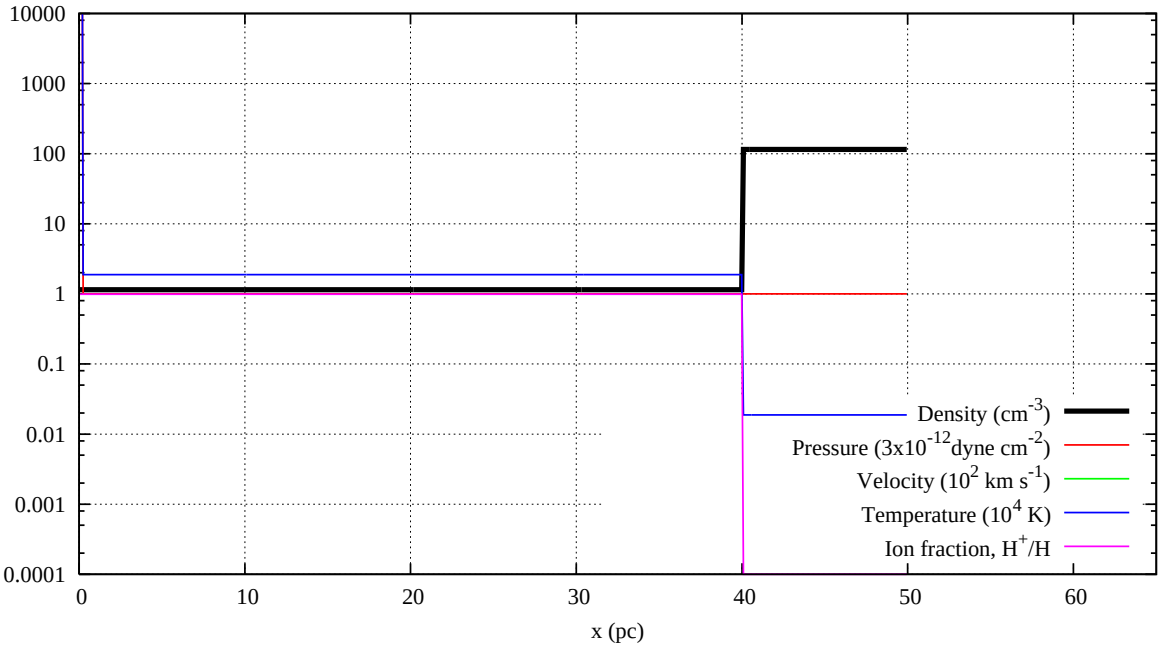

(a) Physical parameters

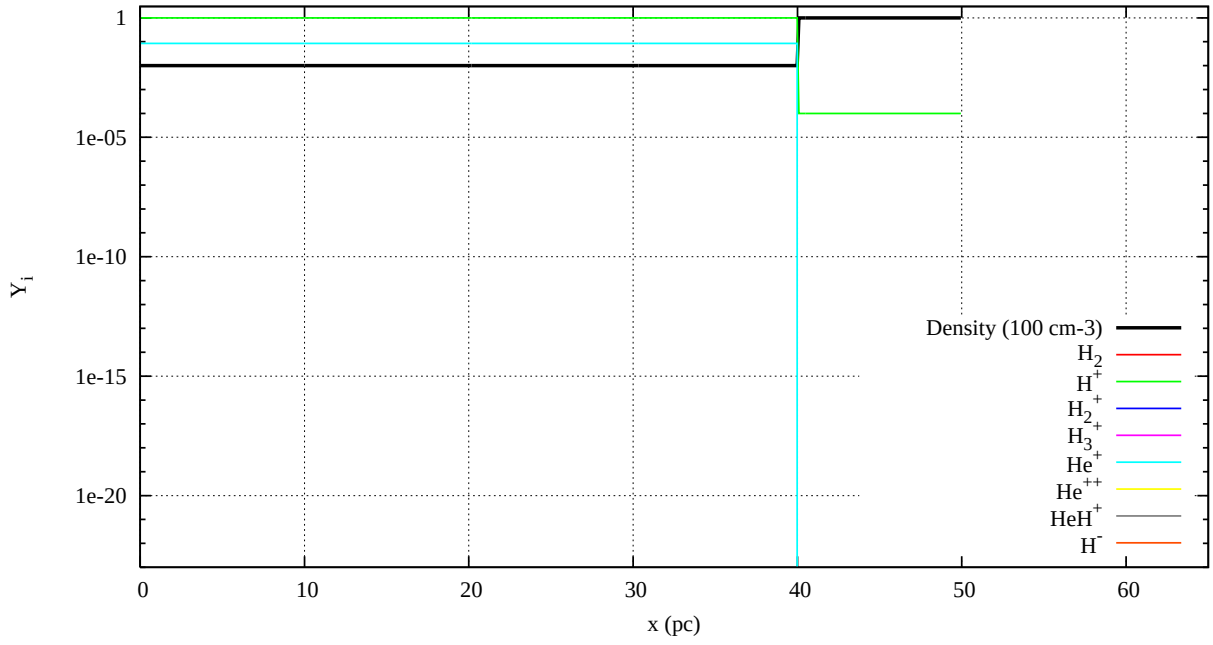

(b) Fractional abundances of the chemical species

Figure 3.9: Initial conditions of 1D SN model (t =0.0 s), prior to SN explosion.

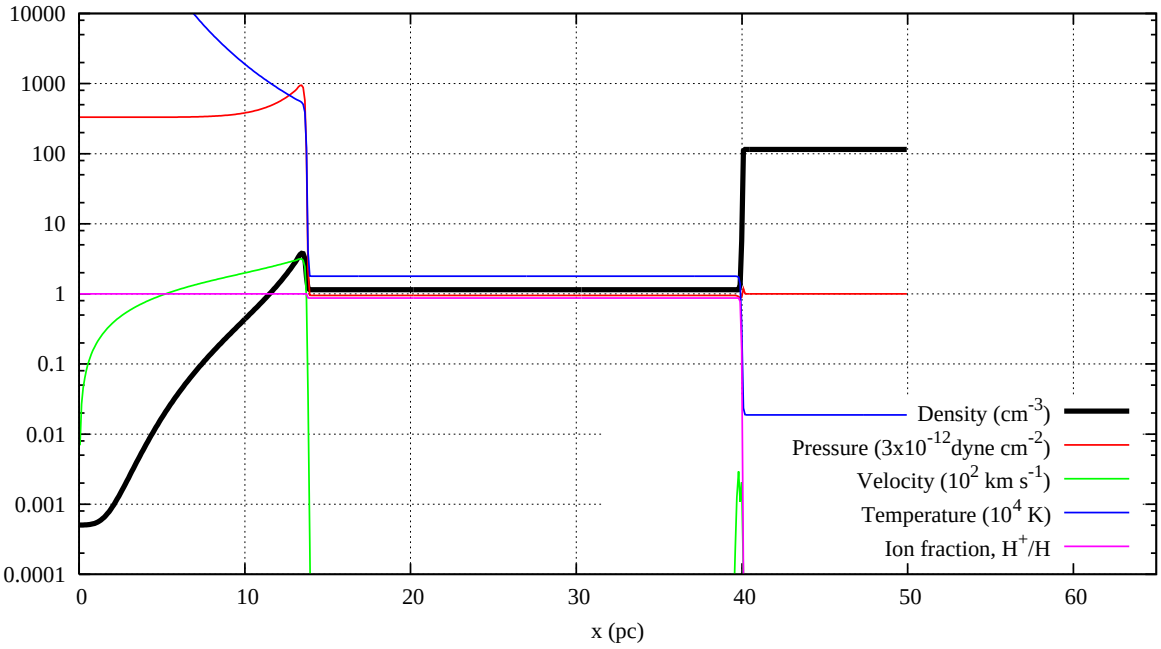

(a) Physical parameters

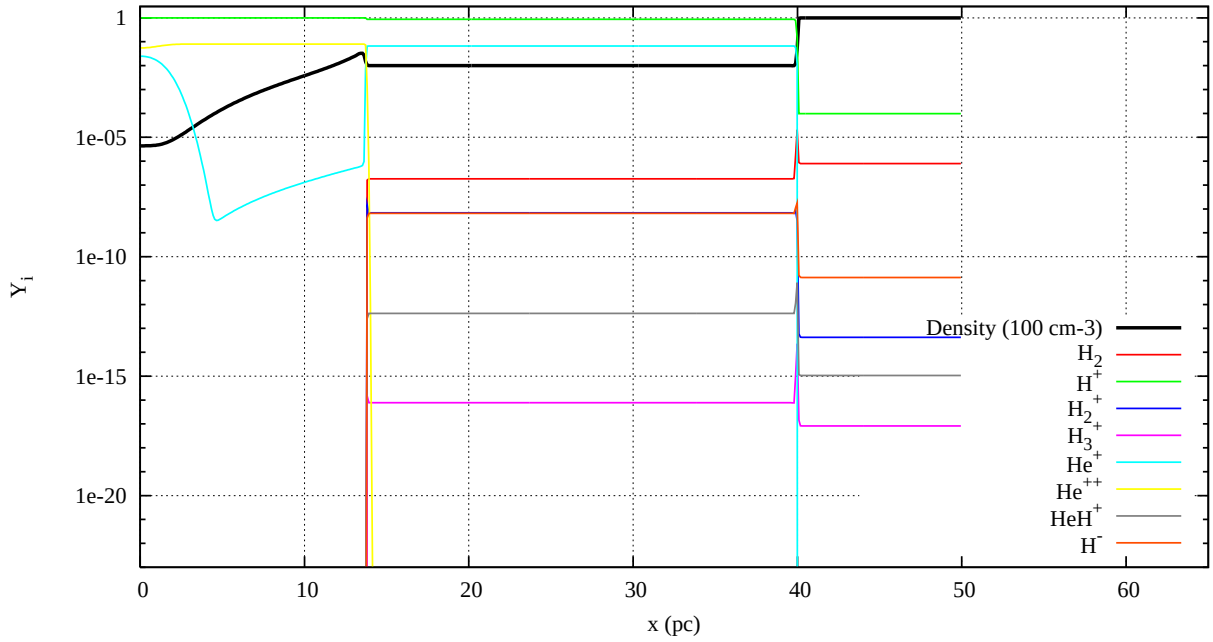

(b) Fractional abundances of the chemical species

Figure 3.10: 1D SN model after $t \sim$ 12,000 years

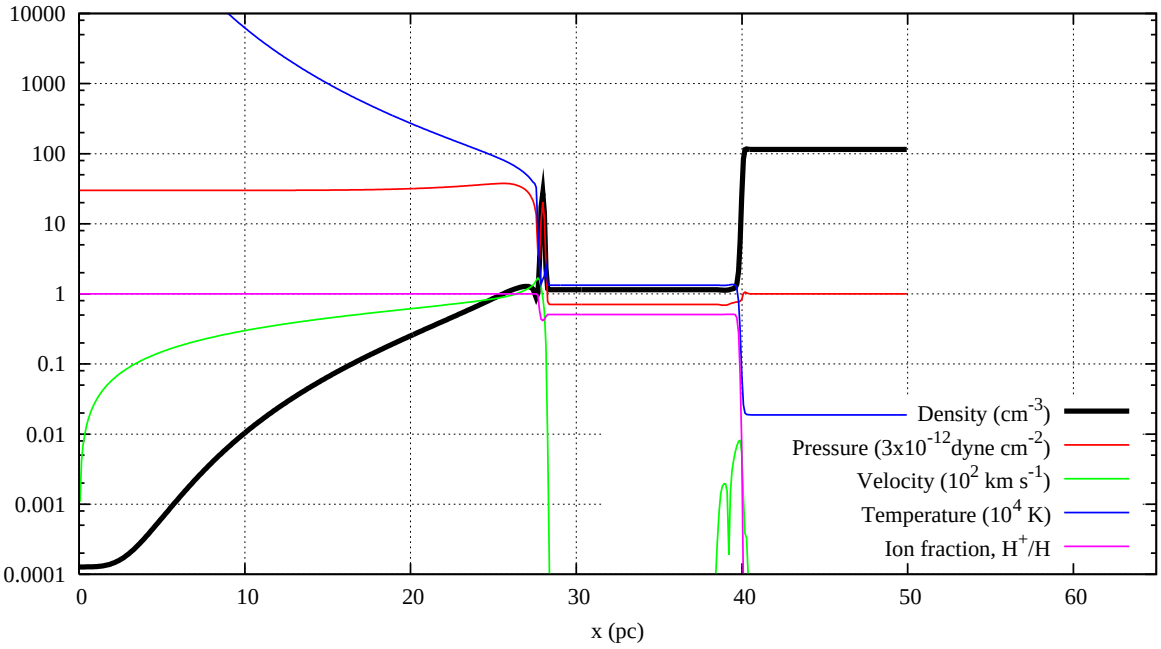

(a) Physical parameters

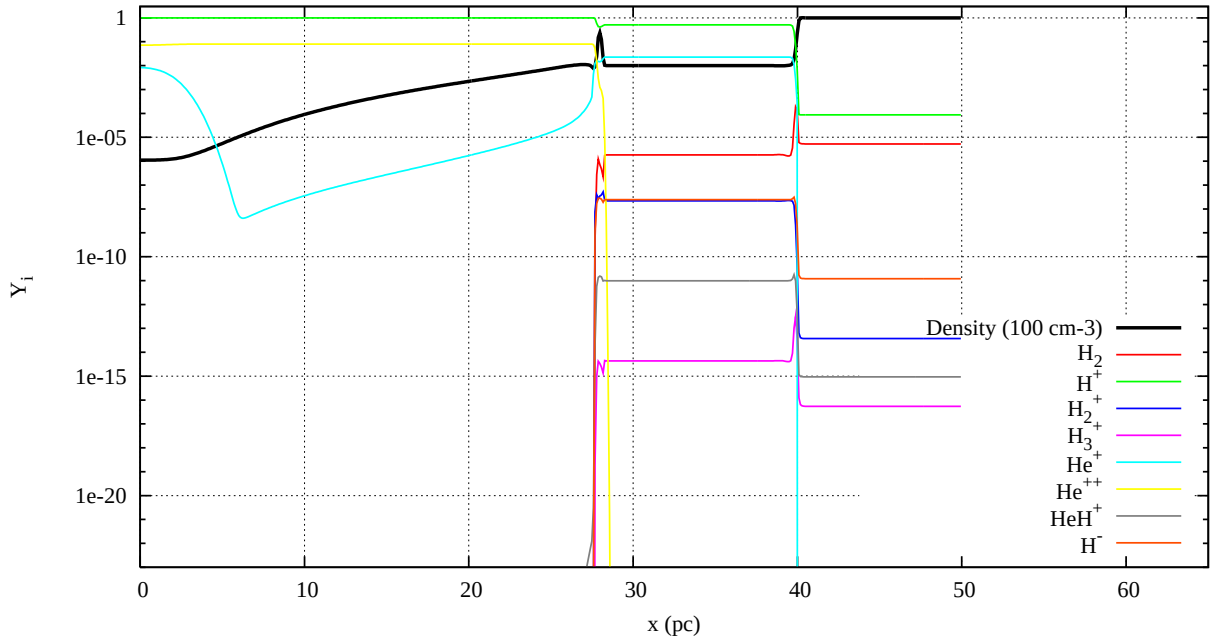

(b) Fractional abundances of the chemical species

Figure 3.11: 1D SN model after $t \sim 86,700$ years

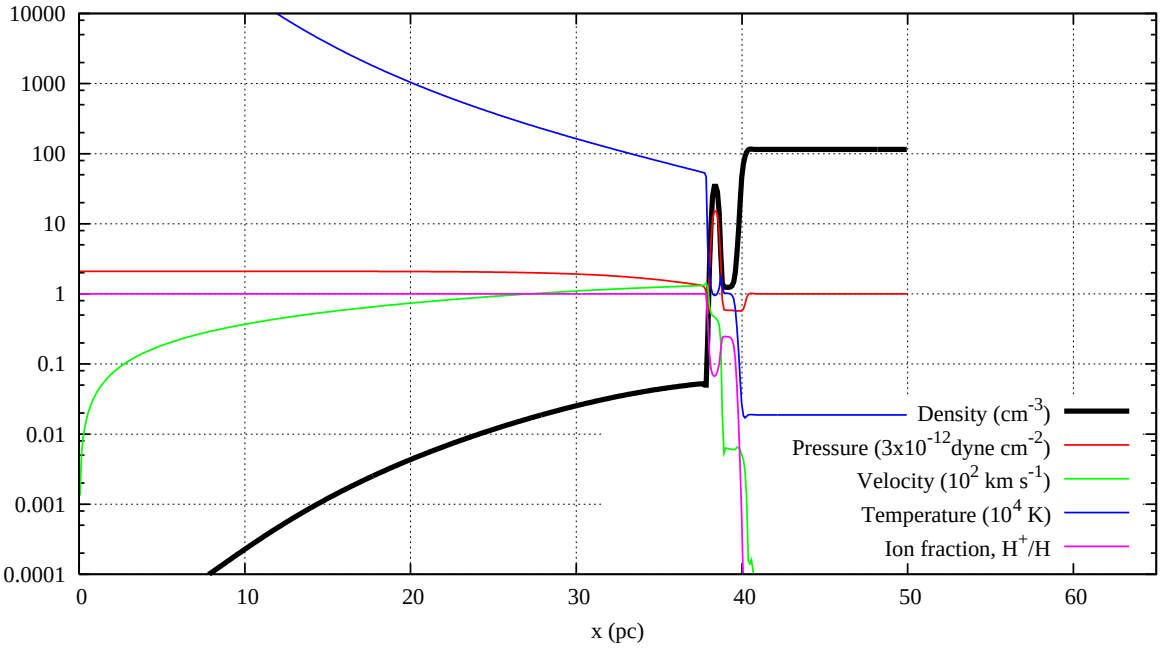

(a) Physical parameters

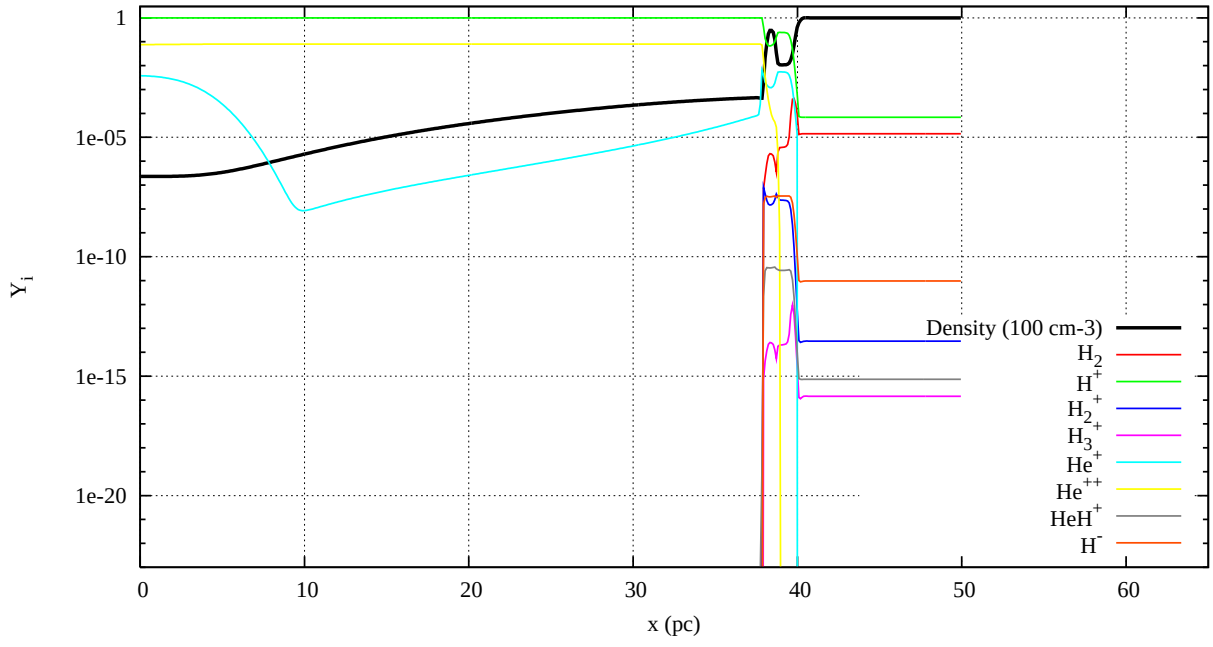

(b) Fractional abundances of the chemical species

Figure 3.12: 1D SN model after $t \sim 258,000$ years

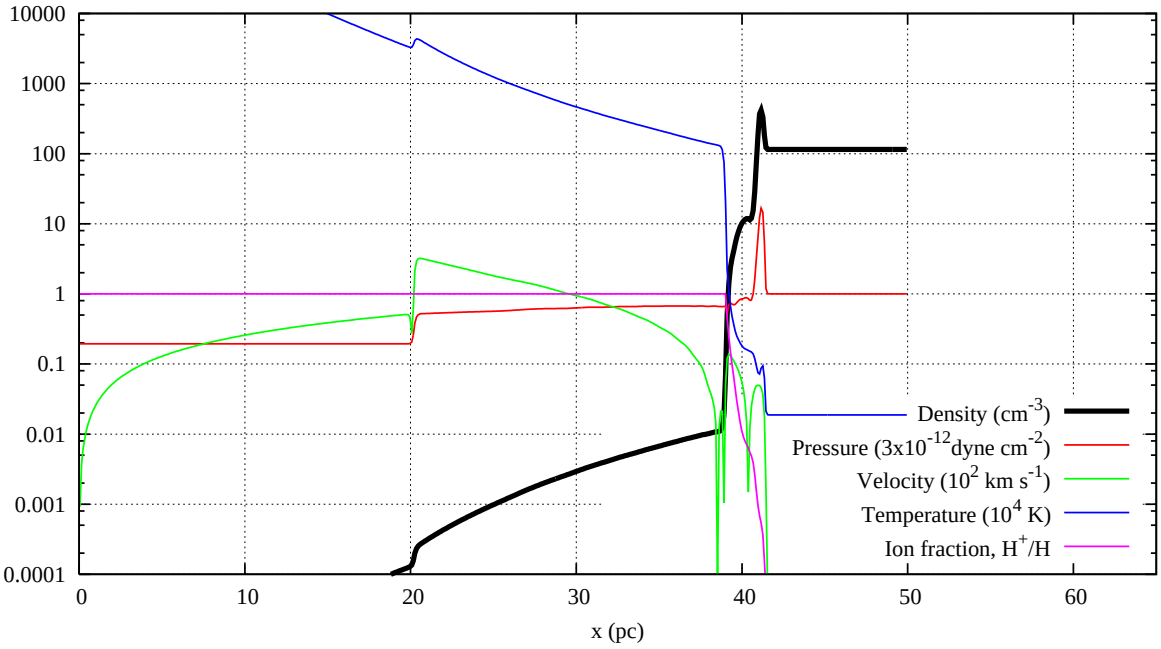

(a) Physical parameters

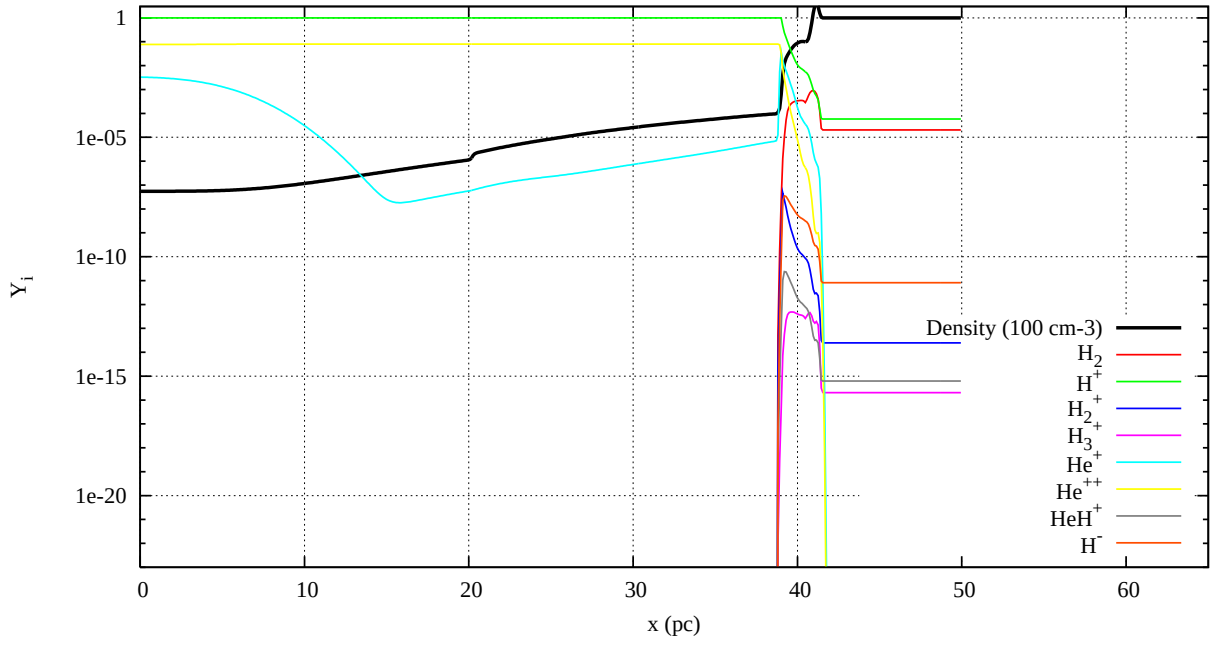

(b) Fractional abundances of the chemical species

Figure 3.13: 1D SN model after $t \sim 408,000$ years

3.5 2D Toy Model: The interaction of SN shell with the cloud

For the 2D model the initial conditions are obtained from the output of 1D model toy model (§ 3.4). A high resolution 1D model of 5120 grid points was run and when the SN shell reaches 39 pc (for example Figure 3.12) the output was mapped on to a 2D grid (both the dynamic properties and chemical abundances). The 2D model concentrates on the area 37.0 - 44.68 pc from SN progenitor. This mapping is achieved by plotting the 1D output of the shell linearly in the y-direction; however the area from 39.5 pc to 41 pc is rotated 180° about the 41.0 pc point to form a semi-circle. This creates a half a spherical cloud (1 pc radius), as seen in Figure 3.14(a).

All properties were mapped directly in this way, with the exception of the velocity. When velocity was mapped rotationally from the 1D x-direction, it was converted in a way that made sure its direction is always pointing radially outwards from the center of the cloud. The dimensions of the simulation box are 7.68 pc by 3.2 pc (384×160 gridpoints). The simulation is axial-symmetric, so can be reflected in the x-direction to represent a spherical cloud.

Figure 3.14 displays the evolution of the density of gas as the shock collides with the cloud, the legend represents the mass density in $\mathrm{g{\cdot}cm^{-3}}$ units which equates to maximum number density of 981.6 $\mathrm{cm^{-3}}$ and a minimum value of 0.0098 $\mathrm{cm^{-3}}$. Figures 3.14(a) and 3.15(a) represent the initial conditions for density and temperature, and as we initiate a new model the time has been reset to $t = 0$. The SN shell can be split into two parts: the front part which has a density of 39 $\mathrm{cm^{-3}}$ and the trailing part which is being compressed by the hot gas behind which has a maximum density of 74 $\mathrm{cm^{-3}}$.

The temperature across the shock is shown in Figure 3.17(a). The front part of the shock has a temperature of ∼7000-8000 K, which is similar to the temperature of the ISM. The front edge of the shock separates the front half of the shock and the ISM with a thin compressed region which has a temperature of 15,000 K. The trailing part of the shock is much cooler and reaches a minimum temperature of 2000 K. The two regions of the shock are also travelling at slightly different speeds which can be seen in Figure 3.17(b). The trailing part is travelling at 117 $\mathrm{km{\cdot}s^{-1}}$ in the positive x direction, so the shock has a maximum velocity at this interface of 50 $\mathrm{km{\cdot}s^{-1}}$ and reduces down to a constant 46 $\mathrm{km{\cdot}s^{-1}}$ within the front part of the shock.

The ISM density remains at 1 $\mathrm{cm^{-3}}$ and the cloud has a total number density of 115 $\mathrm{cm^{-3}}$. The edge of the cloud have the minimum temperature of 146 K where there is a density decrease,

due to the increase in H_2 in this region (see Figure 3.16). Due to the low fractional abundance of H_2, compared to dark molecular clouds in at $z = 0$, the average mass of each particle remains close $\mu = 1.22$, which is the value observed for atomic gas. The center of the cloud has a temperature 180 K.

Figure 3.14(b) shows that by $\sim$ 92,000 years the SN shock has moved through the cloud; compressing the SN-facing side of the cloud, and a shock passes through the rest of the cloud (seen as the high density region in pink). After about 152,000 years the ridge has become more pronounced and the shock has moved through to the righthand side of the cloud as seen in Figure 3.14(c). The shock has continued to move forward in the positive x-direction causing the gas to flow along with it, and the dense ridge experiences instabilities (Figure 3.14(d)). After 501,000 years these instabilities grow and form into clumps seen at the end of the simulation in Figure 3.14(f). The temperature of the final step is shown in the Figure 3.15(b). The temperature of the ISM is $\sim$ 73,000K, with higher temperature present as gas is still being shocked. From 3.16(b) we can see that once the shock has passed , there is a high fractional abundance of molecular hydrogen in all the gas which previously formed the neutral cloud, and not just within the high density clumps.

Four clumps are formed by the end of the simulation, labelled in Figure 3.14(f). We categorised a clump as having a mass density above 1.0×10^{-22} g·cm^{-3}. The central clump A1 has a maximum density of 515 cm^{-3} with a minimum temperature of 220K. It is connected to a smaller clump A2; which is the smallest clump, it has a minimum temperature of 450 K and a maximum density of 147 cm^{-3}. Clumps B and C are formed on the outer edge of the ridge and have higher temperatures than A1 and A2. Clump B has a maximum density of 127 cm^{-3} and a minimum temperature of 500K. Whereas Clump C has a maximum density of 93 cm^{-3} and temperature of 800 K.

To estimate the mass of the largest clump A1, we assume it has the shape of a prolate ellipsoid. So it has the volume, V:

$$V = \frac{4}{3}\pi a b^2. \tag{3.13}$$

The clump has a mass of $\sim 0.3\,\mathrm{M}_\odot$ and the parameters used to estimate this are listed in Table 3.5. The estimated Jeans mass of the clump is $m_J \approx 3000\,\mathrm{M}_\odot$, so this clump will not undergo gravitational collapse. Due to the low density of the clump ($< 10^4$ cm^{-3}) survival of the clump is uncertain, as it may later expand and diffuse into the ISM. It is unlikely that this clump will form a pre stellar core.

The simulation is axisymmetric, and so the other clumps would be rings in 3D. To give a rough estimation of the mass of these clumps it is assumed that the third radius of the ellipsoid is equal to the shorter radius b (also shown in Table 3.5). All these clumps are much smaller than central clump and hence we infer they will not form prestellar cores either.

The 2D toy model will be utilised as a tool to investigate different processes that may affect the chemistry and in turn the fragmentation of the cloud. The basic model described here will be used to compare against more complex chemical and thermal models. This will give us the opportunity to determine which processes have negligible effect on the thermal evolution and hence can be neglected. Each model uses the initial conditions described for the 1D model. Therefore using the chemical abundances from the 1D output allows the cloud to chemically evolve to equilibrium values which are specific to the physical conditions of the model in question. We have investigated the effect of cosmic rays, CMB ionisation, chemical heating and deuterium chemistry. Please see sections §3.5.1 – §3.5.2 for details.

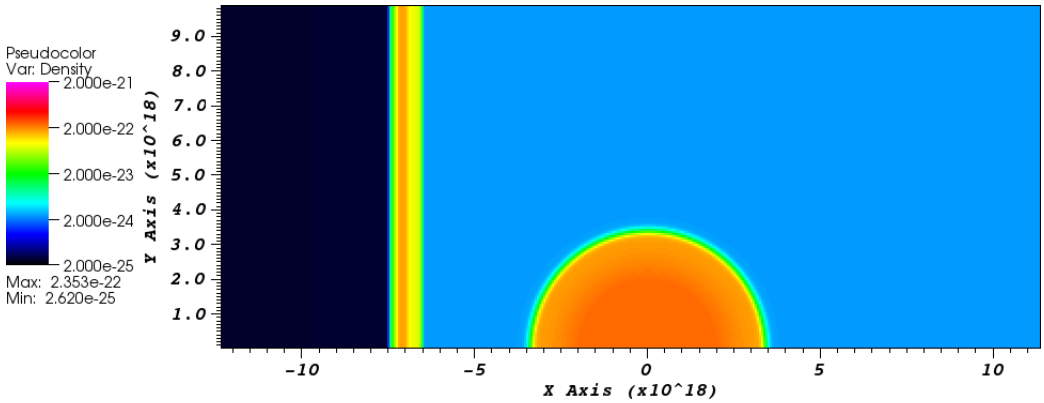

(a) t=0.0 s

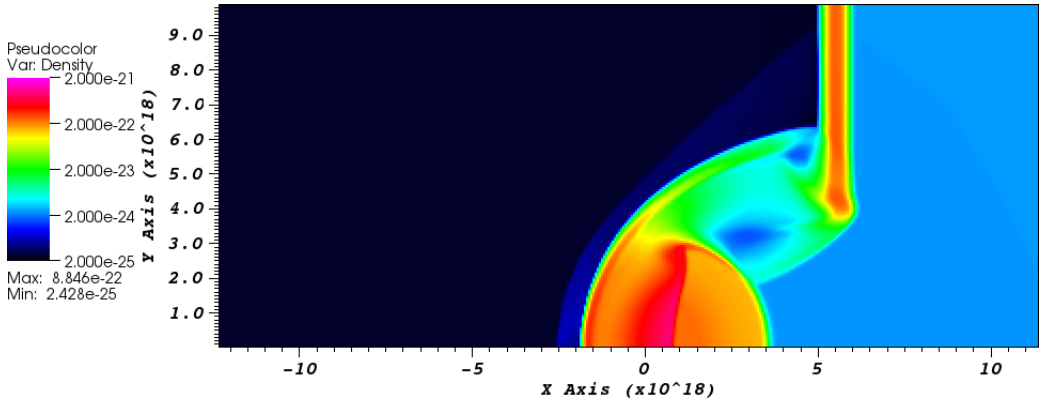

(b) t=2.9129 $\times 10^{12}$ s

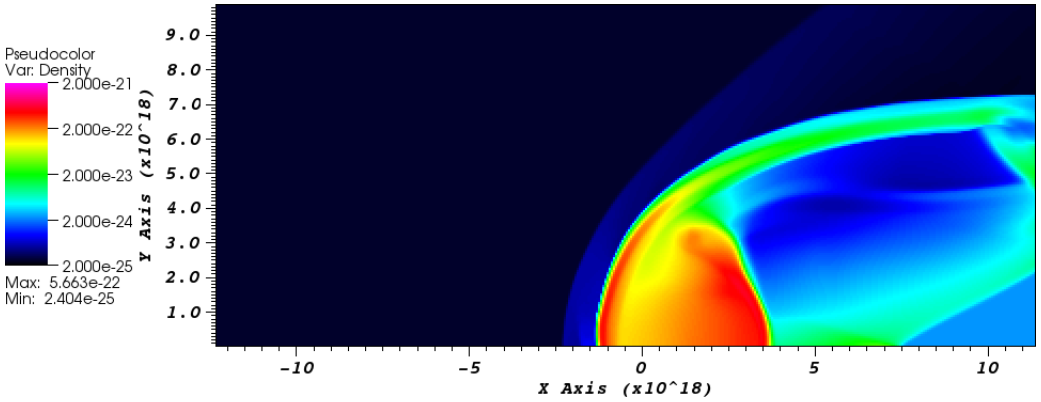

(c) t=4.83124 $\times 10^{12}$ s

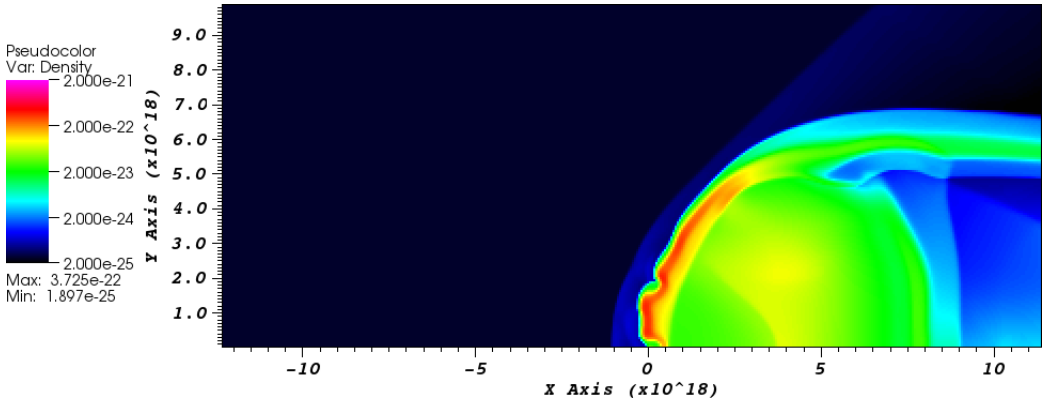

(d) t=8.13214 $\times$ 10^{12} s

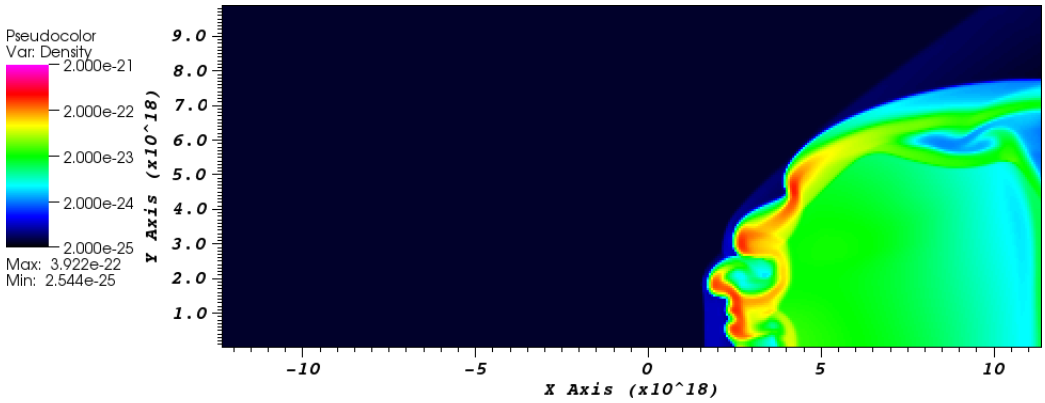

(e) t=1.15281 $\times$ 10^{13} s

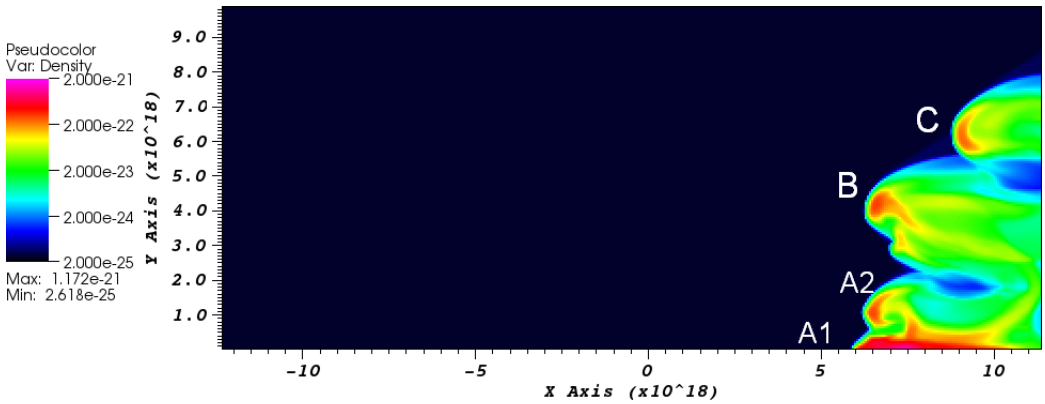

(f) t=1.58 $\times$ 10^{13} s

Figure 3.14: 2D toy model - density of the gas is displayed as the shell collides with the clump to form four smaller dense clumps. The legend displays mass density (g·cm^{-3}), which equates to max. $n = 981.6\,\mathrm{cm}^{-3}$ and min. $n = 0.0098\,\mathrm{cm}^{-3}$. [The x and y axis represent the distance from the centre of the clump at t= 0 s (in 10^{18} cm)]

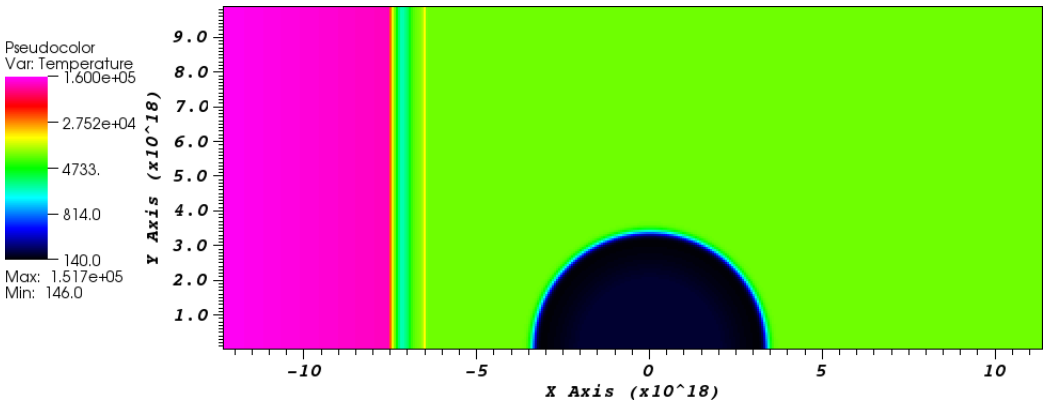

(a) $t = 0$ s

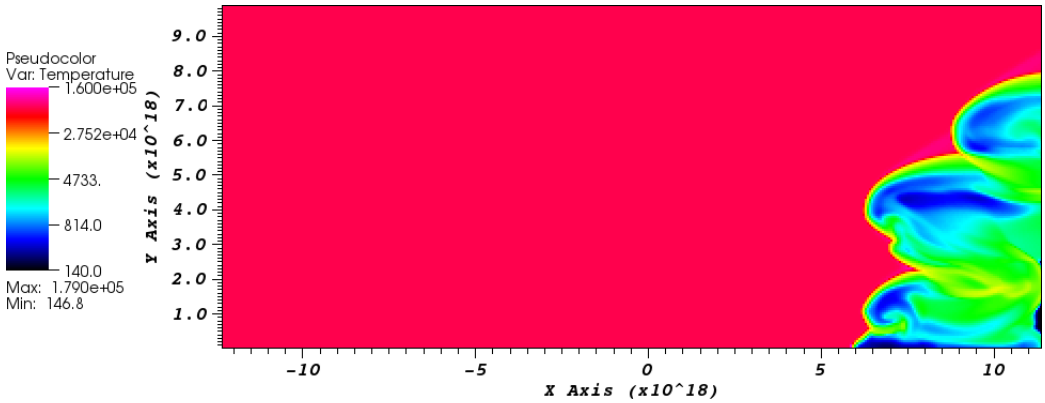

(b) $t = 1.58 \times 10^{13}$ s

Figure 3.15: Graphs displaying the temperature (K) of the 2D toy model at the start and end of the simulation. [The x and y axis represent the distance from the centre of the clump at t= 0 s (in 10^{18} cm)]

3.5.1 Cosmic rays

Previous early SN studies (Machida *et al.* 2005; Nagakura *et al.* 2009; Vasiliev *et al.* 2008) have neglected to include the effects of cosmic rays (CRs) on chemistry, even though SN are known to be production sites for CRs. It has been observed that molecular clouds interacting with SNRs have CR ionisation rates one hundred times higher than the background rate for the galaxy (Ceccarelli *et al.* 2011). Hence the chemical evolution of a gas cloud that interacts with SNR are strongly driven by cosmic rays. SNR can transfer $\sim 10\%$ of the SN energy into CRs (Dorfi 1991, 2000). However there are many unknowns factors about the explosion mechanism that contribute to the production of CRs from a metal-free SN event. For an in depth summary on the subject please see Stacy & Bromm (2007) or Jasche *et al.* (2007). Due to the huge uncertainty in the cosmic ray rate within the first galaxies we will investigate the effect of different CR ionisation rates on the thermal

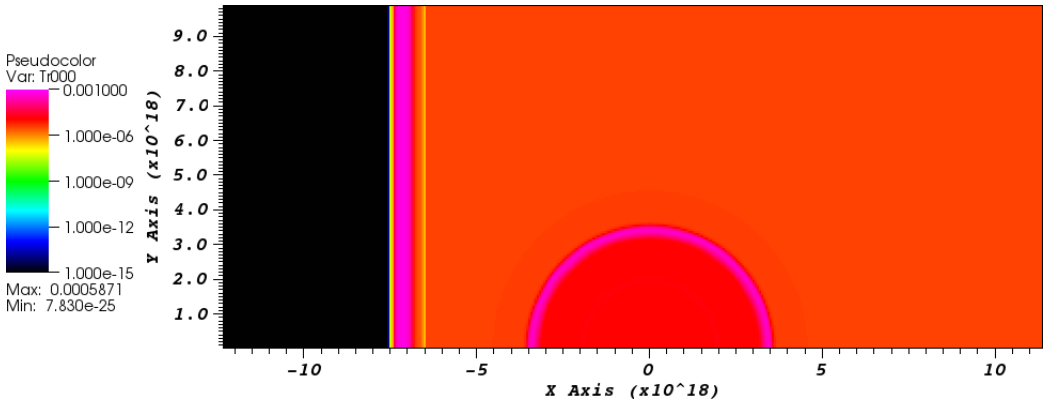

(a) $t = 0$ s

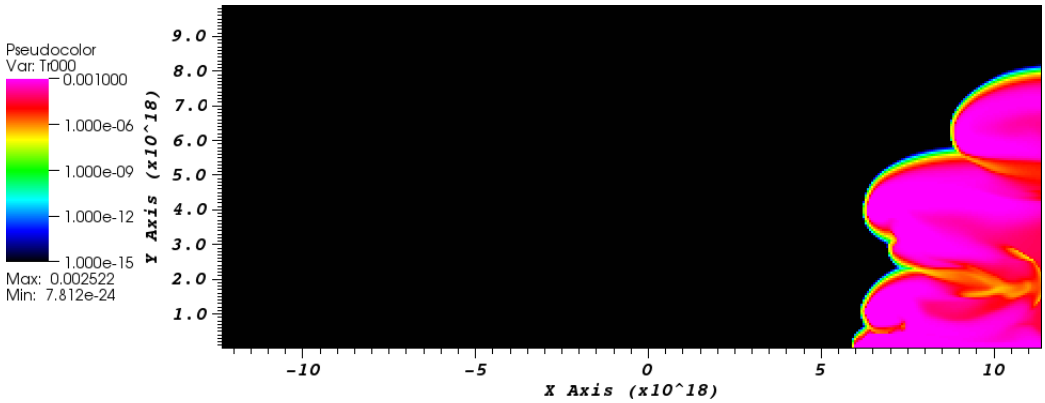

(b) $t = 1.58 \times 10^{13}$ s

Figure 3.16: 2D toy model - graphs displaying the fractional abundance H_2 at the start and end of the simulation. [The x and y axis represent the distance from the centre of the clump at t= 0 s (in 10^{18} cm)]

	Reaction	ionisation rate ratio ($k_i : k_H$)	Reference for rate
R37	H + CR $\rightarrow$ H^+ + e^-	1	UM06
R38	He + CR $\rightarrow$ He^+ + e^-	1.087	UM06
R39	H_2 + CR $\rightarrow$ H^+ + H + e^-	0.03	UM06
R40	H_2 + CR $\rightarrow$ H + H	0.217	UM06
R41	H_2 + CR $\rightarrow$ H^+ + H^-	6.52e-4	UM06
R42	H_2 + CR $\rightarrow$ H_2^+ + e^-	2.006	UM06

Table 3.3: Cosmic ray ionisation reactions, where UM06 = UMIST database for astrochemistry 2006 (Woodall *et al.* 2007*a*)

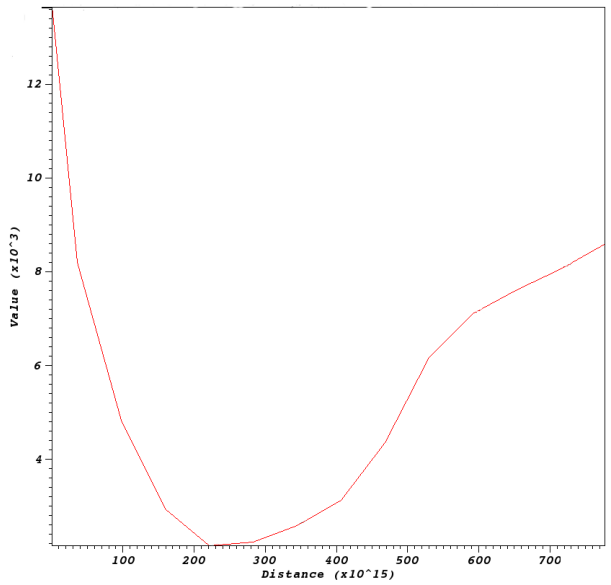

(a) Temperature

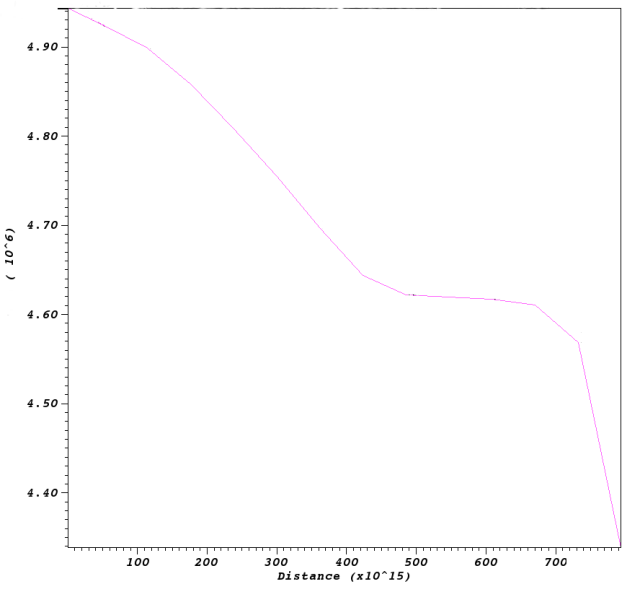

(b) Velocity

Figure 3.17: The graphs display the temperature and velocity through a 1D axial slice of the SN shell (at t=0 s for the 2D model). The x-axis represents the radius of the shock in cm. The y-axis displays (a) temperature in 10^3 K and (b) the velocity in 10^6 cm s^{-1}.

fragmentation of the cloud.

Cosmic rays directly ionise some species and indirectly photoionise or photodissociate others. The direct ionisation by cosmic rays is simple to treat and the reactions (k_i) are listed in table 3.3. All the rates for these reactions were obtained from the UMIST 06 database, and are attenuated to $\zeta_0 = 1.37 \times 10^{-17}$ s^{-1}, which is the local ISM CR ionisation rate of hydrogen at $z = 0$. By using the UMIST rates, we are assuming that the CR spectrum is the same at high redshift. Without observations or a well understood explosion mechanism for metal-free stars this is a reasonable approximation. This ionisation rates within a molecular cloud is derived from H_3^+/H_2 ratio, as H_3^+ is produced by the products of CR reactions with H and H_2. We are investigating the CR ionisation rate as a free parameter ζ, therefore the reaction rates for reactions R37 - R42 are calculated in the following way

$$k_{CR} = \frac{\zeta}{\zeta_0} \times \frac{k_i}{k_{\rm H}}. \tag{3.14}$$

The indirect effects of cosmic rays in metal-free gas are not simple to treat. Prasad & Tarafdar (1983) were the first to discuss these effects occurring in molecular clouds, they noted that the energetic secondary electrons produced by cosmic ray ionisations could excite the electronic states of H_2. The excited H_2 molecules radiatively decay and produce UV photons. This is known as the secondary UV flux induced by cosmic rays.

Within our Galaxy the secondary flux can be modelled as a purely local process. The accurate treatment of the propagation of photons produced by both H and H_2 is needed in a metal-free environment, which is beyond the scope of this work and therefore we have neglected this process. This is because the approximation that the secondary flux is a local process in a metal-free gas cannot be made. The first reason is that the continuum opacity of metal-free gas is very low without dust and therefore the mean free path of a photon from H_2 is much larger than that of a CR induced photon within a gas cloud observed today (Glover & Savin 2009). The second reason is at densities $n < 10^{10}$ cm^{-3} the maximum H_2 fraction is small in primordial gas ($\leq 10^{-3}$). Therefore CRs are more likely to ionise atomic hydrogen (Glover & Savin 2009; Greif *et al.* 2010). Dijkstra *et al.* (2006) have shown that CR-induced photons from atomic hydrogen are more likely to scatter many times and then escape the gas. Hence one cannot assume the photons are absorbed locally in the gas, which makes the reaction rates that are calculated for the Galactic environment irrelevant. We

do not include double ionisation of H_2 or He by cosmic rays i.e.

$$H_2 + CR \rightarrow H^+ + H^+ + e^- + e^- \tag{3.15}$$

$$He + CR \rightarrow He^{++} + e^- + e^-, \tag{3.16}$$

as the probability of this event occurring is expected to be low (Glassgold & Langer 1973).

CRs have two effects on the thermal evolution of the gas. The first is by imparting heat into the gas via direct ionisations (Goldsmith & Langer 1978). The second is more indirect, CR ionisations catalyse the formation of molecules such as H_2 and $H_3{}^+$. These molecules act as coolants via collisional line cooling. Previous works have neglected $H_3{}^+$ as a prominent primordial coolant especially at low densities. Glover & Savin (2009) proved that CR induced $H_3{}^+$ only contributed to the overall cooling of gas within a mini halo for densities greater than 10^8 cm^{-3}.

The question is whether the abundance of $H_3{}^+$ become large enough to contribute significantly to the cooling process close to the SNR at high redshift. To investigate this, we set the upper limit of ζ to be 10^{-15} s^{-1}, as this is the observed value within clouds interacting with intermediate aged SNRs (Indriolo *et al.* 2010; Ceccarelli *et al.* 2011). These clouds are 7–11 pc from the original SN site and would experience much higher CR rates than a cloud at 40 pc. The enhanced cosmic ray rate from a SN explosion is experienced for a few Myears (Fatuzzo *et al.* 2006), which is longer than our simulation time. Therefore we can assume a constant CR ionisation rate.

We have chosen to test what the individual effects of all three processes caused by CRs (i.e. CR ionisations, CR heating and $H_3{}^+$ cooling) will be on the 1D toy model, which translate as the initial conditions for the 2D model. The model has the same initial conditions described in section § 3.5, except that the basic chemistry network outlined in §3.3.1 is extended to include the reactions due to direct ionisations caused by CRs (Table 3.3). We chose to use the high CR ionisation rate of 10^{-15} s^{-1} as this would provide more contrast to the basic model.

Figures 3.18(a) and 3.19(a), display the model which only takes into account the CR ionisations. Figures 3.18(b) and 3.19(b) display the model which includes both the CR ionisations and the cooling contributed from the $H_3{}^+$ molecule. The cooling rate for $H_3{}^+$ was obtained from Glover & Savin (2009) and is in the form Equation (3.12) and is added to the thermal model described in §3.3.2. Finally the initial conditions for the model with all three processes is displayed in Figures 3.18(c) and 3.19(c). The CR heating model introduced by Goldsmith & Langer (1978), was adapted

Model	CR rate (s^{-1})	Min shock temperature (K)	Max shock density (cm^{-3})	shock velocity ($km \cdot s^{-1}$)	Min cloud temperature (K)	Max Cloud density (cm^{-3})
Basic	0	2150	78.53	46.2	146.0	115.48
crp18	10^{-18}	2180	80.00	46.4	146.4	115.48
crp17	10^{-17}	2100	84.42	46.0	149.1	115.48
crp16	10^{-16}	2200	80.98	46.3	176.9	115.34
crp15	10^{-15}	2300	80.98	45.5	444.8	114.95

Table 3.4: Initial conditions of all 2D metal-free models

in a similar way to Glover & Jappsen (2007):

$$\Gamma_{\rm CR} = 3.2 \times 10^{-11} \Sigma_i \zeta_i n_i \, {\rm erg \, cm^{-3} \, s^{-1}} \tag{3.17}$$

which is the sum of CR ionisation rates of chemical species, where $i = H_2$ and H. This works on the assumption that each ionisation releases 20 eV of energy as heat into the gas cloud (Stacy & Bromm 2007; Goldsmith & Langer 1978).

When only direct CR ionizations are included the minimum temperature of the cloud is 145.7, compared to 146 K in the basic model without cosmic rays (§3.5). This slight decrease from the basic model is caused by the formation of H_2 from the extra ions formed via the CR collisions. The density of the cloud does not change. Due to the decrease in the amount of molecular hydrogen in the shell, the minimum temperature increases to 2180 K compared to 2150 K in the basic model. The maximum density within the shock increases to 82.45 $\rm cm^{-3}$. When the cooling from $H_3{}^+$ molecules is added to the model, there is no change to the initial conditions. The abundance of $H_3{}^+$ never becomes large enough to make a contribution to the thermal state of the gas.

The greatest contribution of all the CR processes is from the heating. From Figure 3.19(c) one can see that the heating outweighs any cooling from extra H_2 molecules in the cloud and the minimum temperature raises to 444.8 K. The minimum temperature within the SN shell is also raised to 2300 K. The heating from CR ionisations also slightly affects the density of the cloud, as there is a increase in the diffusion at the cloud edge. Hence the cloud extends further than the basic model, as the velocity of the outflow has greatly increased to $\sim$2 km $\rm s^{-1}$.

We now investigate the combined effects for CRs on the final state of fragmentation of the clump using the following ionisation rates: $\zeta = 10^{-18}$, 10^{-17}, 10^{-16} and 10^{-15} $\rm s^{-1}$. The lowest CR rate is considered because Stacy & Bromm (2007) found it was the minimum CR ionisation

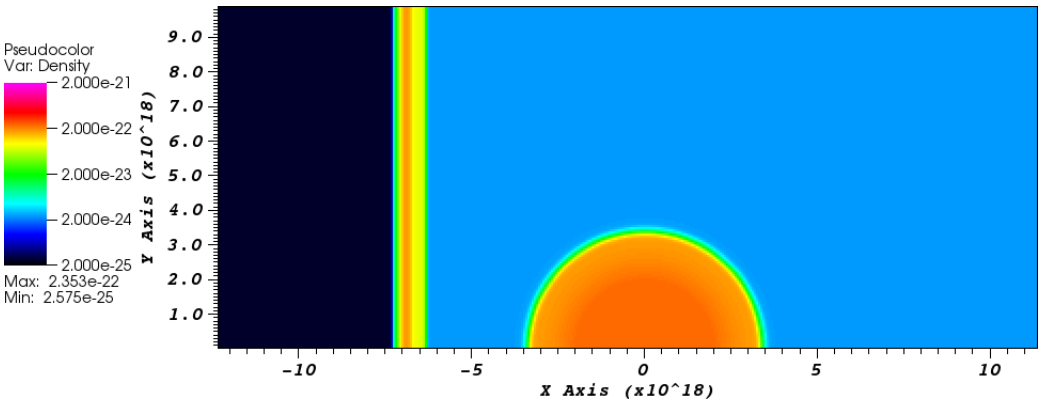

(a) Direct CR ionisations only

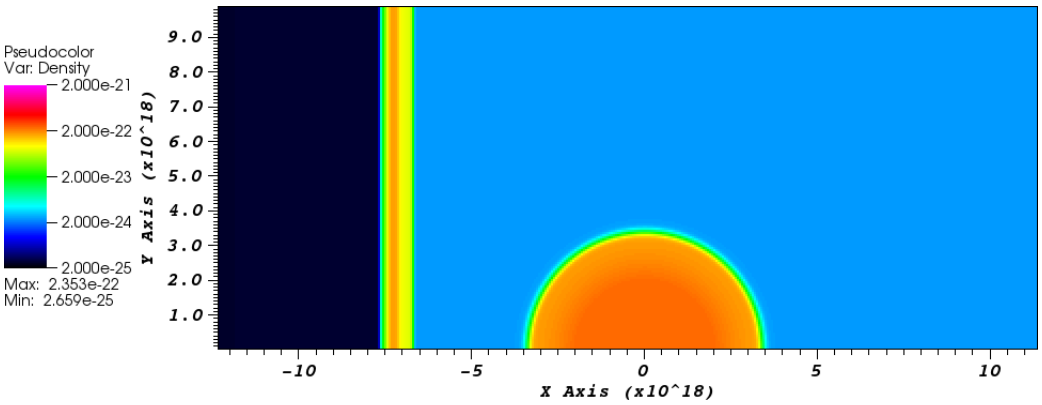

(b) Direct CR ionisations and $H_3{}^+$ cooling

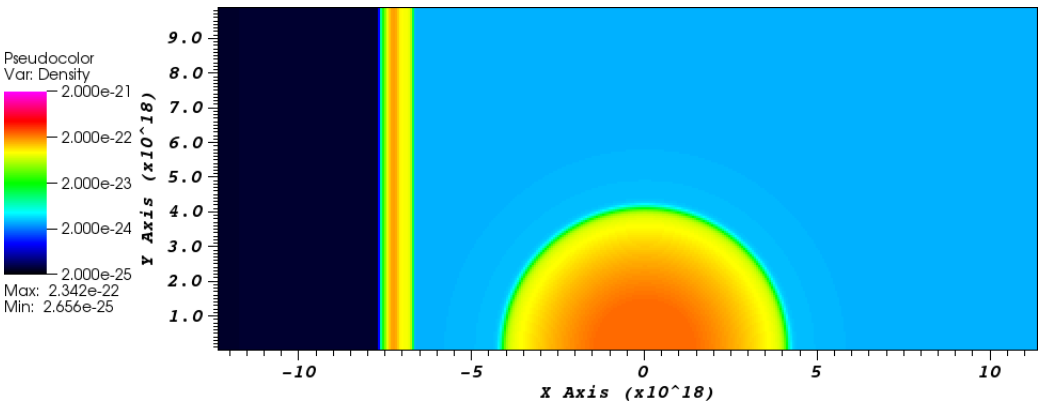

(c) Direct CR ionisations, $H_3{}^+$ cooling and CR heating

Figure 3.18: Initial density profile for 2D model with CR ionisation rate=$10^{15}\,\mathrm{s}^{-1}$, each graph shows the effect of including different CR microphysical processes. [The x and y axis represent the distance from the centre of the clump at t= 0 s (in 10^{18} cm)]

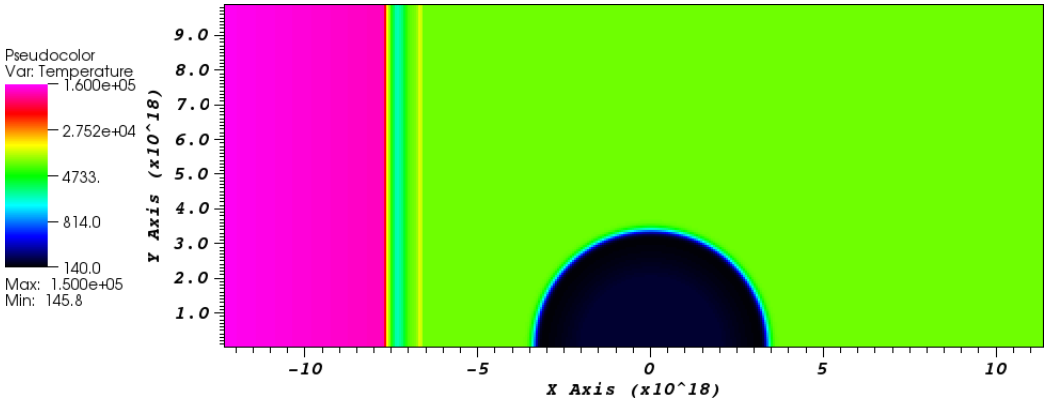

(a) Direct CR ionisations only

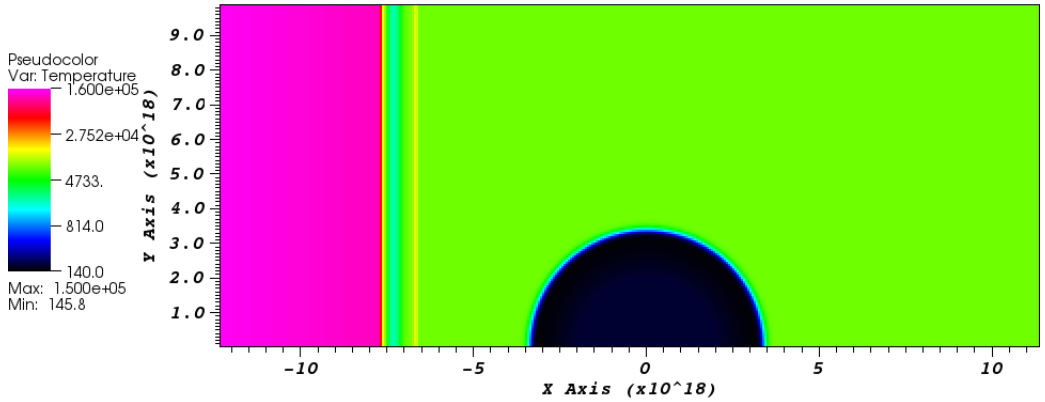

(b) Direct CR ionisations and $H_3{}^+$ cooling

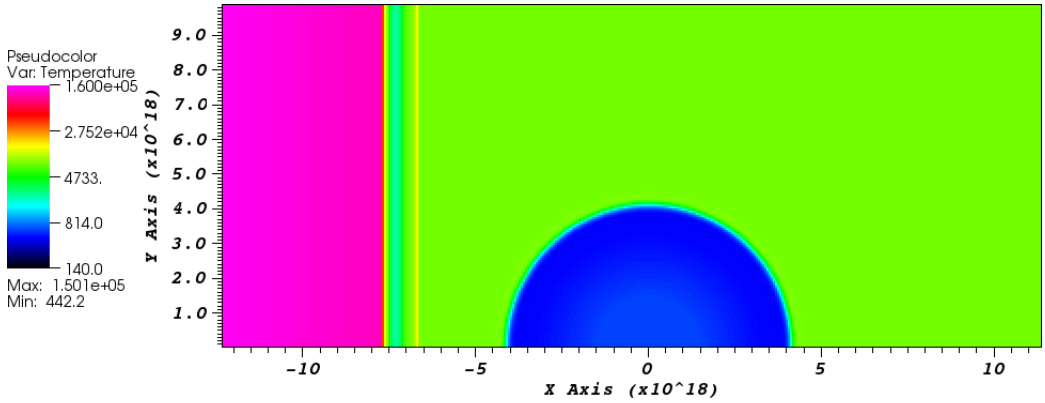

(c) Direct CR ionisations, $H_3{}^+$ cooling and CR heating

Figure 3.19: Initial temperature profile for 2D model with CR ionisation rate=$10^{15}\,\mathrm{s}^{-1}$, each graph shows the effect of including different CR microphysical processes. [The x and y axis represent the distance from the centre of the clump at t= 0 s (in 10^{18} cm)]

rate needed to have an affect on the thermal evolution of primordial gas. The 2D initial conditions for these models are listed in Table 3.4. The lowest CR rate we consider $\zeta = 10^{-18}\,\mathrm{s}^{-1}$, causes very little change to the initial conditions compared to the basic model, except that the minimum temperature of the shock is raised to 2180 K and the maximum density of the shock has increased to 80 cm^{-3}. Except for the case of of $\zeta = 10^{-17}\,\mathrm{s}^{-1}$ when the minimum shock temperature is lower than the basic model, there is a general trend that increasing the CR rate causes both the minimum shock and minimum cloud temperature to increase. Model crp15 has the highest CR rate ($\zeta = 10^{-15}\,\mathrm{s}^{-1}$) and increase in temperature, causes a decrease in the density of the cloud. The velocity of the shell in Table 3.4 refers to the value of the constant velocity within the front half of the shell. This does not vary much between the different CR cases, except for model crp15 where the velocity is no longer constant in this region. The velocity stated for case crp15 is the average value of the front half of the shell, as the velocity in this region decreases from 46.2 to 45.3 km s^{-1}.

Figure 3.20 shows the final state for the model with CR ionisation rate of $\zeta = 10^{-18}\,\mathrm{s}^{-1}$: Four clumps are formed in the same position as the basic model and so are referred to by the same labels in section §3.5. The central clump A1 has become slightly more dense with a maximum density of 690 cm^{-3}. The smaller connecting clump A2 has become even smaller. The other two clumps B and C are very similar to the basic model, with slightly less density due to the loss of H_2 molecules via CR ionisations.

The end state of model crp17, which has a CR ionisation rate of $\zeta = 10^{-17}\,\mathrm{s}^{-1}$, is displayed in Figure 3.21. Four clumps are formed in same position as the basic model, therefore they have the same labels. There is now a visible difference in structure between the clumps seen here and the basic model. Clumps A1 and B are now connected via a gas filament, causing the dense left hand side of clump A1 to retain its matter and grow in size and density, whereas the tail of the clump has lost mass, which has been swept by the shock. Clump B has become smaller, loosing mass to form the filament which connects to clump A1. Clump A2 is also much smaller than previous models, its radius is half the size. Due to the CR heating clump C is also no longer as compact, becoming stretched and less dense.

When the CR rate is increased to $\zeta = 10^{-16}\,\mathrm{s}^{-1}$, an overall increase in density can be seen within the gas fragments i.e. the four clumps and the filament (Figure 3.22). All of the Clump A1 is formed in front of the connection to the filament. The smaller clump A2 has merged into the main clump, becoming larger and more dense in the process. Both clumps B and C have increased

in radius and density, creating clumps with larger mass than previous models. The dense filament creates a shielding from the shock, allowing a much colder region to be created with a minimum temperature of 114 K.

As with the initial conditions, the three individual contributions of CRs have been investigated for model crp15 and are displayed within Figures 3.23 and 3.24. When only considering the mechanism of CR ionisations, the high CR rate of $\zeta = 10^{-15}\,\mathrm{s}^{-1}$ has a strong affect on the structure of the clumps compared to the basic model (Figures 3.23(a) & 3.24(a)). The increase in H_2 causes clumps A1, A2 and B to become much larger and connected. However the ionisations cause Clump C to loose H_2 resulting in an increase in temperature and therefore an increase in mass loss. Figures 3.23(b) & 3.24(b) display the affect of including $H_3{}^+$ cooling, which we find does has an affect in a high CR environment ($10^{-15}\,\mathrm{s}^{-1}$), as it causes the merging of the clumps A1 and A2. Both models have a layer of dense gas formed at the x-axis, but this is due to the fact this boundary is reflective.

When all components are combined, the high CR rate of $\zeta = 10^{-15}\,\mathrm{s}^{-1}$ and hence the higher heating rate means the general structure of the clumps found in the previous models (with lower CR rates) is no longer found. The new structure of the gas is shown in Figure 3.23(c); there is now a main clump central to the X-axis labelled as A and a smaller B. The heating from the CR ionisation causes less thermal instability within the gas and hence less fragmentation. The mass of these clumps are listed in Table 3.5. The central clump is large but diffuse, so with a large heating rate the clump may not contract into a star forming structure.

Clump (Model)	Average density ($g \cdot cm^{-3}$)	Minimum Temperature (K)	Diameter 2a (cm)	Diameter 2b (cm)	Estimated Mass ($M_\odot$)
A1 (Basic)	6.70×10^{-22}	214	4.20×10^{18}	0.30×10^{18}	0.279
A2 (Basic)	2.45×10^{-22}	570	0.63×10^{18}	0.37×10^{18}	5.82×10^{-3}
B (Basic)	2.25×10^{-22}	543	0.80×10^{18}	0.56×10^{18}	1.56×10^{-2}
C (Basic)	1.60×10^{-22}	460	0.84×10^{18}	0.34×10^{18}	4.28×10^{-3}
A1 (crp18)	6.00×10^{-22}	203	4.2×10^{18}	0.35×10^{18}	0.340
A2 (crp18)	2.60×10^{-22}	563	0.63×10^{18}	0.27×10^{18}	3.41×10^{-3}
B (crp18)	2.20×10^{-22}	527	0.90×10^{18}	0.46×10^{18}	1.15×10^{-2}
C (crp18)	2.00×10^{-22}	464	0.95×10^{18}	0.315×10^{18}	5.20×10^{-3}
A1 (crp17)	6.50×10^{-22}	218	3.2×10^{18}	0.5×10^{18}	0.265
A2 (crp17)	1.95×10^{-22}	576	0.51×10^{18}	0.22×10^{18}	1.15×10^{-3}
B (crp17)	2.00×10^{-22}	669	0.88×10^{18}	0.4×10^{18}	4.97×10^{-3}
C (crp17)	2.10×10^{-22}	530	1.1×10^{18}	0.4×10^{18}	6.12×10^{-3}
A1 (crp16)	4.35×10^{-22}	355	3.1×10^{18}	0.355×10^{18}	0.187
A2 (crp16)	2.40×10^{-22}	623	0.7×10^{18}	0.40×10^{18}	7.41×10^{-3}
B (crp16)	2.40×10^{-22}	570	1.1×10^{18}	0.37×10^{18}	9.96×10^{-3}
C (crp16)	2.30×10^{-22}	510	1.2×10^{18}	0.35×10^{18}	9.32×10^{-3}
A1 (crp15)	3.00×10^{-22}	530	2.3×10^{18}	1.2×10^{18}	0.274
A2 (crp15)	5.50×10^{-22}	600	0.55×10^{18}	0.52×10^{18}	0.18
B (crp15)	1.60×10^{-22}	700	1.4×10^{18}	0.42×10^{18}	1.09×10^{-2}

Table 3.5: Parameters of clumps formed by SN shock for all 2D models

3.5.2 Neglected Processes

The following processes were found to have negligible effect: cooling from deuterated hydrogen (HD), CMB ionisation and heating from H_2 formation. The details are given below.

3.5.2.1 Deuterium chemistry

The chemical network consists of 13 species, the following chemical species were added to the previous model: D, D^+, HD, HD^+ and H_2D^+. The reactions that include the deuterated species are listed in Table 3.6. The details of how the rates were adapted for the temperature range (10^{12} – 10 K) are in the Appendix. The value for the fractional abundance of primordial deuterium used was 2.78×10^{-5} (Spergel *et al.* 2007). We include molecular cooling by HD (Lipovka *et al.* 2005) and HD^+(Glover & Abel 2008). Cosmic rays were neglected in this model, so that a direct comparison with the basic model could be made.

We found that including deuterium chemistry and its associated cooling did not affect the density or temperature of the clumps formed in our model. This supports previous studies which

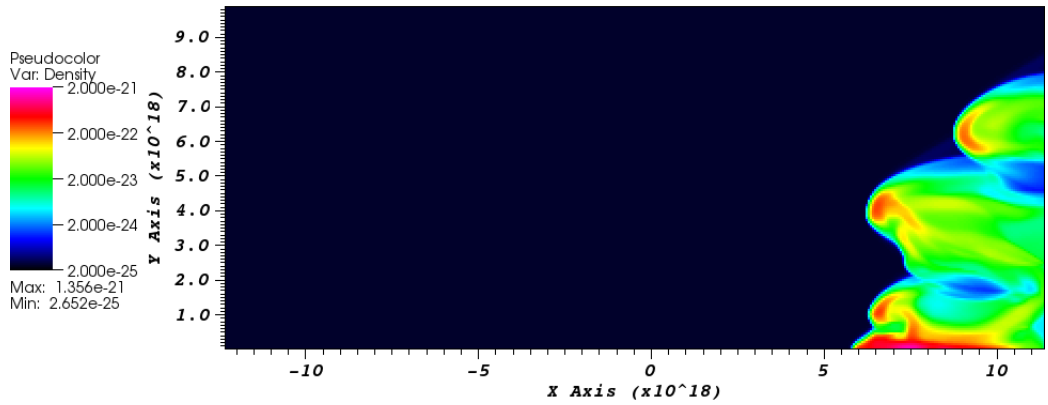

(a) density

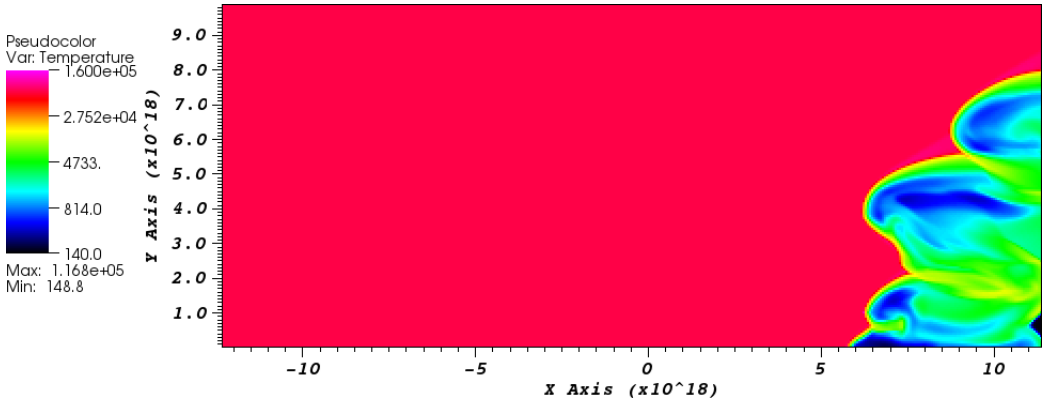

(b) temperature

Figure 3.20: 2D toy model with CR ionisation rate $= 10^{-18}\,\mathrm{s}^{-1}$ at final time =1.58e13 s - (a) density of the gas is displayed as the main clump has fragmented into smaller dense clumps. The legend displays mass density ($\mathrm{g{\cdot}cm^{-3}}$), which equates to max. $n = 981.6\,\mathrm{cm}^{-3}$ and min. $n = 0.0098\,\mathrm{cm}^{-3}$ (b) displays the temperature of the clumps which have formed. [The x and y axis represent the distance from the centre of the clump at t= 0 s (in 10^{18} cm)]

state that HD cooling only becomes effective at high densities i.e., $n > 10^5$ cm^{-3} (Glover & Abel 2008; Nagakura & Omukai 2005; Nakamura & Umemura 2002).

3.5.2.2 CMB ionisation

This is the process where Cosmic microwave background (CMB) photons react with neutral species in the following manner:

$$\mathrm{X} + \gamma_{\mathrm{cmb}} \rightarrow \mathrm{X}^{+} + \mathrm{e}^{-}$$

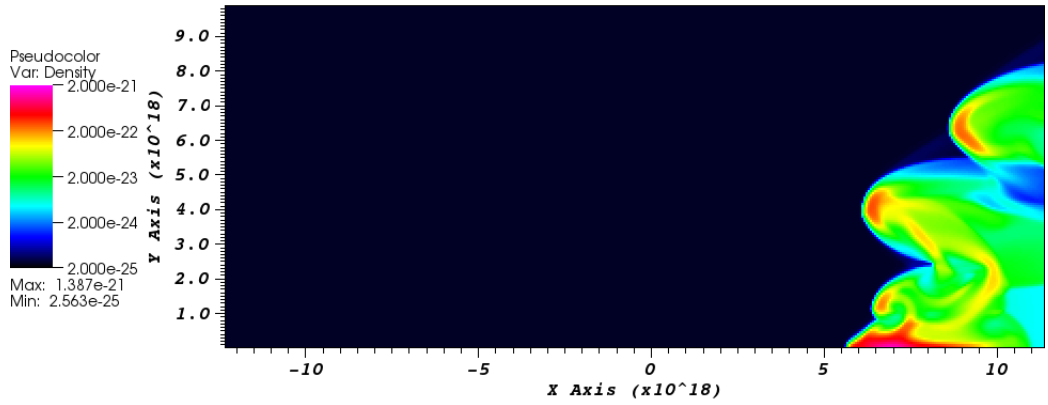

(a) density

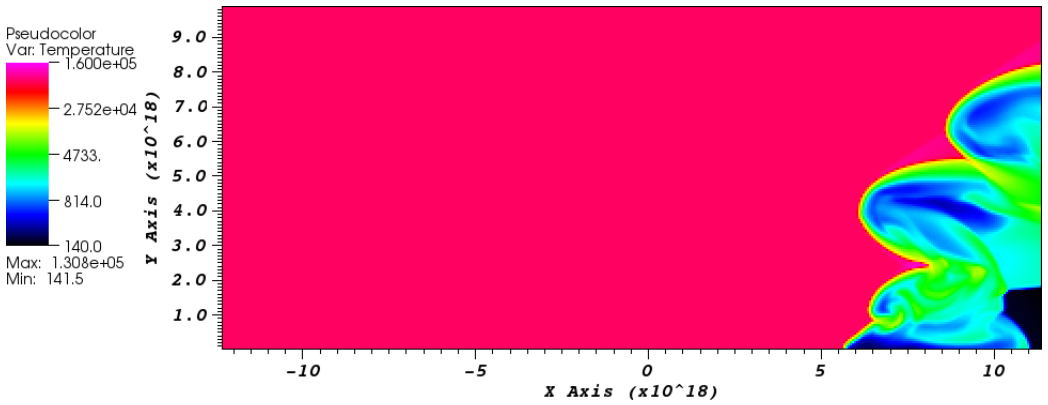

(b) temperature

Figure 3.21: 2D toy model with CR ionisation rate $= 10^{-17}\,\mathrm{s}^{-1}$ at final time =1.58e13 s - (a) density of the gas is displayed as the main clump has fragmented into smaller dense clumps. The legend displays mass density ($\mathrm{g{\cdot}cm^{-3}}$), which equates to max. $n = 981.6\,\mathrm{cm}^{-3}$ and min. $n = 0.0098\,\mathrm{cm}^{-3}$ (b) displays the temperature of the clumps which have formed. [The x and y axis represent the distance from the centre of the clump at t= 0 s (in 10^{18} cm)]

The reaction rates were taken from Galli & Palla (1998) and the rates are presented in Table 3.7. This ionisation rate did not make a difference on the H_2 fraction or subsequent cooling, as the ionisation rate is not large at redshift $z = 10$.

3.5.2.3 H_2 formation heating

The heating rate was obtained from Glover & Jappsen (2007). This process is density dependent and the density within our simulation does not become high enough for this process to become significant.

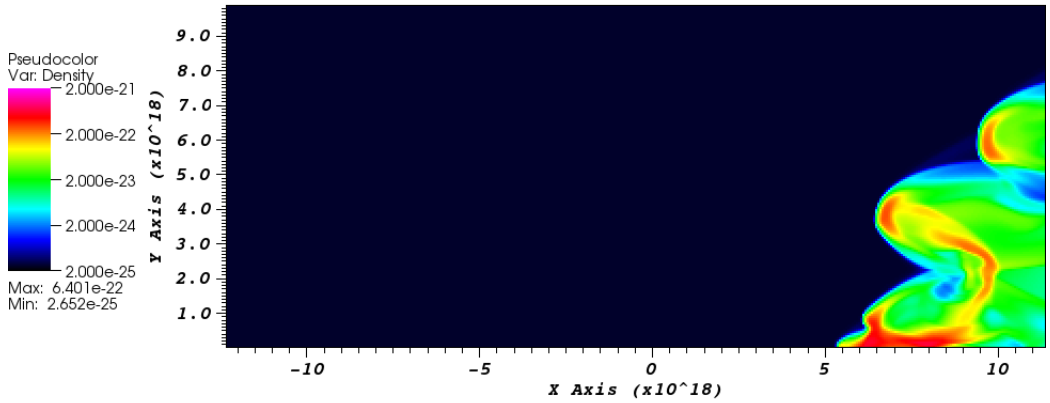

(a) density

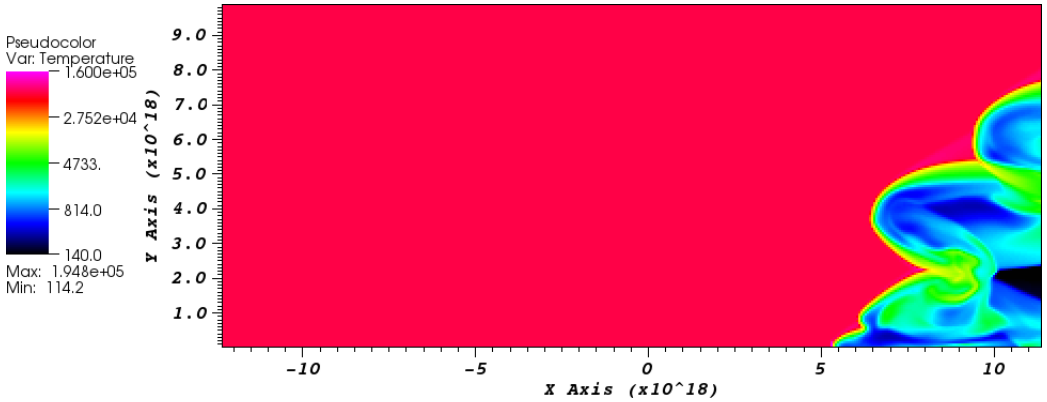

(b) temperature

Figure 3.22: 2D toy model with CR ionisation rate $= 10^{-16}\,\mathrm{s}^{-1}$ at final time =1.58e13 s - (a) density of the gas is displayed as the main clump has fragmented into smaller dense clumps. The legend displays mass density ($\mathrm{g{\cdot}cm^{-3}}$), which equates to max. $n = 981.6\,\mathrm{cm}^{-3}$ and min. $n = 0.0098\,\mathrm{cm}^{-3}$ (b) displays the temperature of the clumps which have formed. [The x and y axis represent the distance from the centre of the clump at t= 0 s (in 10^{18} cm)]

	Reaction	Reference for rate
R43	$D + e^- \rightarrow D^+ + e^- + e^-$	VF*
R44	$D^+ + e^- \rightarrow D + \gamma$	H*
R45	$D + H^+ \rightarrow D^+ + H$	S02
R46	$D^+ + H \rightarrow D + H^+$	S02
R47	$HD^+ + e^- \rightarrow H + D$	GA08
R48	$H_2D^+ + e^- \rightarrow H + H + D$	GA08
R49	$HD + e^- \rightarrow H + H + e^-$	UM06*
R50	$HD^+ + e^- \rightarrow H^+ + H + e^-$	hd*

	Reaction	Reference for rate
R51	H + HD $\rightarrow$ H + H + D	UM06*
R52	H_2 + HD $\rightarrow$ H_2 + H + D	UM06*
R53	D + H^+ $\rightarrow$ HD^+ + photon	GA08
R54	D^+ + H $\rightarrow$ HD^+ + photon	GA08
R55	D + H $\rightarrow$ HD + photon	GA08
R56	D + H_2 $\rightarrow$ H +HD	GA08
R57	HD^+ + H $\rightarrow$ H^+ + HD	GA08
R58	D^+ + H_2 $\rightarrow$ H^+ + HD	GA08
R59	HD + H $\rightarrow$ H_2 + D	GA08
R60	HD + H^+ $\rightarrow$ H_2 + D^+	GA08
R61	H_2D^+ + e^- $\rightarrow$ H_2 + D	GP98
R62	H_2D^+ + e^- $\rightarrow$ HD + H	GP98
R63	H_2D^+ + H_2 $\rightarrow$ H_3^+ + HD	GP98
R64	H_2D^+ + H $\rightarrow$ H_3^+ + D	GP98
R65	HD^+ + H_2 $\rightarrow$ H_2D^+ + H	GP98
R66	HD^+ + H_2 $\rightarrow$ H_3^+ + D	GP98
R67	D + H_3^+ $\rightarrow$ H_2D^+ + H	GP98
R68	HD + H_2^+ $\rightarrow$ H_2 + H_2D^+	GP98

Table 3.6: Deuterium reactions:

S02= Savin (2002); GP98 = Galli & Palla (1998); GA08 = Glover & Abel (2008); UM06 = UMIST database for astrochemistry 2006 (Woodall *et al.* 2007*a*); H = Hummer (1994); VF = Verner & Ferland (1996); hd= same value as R14 rate; *= rates for deuterated species are taken from the equivalent rates for hydrogen species.

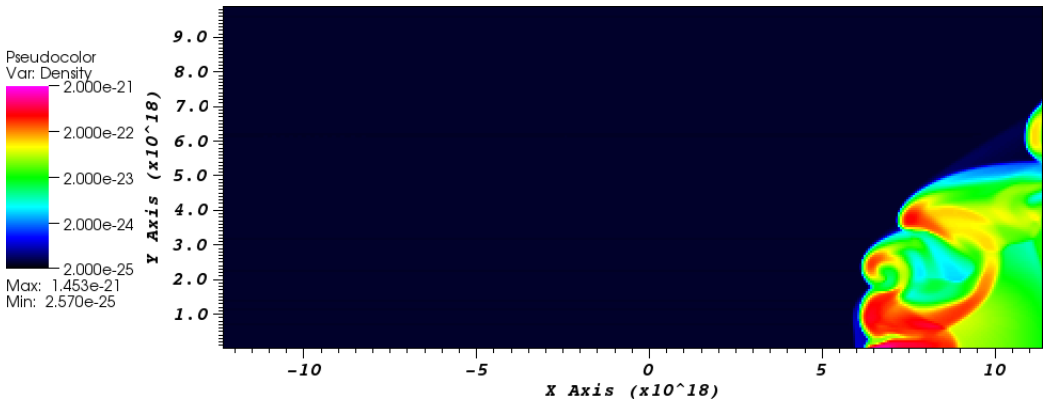

(a) CR ionisations only

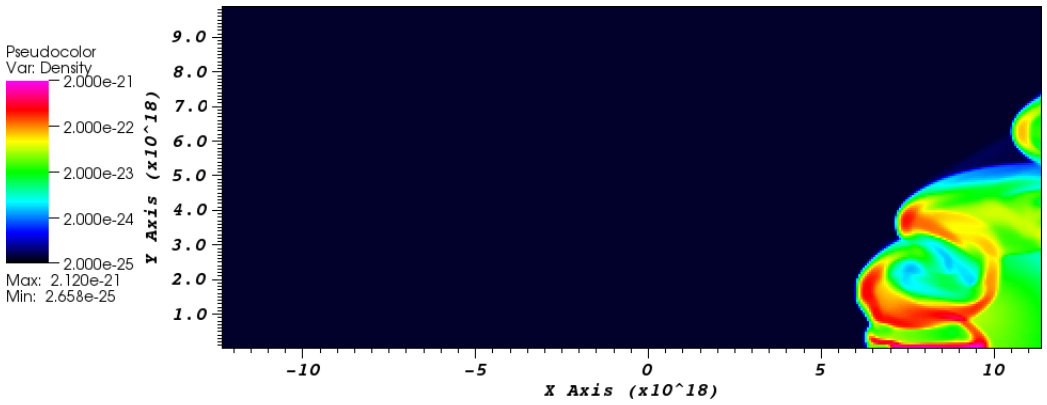

(b) CR ionisations & $H_3{}^+$ cooling

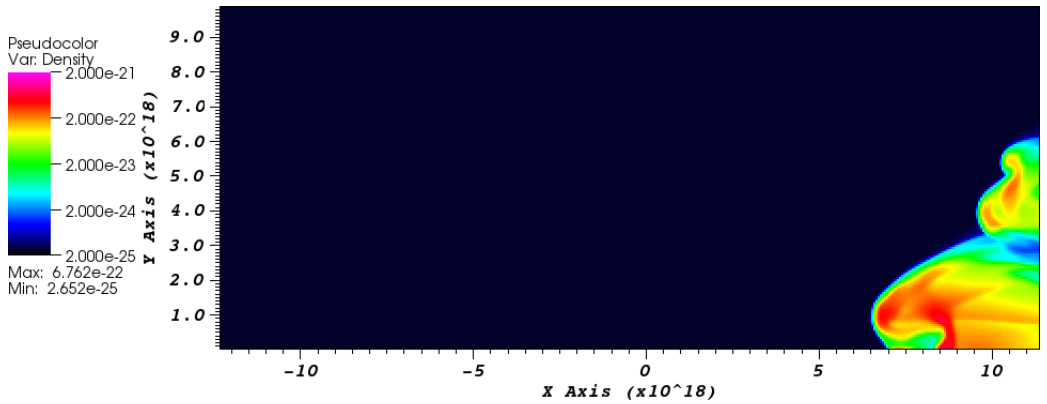

(c) CR ionisations and heating with $H_3{}^+$ cooling

Figure 3.23: Density of clumps formed by 2D toy model with CR ionisation rate $= 10^{-15}\,\mathrm{s}^{-1}$ at final time =1.58e13 s - graphs display the effect of the different microphyical process related to CRs. The legend displays mass density ($\mathrm{g{\cdot}cm}^{-3}$), which equates to max. $n = 981.6\,\mathrm{cm}^{-3}$ and min. $n = 0.0098\,\mathrm{cm}^{-3}$ [The x and y axis in 10^{18} cm]

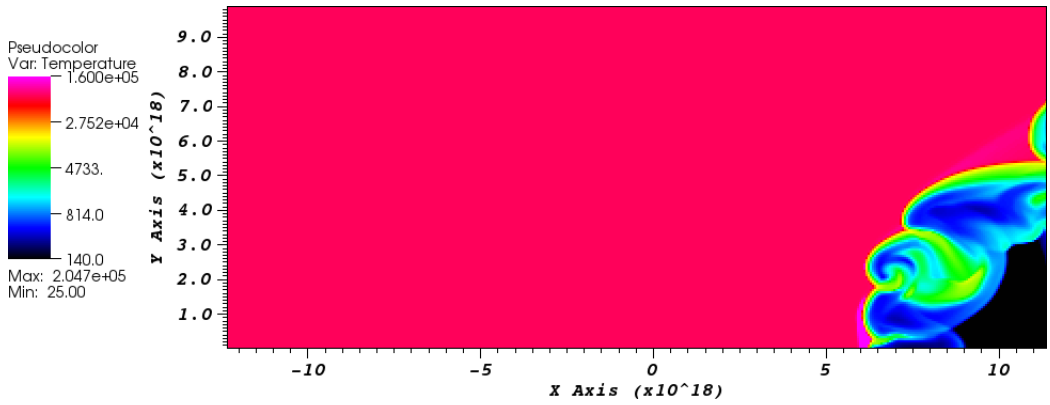

(a) CR ionisations only

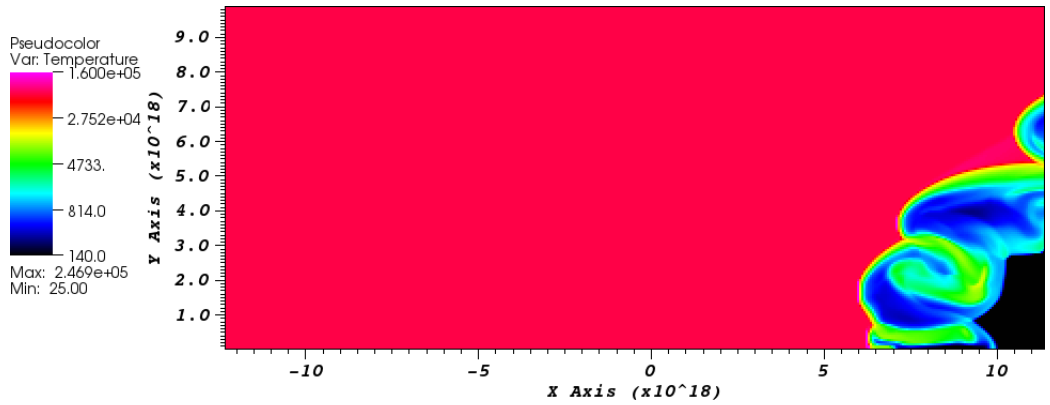

(b) CR ionisations & H_3^+ cooling

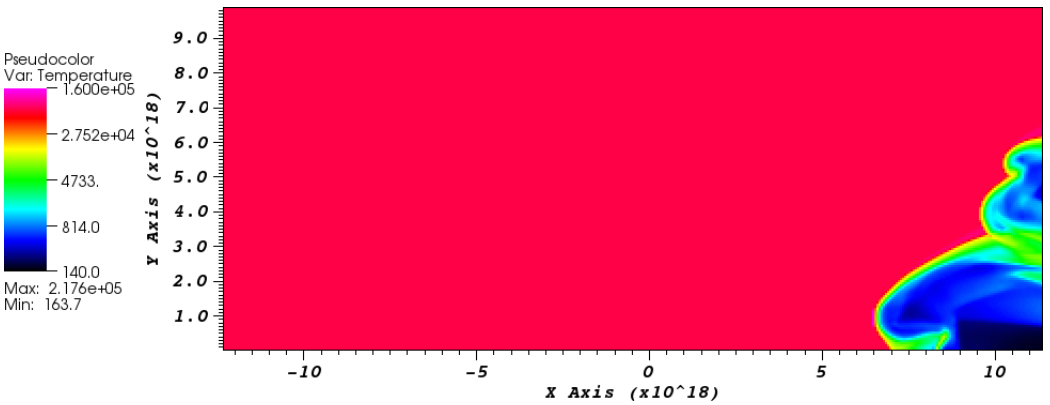

(c) CR ionisations and heating with H_3^+ cooling

Figure 3.24: Temperature of clumps formed by 2D toy model with CR ionisation rate $= 10^{-15}\,\mathrm{s}^{-1}$ at final time =1.58e13 s - graphs display the effect of the different microphyical process related to CRs. [The x and y axis in 10^{18} cm]

	Reaction	Reference for rate
R69	$H + \gamma_{cmb} \rightarrow H^+ + e^-$	GP98
R70	$H^- + \gamma_{cmb} \rightarrow H + e^-$	GP98
R71	$H_2{}^+ + \gamma_{cmb} \rightarrow H + H^+$	GP98
R72	$H_2{}^+ + \gamma_{cmb} \rightarrow H^+ + H^+ + e^-$	GP98
R73	$H_2 + \gamma_{cmb} \rightarrow H_2{}^+ + e^-$	GP98
R74	$He^+ + \gamma_{cmb} \rightarrow He^{++} + e^-$	GP98
R75	$He + \gamma_{cmb} \rightarrow He^+ + e^-$	GP98
R76	$HeH^+ + \gamma_{cmb} \rightarrow He^+ + H$	GP98
R77	$HeH^+ + \gamma_{cmb} \rightarrow He + H^+$	GP98

Table 3.7: Ionisation reactions by CMB photons, GP98 = Galli & Palla (1998)

3.6 Discussion

3.6.1 Basic Toy Model

We modelled the shocking and fragmentation of a metal-free cloud of density 100 cm^{-3}, embedded 40 pc from the progenitor star within a 1 cm^{-3} ambient medium. The SN has an explosion energy of 10^{51} erg and the shell starts to form from the swept up ISM at 27 pc and collides with the cloud at velocity of $\sim$46 km s^{-1}. The first half of the cloud is compressed and forms a ridge. This causes another shock to form within the rest of the cloud, which causes this part of cloud to flow away with it. The ridge experiences instabilities which cause it to fragment and forms four clumps. The central largest clump formed has mass of 0.3 $M_\odot$, and could not be defined as a potential star forming site. The initial conditions did not include the HII region formed around a progenitor star and so we labelled this a toy model. With these simplistic initial conditions we find it is possible to form metal-free clumps via this method. We need to include more realistic initial conditions of the ISM to determine whether it is possible to form dense clumps which may undergo gravitational collapse to form pre-stellar cores. A thorough parameter investigation and 3D modelling is needed.

These results assume that the overall system is metal-free, which is not true when modelling SN. However, within hydrodynamic modelling there is an assumption that the shell made of swept up material remains metal free. This assumption is based on the fact that there is a contact discontinuity separating the ejecta and the swept up material. This only holds if the contact discontinuity is not disrupted by mechanisms such as cloud crushing, hydrodynamical instabilities, fragmenting ejecta (Tenorio-Tagle 1996). To obtain the precise metallicity of the shell, one must follow the mixing of the ejecta and take into account all these complex processes. This requires the implementation of

multidimensional ultra-high resolution simulations. There are models by Grief et al (2010) that follow the diffusion and mixing of metals from metal-free stars exploding as supernovae. They predict a metallicity of around $10^{-3}\,Z_{\odot}$ for a region 10-30 pc from the progenitor star. However the models do not have the resolution required to follow the mixing within the shell. In the absence of this information, authors have used free parameter called the mixing factor to predict the metallicity of the shell. Salvaterra *et al.* (2004) states that this factor is close to zero, hence mixing is inefficient and it is possible to form low-mass metal free stars. If this is true, then modelling the shock and cloud as metal-free is a good approximation.

We have modelled a SN with an explosion energy of 10^{51} erg. This is the energy of an average core collapse SN at z=0. However the explosion mechanism for metal-free stars is uncertain, and so are their explosion energies. Previous studies (Salvaterra *et al.* 2004; Machida *et al.* 2005; Vasiliev *et al.* 2008), have modelled star formation induced by SN with explosion energies greater than 10^{52} erg. This corresponds to hypernovae or pair instability SN. Studies which model SN energies and yields and match them to the elemental abundances observed in EMP stars, point to a range of explosion energies: $0.6 \times 10^{51} - 2.0 \times 10^{51}$ erg (Joggerst *et al.* 2010; Tominaga 2009; Ekström *et al.* 2008). The effect of different explosion energies should be investigated, as this would change the dynamics of the shock as it approaches the clump.

It is not only the explosion energy of the SN that needs to be taken into account. The shape and structure of the ISM into which the SN explodes into also plays a major role (Vasiliev *et al.* 2008). The idealised case of a constant density ISM may not reflect the true nature of the environment. Just increasing the ambient density from 1 cm^{-3} to 2 cm^{-3} causes the shell to develop much quicker and a larger shell travels slower. There is also a difference in pressure of a SN shell sweeping into a hot ionised gas ($\sim 10^4$ K) and when it sweeps colder neutral gas. All these factors need to be taken into account, which entails modelling the HII region prior to the SN explosion. If the cloud is found within the HII region, it may be subjected to a harsh radiation field and therefore evaporate.

The strongest feedback on the chemistry comes from radiation within the (11.18-13.6) eV band, as this photodissociates the H_2 molecules and has a knock-on effect on the thermal state of the gas. Massive stars can create large photodissociation regions (PDR) (Haiman *et al.* 1997). It is important that the cloud is not within the PDR of the progenitor star, as we could no longer assume it is neutral. Following Vasiliev *et al.* (2008), after the SN explosion the dissociative photons produced by the hot gas are assumed to be negligible. Therefore, we can argue that photo-dissociation of H_2 is not an important mechanism after SN explosions.

3.6.2 Cosmic Rays

The results show that cosmic rays play an important role in the chemical and thermal evolution of gas near a supernova remnant. Even though it is uncertain what flux of cosmic rays will be produced in a metal-free stellar explosion, our results show they should be included as a free parameter in early universe SN models. We investigated four cosmic ray ionisation rates: $10^{-18}\,\mathrm{s}^{-1}$, $10^{-17}\,\mathrm{s}^{-1}$, $10^{-16}\,\mathrm{s}^{-1}$ and $10^{-15}\,\mathrm{s}^{-1}$. From investigating the different contributions from cosmic rays on the initial conditions it can be seen that the most important contribution is thermal heating (Figure 3.19). There is a range of clump sizes produced (see Table 3.5); generally an increase in cosmic ionisation rate translates to less thermal instability and therefore the formation of lower mass clumps, except for the model with CR ionisation rate of $10^{-18}\,\mathrm{s}^{-1}$ where the mass of the central clump is larger than the model without cosmic rays. This is because the heating rate from CRs is less than the increase in the cooling rate due to the increase in molecular hydrogen. This causes the central clump to be cooler and denser than the basic toy model.

The CR production from metal-free supernovae is very uncertain. A simple calculation by Stacy & Bromm (2007) show that a mini-halo will have a background CR ionisation rate of $10^{-19}\,\mathrm{s}^{-1}$ from a single PISN at $z = 20$. As the lower energy CRs, that cause the ionisation of H_2 decrease with distance from the SN source, we expect a larger rate close to the SNR. The spectrum of cosmic rays produced is assumed to be close to the observed spectrum in the Milky Way. Hence our use of cosmic ray rates is reasonable.

We did not incorporate X-rays in this work, which are produced by the SNR. Although X-rays are known to have a minor influence on the H_2 abundance within the SN shell (Vasiliev *et al.* 2008), they can positively influence the H_2 abundance of gas ahead of the shell (Ferrara 1998; Haiman *et al.* 1997). Although the effect may be negligible once the shock has passed through the cloud, there will be a difference in the temperature of the cloud as X-rays have an influence on the amount of H_2 present. X-rays affect molecular gas in a very similar way to cosmic rays and therefore should be investigated in future work.

3.6.3 Other processes

It was shown that HD is not an effective coolant for the low-density regime we investigated. There are other molecules which were not included within the thermal model that may be efficient coolants within a metal-free environment, e.g. HeH^+. This could be an important molecule in a metal-free

environment as its cooling function is tens times greater in magnitude than H_2 for the LTE case (Miyake & Stancil 2007). We have a large amount of HeH^+ formed in the post-shock gas, this may make a significant contribution to the cooling. This should be a considered for future work.

3.7 Conclusions

We have explored the evolution of a primordial supernova remnant and its subsequent collision with a small dense cloud. Previous early universe supernova models (e.g. Machida *et al.* 2005; Nagakura *et al.* 2009; Chiaki *et al.* 2013) have only included non-equilibrium cooling for temperatures below 10^4 K and therefore neglected molecular cooling above this temperature. These models also assume equilibrium abundances at T $= 10^4$ K, which is may not represent the true abundances of the chemical species, as the gas is dominated by non-equilibrium chemistry. Therefore, we have incorporated the non-equilibrium chemistry and associated radiative cooling that occurs at all temperatures within this SN model.

We have presented the first high redshift model which investigates the interaction between a shock and cloud (shock-cloud model). The focus of this chapter was to ascertain the dominant microphysical processes occurring during the shock-cloud interaction, as we know the chemistry dictates the thermal state of the gas, and hence the dynamics of the system. A number of different chemistry networks and feedback effects were investigated on the following initial conditions: a small metal-free cloud (radius $\sim$ 1 pc) is situated $\sim$ 40 pc from the progenitor star, and was shocked by a SN (10^{51} erg). We found that the cloud was compressed and fragments into small clumps. However, these were clumps were not Jeans unstable. The inclusion of deuterium, heating from H_2 formation and CMB ionisation had negligible effect on the thermal state of the gas.

Molecular hydrogen is the dominant coolant in this metal-free environment, and therefore the mass/size of these clumps is determined by its abundance. Feedback effects from cosmic rays play an important role in the formation of H_2 and heating the system. The ionisation rate and spectrum of cosmic rays at high redshifts is unknown, and so is a free parameter in our work ($\zeta = 10^{-18} - 10^{-15}\,\mathrm{s}^{-1}$). We found that only cosmic ionisation rate $\zeta = 10^{-18}\,\mathrm{s}^{-1}$ had an overall cooling effect of the gas, because the production of H_2 via ionisations is more dominant than the heating effects. From this we can extrapolate that X-rays and stellar radiation fields are also important to investigate in future work, because they can have positive feedback effects on the formation of H_2 (Haiman *et al.* 1997). Cosmic rays and other ionisation effects have been neglected

from early universe SN models. In order to get realistic results these effects should be investigated in multidimensional SN simulations.

We have modelled the interaction between a SN shock and small cloud, and we found that clumps formed were not possible low-mass star formations sites. However, a much wider parameter range (e.g. cloud size, cloud & ambient density and explosion energy) needs to be investigated in order to establish if low-mass star formation occur via this method. Introducing metals and dust into the chemical network will also increase the cooling and therefore lower the Jeans mass of the clumps.

CHAPTER 4

THE EFFECT OF A MULTIPHASE NEUTRAL MEDIUM ON THE EVOLUTION OF A SNR AND SUBSEQUENT FRAGMENTATION OF CLUMPS

Based on paper by Dhanoa, Mackey & Yates (2014)

4.1 Introduction

In this chapter, we extend the shock-cloud model to include more realistic pre-supernova conditions. Vasiliev *et al.* (2008, hencefoth VVS08) highlighted an important link between the formation of extremely metal poor (EMP) stars within proto-galaxies and the radial distribution of primordial gas prior to the supernova (SN) explosion. This distribution is heavily dependent on the size of the metal-free star and its H II region prior to the explosion; the size of the H II region is then dependent on the state of the gas before the formation of the star. The distance a H II region can extend depends on the size of the dark matter halo the star is situated within. A H II region formed within a mini-halo ($\sim 10^6\,\mathrm{M}_\odot$) at redshift $z = 20$ by a large mass star ($M \geq 100\,\mathrm{M}_\odot$) can extend to 100 pc and can even blow the gas completely out of the Halo (Whalen *et al.* 2004), whereas a similar star within a 10^7 $\mathrm{M}_\odot$ Halo at redshift $z = 12$ forms a H II region which is well confined within a 10 pc region (Kitayama *et al.* 2004, VVS08). Kitayama & Yoshida (2005) state that the

size of the H II region is also dependent on the dark matter profile of the proto-galaxy; which is expected to be larger in proto-galaxies with a flat central density profile.

Within our Galaxy it is observed that a blast wave from a SN collides with the shell created by the progenitor's H II region and it produces a reverse shock. Once the forward SN shock begins to travel within neutral matter, it interacts with a multi-phase medium which can not be characterised by a single density. Three different density regimes in the pre-shock medium are detected in SNR propagating into giant molecular clouds (Reach *et al.* 2005): i) an interclump medium ($\sim 5\,\mathrm{cm}^{-3}$) of atomic gas ii) a molecular gas of moderate density ($\sim 100\,\mathrm{cm}^{-3}$) and iii) a dense clump material ($\sim 10^4\,\mathrm{cm}^{-3}$). Please see figure 1.4 for a schematic diagram of a SN shell interacting with a multiphase neutral medium. This neutral medium changes the dynamics of the SN shell, which 'sweeps up' more matter than predicted by models which use a single ambient density. More importantly, it is observed that SN-triggered star formation occurs in these multi-phase gas clouds, as the dense cores or clumps within the cloud are shocked into collapse (Reach *et al.* 2002).

Melioli *et al.* (2006) investigated star formation triggered in the Galactic environment, via the interaction of a supernova shell and molecular cloud. The authors produce constraints on cloud collapse (and therefore possible star formation) in the 'supernova remnant radius vs. cloud density' parameter space. This was achieved by an analytic study comparing the gravitational free-fall time and destruction time scale of the cloud (which depends on a number of parameters including radiative cooling). By running a suite of 3D hydrodynamic simulations, they were able to confirm that these numerical models were consistent with their analytic constraints. This work was extended by Leão *et al.* (2009) to include magnetic fields and the authors also found their results were consistent with analytic constraints. Both authors recognise that using an approximate polytropic pressure equation to represent radiative cooling maybe an over simplification and more realistic cooling functions are required.

Johansson & Ziegler (2013) have concentrated on the compression of smaller clouds (radius $\sim$ 1 pc) found in the local interstellar medium as a method of triggered star formation. Their MHD simulations (without self-gravity) concentrate on the radiative interaction between the shock and the cloud. The cooling function utilised is a piecewise power-law given by Sánchez-Salcedo *et al.* (2002) and Slyz *et al.* (2005), and assumes collisional ionization equilibrium. They find that the cloud fragments into small dense cool clumps and do not become Jeans unstable. Importantly they find that initial density enhancements within the cloud can increase by a factor of $10^3 - 10^5$, which

eventually relaxes to a final density enhancement of $10^2 - 10^3$. This is consistent with results by Vaidya *et al.* (2013), who have a similar model which includes self gravity. They find that gravity does not contribute to the large increase in density but plays an important role by preventing the re-expansion of the high density region.

These Galactic studies have highlighted that radiative cooling is a crucial process in the interaction between shocks and clouds. Within a primordial protogalaxy cold a creation drives turbulence and produces an interstellar medium with a range of densities and temperatures (Greif *et al.* 2008). Hence we expect the supernova rem ant to interact with a clumpy neutral medium. Mackey *et al.* (2003) modelled an equilibrium primordial gas cloud that is shocked by a supernova. The shocked cloud is heated to a higher entropy state and it is assumed to cool isobarically back to its original equilibrium temperature, but now at a much higher density than before. In this way the Jeans mass of the gas could be reduced by a large factor, allowing much lower-mass stars to form. This argument also applies to smooth ISM distributions, as discussed above (Machida *et al.* 2005; Nagakura *et al.* 2009; Chiaki *et al.* 2013), as long as isobaric conditions hold in the decelerating shell.

The one-zone model of Mackey *et al.* (2003) also crucially depends on the isobaric assumption to increase the gas density in the cooling cloud. In reality, however, pressure is a decreasing function of time in a supernova remnant, because the explosion is (by definition) vastly over-pressured compared to its surroundings. As long as the expansion timescale of the supernova $t_{\rm exp} = R_{\rm sh}/\dot{R_{\rm sh}}$ (where $R_{\rm sh}$ is the shock radius and $\dot{R_{\rm sh}}$ its velocity) is short compared to the local timescale for gravitational effects (i.e the free-fall time $t_{\rm ff} = 1/\sqrt{G\rho}$, where ρ is the gas density and G the gravitational constant) then the time-dependence of the external pressure is an important part of the solution. The passage of a strong shock through a dense cloud can also have catastrophic consequences for the cloud (Klein *et al.* 1994) through turbulent hydrodynamic instabilities. Both of these considerations are best addressed with multi-dimensional hydrodynamic simulations and cannot be captured in one-zone models.

There is a uncertainty in the explosion mechanism in metal-free stars, hence in this chapter we will focus our investigation on the effect of different SN explosion energies on a more realistic pre-SN environment (i.e. the H II region of the progenitor star within a multi-phase neutral cloud). This will give us a more self-consistent model, in which we can follow the post-shock fragmentation of the clumps embedded within neutral clouds. We explore a range of clouds with differing density profiles with the intention to constrain the environment which is favourable to form dense clumps

which may produce low-mass stars ($< 1\,\mathrm{M}_{\odot}$). Overall four cases are studied. The first two cases consider a cloud which has a constant ambient density of 5 cm^{-3} and 10 cm^{-3} and a radius ≥ 50 pc. A cloud with a density of 100 cm^{-3} has a Jeans length of 10 pc, therefore we investigate two cases of a cloud with non-uniform density: i) density $= 1000 \times (R^{-3}/pc)\,\mathrm{cm}^{-3}$ where R is the radius from the centre of the cloud; ii) initial conditions from a cosmological simulation of $10^6\,\mathrm{M}_{\odot}$ dark matter halo by Abel *et al.* (2007).

4.2 Model Outline

In this chapter we build on the SN model previously investigated, by generating the initial conditions from a model which simulates the H II region surrounding the progenitor star. In lieu of using cosmological initial conditions, we investigate a range of gas densities which are utilised as the initial conditions for the H II region model. Therefore we can constrain the type of environment which is favourable for star formation via this method. We outline the general model in this section and discuss the specific initial conditions for the four cases we investigate in sections §4.2.1 – §4.2.4. The clouds considered for the three cases (§4.2.1 - §4.2.3) are assumed to be contained within a 10^7 $\mathrm{M}_{\odot}$ dark matter halo at redshift $z = 10$. In a ΛCDM universe, the growth of structure occurs by the hierarchical merging of dark matter haloes. So we make the assumption that during the formation of this dark matter halo, there were no mergers with haloes that had been contaminated by metals. We also assume the dark matter halo's radius is large enough to contain the H II region and 50-60 pc of neutral matter, without the need to consider the influence of the edge of halo (VVS08). The final case we consider is the interaction of a SN shell and the H II region that has evolved in a smaller dark matter halo of mass $10^6\,\mathrm{M}_{\odot}$ (§4.2.4), the initial conditions are obtained from Abel *et al.* (2007).

We have modelled the interaction of a supernova shell with a dense clump in three stages:

1. the pre-supernova phase, where the dynamical effects of photoionization heating from the star are modelled;
2. the post-supernova phase, where the supernova blast wave expands into the relic H II region left by the star; and
3. the shock-cloud interaction, where the expanding supernova shell compresses a dense cloud.

The first two stages are simulated in one dimension (1D) with spherical symmetry, whereas the third stage is simulated in two dimensions (2D) with rotational symmetry. This is because compression

and fragmentation of the clump cannot be captured within 1D models. However, it is possible to achieve a good representation of the evolution of the supernova remnant in 1D models, assuming that the shell has not interacted with any dense clumps (Jun *et al.* 1996).

The first phase in modelled using the radiative hydrodynamic code PION (Mackey & Lim 2010), to simulate the H II region created by the progenitor star (henceforth the H II region model). The star was modelled by a point source of ionising radiation placed at the centre of a spherically symmetric cloud. A metal-free star of mass 40 $M_{\odot}$ is switched on for its main sequence life time of 3.86×10^6 years with an ionising rate of $2.469 \times 10^{49}\,s^{-1}$ (Schaerer 2002). We ignore any post main sequence stages of evolution. The choice of progenitor mass was determined by studies by Joggerst *et al.* (2009, 2010), which found that EMP stars were formed by metal-free stars of mass 40 $M_{\odot}$ and lower. This is the largest progenitor mass we can consider; as it is predicted that non-rotating primordial stars with masses greater than 40 $M_{\odot}$ will explode and form a direct black hole which sweeps all the heavy metals inside (Heger & Woosley 2002). The explosion mechanism for metal-free stars is not well understood and there are even more uncertainties for primordial stars with masses above 30 $M_{\odot}$ (Fryer *et al.* 2012). In light of this we investigate a number of explosion energies (which relate to different explosion mechanisms): 0.6×10^{51} erg, 1.0×10^{51} erg, 2.0×10^{51} erg (predicted for core collapse SN, Joggerst *et al.* (2010)) and 1.0×10^{52} erg (predicted for hypernovae, Tominaga (2009)).

Within the H II region model, the gas is assumed to be atomic with a hydrogen to helium number density ratio of 1.00 : 0.08. All the molecular hydrogen within $R < 50$ pc is assumed to be dissociated by Lyman Werner radiation and therefore the gas is cooled via atomic processes only. As the hydrodynamics are linked with radiative processes in the simulation, this allows evolution of both the H II region and H II shell to occur. We can also determine if the clump interacts with any ionising radiation prior to SN explosion, i.e. if the ionisation front of the star extends to the original position of the clump.

The initial conditions for the second phase (post-SN) are generated by the H II region model output. there are not any molecular species present (atomic only as H_2 assumed to be photodissociated); only atomic or ionised hydrogen. It is assumed that the percentage of helium atoms that are singly ionised (He^+) is the same as hydrogen, which is correct for a metal-free 40 $M_{\odot}$ star (Draine 2011; Schaerer 2002). We use a chemical network of 11 species (H, He, H_2, H^+, H_2^+, H_3^+, HeH^+, He^+, He^{++}, H^- and e^-) and 42 reactions. The chemical rates are adapted to cover the temperature

range $10 - 10^{10}$ K. The abundances of the atomic species and electron fraction are calculated using conservation equations. The brief flash (10 – 100 s) of hard UV radiation that is associated with a core collapse SN has not been included in this model. It is is assumed that this flash has a negligible effect on the ionisation of the neutral medium. We set the cosmic ray ionisation rate to 10^{-18} s^{-1}, assuming the SN remnant to be the source.

The SN explosion is modelled by injecting thermal energy, not kinetic (i.e. we ignore the free-expansion phase). Therefore at very early times the newly shocked gas has an artificially high temperature (T$>$ 10^{10} K), and at these temperatures we utilise the value of the reaction rates at 10^{10} K. To avoid artificial overcooling at early times, we only switch on the cooling when the gas has adiabatically cooled down to 10^8 K. The thermal model includes atomic cooling (Fukugita & Kawasaki 1994; Hummer 1994), Bremmstrahlung cooling (Hummer 1994; Shapiro & Kang 1987), inverse Compton scattering (Peebles 1971) and molecular line cooling from H_2, H_2^+ and H_3^+ (Glover & Abel 2008; Hollenbach & McKee 1979; Glover & Savin 2009). The heating processes included in the model are CMB heating (assumed equal to $\Lambda(T_{CMB})$) and cosmic ray heating (Glover & Jappsen 2007). Post explosion, photodissociating and ionising radiation are neglected. Further discussion of the parameters and full details of the chemical model are presented in Chapter 3.

In the following sections (§4.2.1 – §4.2.4) we describe the initial conditions and results for both the H II region model (phase 1) and the SN model (phase 2) for the four different cases we consider. For all the 2D shock- cloud models (phase 3) presented below the initial conditions are obtained in the same way; a 1D post shock model (5120 grid points) is run until it the SN shell reaches ~ 1 pc from the clump, then the output of this phase 2 model (both chemical and dynamic properties) is mapped onto a 2D grid (384$\times$160 grid points) which concentrates on the area 7 pc around the clump where the clump is centred at 3 pc (represented by the origin on the graphs of the 2D output). For further details of the mapping process please see section §3.5. This creates a spherical clump with 1 pc radius, average density $n \approx 100\,cm^{-3}$ and mass ~ 13 $M_\odot$. The clumps are not placed closer than 20 pc to the progenitor star, as it has been observed that OB stars evaporate small clumps in this region or eject larger clumps via the 'rocket method' (Chevalier 1999; Leão *et al.* 2009). As we initiate a new model the time has been reset to t = 0 s and run for a minimum of 1.5×10^{13} s, the simulation time is extended if needed.

4.2.1 Model 1

4.2.1.1 Phase 1: The H II region model

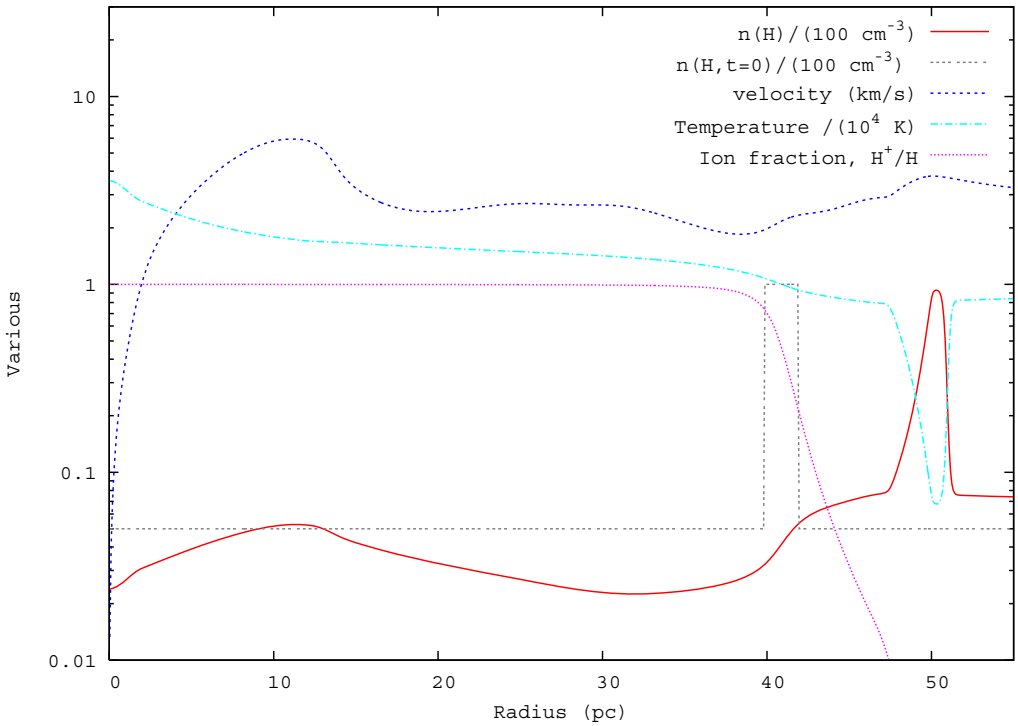

Figure 4.1: The H II model output for Model 1 - the initial density of the gas is shown in grey dashed line. The red line displays the density of the gas at 3.86×10^6 years, once the H II region has developed around the star. The star was modelled as a point source at x=0.

In this model we investigate the evolution of 5 cm^{-3} ambient gas surrounding a 40 M$_\odot$ star, which contains a 100 cm^{-3} clump embedded at 40 pc from the star. Without any observations, and due to the lack of spatial resolution in cosmological simulations to capture the formation of clumps; we use the observed interclump density (5 cm^{-3}) of a multiphase cloud by Reach *et al.* (2005) as a starting point. Without efficient coolants, we are unlikely to find high density cores that are observed within the molecular part of these clouds. The choice for the density of the clump was determined by the maximum density reached in simulations by Greif *et al.* (2010). The initial density of the gas is represented by the black dashed in line in Figure 4.1 where the diameter/thickness of the clump is 2pc. The parameters in this model are similar to the initial conditions investigated in the metal-free toy model (§3.4); the output of this simulation will also allow us to determine if the clump investigated in the previous chapter is likely to interact with stellar ionising radiation.

The output of the H II simulation is also displayed in Figure 4.1. The radiation of the star produces a H II region that reaches 40 pc and a H II shell that extends to 43 pc. The ambient density within the H II region ranges between 2 cm^{-3} - 5 cm^{-3}. The clump that was first positioned at 40 pc interacts with the ionising radiation and is moved to 50 pc. If the clump was able to survive this ionising radiation, it would no longer be considered neutral. To model this situation properly, we would need to include a Photo Dissociation Region (PDR) model. In light of these two points, we approximate this output of this H II region model with initial conditions of the toy model in the previous chapter (§3.4), but the clump is now placed at 50 pc, which means initial conditions of i) ISM: $n = 1\,\mathrm{cm}^{-3}$, T = 10000 K, $\mathrm{x_{H^+}} = 1.0$ & $\mathrm{x_{H^+}} = 1.0$ and ii) the clump: $n = 100\,\mathrm{cm}^{-3}$, T = 200 K, $\mathrm{x_H} = 0.9999$ & $\mathrm{x_{H^+}} = 10^4$.

4.2.1.2 Phase 2 and 3: The supernova - cloud model

A supernova explosion was initiated within an environment described by the metal-free toy model, where a clump (100 cm^{-3}) is embedded at 50 pc within an ambient gas (1 cm^{-3}). This 1D model is allowed to run until the SN shell reaches ~ 49 pc and then is mapped onto a 2D grid. The three explosion energies investigated for this model are described below. The hypernova explosion is not presented as the SNR was still in the adiabatic stage when it interacts with the clump.

The first scenario investigated was the explosion energy of 0.6×10^{51} erg. The initial conditions (density and temperature) for this 2D SN model are displayed in Figures 4.2(a) and 4.3(a). The cloud has a radius of 1pc, a maximum density of 108 cm^{-3} and a minimum temperature of 135.5 K. The width of the SN shell is 1.7 pc. The high density part of shell has a minimum temperature 360 K and maximum density of 40.25 cm^{-3}. The lower density part of the shell has an average temperature 6600 K and average density 7.6 cm^{-3}. The two parts of the shell have similar velocity; the high density part has a velocity of 16.8 km s^{-1}, while the low density part of the graph has an average velocity of 15.5 km s^{-1}.

The results of this simulation are shown in Figures 4.2 & 4.3. Due to the low velocity of the shock the simulation was run for $950,000$ years, compared to the previous toy model which had a simulation time of $475,000$ years. From Figure 4.2(b) one can see that at simulation time $475,000$ years the shock has only just passed through the cloud. In Figure 4.2(c) it is clear that a high density ridge was not formed, hence the cloud does not fragment. The cloud flows away and star formation can not occur.

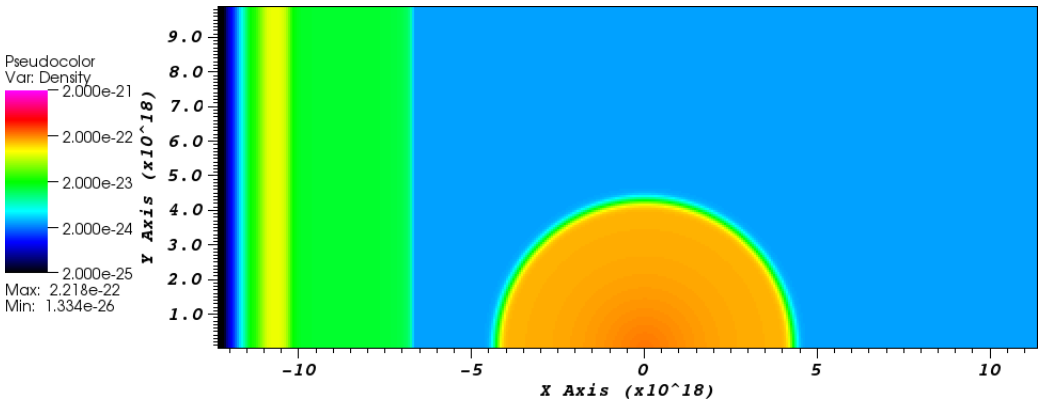

(a) $t = 0$ yr

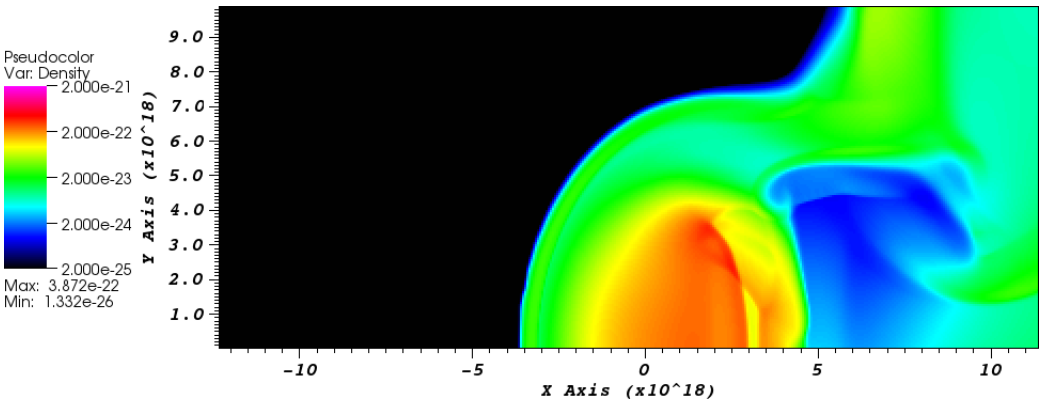

(b) $t = 475,000$ yr

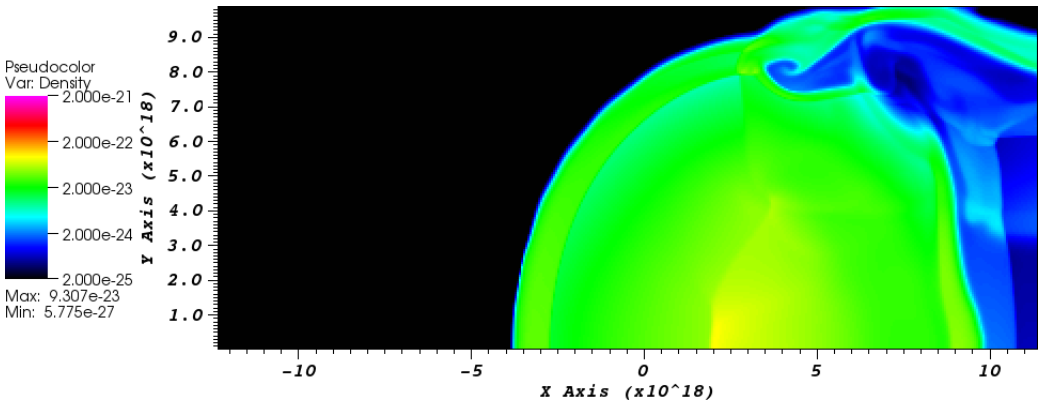

(c) $t = 950,000$ yr

Figure 4.2: 2D SN model of Model 1- density is displayed as shell of a $0.6{\times}10^{51}$ erg SN collides with a clump embedded in the ISM. The legend displays mass density ($\mathrm{g{\cdot}cm^{-3}}$), which equates to max. $n = 981.6\,\mathrm{cm^{-3}}$ and min. $n = 0.0098\,\mathrm{cm^{-3}}$. [The x and y axis represent the distance from the centre of the clump at t= 0 s (in 10^{18} cm)]

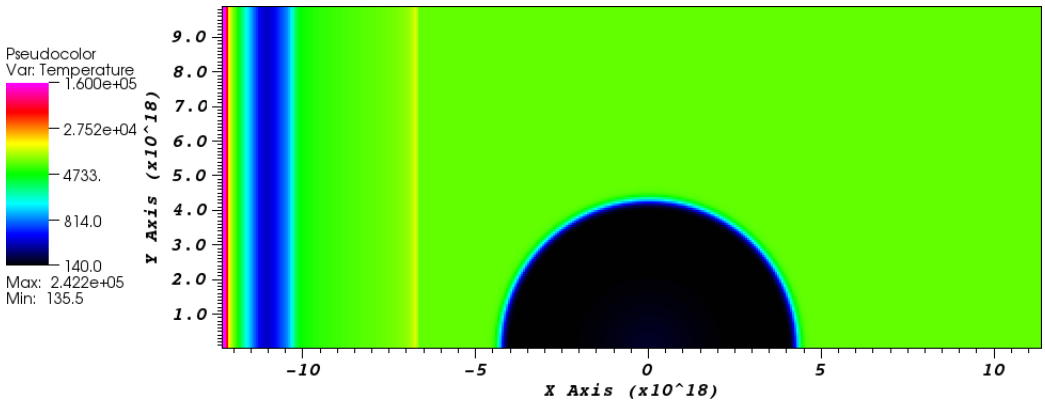

(a) $t = 0$ yr

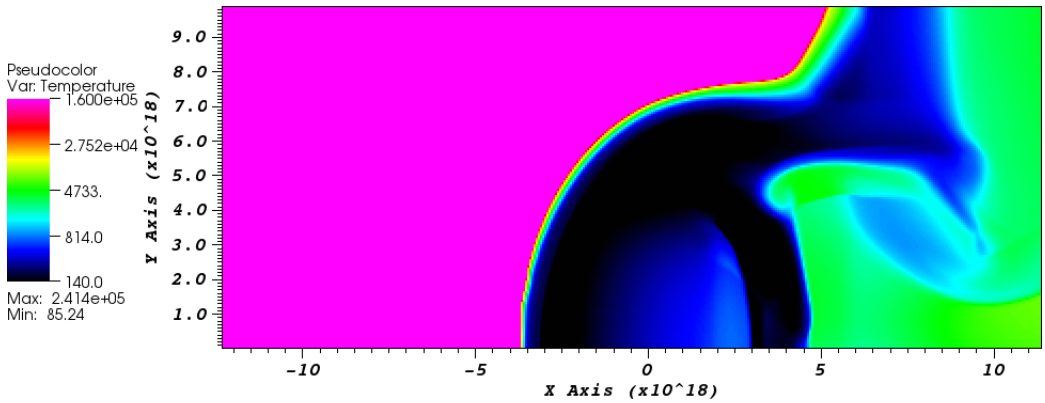

(b) $t = 475,000$ yr

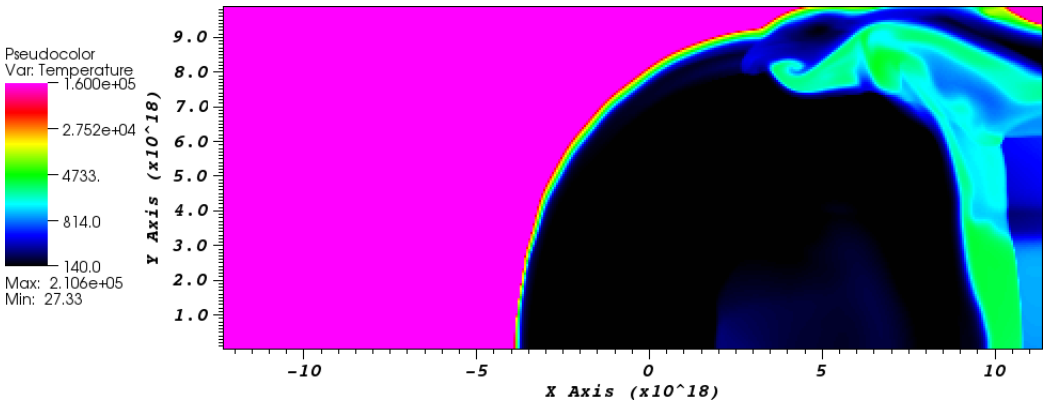

(c) $t = 950,000$ yr

Figure 4.3: 2D SN model of Model 1 - temperature is displayed as shell of a 0.6×10^{51} erg SN collides with a clump embedded in the ISM. The legend displays temperature in Kelvin [The x and y axis represent the distance from the centre of the clump at t= 0 s (in 10^{18} cm)]

Next we investigate an explosion energy of 1.0×10^{51} ergs. The initial conditions for the 2D model are shown in Figures 4.4(a) and 4.5(a). The cloud has a minimum temperature of 138 K and a maximum density 115 cm^{-3}. The thickness of the shell is 0.65 pc, the higher explosion energy means the shell is much thinner than the 0.6×10^{51} erg case. The shell has a minimum temperature of 540 K and a maximum density of 88.35 cm^{-3}. The low density region of the shell has an average temperature of 7000 K and an average density of 16.20 cm^{-3}. The average velocity of the shell is 26 km s^{-1}.

The results of the simulation are shown in Figures 4.4 & 4.5. Again the simulation time is extended to 3.0×10^{13} s. As shown in Figure 4.4(b) at $475,000$ years the cloud has been compressed but not had enough time to fragment. From Figure 4.4(c) one can see that by the end of the simulation, the low density instabilities that were forming on the ridge do not fragment. Most of the clump is destroyed, as the gas flows with the shock and disperses.

The initial conditions for the 2D model with explosion energy 2.0×10^{51} erg are shown in Figure 4.6(a) and 4.7(a). The cloud has a maximum density of 115 cm^{-3} and a minimum temperature of 143 K. Unlike the previous cases, a higher shell velocity (average $\sim$ 48 km s^{-1}) causes the density profile of SN shell to be 'gaussian like'. It has a thickness of 0.25 pc, a maximum density of 149 cm^{-3} and a minimum temperature of 1300 K. The results at $475,000$ years are shown in Figures 4.6 & 4.7. The clump undergoes compression and fragmentation. The clumps have a maximum number density of $n = 112\,\mathrm{cm}^{-3}$. The estimated Jeans mass of these clumps is $m_J \approx 9900\,\mathrm{M}_{\odot}$, so they are not gravitationally bound and are not expected to collapse.

This model is analogous to the study of SNR interacting with a homogenous diffuse neutral cloud ($\sim 100\,\mathrm{cm}^{-3}$) observed in our Galaxy. This method of triggered star formation has been modelled by Melioli *et al.* (2006) and Leão *et al.* (2009) and they provide analytic constraints on the gravitational instability of the cloud after the interaction of a SNR. Their numeral analysis has been tested successfully against 3D-MHD simulations that include self gravity. For a SNR in its radiative phase interacting with material in the absence of a magnetic field, assuming a planar shock the condition for collapse is

$$R_{SNR} \lesssim 55.1 \frac{E_{51}^{0.33}\, f_{10}^{0.2}\, n_{c,10}^{0.4}\, r_{c,10}^{2.4}}{T_{c,100}^{0.8}\, n^{0.17}} \text{ pc}, \tag{4.1}$$

where R_{SNR} is the radius of the SNR, E_{51} is the explosion energy in units of 10^{51} erg, f_{10} is the density contrast between the shell and ISM density in units of 10, $n_{c,10}$ is the cloud density in units

of 10 cm^{-3}, $r_{c,10}$ is the cloud radius in units of 10 pc, $T_{c,100}$ is the cloud temperature in units of 100 K and n is the density of the ambient density in cm^{-3}. According to this criterion, for the explosion energy 2×10^{51} erg the cloud must be placed at 60 pc for gravitational collapse to occur. Further numerical investigation is needed to confirm this.

4.2.2 Model 2

4.2.2.1 Phase 1: The H II region model

The second density profile we investigate is a $100\,\mathrm{cm}^{-3}$ clump that is embedded within a uniform ambient medium of density 10 cm^{-3}. Just like the previous case, a 100 cm^{-3} clump is placed at 40 pc from the centre of the cloud. This is similar to the clumpy molecular environment investigated by Chevalier (1999). The clump is in pressure equilibrium, as the ambient cloud temperature is10^4K and the clump has an initial temperature of 1000 K. A 40 $M_\odot$ is simulated as a point source at the centre of a spherically symmetric cloud (at x=0 pc) and the output of the H II model is displayed in Figure 4.8.

The larger ambient density compared to the previous case, means that the H II region is smaller and extends to ∼30 pc. The ambient density within the H II region is split into two discrete regions; the first which extends to 16 pc and the density is between 1 – 2 cm^{-3} and the second which has a density range between 3 – 4 cm^{-3}. By the end of the simulation the clump has been moved to 45 pc by a weak shock, which is driven by dynamical expansion of the H II region. The clump does not interact with any ionising radiation and so it contains neutral gas with an average electron fractional abundance of 10^{-6}. This value is lower than than the assumed ionisation fraction within the clump for the toy model in Chapter 3. The clump cools to $\sim$ 900 K because the low-levels of electrons within clump do not form much molecular hydrogen.

4.2.2.2 Phase 2 and 3: The supernova - cloud model

In the model, we investigate four explosion energies (E_{SN}): 0.6×10^{51} erg, 1.0×10^{51} erg, 2.0×10^{51} erg and 1.0×10^{52} erg. The output from the 1D SN simulations for the explosion energies 0.6×10^{51} erg and 1.0×10^{51} erg, are shown in Figure 4.9. Once a SNR is travelling below 10 km s^{-1} it is no longer considered a shock. Observed SNRs at this speed, equal to the random speeds of the ambient medium, start to merge into turbulent flow and dissipate into the ISM (Draine 2011). Hence the SNR is assumed to terminate once they travel below this speed. For both of these cases the shock velocity reaches below 10 km s^{-1} and do not reach the clump. The reverse shock has

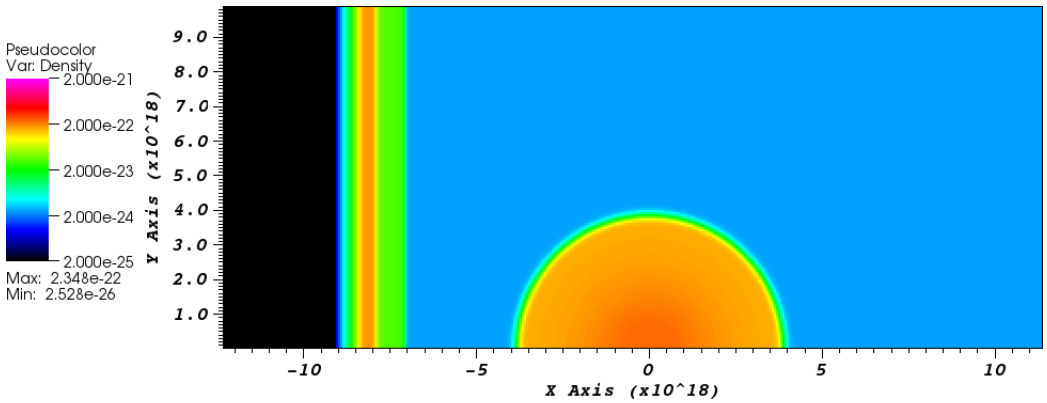

(a) $t = 0$ yr

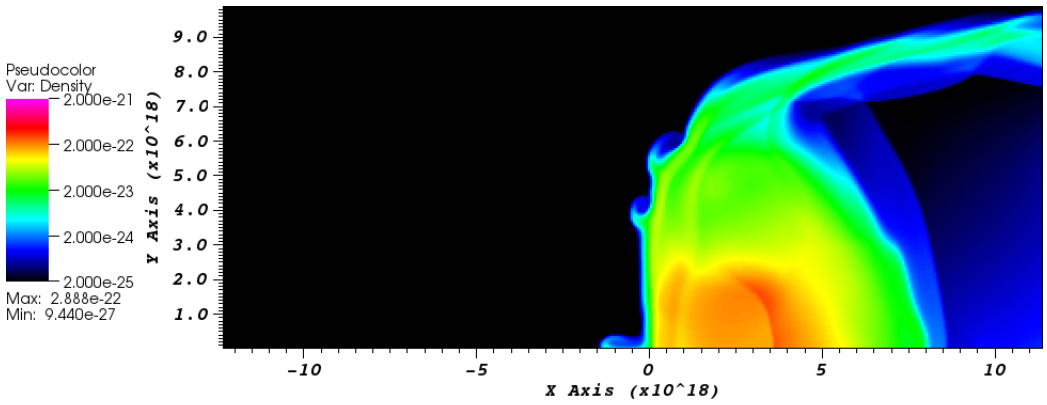

(b) $t = 475,000$ yr

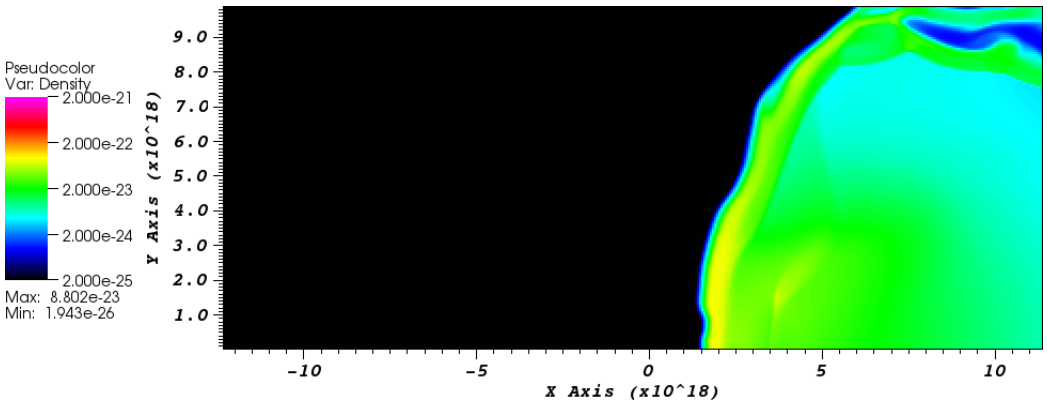

(c) $t = 950,000$ yr

Figure 4.4: 2D SN model of Model 1- density is displayed as shell of a $0.6{\times}10^{51}$ erg SN collides with a clump embedded in the ISM. The legend displays mass density ($\mathrm{g{\cdot}cm^{-3}}$), which equates to max. $n = 981.6\,\mathrm{cm^{-3}}$ and min. $n = 0.0098\,\mathrm{cm^{-3}}$. [The x and y axis represent the distance from the centre of the clump at t= 0 s (in 10^{18} cm)]

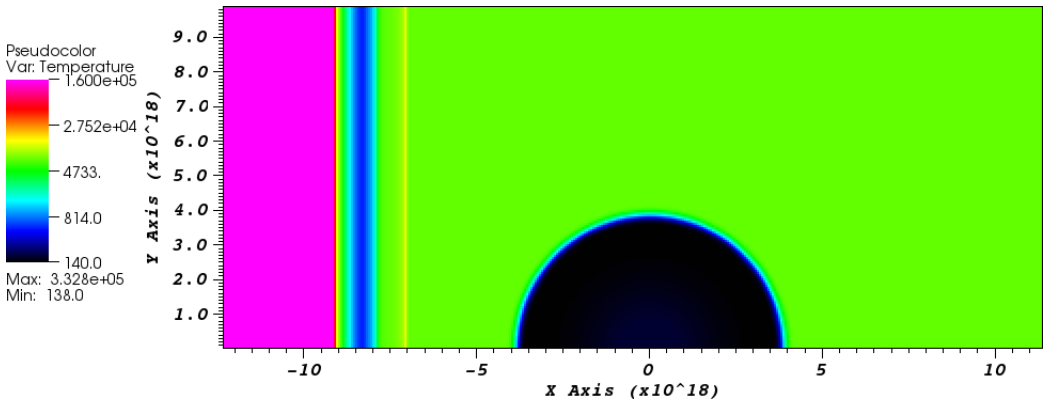

(a) $t = 0$ yr

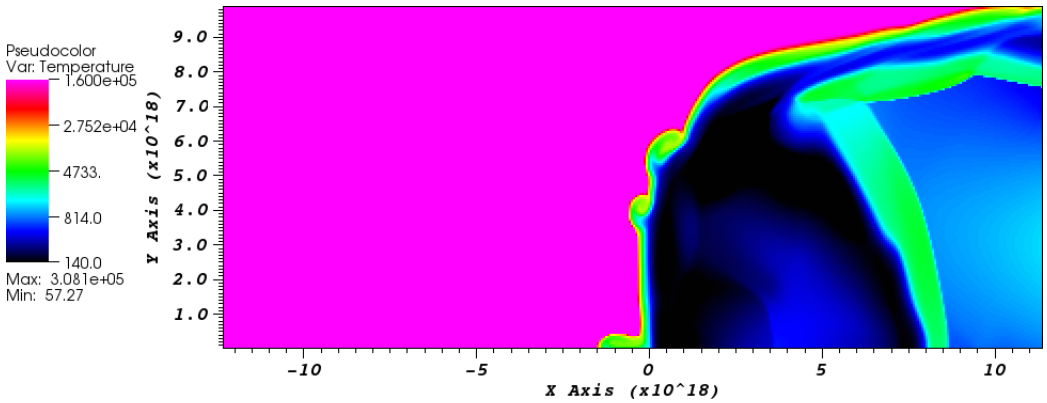

(b) $t = 475,000$ yr

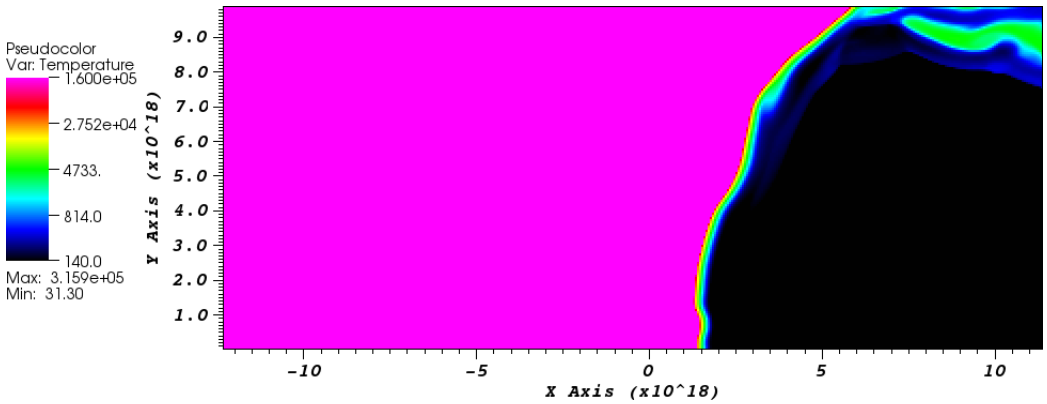

(c) $t = 950,000$ yr

Figure 4.5: 2D SN model of Model 1- temperature of the gas is displayed as shell of a 1.0×10^{51} erg SN collides with a clump embedded in the ISM. The legend displays temperature in Kelvin [The x and y axis represent the distance from the centre of the clump at t= 0 s (in 10^{18} cm)]

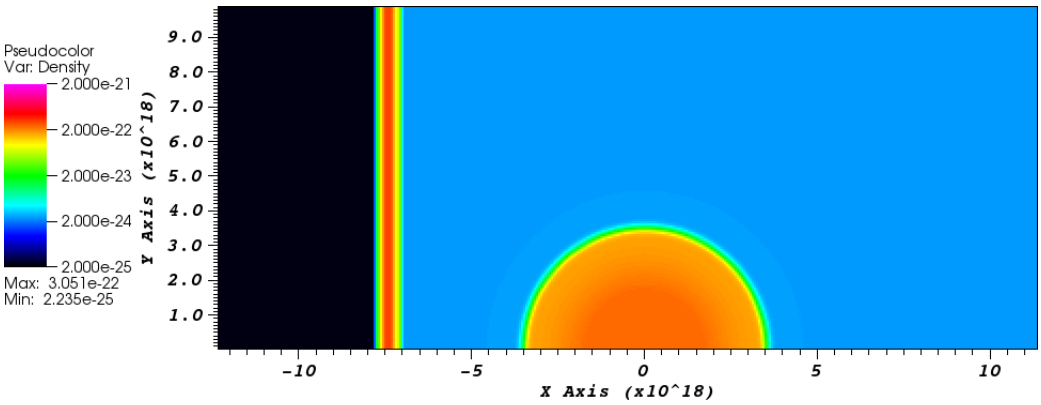

(a) $t = 0$ yr

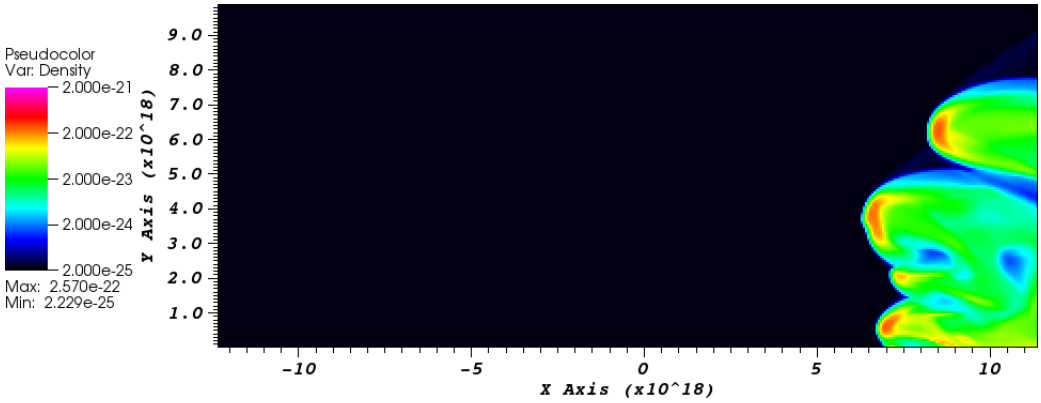

(b) $t = 475,000$ yr

Figure 4.6: 2D SN model of Model 1- density is displayed as shell of a $2.0{\times}10^{51}$ erg SN collides with a clump embedded in the ISM. The legend displays mass density ($\mathrm{g{\cdot}cm^{-3}}$), which equates to max. $n = 981.6\,\mathrm{cm^{-3}}$ and min. $n = 0.0098\,\mathrm{cm^{-3}}$. [The x and y axis represent the distance from the centre of the clump at t= 0 s (in 10^{18} cm)]

been reflected a number of times, hence the velocity of the hot gas displays a oscillatory pattern. When an observed SNRs undergo this process they are expected to have mixed with the SN ejecta (Vishniac 1983). Hence these SN shells can no longer be considered metal-free.

The 2.0×10^{51} erg case is similar (Figure 4.10(a)); in this model the shock is travelling at a velocity of 8.2 km $\mathrm{s^{-1}}$ at 39 pc. However the shell does reach the clump. The shell has a thickness of 2.7 parsec, which can be characterised as having a high density trailing part and an extended leading low-density part. The former has a maximum density of 290 $\mathrm{cm^{-3}}$ and a minimum density of 174K; and latter has an average density of 23.8 $\mathrm{cm^{-3}}$ and average temperature 8250 K. The cloud has a maximum density of 98 $\mathrm{cm^{-3}}$ and a minimum temperature of 725 K.

From Figure 4.10 the evolution of SNR can be seen, and the shock stops before the high density part reaches the clump. There is a reverse shock in the shell as it collides with the clump. The

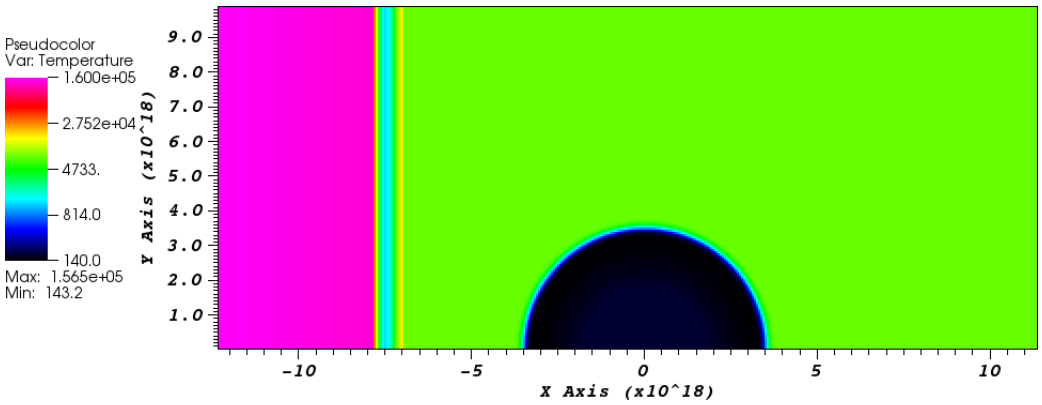

(a) $t = 0$ yr

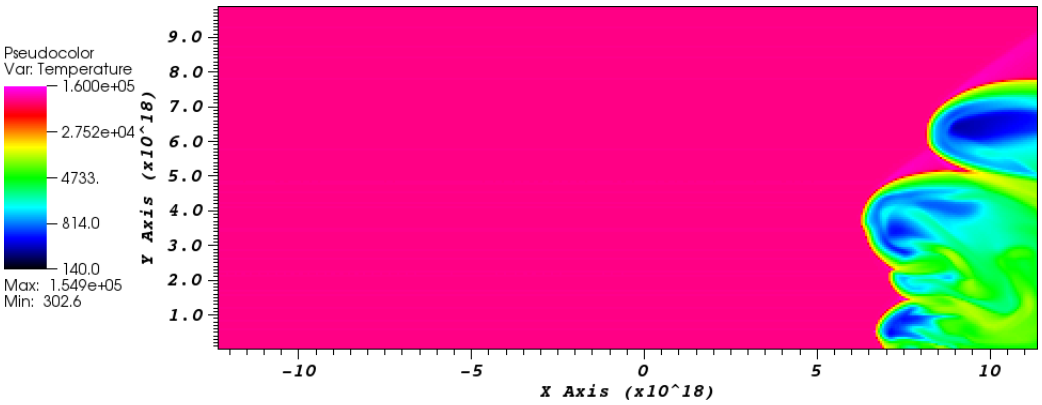

(b) $t = 475,000$ yr

Figure 4.7: 2D SN model of Model 1- temperature of the gas is displayed as shell of a 2.0×10^{51} erg SN collides with a clump embedded in the ISM. The legend displays temperature in Kelvin [The x and y axis represent the distance from the centre of the clump at t= 0 s (in 10^{18} cm)]

clump is compressed but does not fragment. The compression of the clump causes the H_2 fraction within it to increase, due to the increase in temperature and density. As can be seen from Figure 4.11(b), the clump cools from 800K to around 140 K. By the end of the simulation, the density of the clump is very low as gas within the clump has expanded and diffused into the material of the shell.

Finally the hypernova explosion ($E_{SN} = 1.0 \times 10^{52}$ ergs) is investigated, the initial conditions are shown in Figures 4.12(a) and 4.13(a). In this case, the SN shell is much thinner than in the previous cases, with a width of 0.08 pc, a maximum density of $n = 12597$ cm^{-3} and minimum temperature of 920 K. The shock travels at a velocity of 39 km s^{-1}. As the shock arrives at the cloud quicker than in the lower explosion energy models, the cloud cools to a minimum temperature of 880 K and has a maximum density of 104 cm^{-3}.

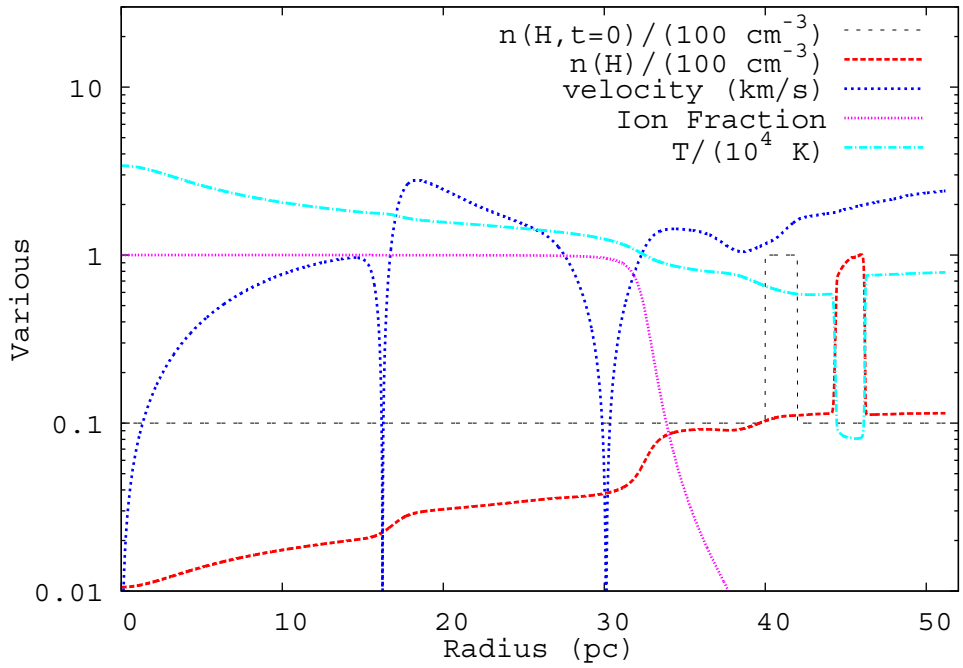

Figure 4.8: The H II model output for Model 2 - the initial density of the gas is shown in grey dashed line. The red line displays the density of the gas at 3.86×10^6 years, once the H II region has developed around the star. The star was modelled as a point source at x=0.

The evolution of the shock as it interacts with the clump is shown in Figure 4.12. In Figure 4.12(b), it can be seen that the clump is compressed much more than in any previous models. After 359,000 years the shock has passed through the clump, causing it to compress and form a very dense central core. This core has a maximum density of $n = 7740\,\mathrm{cm}^{-3}$ and a minimum temperature of 56 K. We use a program which calculates the mass of the clump $\approx$18 $M_\odot$ from the output of 2D axial symmetric model displayed in Figure 4.12(f). The core was previously denser at $\sim 291,000$ years (Figure 4.12(e)) with a maximum density of ~ 78000 cm^{-3} around 0.47 Myrs after the initial blast wave and, although the minimum temperature within the lower density region of the clump is 30K, the temperature of this maximum density region is $\sim$300 K. During the shock-cloud interaction, the clump mass has increased from 19 $M_\odot$ to 40 $M_\odot$. We do not expect this clump to be gravitationally unstable as the minimum Jeans mass is 1000 $M_\odot$.

We extend the simulation to observe how much the clump will expand and/or disperse; the simulation grid size was extended to represent the area $40.08 - 59.28$ pc from the progenitor star (960$\times$160 grid points) from the centre of the cloud. Then the simulation was reset and the clump evolution is followed for 635,000 years. The results are shown in Figure 4.14. Note that the scale

of this figure has been increased compared to density figures. This is so that the gas within the clump can be easily followed throughout the simulation. The first figure represents the state of the clump at 359,000 years and is the same as Figure 4.12(f) but within the extended frame. After 635,000 years it can be seen that the clump has survived and reached pressure equilibrium (see Figure 4.14(c)), with an average density of $n = 3000\,\mathrm{cm}^{-3}$ and average temperature of 100 K. The highest H_2 abundance formation is found at the front of the clump (left side) $x_{H_2} = 0.006$ and the rest of the clump has an average of $x_{H_2} = 0.004$. Due to the x-axis being a reflective boundary, a thin high density plume of gas has formed in the wake of the shock. This gas contains the highest amount of H_2 ($x_{H_2} = 0.008$) and cools down to 25 K.

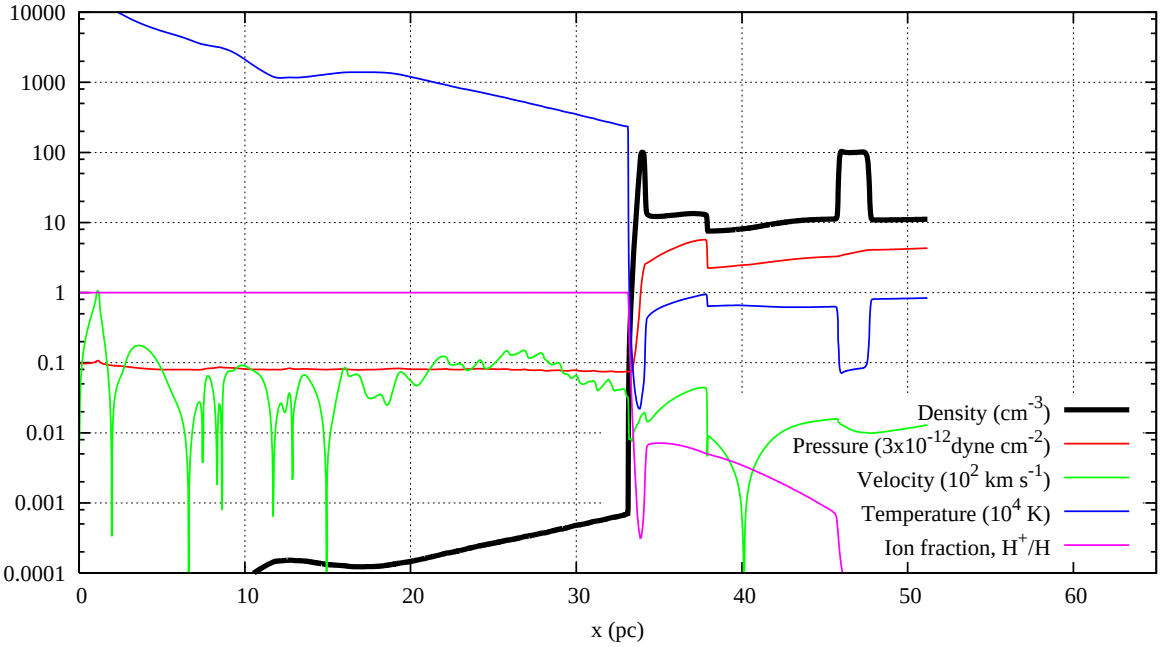

(a) $E_{SN} = 0.6 \times 10^{51}$ erg

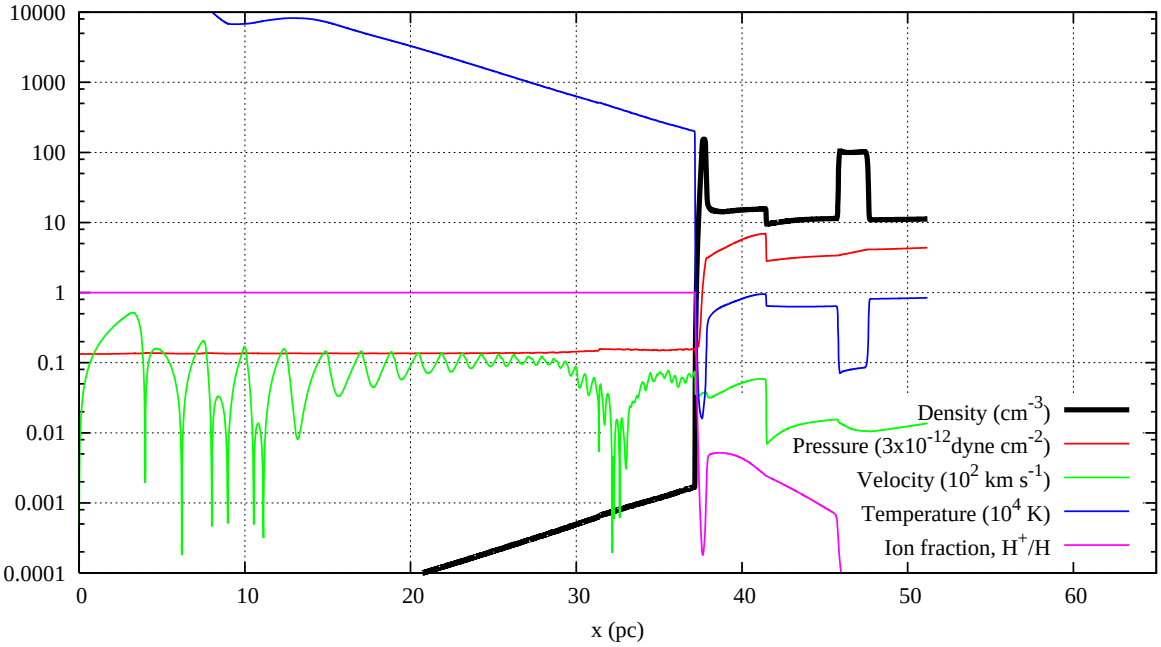

(b) $E_{SN} = 1.0 \times 10^{51}$ erg

Figure 4.9: 1D SN model outputs for both the SN explosion energies 0.6×10^{51} erg and 1.0×10^{51} erg. Both shocks dissipate before they reach the clump, as they are travelling under 10 km s^{-1}

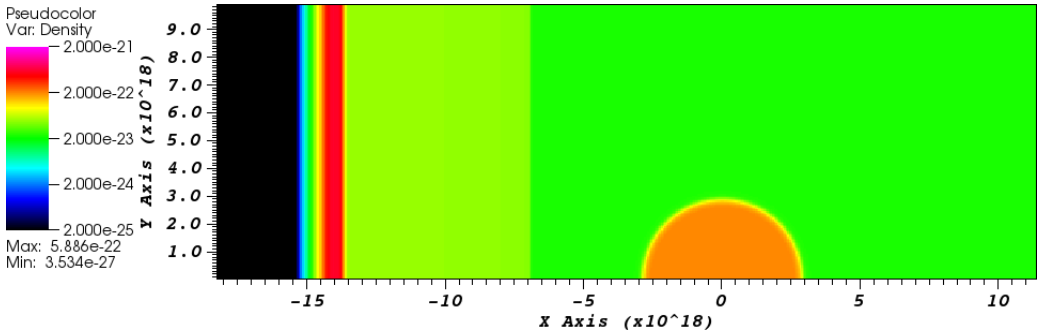

(a) $t = 0$ yr

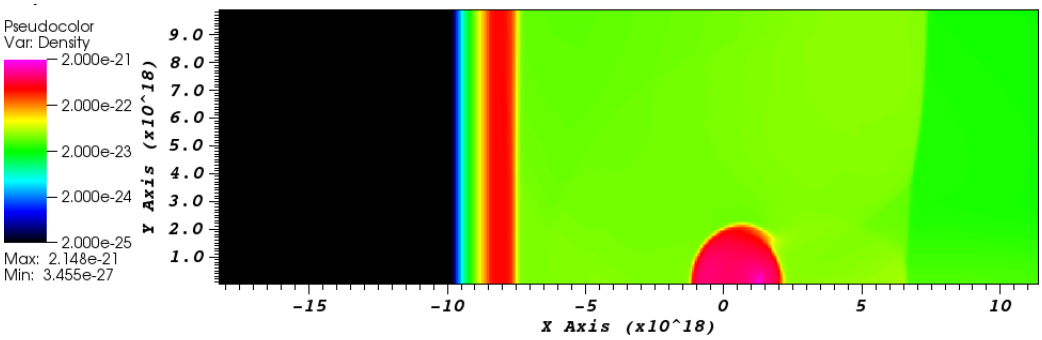

(b) $t = 272,000$ yr

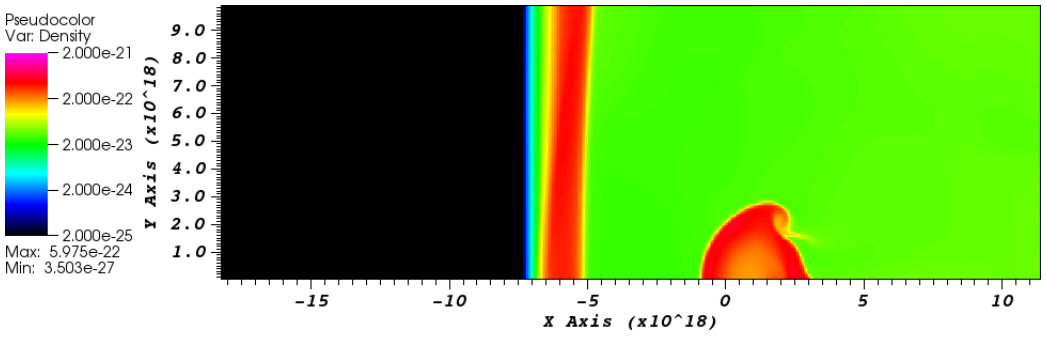

(c) $t = 444,000$ yr

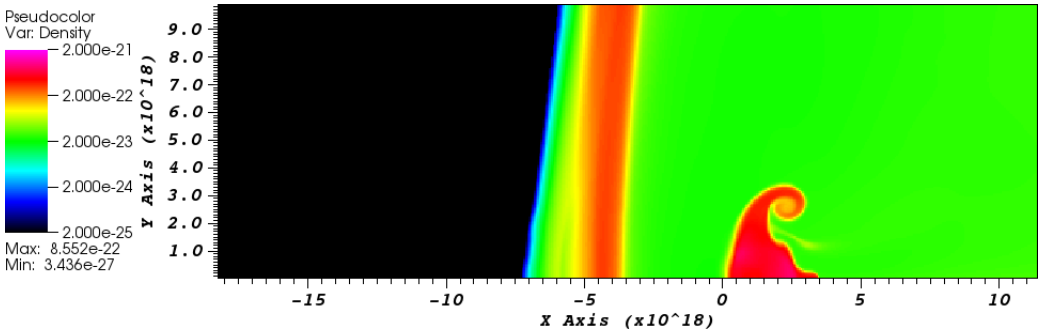

(d) $t = 830,000$ yr

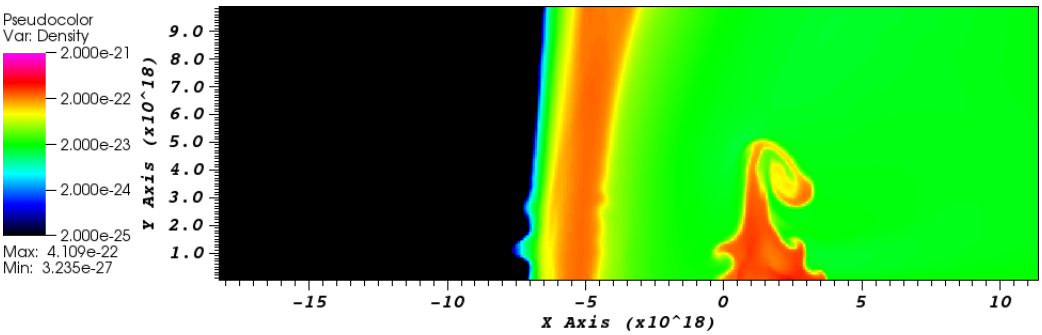

(e) $t = 1,365,000$ yr

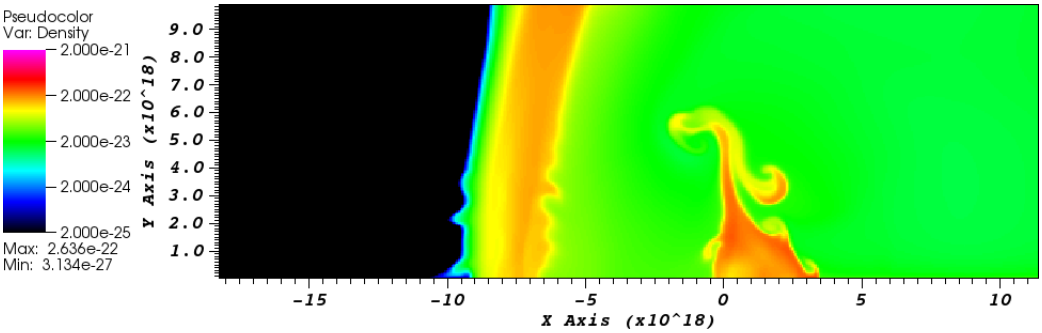

(f) $t = 1,900,000$ yr

Figure 4.10: 2D SN model of Model 2 - density is displayed as shell of a 2.0×10^{51} erg SN collides with a clump embedded in the ISM. The legend displays mass density ($\mathrm{g\cdot cm^{-3}}$), which equates to max. $n = 981.6\,\mathrm{cm^{-3}}$ and min. $n = 0.0098\,\mathrm{cm^{-3}}$. [The x and y axis represent the distance from the centre of the clump at t= 0 s (in 10^{18} cm)]

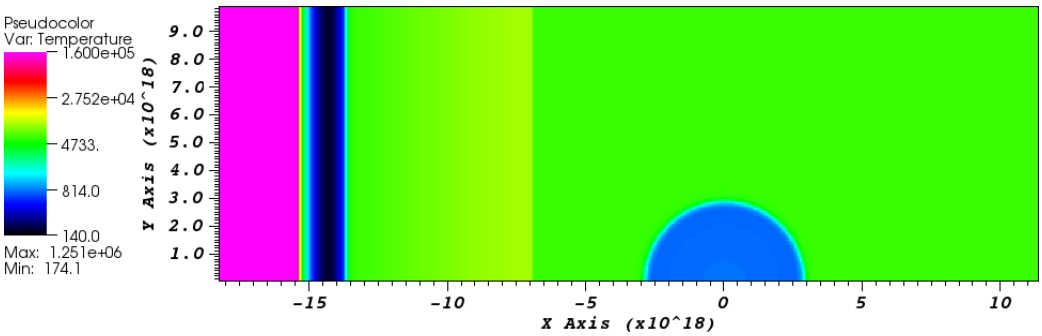

(a) $t = 0$ yr

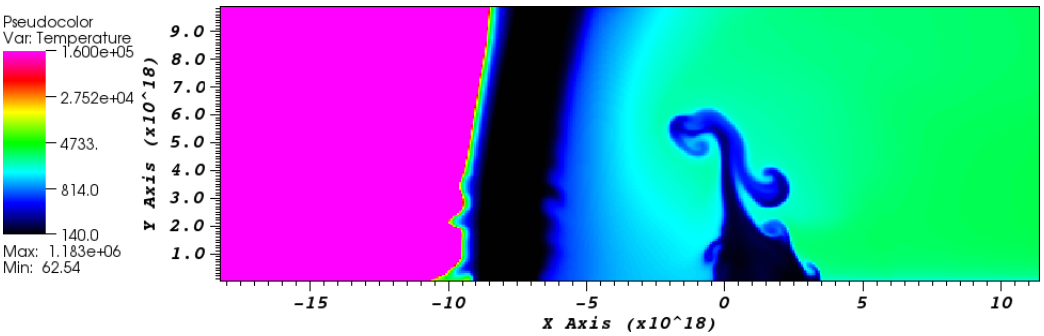

(b) $t = 1,900,000$ yr

Figure 4.11: 2D SN model of Model 2 - temperature of gas is displayed as shell of a 2.0×10^{51} erg SN collides with a clump embedded in the ISM. The legend displays temperature in Kelvin [The x and y axis represent the distance from the centre of the clump at t= 0 s (in 10^{18} cm)]

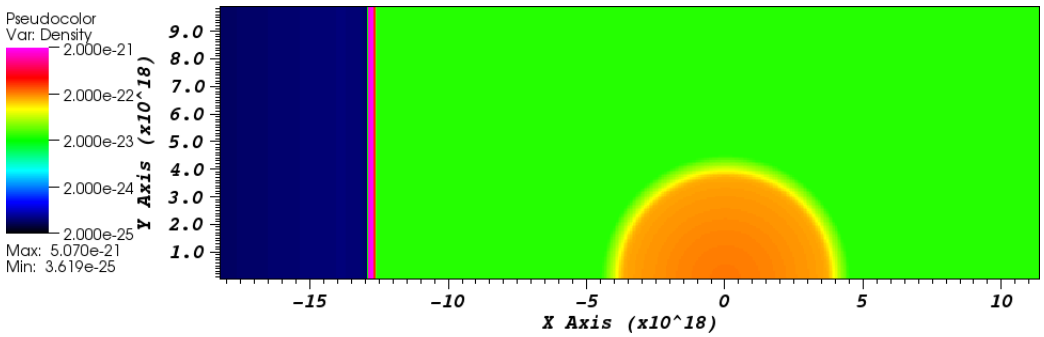

(a) $t = 0$ yr

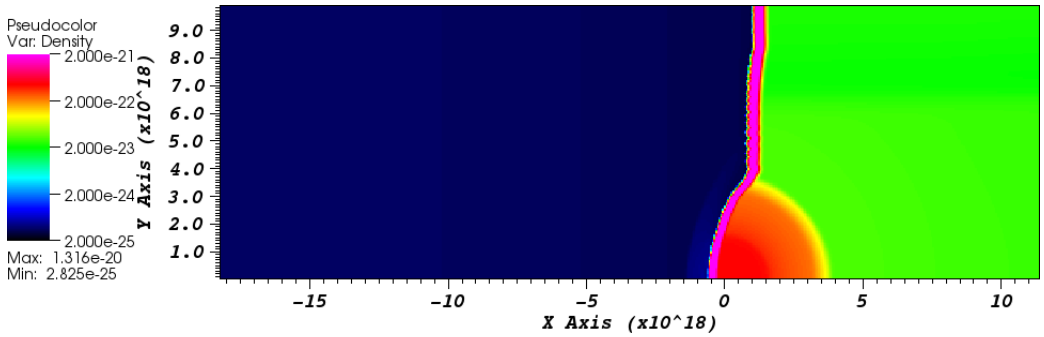

(b) $t = 118,000$ yr

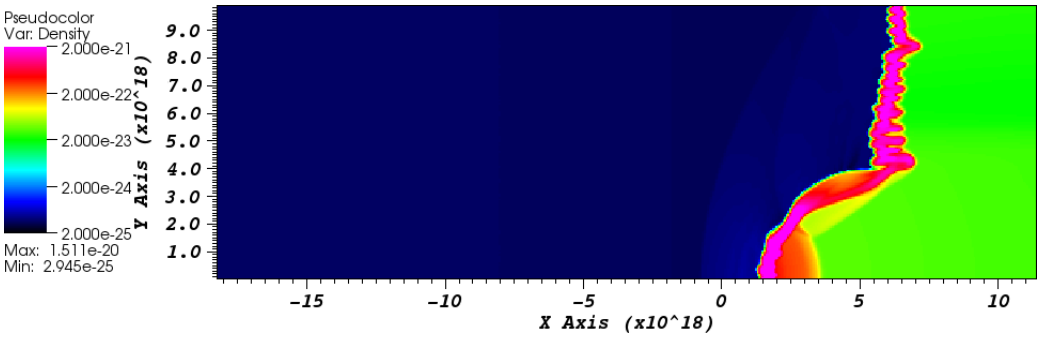

(c) $t = 171,000$ yr

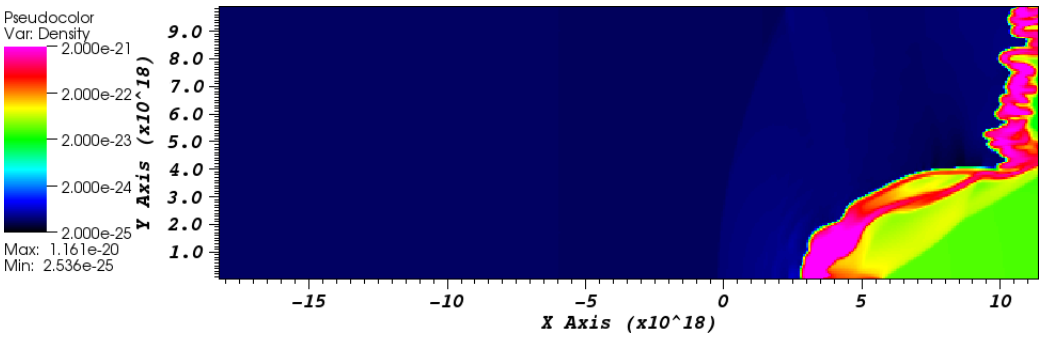

(d) $t = 225,000$ yr

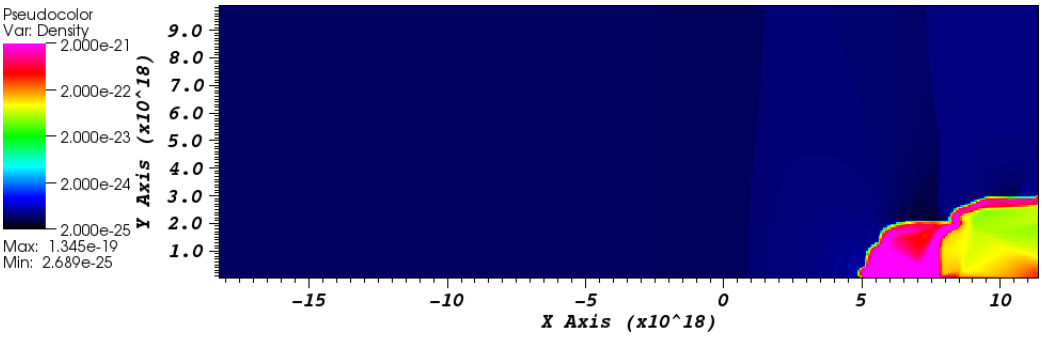

(e) $t = 291,000$ yr

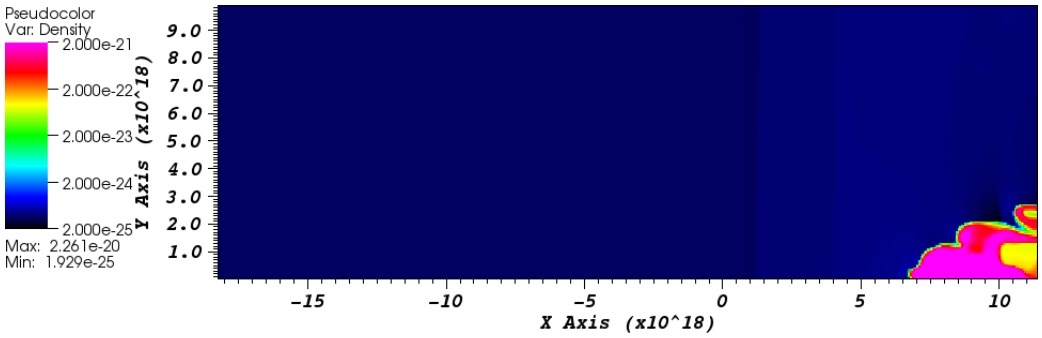

(f) $t = 359,000$ yr

Figure 4.12: 2D SN model of Model 2 - density is displayed as shell of a $1.0{\times}10^{52}$ erg SN collides with a clump embedded in the ISM. The legend displays mass density ($\mathrm{g{\cdot}cm^{-3}}$), which equates to max. $n = 981.6\,\mathrm{cm^{-3}}$ and min. $n = 0.0098\,\mathrm{cm^{-3}}$. [The x and y axis represent the distance from the centre of the clump at t= 0 s (in 10^{18} cm)]

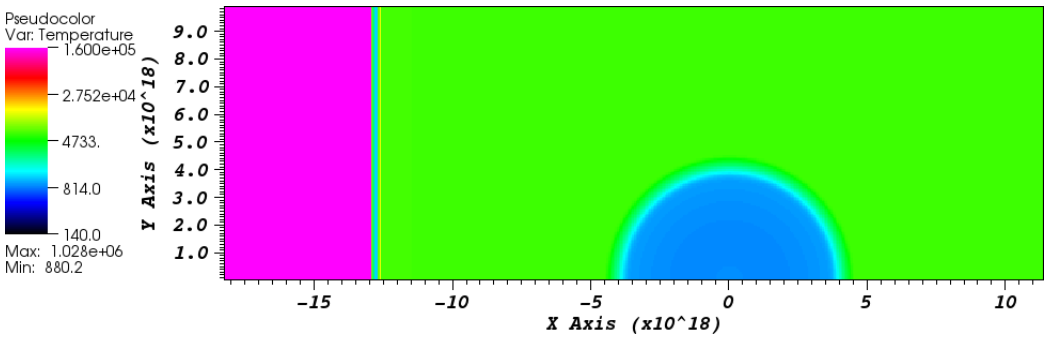

(a) $t = 0$ yr

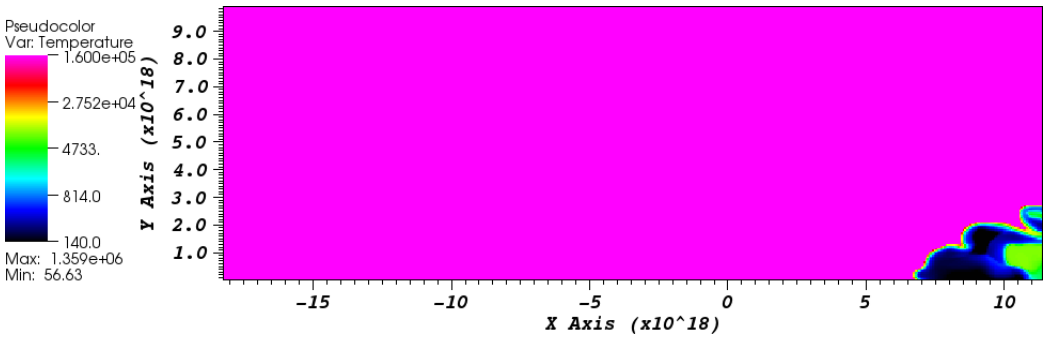

(b) $t = 359,000$ yr

Figure 4.13: 2D SN model of Model 2 - temperature of gas is displayed as shell of a 1.0×10^{52} erg SN collides with a clump embedded in the ISM. The legend displays temperature in Kelvin [The x and y axis represent the distance from the centre of the clump at t= 0 s (in 10^{18} cm)]

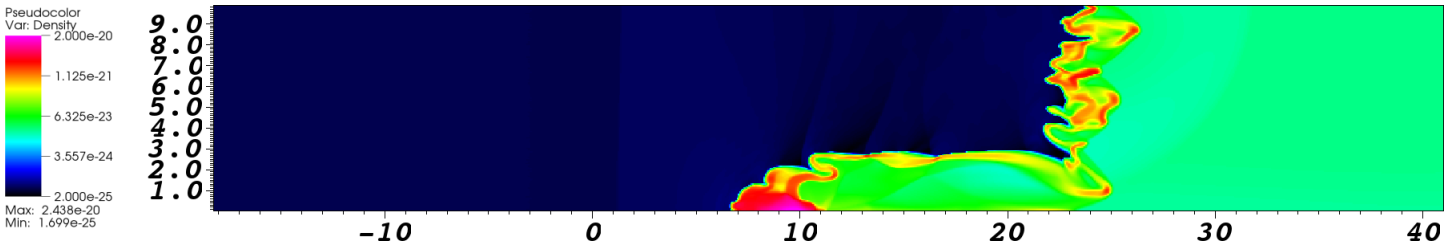

(a) $t = 359,000$ yr

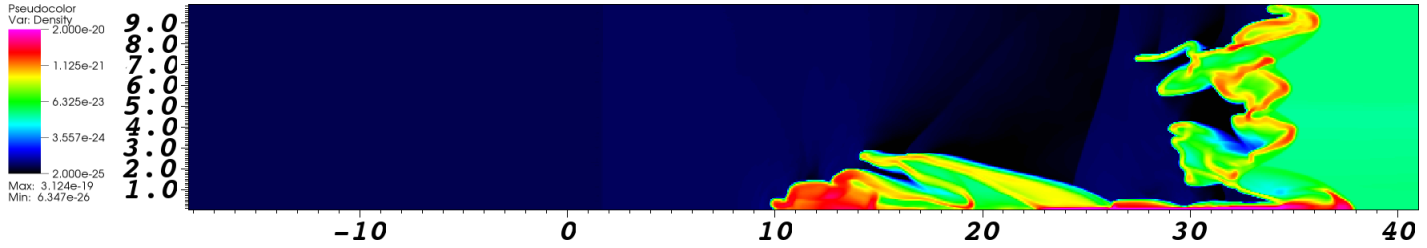

(b) $t = 466,000$ yr

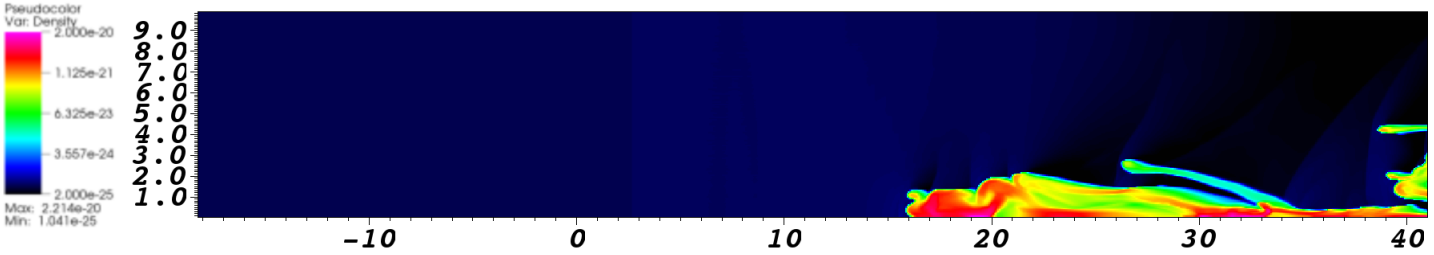

(c) $t = 635,000$ yr

Figure 4.14: 2D extended SN model of Model 2 - density is displayed as shell of a $1.0{\times}10^{52}$ erg SN collides with a clump embedded in the ISM. The legend displays mass density ($\mathrm{g{\cdot}cm^{-3}}$), which equates to max. $n = 981.6\,\mathrm{cm^{-3}}$ and min. $n = 0.0098\,\mathrm{cm^{-3}}$. [The x and y axis represent the distance from the centre of the clump at t= 0 s (in 10^{18} cm)]

4.2.3 Model 3

4.2.3.1 Phase 1: The H II region model

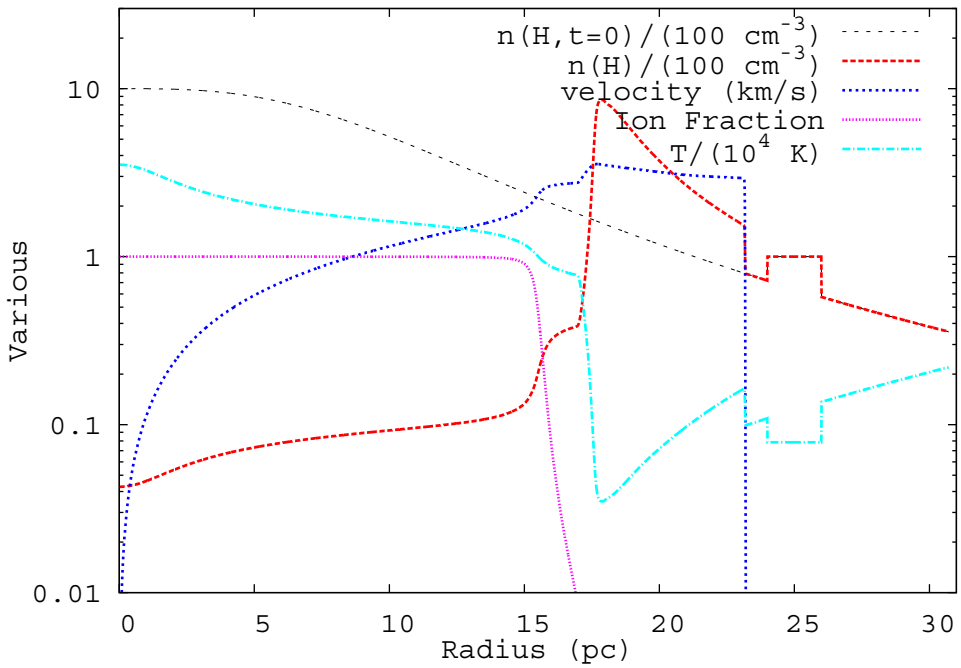

Figure 4.15: The H II model output for Model 3 - the initial density of the gas is shown in grey dashed line. The red line displays the density of the gas at 3.86×10^6 years, once the H II region has developed around the star. The star was modelled as a point source at x=0.

Next we want to investigate a much denser cloud, as it would be beneficial to see how the SN shell evolves once it interacts with a much denser ambient medium or H II shell before reaching the clump. Greif *et al.* (2010) simulate the formation of a dark matter halo of mass M$\sim 10^8$ M$_\odot$ from cosmological initial conditions and find that the maximum density of the gas is 100 cm^{-3}. It is unlikely a large cloud (radius $R \sim 50$ pc) with a constant density of 100 cm^{-3} can be stable against collapse, as the Jeans length at this density is $\sim$10 pc. Therefore large clouds ($\gtrsim 10$ pc) are unlikely to have a uniform density and will exhibit a density profile that can be described by a power-law i.e. $n \propto n_0(R/\mathrm{pc})^{-\alpha}$, where n_0 is the value of the central density and α is a constant. It is worth noting that due to resolution of the simulations by Greif *et al.* (2010), it is unlikely that they can resolve the clumping of gas that occurs at scales of $\sim$10 pc.

In this model we investigate a cloud with a central density of n_0 =1000 cm^{-3} and a power law of $\alpha = 3$. The slope of the density profile was chosen to reflect a high density gas cloud found

within a dark matter halo with a flat central profile (Kitayama & Yoshida 2005, M$\geq 10^7\,M_\odot$). Although this model can only be regarded as a simplistic or toy model, it will allow us to comment on the interaction of the SNR with a high density H II shell. The initial conditions for this model are displayed in Figure 4.15, the clump is placed 24 pc from the progenitor star. This is closer to the progenitor star than previous models, as the high density ambient medium would cause the formation of the radiative shell at much smaller distances. Due to the high density of the cloud, the ionisation front of H II region only extends to 15 pc and a very dense shell is formed between 18 – 23 pc. The clump does not interact with the ionising radiation or stellar winds. The clump has a temperature of 800 K and the H II shell has a minimum temperature of 300 K.

4.2.3.2 Phase 2: The 1D supernova - cloud model

In Figure 4.16, we see the evolution of a SNR with explosion energy 1.0×10^{52} erg. The SN shell reaches the H II shell after $\sim 32,500$ years at a velocity of around 400 km s^{-1} (Figure 4.16(b)). The H_2 fractional abundance in these H II shell and clump only amounts to $\sim 10^{-15}$, due to completely atomic initial conditions the formation of H_2 is caused by ionisation by cosmic rays. Hence the temperature has not changed much from the initial conditions. Results of the SN model after $\sim 155,000$ years, are displayed in Figure 4.16(c). The shock has travelled to ~ 20 pc and has compressed the H II shell against the clump. However after $\sim 246,000$ years (Figure 4.16(d)) the shock has only reached 22pc and is travelling at a velocity less than 10 km s^{-1}. Hence we can assume the SN shock has dissipated. The SN shell has compressed 50% of the clump within the former H II shell.

From the results of this model it can be seen that the shock pushes the H II shell back and does not 'break through' it to shock the clump. In this model we present the results for the highest explosion energy we consider; obviously, models with lower explosion energies would not reach the clump either. There is a very high density region ($\sim 10,000\,\mathrm{cm}^{-3}$) of the SN shell that can be seen in Figure 4.16(d), which may fragment. However, in reality a H II shell is made of many clouds that cannot be represented by a 1D model and requires multi-dimensional simulations (Dale *et al.* 2012).

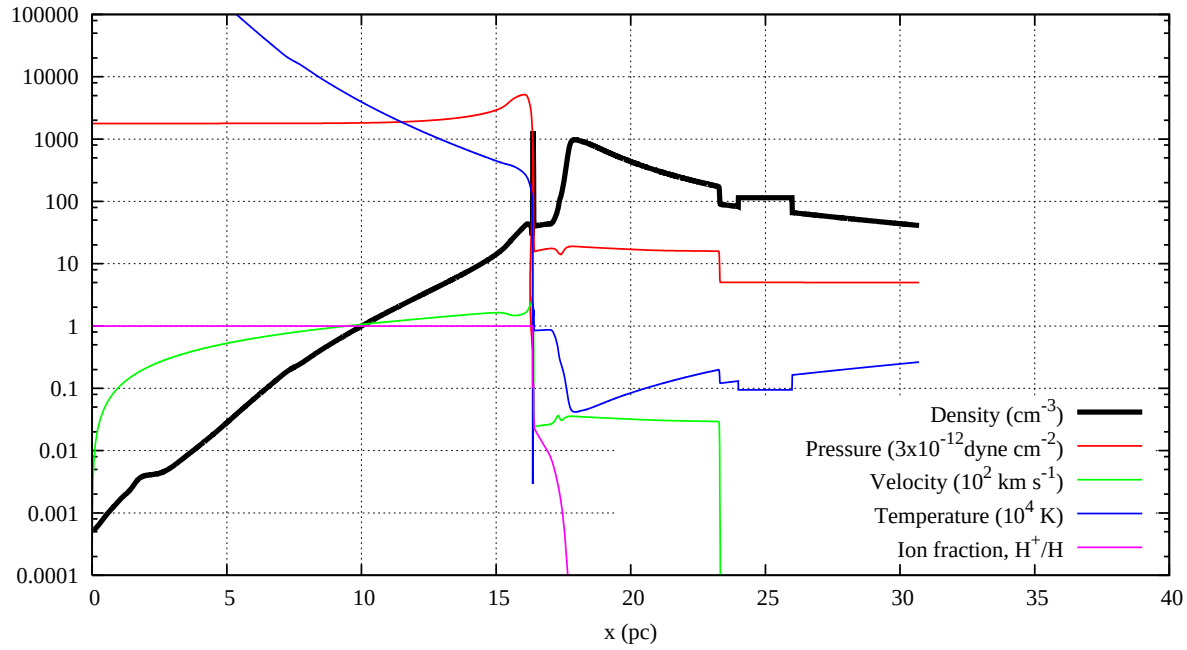

(a) $t = 21,000$ yr

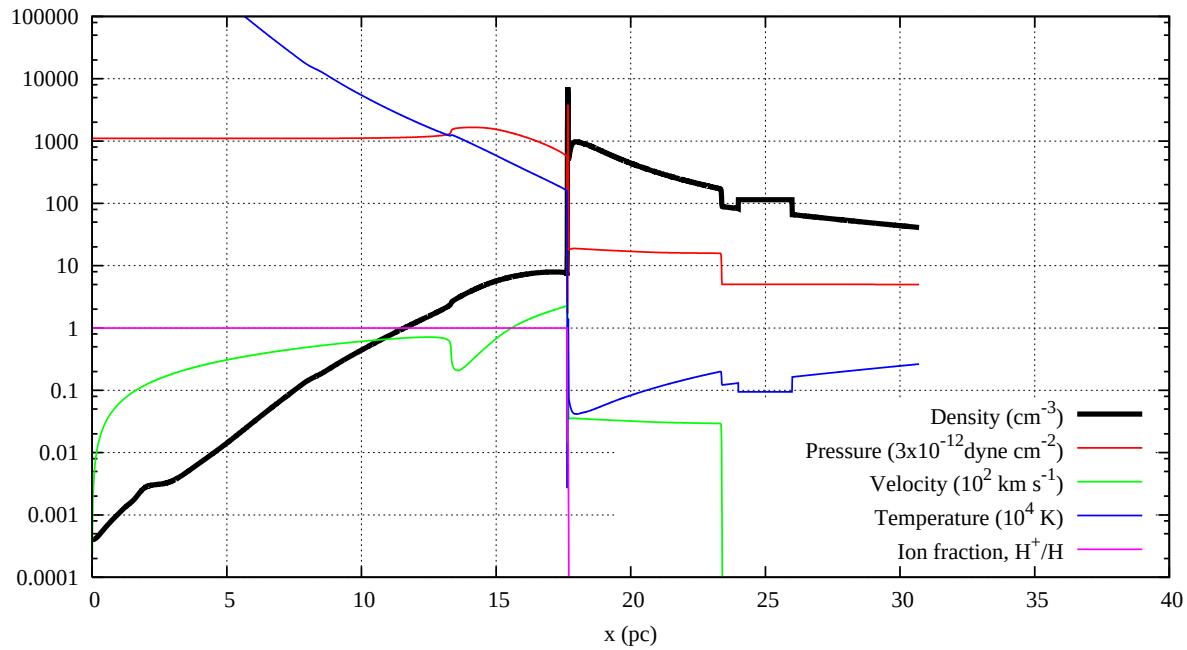

(b) $t = 33,000$ yr

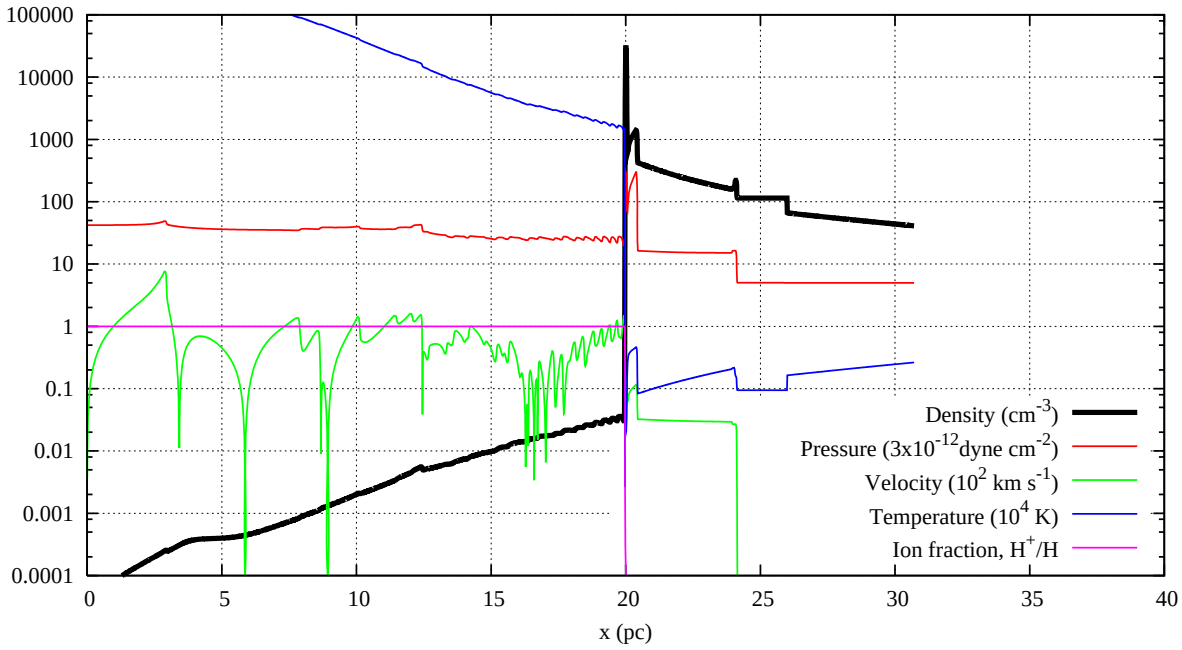

(c) $t = 155,000$ yr

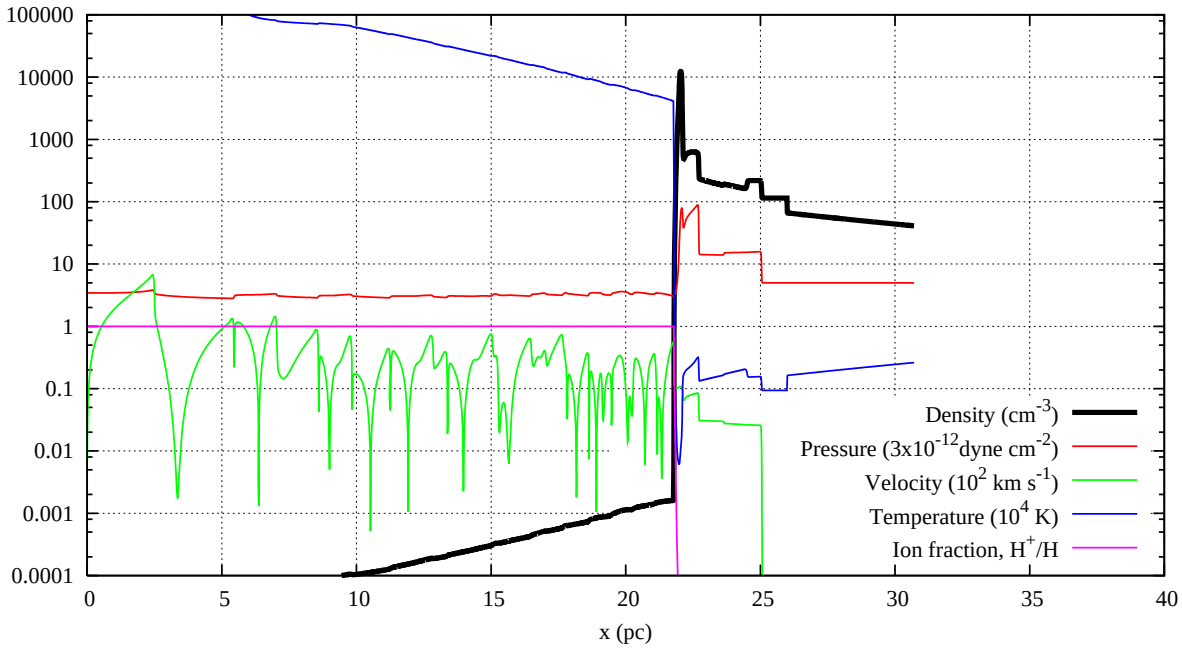

(d) $t = 246,000$ yr

Figure 4.16: Model 3 - The evolution of the SNR as it interacts with a high density H II shell. The explosion energy of the hypernova is 1.0×10^{52} erg.

4.2.4 Model 4

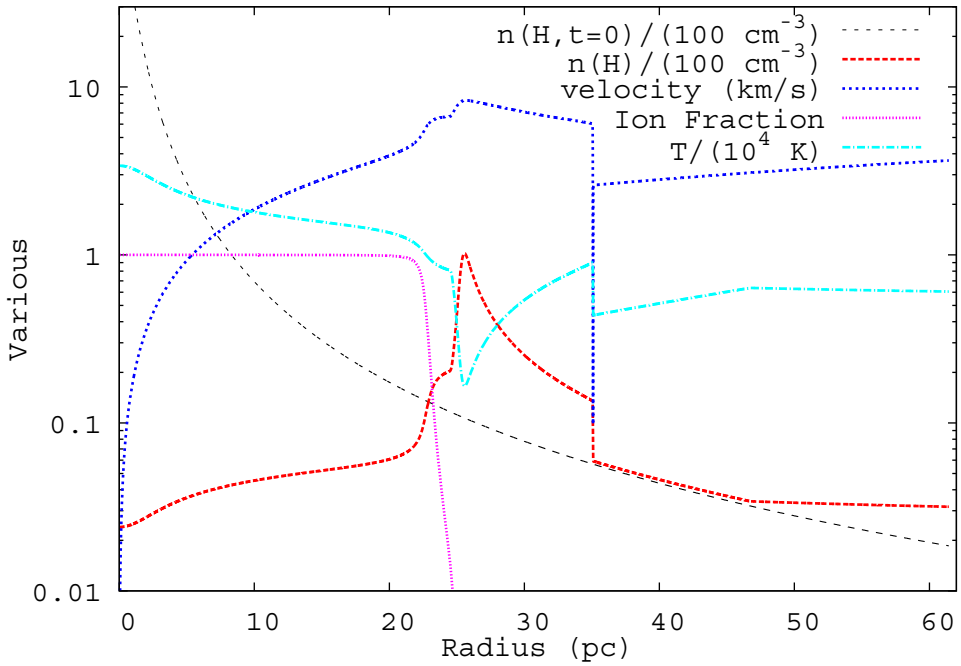

Figure 4.17: The H II model output for Model 4 - the initial density of the gas is shown in grey dashed line. The red line displays the density of the gas at 3.86×10^6 years, once the H II region has developed around the star. The star was modelled as a point source at x=0.) the final density profile of the gas is shown with the red dashed line.

4.2.4.1 Phase 1: The H II region model

We next consider the initial conditions from a cosmological simulation by Abel *et al.* (2007), which represents the gas profile found within a dark matter halo of mass 10^6 $M_\odot$ before star formation has occurred. Abel *et al.* (2007) simulate the formation of a H II region in this metal-free environment by a massive star (M$>$ 100 $M_\odot$) at redshift $z = 20$. Though it is possible that these mini-haloes are still present at lower redshifts, due to external affects (such as UV radiation, cosmic rays, gas accretion) the physical state of the gas may not be the same as it was at $z = 20$.

As a numerical experiment, we have investigated the initial conditions described by Abel *et al.* (2007) at redshift $z = 10$. The initial density profile can be approximated by $2000 \times (R/\mathrm{pc})^{-2}$, where R is the radius from the star. This gives us the opportunity to investigate the SN shell as it interacts with a H II shell that is less dense than the previous case explored in Model 3. Figure 4.17 displays the initial density profile of the cloud and the subsequent formation of a H II region

formed arounds a 40 $M_{\odot}$ metal-free star. The H II shell forms at 25 pc; it has a maximum density of $\sim 100\,\mathrm{cm}^{-3}$ and a minimum temperature of ~ 2000 K.

4.2.4.2 Phase 2: The 1D supernova model

The evolution of the SNR with an explosion energy of 2.0×10^{51} erg, is shown in Figure 4.18. Due to the high initial density, the SN shell forms at ∼18 pc (Figure 4.18(a)). After $\sim 127,000$ years the SN shell reaches the H II shell with a velocity of 110 km s^{-1}. Figure 4.18(d) displays the SNR after $\sim 800,000$ years, by which time the SN shell has pushed the H II region back to 35 pc. As the velocity of the shell is less than 10 km s^{-1}, we can assume the shell has terminated. The final maximum density ($\sim 1000\,\mathrm{cm}^{-3}$) of the shell is quite a bit lower than the maximum density of the shell in Model 3. The minimum temperature of the shell is 1000 K. Even though the H II shell has a lower density than in Model 3, the SN shock was not able to break through the H II shell. Again, 2D/3D simulations are needed to ascertain if the SN shock can pass through the H II shell and continue on to shock a clump.

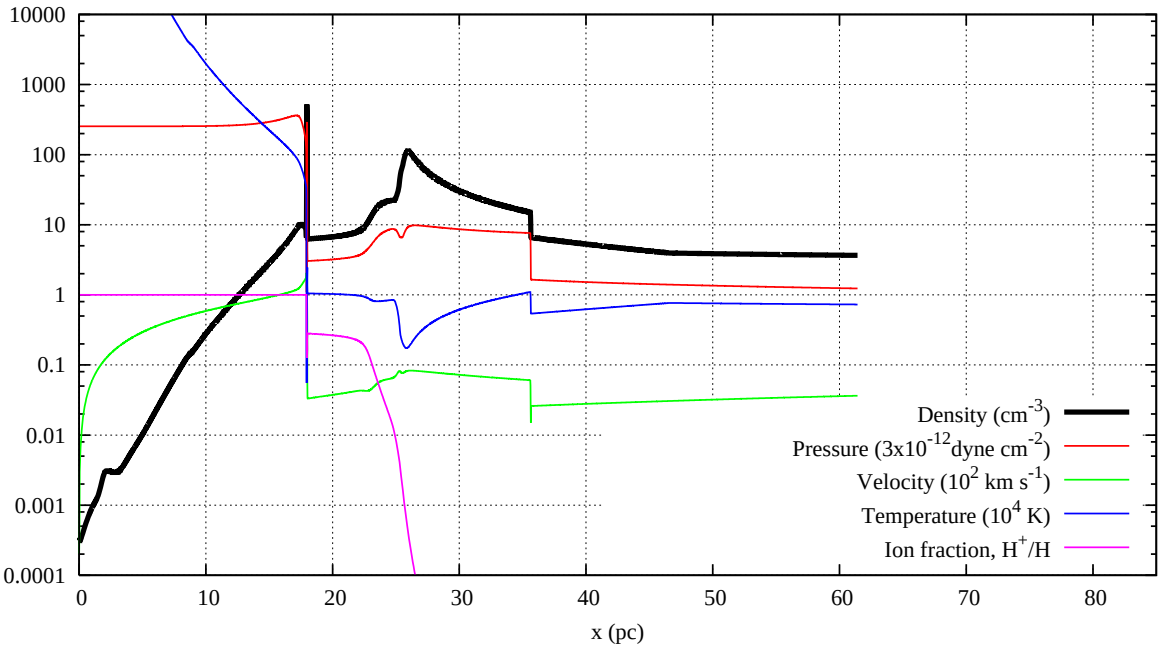

(a) $t = 43,000$ yr

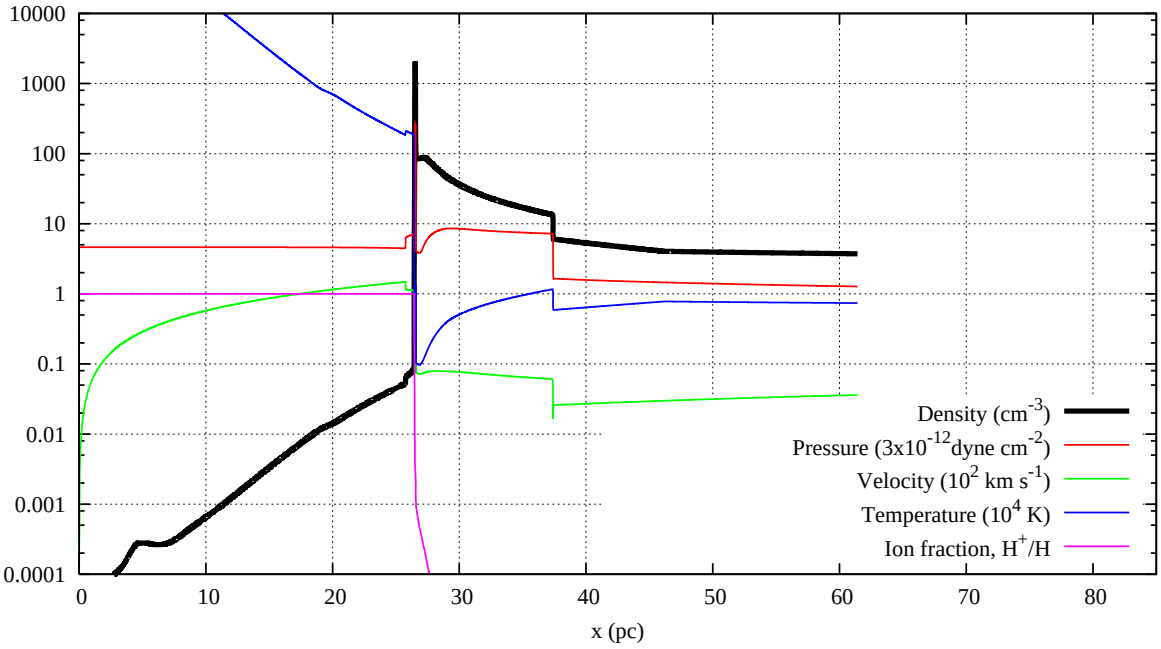

(b) $t = 127,000$ yr

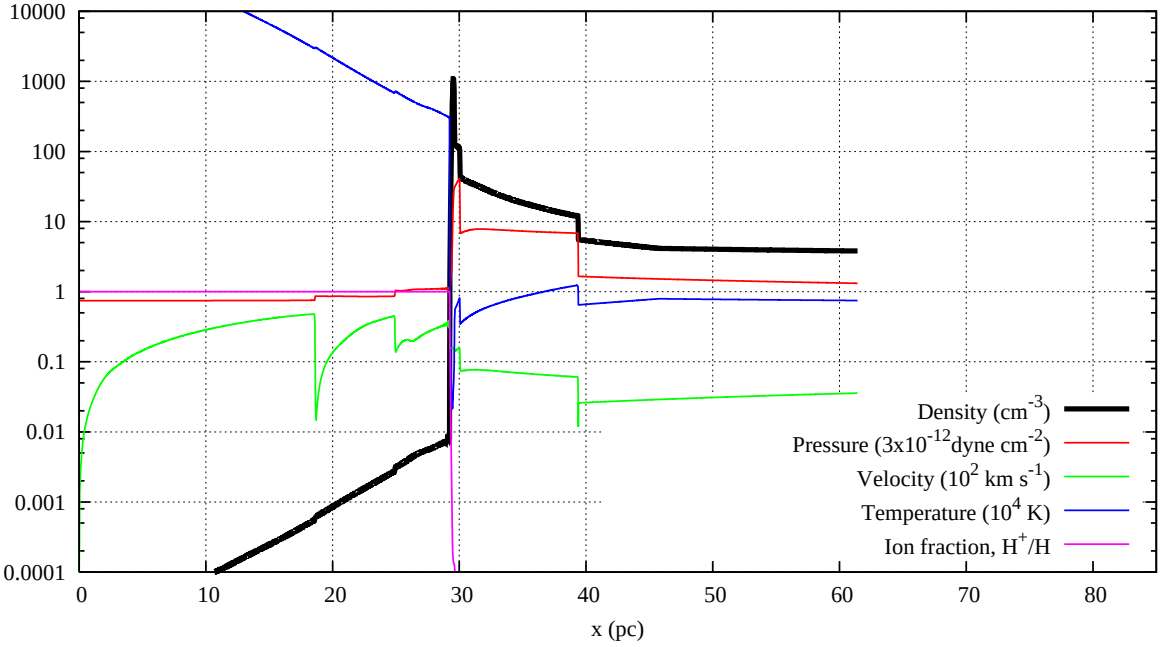

(c) $t = 317,000$ yr

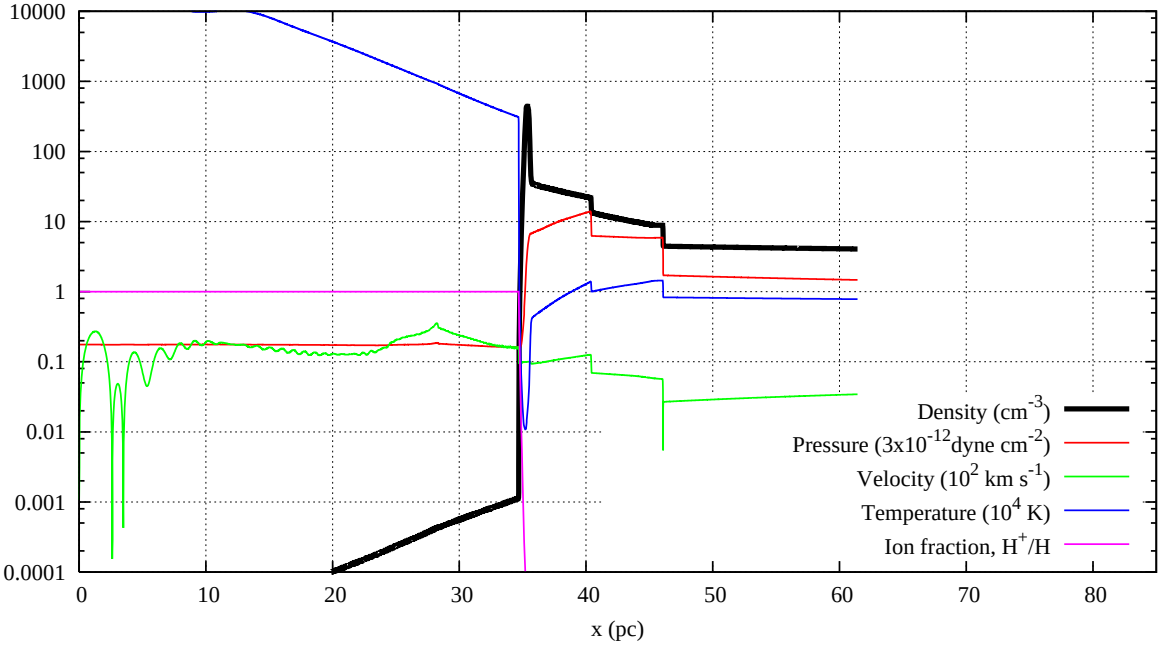

(d) $t = 800,000$ yr

Figure 4.18: Model 4 - 1D SN model with explosion energy 2.0×10^{51} erg

Model No	Supernova Energy (10^{51} erg)	Ambient cloud density (cm^{-3})	H II region included	Clump density (cm^{-3})	Temperature of clump (K)	Clump distance (pc)	Shock velocity (km s^{-1})	Clump fate
Model 2	10	10	Yes	100	872	46	39	compressed clump
Model 2	2.0	10	Yes	100	872	46	-	shell stalled
Model 2	1.0	10	Yes	100	872	46	-	shell stalled
Model 2	0.6	10	Yes	100	872	46	-	shell stalled
Model 1	10	1	No	100	200	50	200	destroyed
Model 1	2.0	1	No	100	200	50	46	small fragments
Model 1	1.0	1	No	100	200	50	26	destroyed
Model 1	0.6	1	No	100	200	50	16	destroyed
Toy model	1.0	1	No	100	200	40	49	small fragments

Table 4.1: This table presents the initial conditions of a number of 2D shock-cloud models and the corresponding fate of the clump at the end of the simulation. There are four end states of the clump: i) the clump is unaffected by the shock as the shell stalled before reaching the clump, ii) the clump is fully compressed into a single core, iii) the clump fragments into smaller dense pieces and iv) the clump no longer exists and is destroyed.

4.3 Discussion

We have modelled the evolution of a metal-free SN remnant (explosion energies: 0.6×10^{51}, 1.6×10^{51}, 2.0×10^{51} & 10^{52} erg) and its subsequent collision with a clump of density 100 cm^{-3} (radius = 1 pc) embedded within a range of clouds ($1\,\mathrm{cm}^{-3}$, $10\,\mathrm{cm}^{-3}$, $1000 \times R^{-3}\,\mathrm{cm}^{-3}$ & $2000 \times R^{-2}\,\mathrm{cm}^{-3}$, where R is the radius from the centre of the cloud). The pre-SN conditions were considered by including a H II region that would be produced by a 40 $\mathrm{M}_{\odot}$ metal-free star. The radiative cooling that dominates the shock-cloud interaction was captured by modelling the non-equilibirum chemistry that occurs at all stages of the SNR evolution.

It emerges when considering all the 2D shock-cloud models (listed in Table 4.1), that the velocity of the shock determines the fate of the neutral clump. If the shock is too fast the clump is destroyed. When the supernova shock is too slow, the clump is only slightly compressed but inevitably destroyed. This is because the initial shock causes a secondary shock to travel through the rest of the clump, finally the gas disperses and flows downstream with the supernova shock. We therefore find that a small range of shock velocities ($30 - 50$ km s^{-1}) which can cause the clump to compress or fragment. Here the cooling time is equal to or less than the collapse/compression time and the velocity of the shock causes at least half of the clump to be compressed. Shock velocities above 40 km s^{-1} cause the clump to fragment into smaller clumps, while below this velocity we find the clump is compressed.

Clumps formed in low density gas ($\leq 5\,\mathrm{cm}^{-3}$) within 45 pc of the progenitor 40 $\mathrm{M}_{\odot}$ star will be irradiated and therefore their thermal state will be different to the neutral clumps we simulate. Clouds found closer to the progenitor star may evaporate, or at a minimum, have a different thermal state to a neutral cloud. Radiation between 11.18 - 13.6 eV photodissociates H_2 molecules and so has a knock-on heating effect on the gas. This dissociation radiation propagates further than ionising radiation, and without any dust present we expect that the clumps are completely atomic in the pre-supernova stage. In the 2D model dissociative photons from the hot gas is assumed to be negligible (Vasiliev *et al.* 2008), but the possible effects of UV radiation on the clump should be investigated in more detail in future work.

When exploring initial conditions with non-uniform ambient densities (Model 3 & 4), we found that the 1D model is not sufficient to model the realistic interaction of a SNR and H II shell. This is because H II shells are comprised of many clouds and are not solid structures, therefore a SN shock can 'break through' to interact with the subsequent multiphase neutral medium. Including PDR

model of these H II regions could be a significant improvement (Haiman *et al.* 1997) and is a subject that should be considered for future work. It is also unlikely that a SN shell remains completely unmixed with ejecta materials, due to instabilities arising in the SN shell (Wang & Chevalier 2001; Blondin & Ellison 2001). Hence by the later stages of the SN remnant hydrodynamic instabilities become dominate, and when the SN shell fragments it is likely to be polluted by metals from the ejecta and so may be too enriched to form stars with a metallicity $Z \leq 10^{-5}$ $Z_{\odot}$ stars. Hence 1D models (without metal diffusion) may not be adequate to study the formation of the second generation of stars and multidimensional simulations of the SN remnant should be considered for future work.

The particular case of the hypernova explosion investigated in Model 2, compressed the clump to high densities. After the passage of the shock the dense cloud is embedded in the high pressure, hot, low density interior of the SN remnant. Our simulations do not have the spatial resolution to resolve the boundary layer between these two phases (each grid cell = 0.01×0.01 pc), we also do not include thermal conduction or model the external irradiation of the cloud, so the details of the boundary layer are probably not very reliable. However, the dominant physical process is the simple pressure confinement of the cloud. As the expansion timescale of the supernova $t_{exp} = R/\dot{R}$ is short compared to the local timescale for gravitational effects (the free-fall time $t_{ff} = 1/\sqrt{G\rho}$). This pressure confinement is well-captured by our calculation. When the cloud is accelerated off the original simulation domain and reached 48 pc from the progenitor star t$= 1.5 \times 10^{13}$ s (see Figure 4.14(b)), it enters an equilibrium phase of a pressure-confined cloud, similar to the cometary phase for irradiated clouds (Bertoldi & McKee 1990). The maximum density of the clump, it is close to 10^{5} cm^{-3} observed density of shocked clumps expected to form stars (Reach *et al.* 2005).

The shocked clump of model M01 implodes because of the passage of the supernova shock (Figure 4.12). This is the same behaviour seen in 3D simulations of clouds interacting with clumps (Melioli *et al.* 2006; Leão *et al.* 2009; Johansson & Ziegler 2013), and earlier 2D work (e.g. Klein *et al.* 1994). We find that in our simulation the clump gains a maximum density of ~ 78000 cm^{-3}, which is a density enhancement of $10^{2.89}$ but does not become Jeans unstable. Vaidya *et al.* (2013) show that self-gravity has no effect on the clump at this point of the shock interaction, where the implosion is pressure-driven and the clump reaches its maximum density. This gives us confidence that the implosion phase is correctly captured by our simulation. Johansson & Ziegler (2013) investigate the compression of a $n = 17\,\mathrm{cm}^{-3}$ cloud (with radius 1.5 pc) including a weak initial magnetic field and find higher densities enhancements of $10^{3} - 10^{5}$. They also conclude that the

clump will not become Jeans unstable. It is worth noting that their work considers solar metallicity gas with an equilibrium cooling function. Hence this may change when the model is refined to include non-equilibrium cooling.

Primordial supernovae pollute their surrounding environment with metals (Greif *et al.* 2010). Rayleigh-Taylor instabilities between the SN ejecta and shell of swept up material are known to develop, causing the mixing of the ejecta within the SN shell (Wang & Chevalier 2001). However these instabilities grow on times scales larger than the age of the SNR for the case we explore in Model 2 (hypernova explosion). Though the shock is not travelling in uniform density, the shell can be described as thin-shell i.e. where the radius of the shell is small in comparison to the shocked region. Vishniac (1983) states that when the shell can be described this manner it is stable to perturbations. Hence he describes the criterion for Rayleigh-Taylor instabilities as $k < 1/6\Delta R$ where k is the wavenumber and ΔR is the thickness of the shell. Even though we do not include metal diffusion within our model, it is therefore valid to model the swept up material within the shell as metal-free. Cen & Riquelme (2008) studied the metal enrichment of primordial gas contained in dark matter haloes (10^6, 10^7 $M_\odot$) interacting with a range of intergalactic shocks (10, 30,100 & 300 km s^{-1}) at redshift $z = 10$. The shocks are meant to originate from supernova explosions in larger 'galaxies'. They found that when the slower shocks (i.e. ≤ 30 km s^{-1}) collided with a spherical gas contained within a halo gas (500 cm^{-3}) it remained fairly uncontaminated (90 %). Although the scale is much larger than our own simulation the set up is similar, we can extrapolate that the dense clump formed in our model will remain mostly unaffected by metal pollution. Reach *et al.* (2002) suggest that due to the stripping of the outer layers, the pressure-driven cores formed by this method are likely to accrete less of the ejected SN material.

4.4 Conclusions

We have presented a metal-free shock-cloud model, which simulates a supernova remnant interacting with a cloud at redshift $z = 10$. We model the interaction of a supernova shell and a dense clump embedded in a range of cloud densities. We consider realistic pre-supernova conditions by including the effects of stellar radiation from a 40 $M_\odot$ metal-free star on the multi-phase neutral medium. At the end of the star's main-sequence lifetime, we investigate a range of explosion energies and follow the evolution of the supernova shell and its subsequent interaction with the dense clump. Radiative cooling is a crucial process in the shock-cloud interaction, allowing the formation of dense cold gas

that may be susceptible to gravitational collapse. During this process we have comprehensively modelled the radiative (non-equilibirum) cooling taking place.

We have investigated a hypernova interacting with a dense clump ($n = 100$ cm^{-3}, $r = 1$ pc) embedded in a 10 cm^{-3} ambient cloud and is 40 pc from the progenitor star. We followed the evolution of the supernova remnant and its interaction with the surrounding ionised and neutral medium. When the radiative shell interacts with the metal-free clump, the clumps reaches a maximum of density ~ 78000 cm^{-3}. This is a $10^{2.89}$ density enhancement and is consistent with Galactic shock-cloud models considering solar metallicity gas with equilibrium cooling functions. The clump undergoes a reduction in Jeans mass from 10^5 M$_\odot$ to 10^3 M$_\odot$, but does not become gravitationally unstable. Further work is required to ascertain the effects of X-rays and UV radiation on the clump during the supernova phase.

In this chapter, we found an optimal range of shock velocities ($30 - 50$ km s^{-1}) which compress small metal-free clouds. Below this range the cloud is slightly perturbed by the supernova shock and is not subject to any appreciable density enhancement. Above this range the clumps are destroyed, therefore the results by Mackey *et al.* (2003) are overoptimistic, as they assume the cloud survives a 200 km s^{-1} interaction. The shock is in its radiative phase when it collides with the dense clump. Hydrodynamic instabilities are likely to be more important than gravity in radiative supernova shells Vishniac (1983), especially once the shell has encountered neutral matter, hence 1D models (without metal diffusion) may not be adequate to study the formation of the second generation of stars. Consequently it is still an open question where these hyper metal poor stars form.

When investigating the hypernova in model 2, we have achieved an appreciable Jean mass reduction of a small dense clump and a density enhancement comparable to Galactic studies, by including non-equilibrium metal-free radiative cooling. Further refinement of this model by including low-metallicity chemistry and thermal models plus positive feedback effects from X-rays and UV radiation, may cause a further reduction in Jeans mass. Galactic models should be extended to include non-equilibrium cooling, as this work has shown that it is the dominant process in shock-cloud interactions.

CHAPTER 5

THE PRESSURE-DRIVEN FRAGMENTATION OF LOW-METALLICITY CLUMPS

5.1 Introduction

There is a consensus in the astrophysics community that the first population II stars were formed in the first galaxies (Bromm & Yoshida 2011). However, there is not a universal definition for what constitutes a 'First Galaxy' or protogalaxy. In the most basic sense a protogalaxy must be able to retain the ejecta of a supernova, so there can be sustained star formation. Simulations suggest that this would occur in dark matter haloes $10^7 - 10^8 M_\odot$ (Bromm & Yoshida 2011). Greif *et al.* (2010) model the diffusion of metals when a SN explosion occurs in a $10^8\,M_\odot$ halo, and found that the gas has a range of metallicities ($10^{-10} - 10^{-3}\,Z_\odot$) depending on its distance from the explosion site. With the presence of metals, metal-bearing molecules and dust, the gas is much more efficient at cooling than previous compositions, thereby allowing the fragmentation of gas to smaller masses and allowing formation of low mass stars.

In this chapter we explore the effect of metals on the shock-cloud interaction that can occurr within these protogalaxies. If a low-mass star i.e. $< 1 M_\odot$ could form in these protogalaxies, it has a life span larger than the age of the universe and would be present today. The extremely metal poor (EMP) stars and hyper metal poor (HMP) stars observed in the Galaxy are thought to be exactly these stars; i.e. their formation is triggered by a single primordial supernova. These stars carry invaluable information on the early chemical evolution of the Galaxy (Christlieb *et al.* 2002) and the chemical imprint of their progenitors (Joggerst *et al.* 2010). It was previously thought that

the formation of a sub-solar Population II star was dictated by a critical metallicity of Z$\sim 10^{-3}$ (Santoro & Shull 2006). However, the discovery of a low-mass star ($M < 0.8\ M_{\odot}$) with metallicity of Z $< 10^{-5}$ Z$_{\odot}$ in our Galactic Halo (Caffau *et al.* 2012), has challenged this view and highlighted the need to investigate the affect of microphysical processes such as dust cooling (Klessen *et al.* 2012). However, there is debate over the high (efficient) dust production rate required in metal-poor gas, to be able to form SDSS J1029+1729 (Silvia *et al.* 2010).

The simplicity of modelling the first metal-poor star no longer holds in low-metallicity environments at high redshift. The initial conditions for the formation of the first stars are cosmologically determined, and the relevant physical processes are well known. The second generation of star formation is more complicated and is qualitatively similar to present-day star formation. However, it is distinct not only because of the low level of metallicity but also because the state of the universe was very different. There are many unconstrained factors such as: degree of turbulence, strength of magnetic fields, the amount of dust present and background radiation fields. These factors drive both the microphysics and dynamics of the gas.

Nagakura *et al.* (2009) followed the evolution and fragmentation of a SN shell for a range of metallicities Z= 10^{-4} – 10^{-2} Z$_{\odot}$. The chemical evolution of 15 species was followed: H, H^{+}, H^{-}, H$_2$, H$_2^{+}$, HeH^{+}, He, He^{+}, He^{++}, e^{-}, D, D^{+}, D^{-}, HD, HD^{+}, C, C^{+}, O and O^{+}. The contribution to cooling by metals was neglected above T$> 10^{4}$ K and the cooling was obtained from atomic processes; below this temperature the cooling is obtained from H$_2$, HD, C, C^{+}, O & O^{+}. They assume the ambient medium is fully ionised, therefore neglect the interaction with the H II shell and neutral medium. They applied a linear perturbation analysis on the expanding shell and constrained the parameter range (ambient density, explosion energy, and metallicity) in which fragmentation of the shell occurs. They concluded, that for the explosion energy of 10^{51} ergs (10^{52} ergs), shell fragmentation occurs for ambient densities greater than 100 cm^{-3} (10 cm^{-3}, respectively). This is higher than previously predicted by primordial models such as Machida *et al.* (2005). Importantly, they found this condition had little dependence on the metallicity range examined.

The inclusion of dust has a huge impact on the fragmentation scales in low metallicity environments (Dopcke *et al.* 2011). Chiaki *et al.* (2013) developed an early universe (1D) supernova model, which considers a gas of metallicity 10^{-5} Z$_{\odot}$. This is followed up with a one-zone (point calculation) for the fragmentation stage of the shell. The cooling within the 1D SN model is treated differently for temperatures above and below 10^{4} K. At high temperatures (T$> 10^{4}$ K) they assume

the gas is in collisional ionisation equilibrium and utilise the cooling function by Sutherland & Dopita (1993). Below the temperature T= 10^4 K a metal-free non-equilibrium chemistry and cooling is followed; however, cooling from metal fine structure lines is calculated separately by assuming collisional ionisation equilibrium. The authors model the fragmentation stage of the SN shell using a point calculation, where a they follow a more complex chemical network of 29 species (e^-, H, H+, H^-, D, D^+, D^-, He, He^+, He^-, C, C^+, O, O^+, H_2, H_2^-, H_2^+, HD, HD^+, HD^-, OH, H_2O, H_2O^+, O_2, O_2^+, CO, CO^+, CO_2, and CO_2^+). The coolants included in this one-zone model are C^+, O, H_2, HD and dust. They conclude that the will shell fragment into clumps of density ($10^{18}\,\mathrm{cm}^{-3}$) and mass $10^{-3}\,\mathrm{M}_\odot$, which are possible star formation sites.

Galactic studies have shown that radiative cooling is important in shock-cloud interactions (Johansson & Ziegler 2013; Vaidya *et al.* 2013). Therefore to obtain realistic results non-equilibrium thermal models must be implemented to investigate the evolution of low-metallicity supernova remnants. and their subsequent interaction with dense clouds. It is crucial to include both dust and low-metallicity chemistry for the complete temperature range of the SN model. In this chapter we extend the previous SN model toy model (chapter 3), to include the full the non-equilibrium chemistry of and associated cooling from the following species: carbon and oxygen chemistry (i.e for all ionisation states), metal-bearing molecules and dust.

5.2 Model

We model a low-metallicity gas cloud being hit by a core collapse supernova shock (10^{51} erg), situated at the centre a large dark matter halo of mass $\geq 10^7\,\mathrm{M}_\odot$ at redshift $z = 10$. The clump ($n = 100\,\mathrm{cm}^{-3}$) is embedded 40 pc from the progenitor cloud, within ambient gas of density 1 cm^{-3}. This is the same environment described as the toy model in chapter 3, therefore further discussion on parameter choices can be found in section §3.2. The intention of this study is to compare the thermal affects of metal line cooling, metal based molecular cooling and dust cooling. We want to compare these models to the basic metal-free toy model and so we neglect the effect of cosmic rays. Greif *et al.* (2010) simulated the assembly of a dark matter halo of mass $10^8\,\mathrm{M}_\odot$, and included metal diffusion from a Pop III SN. At redshift $z = 10$ the centre of the halo consisted of well mixed neutral gas with a uniform metallicity of $10^{-3}\,\mathrm{Z}_\odot$. So we adopt this metallicity for the gas we consider.

Special attention is given to the microphysics involved, as the system is dominated by non-

equilbrium radiative cooling. The set up of the microphysics modules has been described in detail in section §3.2. There are three low-metallicity modules investigated. Each one extends the previous metal-free module with different metal chemical networks: i) all carbon and oxygen atoms and ions, ii) metal ions plus metal-bearing molecules, and iii) metal ions, metal-bearing molecules and carbonaceous dust. This is to ascertain which chemical species is the dominant coolant (metal line cooling, metal-bearing molecular cooling, or dust cooling) in the shock-cloud interaction. Details of each low-metallicity module are described in the section below (§5.2.1).

5.2.1 The microphysics modules

The chemical and thermal evolution of the gas is followed by solving the following set of equations:

$$\begin{aligned} \frac{\partial E}{\partial t} &= -\Lambda(\Sigma x_m, \mathrm{T}) + \Lambda(\Sigma x_m, \mathrm{T_{CMB}}), \\ \frac{\partial x_i}{\partial t} &= C_i\left(x_j, \mathrm{T}\right) - D_i\left(x_j, \mathrm{T}\right) x_i, \end{aligned}$$

where E is the internal energy density (in erg cm^{-3}), Λ is the cooling function of the gas (in erg cm^{-3} s^{-1}), x_i is the fractional abundance of a chemical species, i, for a total number of chemical species N_{s}, T is the temperature of the gas, $\mathrm{T_{CMB}}$ is the temperature of the cosmic microwave background (CMB), C is the formation rate of the species and D is the destruction rate of the species.

Fang & Cen (2004) found that the amount of carbon and oxygen present in low-metallicity gas determines the transition from Population III to Population II stars, and not necessarily the total amount of "metals". Hence, in this low-metallicity model we only include oxygen and carbon. The atomic species plus electrons are treated as conservation equations which have values of x_{H}=1.0, $x_{\mathrm{He}} = 0.08$, $x_{\mathrm{C}} = 2.69 \times 10^{-4} \times (\mathrm{Z}/\mathrm{Z}_{\odot})$, $x_{\mathrm{O}} = 4.90 \times 10^{-4} \times (\mathrm{Z}/\mathrm{Z}_{\odot})$ and $x_{e^-} = 0.0$. Here Z is the metallicity of the gas and $\mathrm{Z}_{\odot}$ is solar metallicity. The fractional abundances of carbon and oxygen (i.e. the ratio carbon/oxygen nuclei and hydrogen nuclei) were obtained from Asplund *et al.* (2009) and Bayet *et al.* (2012). The total number of chemical species is different for all the three models and are described below; each module includes the metal-free chemical reactions R01-R36 listed in section §3.3.1 and associated cooling described in section §3.3.2.

5.2.1.1 Metal-ion model

H	He	H_2	H^+	H_2^+	H_3^+
HeH^+	He^+	He^{++}	H^-	C	C^+
C^{++}	C^{3+}	C^{4+}	C^{5+}	C^{6+}	O
O^+	O^{++}	O^{3+}	O^{4+}	O^{5+}	O^{6+}
O^{7+}	O^{8+}				

Table 5.1: The chemical species in the metal-ion model, where the number in superscript denotes the ionisation number of the metal species.

To investigate metal-line cooling on the low-metallicity shock-cloud model, this module includes metal ion chemistry and cooling at all temperatures from carbon & oxygen species. All ionisation states are included as C^+, C^{++} , O^+ and O^{++} are shown to be dominant coolants at high temperatures T$\sim 10^5 - 10^6$ K for shocks in the Milky Way (Raga *et al.* 2002); importantly the correct abundances can only be calculated if all ionisation states are considered.

The 27 species included in this module are listed in Table 5.1. The chemical network of 72 reactions consists of R01-R36 (Table 3.1) and the metal-ion reactions M01-M28 (Table 5.2). In this model the metal species only react with electrons and not with other atomic species. The reaction rates for the metal ion reactions are obtained from Voronov (1997) and Badnell (2006), and were extended beyond their maximum temperature range (10^8 K) by keeping the maximum value constant.

The thermal model is extended from §3.3.2 to include collisional excitation of the metal species. The cooling functions are obtained from a mixture of look up tables and analytic fits from Raga *et al.* (1997, 2002) which are valid for T$\leq 10^6$ K (listed in Table 5.5). The collisional ionisation cooling functions are all (bar one) via electronic collisions. The Bremsstrahlung cooling from the metal ions is also taken into account (Shapiro & Kang 1987).

	Reaction	Reference for rate
M01	$C + e^- \rightarrow C^+ + e^- + e^-$	V
M02	$C^+ + e^- \rightarrow C^{++} + e^- + e^-$	V
M03	$C^{++} + e^- \rightarrow C^{3+} + e^- + e^-$	V
M04	$C^{3+} + e^- \rightarrow C^{4+} + e^- + e^-$	V
M05	$C^{4+} + e^- \rightarrow C^{5+} + e^- + e^-$	V
M06	$C^{5+} + e^- \rightarrow C^{6+} + e^- + e^-$	V
M07	$C^+ + e^- \rightarrow C + photon$	B
M08	$C^{++} + e^- \rightarrow C^+ + photon$	B
M09	$C^{3+} + e^- \rightarrow C^{++} + photon$	B
M10	$C^{4+} + e^- \rightarrow C^{3+} + photon$	B
M11	$C^{5+} + e^- \rightarrow C^{4+} + photon$	B
M12	$C^{6+} + e^- \rightarrow C^{5+} + photon$	B
M13	$O + e^- \rightarrow O^+ + e^- + e^-$	V
M14	$O^+ + e^- \rightarrow O^{++} + e^- + e^-$	V
M15	$O^{++} + e^- \rightarrow O^{3+} + e^- + e^-$	V
M16	$O^{3+} + e^- \rightarrow O^{4+} + e^- + e^-$	V
M17	$O^{4+} + e^- \rightarrow O^{5+} + e^- + e^-$	V
M18	$O^{5+} + e^- \rightarrow O^{6+} + e^- + e^-$	V
M19	$O^{6+} + e^- \rightarrow O^{7+} + e^- + e^-$	V
M20	$O^{7+} + e^- \rightarrow O^{8+} + e^- + e^-$	V
M21	$O^+ + e^- \rightarrow O + photon$	B
M22	$O^{++} + e^- \rightarrow O^+ + photon$	B
M23	$O^{3+} + e^- \rightarrow O^{++} + photon$	B
M24	$O^{4+} + e^- \rightarrow O^{3+} + photon$	B
M25	$O^{5+} + e^- \rightarrow O^{4+} + photon$	B
M26	$O^{6+} + e^- \rightarrow O^{5+} + photon$	B
M27	$O^{7+} + e^- \rightarrow O^{6+} + photon$	B
M28	$O^{8+} + e^- \rightarrow O^{7+} + photon$	B

Table 5.2: Metal-ion reactions: V= Voronov (1997), B= Badnell (2006)

5.2.1.2 Metal-molecule model

H	He	H_2	H^+	H_2^+	$H_3{}^+$
HeH^+	He^+	He^{++}	H^-	C	C^+
C^{++}	C^{3+}	C^{4+}	C^{5+}	C^{6+}	O
O^+	O^{++}	O^{3+}	O^{4+}	O^{5+}	O^{6+}
O^{7+}	O^{8+}	CH	OH	CO	H_2O
O_2	CH^+	OH^+	CO^+	H_2O^+	H_3O^+
O_2^+					

Table 5.3: The chemical species in the metal-molecule model, where the number in superscript denotes the ionisation number of the species.

Next we extend the previous model by allowing the metal ions and primordial species to react, and therefore form metal-bearing molecules. We limit the species that we follow to the 33 species displayed in Table 5.3. We focus on the cooling from CO , OH and H_2O which are known to be dominant molecular coolants in local ISM shocks (Hollenbach & McKee 1979). These molecules could be important in low-metallicity shock-cloud interactions, and therefore we can compare this model with the previous model to ascertain if these molecules are dominant contributors to thermal state of the gas.

This module includes the main formation and destruction pathways for the molecules CO, OH and H_2O. Hence the chemical network is composed of 135 reactions: metal-free reactions R01-R36 (Table 3.1) and metal ion reactions (Table 5.2) and metal-bearing molecule reactions M29-M99 (Table 5.4). The exact treatment of the metal-bearing molecular reaction rates to cover the temperature range $10 - 10^9$ K, is presented in the appendix. The cooling functions we utilise for CO, OH and H_2O (valid for temperatures T$\leq 5.0 \times 10^4$K) were obtained from Hollenbach & McKee (1979, 1989) and are listed in Table 5.5.

	Reaction	Reference for rate
M29	$H + CH \rightarrow C + H_2$	UM06
M30	$H + OH \rightarrow H_2 + O$	UM06
M31	$H + H_2O \rightarrow H_2 + OH$	UM06
M32	$H + CO \rightarrow OH + C$	UM06
M33	$H + O_2 \rightarrow OH + O$	UM06
M34	$H_2 + OH \rightarrow H_2O + H$	UM06
M35	$OH + OH \rightarrow H_2O + O$	UM06
M36	$C + OH \rightarrow CO + H$	UM06
M37	$C + O_2 \rightarrow CO + O$	UM06
M38	$C + CO^+ \rightarrow CO + C^+$	UM06
M39	$C + H_2 \rightarrow CH + H$	UM06
M40	$O + CH \rightarrow CO + H$	UM06
M41	$O + OH \rightarrow O_2 + H$	UM06
M42	$O + H_2 \rightarrow OH + H$	UM06
M43	$O + H \rightarrow OH + photon$	UM06
M44	$O + O \rightarrow O_2 + photon$	UM06
M45	$C + O \rightarrow CO + photon$	UM06
M46	$C + H \rightarrow CH + photon$	UM06
M47	$H^+ + CH \rightarrow CH^+ + H$	UM06
M48	$H^+ + O \rightarrow O^+ + H$	UM06
M49	$H^+ + OH \rightarrow OH^+ + H$	UM06
M50	$H^+ + H_2O \rightarrow H_2O^+ + H$	UM06
M51	$H^+ + O_2 \rightarrow {O_2}^+ + H$	UM06
M52	$C^+ + OH \rightarrow CO^+ + H$	UM06
M53	$C^+ + O_2 \rightarrow O^+ + CO$	UM06
M54	$C^+ + CH \rightarrow CH^+ + C$	UM06
M55	$O^+ + H \rightarrow H^+ + O$	UM06
M56	$CO^+ + H \rightarrow H^+ + CO$	UM06
M57	$CH^+ + H \rightarrow C^+ + H_2$	UM06
M58	$O^+ + H_2 \rightarrow OH^+ + H$	UM06
M59	$C^+ + H_2 \rightarrow CH^+ + H$	UM06

	Reaction	Reference for rate
M60	$OH^+ + H_2 \rightarrow H_2O^+ + H$	UM06
M61	$H_2O^+ + H_2 \rightarrow H_3O^+ + H$	UM06
M62	$OH^+ + e^- \rightarrow O + H$	UM06
M63	$H_2O^+ + e^- \rightarrow OH + H$	UM06
M64	$H_2O^+ + e^- \rightarrow O + H + H$	UM06
M65	$H_3O^+ + e^- \rightarrow H_2O + H$	UM06
M66	$H_3O^+ + e^- \rightarrow OH + H + H$	UM06
M67	$O_2^+ + e^- \rightarrow O + O$	UM06
M68	$CH^+ + e^- \rightarrow C + H$	UM06
M69	$CO + e^- \rightarrow O + C + e^-$	UM06
M70	$CO + H \rightarrow O + C + H$	UM06
M71	$H_2O + H \rightarrow OH + H + H$	UM06
M72	$H_2O + H_2 \rightarrow OH + H + H_2$	UM06
M73	$CH + H_2 \rightarrow H_2 + C + H$	UM06
M74	$O_2 + H \rightarrow O + O + H$	UM06
M75	$He^+ + O_2 \rightarrow O^+ + O + He$	UM06
M76	$He^+ + CH \rightarrow H^+ + H + He$	UM06
M77	$He^+ + OH \rightarrow O^+ + H + He$	UM06
M78	$He^+ + CO \rightarrow C^+ + O + He$	UM06
M79	$He^+ + H_2O \rightarrow H^+ + OH + He$	UM06
M80	$H_2^+ + C \rightarrow CH^+ + H$	UM06
M81	$H_2^+ + O \rightarrow OH^+ + H$	UM06
M82	$H_3^+ + O \rightarrow H_2O^+ + H$	UM06
M83	$H_3^+ + C \rightarrow CH^+ + H_2$	UM06
M84	$H^- + O \rightarrow OH + e^-$	UM06
M85	$H^- + C \rightarrow CH + e^-$	UM06
M86	$H^- + OH \rightarrow H_2O + e^-$	UM06
M87	$H^- + C^+ \rightarrow H + C$	UM06
M88	$H^- + O^+ \rightarrow H + O$	UM06
M89	$CO^+ + e^- \rightarrow C + O$	UM06
M90	$H_2^+ + CO \rightarrow CO^+ + H_2$	UM06

	Reaction	Reference for rate
M91	$CH + e^- \rightarrow C + H + e^-$	UM06*
M92	$OH + e^- \rightarrow O + H + e^-$	UM06*
M93	$CH^+ + e^- \rightarrow C^+ + H + e^-$	UM06*
M94	$OH^+ + e^- \rightarrow O^+ + H + e^-$	UM06*
M95	$CO^+ + e^- \rightarrow C + O^+ + e^-$	UM06*
M96	$H_2O + e^- \rightarrow H + OH + e^-$	UM06*
M97	$H_2O^+ + e^- \rightarrow H^+ + OH + e^-$	UM06*
M98	$H_3O + e^- \rightarrow H_2 + OH + e^-$	UM06*
M99	$H_3O^+ + e^- \rightarrow H_2 + OH^+ + e^-$	UM06*

Table 5.4: Metal-molecule reactions: UM06 = UMIST 06 database (*=adapted to cover temperature range $10 - 10^9$ K, see appendix)

Cooling Process	Collisional Partner	Reference
Metal-ion cooling: Collisional excitation		
OI	H, e^-	Raga *et al.* (1997, 2002)
OII	e^-	Raga *et al.* (1997, 2002)
OIII	e^-	Raga *et al.* (1997)
OIV	e^-	Raga *et al.* (1997)
OV	e^-	Raga *et al.* (1997)
CI	e^-	Raga *et al.* (1997)
CII	e^-	Raga *et al.* (1997, 2002)
CIII	e^-	Raga *et al.* (1997, 2002)
CIV	e^-	Raga *et al.* (1997)
Metal-ion cooling: Bremstrahlung cooling		
OII, OIII, OIV, OV, OVI, OVII, OVIII, OIX		Shapiro & Kang (1987)
CII, CIII, CIV, CV, CVI, CVII		Shapiro & Kang (1987)
Molecular cooling:		
CO -rotational cooling	H	Hollenbach & McKee (1979)
CO -vibrational cooling	H, H_2	Hollenbach & McKee (1979, 1989)
OH -rotational cooling	H	Hollenbach & McKee (1979)
H_2O-rotational cooling	H	Hollenbach & McKee (1979)
H_2O-vibrartional cooling	H, H_2	Hollenbach & McKee (1979, 1989)
Dust cooling:		
Collisional heating rate (T$> 10^5$ K)	e^-	Dwek & Werner (1981)
Collisional heating rate (T$\leq 10^5$ K)	H, H^+, e^-	Hollenbach & McKee (1979)
Cooling rate		Dwek & Arendt (1992)

Table 5.5: Metal Cooling processes for all three models

5.2.1.3 Metal-dust model

Finally we investigate the effects of dust cooling by extending the metal-ion model to include dust cooling and H_2 formation on the grain surface. We implement a simple dust model, in which we neglect the effects of grain destruction and the radiative heating of dust grains due to UV. We assume that all the dust grains have a radius of $a = 0.1\,\mu$m. Hence we can neglect the stochastic heating of small dust grains and assume thermal equilibrium for all the grains present. To calculate the dust temperature (T_{gr}) we numerically solve the following energy balance equation:

$$H_{coll}(a, T, T_{gr}, n) = L_{gr}(a, T_{gr}) \tag{5.1}$$

where H_{coll} (erg s^{-1}) is the collisional heating of the grain, and L_{gr} (erg s^{-1}) is the cooling rate by radiative emission of the dust grain (both are detailed below).

At high temperatures (T$> 10^5$ K) we assume that electron collisions dominate over protons, because for the same energy the electrons have higher velocities implying a higher collisional rate (Montier & Giard 2004). We use the electronic collisional heating rate obtained by Dwek & Werner (1981):

$$H_{coll}(a, T_e, n_e) = \begin{cases} 5.38 \times 10^{-18} n_e a^2 T_e^{\frac{3}{2}}, & x^* > 4.5 \\ 3.37 \times 10^{-13} n_e a^{2.41} T_e^{0.88}, & x^* > 1.5 \\ 6.48 \times 10^{-6} n_e a^3 & x^* \leq 1.5 \end{cases} \tag{5.2}$$

where $a(\mu\text{m})$ is the grain radius, $n_e(\text{cm}^{-3})$ is the electronic density, T_e(K) is the electronic temperature (which is assumed to equal to the gas temperature) and $x^* = 2.71 \times 10^8 a^{\frac{3}{2}}/T_e$. For temperatures below T$\leq 10^5$ K, the rate at which energy is transferred from the gas to the dust grain via collisions is given by (Hollenbach & McKee 1979)

$$H_{coll}(T, T_{gr}, n) = n_{\text{H}} \bar{\sigma_{gr}} v_p f (2k_b \text{T} - 2k_b \text{T}_{gr}), \tag{5.3}$$

where n_H is the number density of hydrogen nuclei, $\bar{\sigma_{gr}}$ is the mean dust grain cross section, v_p is the thermal speed of the proton [$= (8k_bT/\pi m_p)^{0.5}$], and f is a factor accounting for the contribution of species other than protons, as well as for charge and accommodation effects. We assume that $\bar{\sigma_{gr}}$ is the same as for Milky Way dust ($\approx 2.1 \times 10^{-21}\,\text{cm}^2$, Walmsley 1991) and the number density of dust is the value of local ISM number density Herbst (1993) scaled with

metallicity, i.e. the fractional abundance is $x_{gr} = 10^{-12} \times Z/Z_{\odot}$.

The cooling rate of a single dust grain via thermal infrared emission is given by Dwek & Arendt (1992)

$$\begin{aligned}\Lambda_{gr}(a, T_{gr}) &= 4\pi a^2 \int_0^{\infty} \pi B_v(T_{gr}) Q_v(a) dv \\ &= 4\pi a^2 \sigma_B T_{gr}^4 < Q(T_{gr}) >, \end{aligned} \tag{5.4}$$

where v is the frequency, Q_v is the absorption coefficient, B_v is the Plank function, σ_B is the Stephan-Boltzmann constant and $< Q(T_{gr}) >$ is Planck-averaged absorption coefficient. For dust temperatures $T_{gr} \leq 70$ K, Dwek & Arendt (1992) obtain a value of $< Q(T_{gr}) > /a(cm) \approx 0.16 T_{gr}^{1.94}$, which is independent of grain size and composition. To be consistent with the carbon chemistry of our model, we assume the dust grain composition is graphite. Dwek (1987) showed that for graphite dust grains with a=0.1 μm, the dust temperature remains under 70 K for temperatures $10^6 - 10^9$ K.

We need to include heating effects from the Cosmic Microwave Background (CMB). If we assume $Q < a >$ is the same for emission and absorption, we can treat the right handside of the equation (5.1) in the following manner:

$$L_{gr} = 4\pi a^2 < Q(T_{gr}) > (T_{gr}^4 - {T_{CMB}}^4). \tag{5.5}$$

Once the dust temperature is calculated we can determine the dust cooling function, which is equation (5.4) multiplied by the number density of dust grains. For a gas with metallicity of 10^{-3} $Z_{\odot}$ the number density of dust grains is 10^{-15} cm^{-3}.

In the local interstellar medium (ISM), H_2 formation occurs on grain surfaces, permitting three-body reactions that are much more efficient than gas-phase reactions (Gould & Salpeter 1963). We extend the metal-ion chemical network (Table 5.2) by adding the following reaction:

$$H + H + \text{dust grain} \rightarrow H_2 + \text{dust grain (M00)}$$

which represents the formation of molecular hydrogen on dust grain surfaces. The rate (K_{M00})

adapted for low-metallicity environments is given by Glover & Jappsen (2007):

$$K_{\rm M00} = 3.0 \times 10^{-18} {\rm T}^{0.5} \left({\rm D/D_{\odot}}\right) \left[1.0 + 4 \times 10^{-2} \left({\rm T} + {\rm T_{gr}}\right)^{0.5} + 2 \times 10^{-3} {\rm T} + 8 \times 10^{-6} {\rm T}^{2}\right]^{-1} \left[1.0 + 10^{4} {\rm exp}\left(-600/{\rm T_{gr}}\right)\right]^{-1}$$

where $\rm T_{gr}$ is the dust temperature, D is the dust-to-gas ratio and $\rm D_{\odot}$ is the dust-to-gas ratio in the local ISM ($z = 0$). Following Glover & Jappsen (2007), we assume that $\rm D/D_{\odot} = Z/Z_{\odot}$. This reaction rate is cut off at $\rm T = 10^4$ K (see appendix). So the chemical network consists of the species displayed in Table 5.1 and 73 reactions (R01-R36 and M00-M28).

5.3 Results

We have investigated the effect of metal ions and metal-bearing molecules on the compression and fragmentation of a clump by a supernova shell (10^{51} erg). The initial conditions for the 1D model are as follows: the neutral cloud (100 $\rm cm^{-3}$, 200 K and 40 pc from the progenitor star) is embedded is low density (1 $\rm cm^{-3}$, 10^4 K) gas. The ambient gas is assumed to be completely ionised (i.e. $\rm x_{H^+} = 1.0$, $\rm x_{He^+} = 0.08$, $\rm x_{O^+} = 4.9 \times 10^{-7}$ and $\rm x_{C^+} = 2.69 \times 10^{-7}$). The gas at redshift $z = 10$ is predicted to have an ionisation fraction of 10^{-4} (Galli & Palla 1998), so the cloud is assume to be atomic and the following ions have the fractional abundances: $\rm x_{H^+} = 10^{-4}$, $\rm x_{O^+} = 4.9 \times 10^{-11}$ and $\rm x_{C^+} = 2.69 \times 10^{-11}$). All other molecular species have an initial abundance of zero.

The 2D initial conditions for these models were obtained from the output from their respective 1D SN models. When the shock reaches $\sim$ 39 pc in the 1D SN model, both the chemical and dynamic properties are mapped on to a 2D grid. This 2D grid which concentrates on the area 37.0 - 44.68 pc from SN progenitor, the centre of the cloud is set as the origin of the grid. This mapping is achieved by plotting the 1D output linearly in the y direction; however the area from 39.5 pc to 41 pc is rotated 180° about the 41.0 pc point to form a semi-circle. This creates a half a spherical cloud (1 pc radius) on the reflective x-axis. The 2D model is then allowed to runs for 475000 years (1.5×10^{13} s). The results of the 2D models are presented in sections §-5.3.1 - §5.3.2.

We investigate a 1D SN model with metal-dust model and follow the evolution of the SN remnant. In order to compare these results to Chiaki *et al.* (2013) we use the following initial conditions: a SN ($E_{SN} = 10^{51}$ erg) explodes into a uniform ambient medium with the following parameters: $n = 1\,\rm cm^{-3}$ T= 10^4 K and $\rm x_{H_2} = 10^{-3}$. The results are presented in section §5.3.3.

Model	Min shock temperature (K)	Max shock density (cm^{-3})	Average shock velocity ($km\,s^{-1}$)	Min cloud temperature (K)	Max Cloud density (cm^{-3})
Basic metal-free	2150	78.53	46.2	146.0	115.48
Metal-ion	2600	76.84	47.0	154.4	120.54
Metal-molecule	2600	76.84	47.0	154.4	120.54

Table 5.6: Initial conditions of all 2D shock-cloud models

5.3.1 Metal-ion model

The initial conditions for the 2D metal ion model are displayed in Figures 5.1(a) and 5.4(a) (density and temperature respectively). The initial conditions of the model are also listed in Table 5.5. The initial conditions of the metal-free toy model are also displayed in this table. The introduction of metals causes an increase in temperature of the cloud and shock. This is probably caused by a decrease in the amount of hydrogen atoms to decrease in our model and therefore a decrease in H_2. This is because when the mass density provided by the hydrodynamic part of the code is converted to number density, the number ratios of the atomic nuclei are no longer just 1.0 : 0.08 (H:He), but $1.0 : 0.08 : 2.69 \times 10^{-7} : 4.90 \times 10^{-4}$ (H:He:C:O). The decrease of H_2 molecules translates as a decrease in the radiative cooling of the gas (where the metal line cooling from electronic collisions is not dominant).

This is evident in the temperature of the cloud which has cooled to 154 K compared to 146 K in the metal-free model, which both have a fractional abundance $x_{H_2} \simeq 10^{-5}$ as seen in Figures 5.2(a) and 3.16(a). The metal-free SN shell reaches ~ 39 pc at 7.55×10^{12} s and the low metallicity SN shell reaches the cloud at 7.38×10^{12} s. Hence the low metallicity cloud has had less time to diffuse (as the cloud is not in pressure equilibrium) and has a higher density than the metal-free cloud.

Figure 5.1 displays the evolution of the clump as the shock passes throughout it. The cooling from metal line cooling means a wider but less dense compressed ridge forms (Figure 5.1(b)) as the shock compresses the clump compared to the metal-free model. Instabilities have developed in the compressed clump by $\sim 370,000$ years (Figure 5.1(d)), which lead to the formation of two connected fragments. The inclusion of metal-line cooling causes the compressed gas to fragment into large fragments. The clumps have an average temperature of 400 K (Figure 5.4(b)) and the largest clump cools to a minimum of 321 K. The maximum density of the clumps is 360 cm^{-3}, which is much much lower than the metal-free model. If we assume that the clump is defined by density above $1.0 \times 10^{-24}\,g\,cm^{-3}$, the approximate the masses of the two large clumps are 0.75

$M_\odot$ and 0.4 $M_\odot$. The clumps have a lower average density (128 cm^{-3}) than the metal -free case and thereby are not expected to be star formation sites.

The abundances of main coolants H_2, C^+ and O^+ are displayed in Figures 5.7 and 5.8. The fraction abundance of H_2 reaches a maximum value of x_{H_2} =0.0028 (similar to the metal-free model). These high abundances are found within the densest gas and the gas interacting with the shock after 475000 years of the simulation (Figure 5.3(a)).

Figure 5.2(b) displays the initial fractional abundance of C^+, which is low within the neutral cloud (10^{-13}) and more abundant in the warm ionised ambient medium ($x_{C^+} = 10^{-11}$). The reason it is so low in the hot gas behind the shock, is because carbon is fully ionised. At the end of the simulation the highest abundances of C^+ traces the gas interacting with the shock, which can be seen in Figure 5.3(b). The lowest abundances of C^+ are found within the gas cloud that did not interact with the shock and is diffusing away.

The initial abundances of O^+ in the 2D shock-cloud are displayed in Figure 5.2(c). It is clear that O^+ is more abundant in the hot post-shock gas than in the pre-shock gas, as the recombination rate for oxygen is double that of carbon at temperatures $T < 10^4$ K. After the shock had passed through the clump (Figure 5.3(c)), the abundance of O^+ is still highest in the hot gas behind the shock, but it has increased in the boundary between the dense clump material and the hot gas. Therefore tracing the gas that interacts with the SN ejecta.

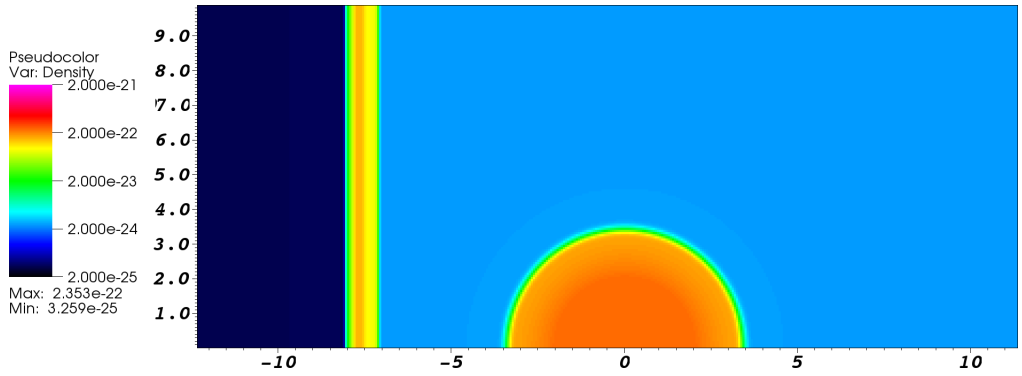

(a) $t = 0$ yr

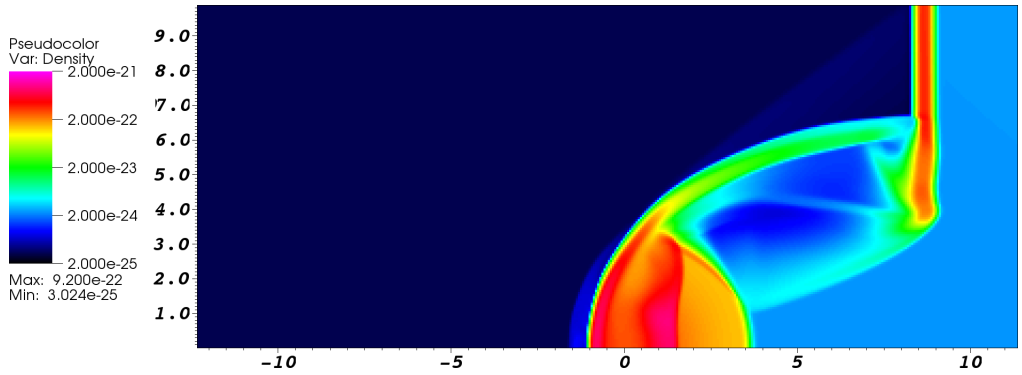

(b) $t = 120,000$ yr

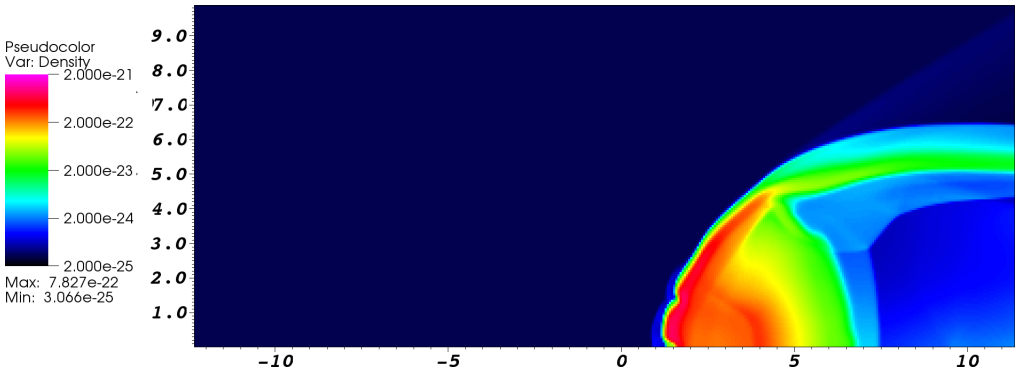

(c) $t = 280,000$ yr

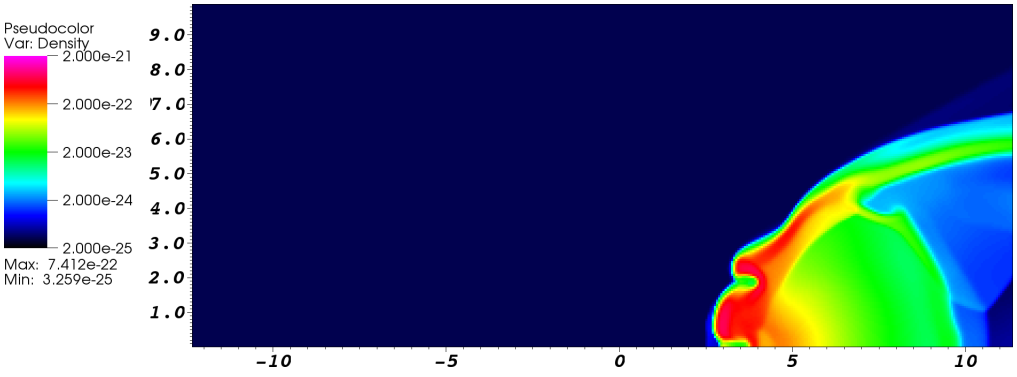

(d) $t = 373,000$ yr

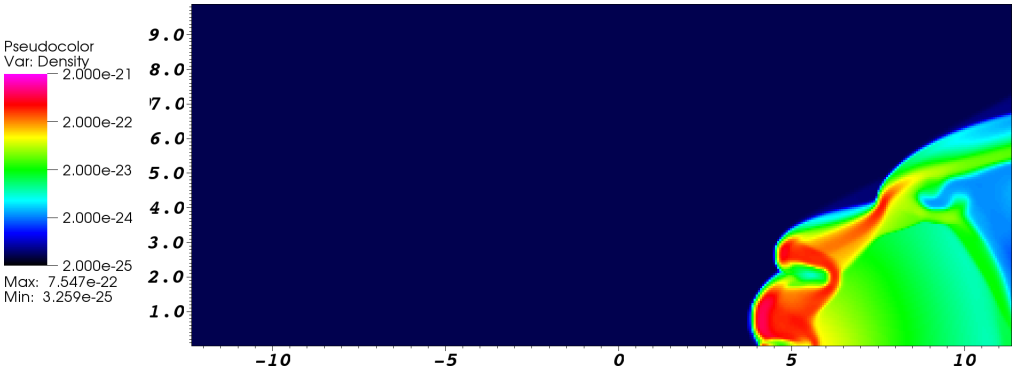

(e) $t = 435,000$ yr

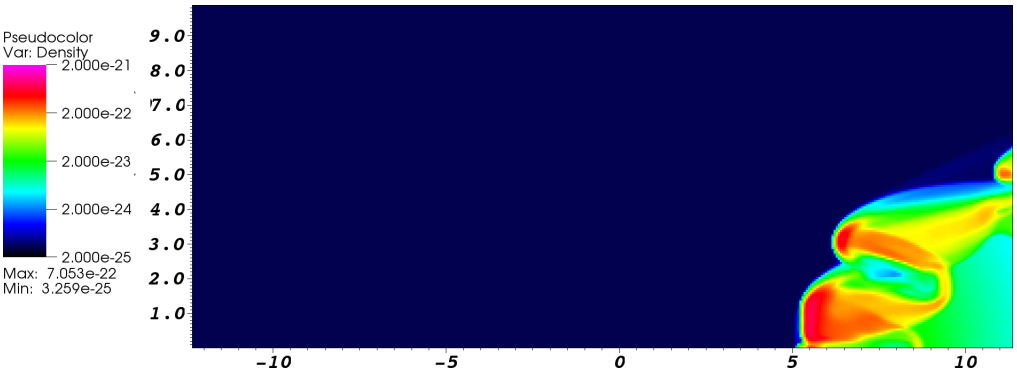

(f) $t = 475,000$ yr

Figure 5.1: 2D metal-ion model - density of the gas is displayed as the shell collides with the clump to form two smaller dense clumps. The legend displays mass density ($\mathrm{g{\cdot}cm^{-3}}$), which equates to max. $n = 981.6\,\mathrm{cm^{-3}}$ and min. $n = 0.0098\,\mathrm{cm^{-3}}$. [The x and y axis represent the distance from the centre of the clump at t= 0 s (in 10^{18} cm)]

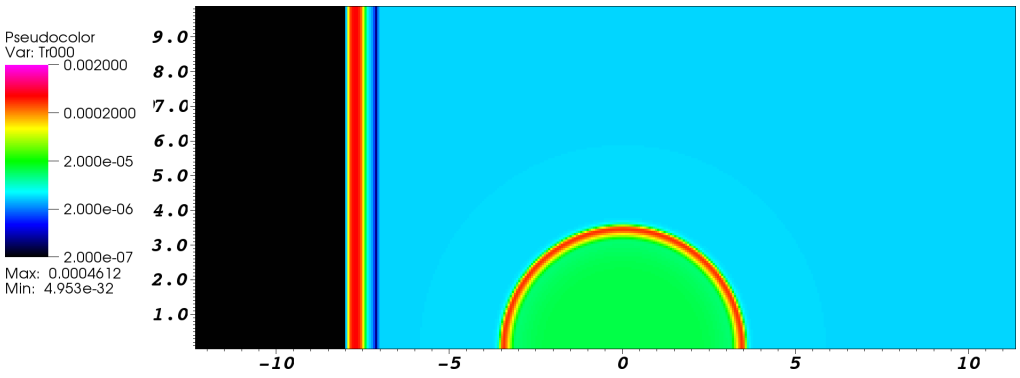

(a) x_{H_2}

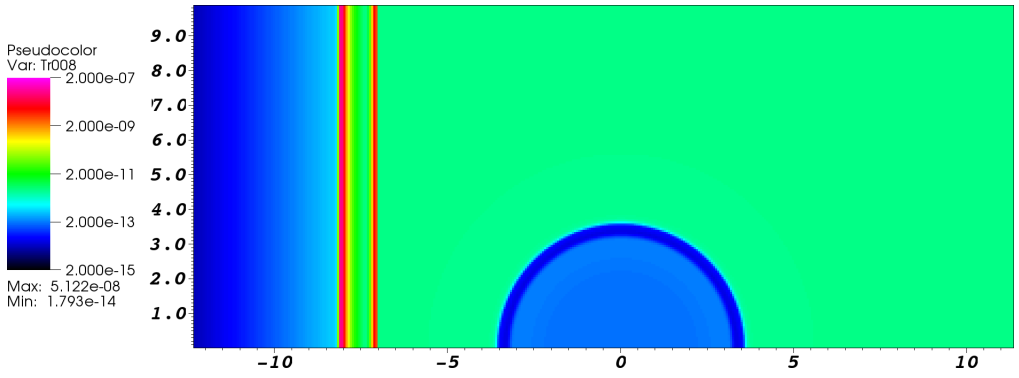

(b) x_{C+}

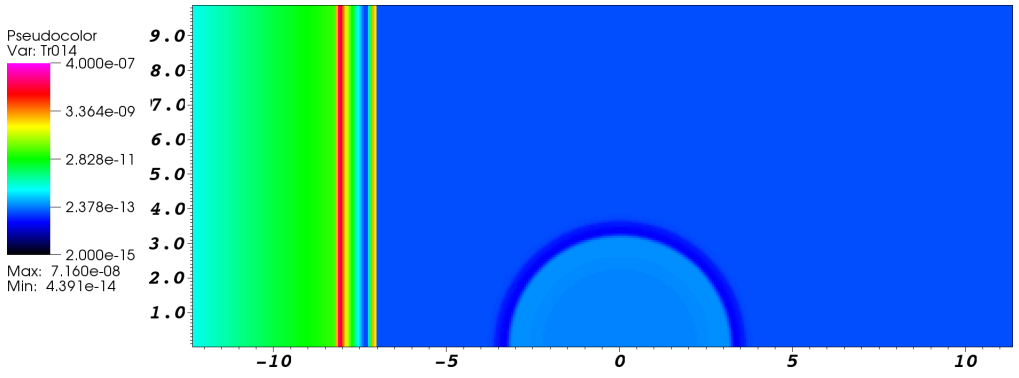

(c) x_{O+}

Figure 5.2: 2D metal-ion model - Fractional abundances of H_2, CII and OII at t=0 s. [The x and y axis represent the distance from the centre of the clump at $t = 0$ yr (in 10^{18} cm)]

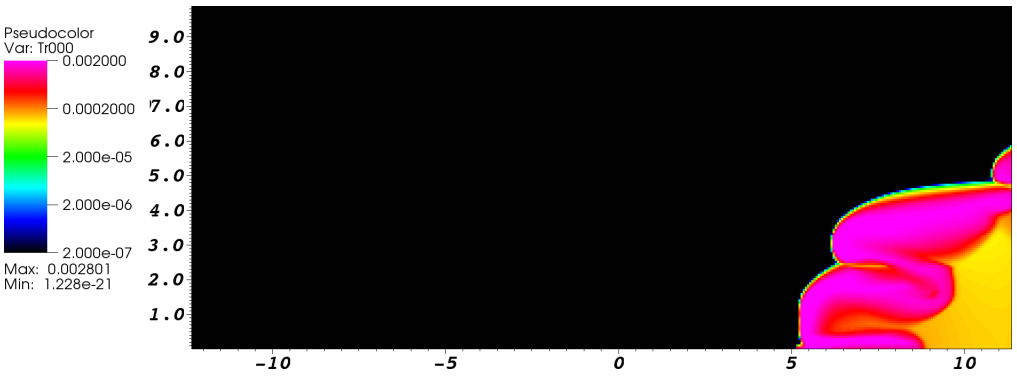

(a) x_{H_2}

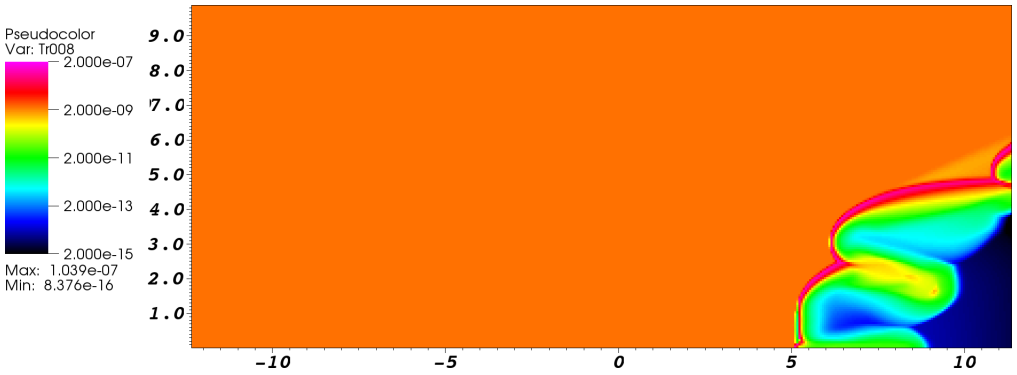

(b) x_{C+}

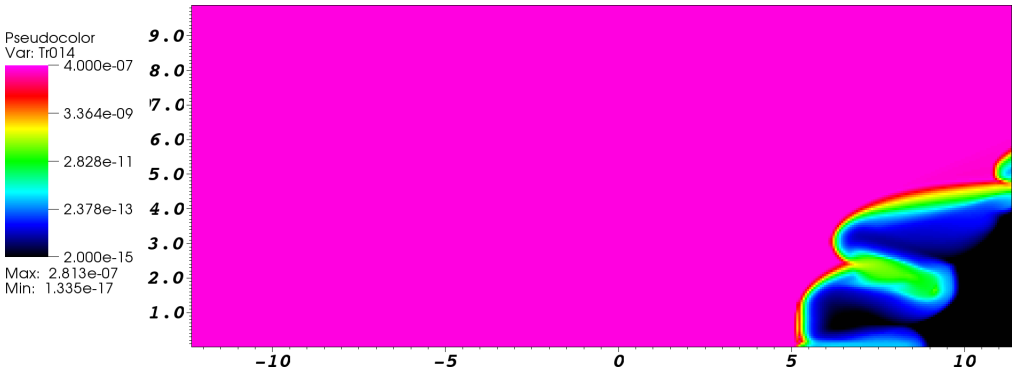

(c) x_{O+}

Figure 5.3: 2D metal-ion model - Fractional abundances of H_2, CII and OII at t$t = 475,000$ yr.[The x and y axis represent the distance from the centre of the clump at t= 0 s (in 10^{18} cm)]

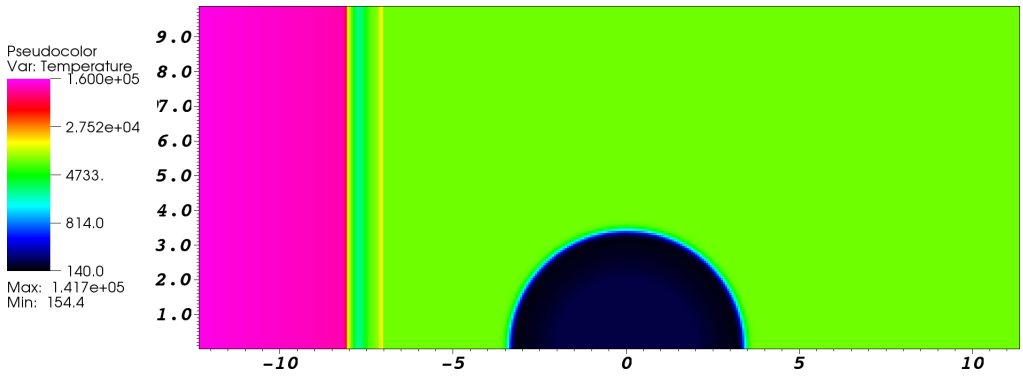

(a) $t = 0$ yr

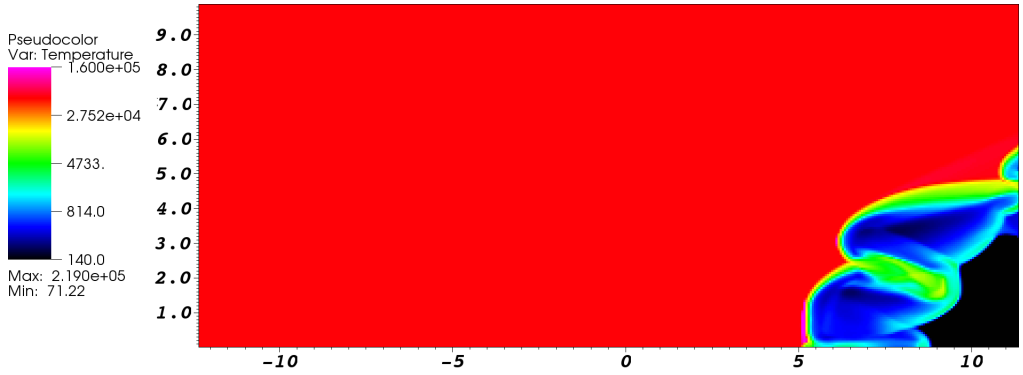

(b) $t = 475,000$ yr

Figure 5.4: Graphs displaying the temperature (K) of the 2D metal-ion model at the start and end of the simulation. [The x and y axis represent the distance from the centre of the clump at t= 0 s (in 10^{18} cm)]

5.3.2 Metal-molecule model

The initial conditions for this model are presented in Table 5.5 and it can be seen that the temperature and dynamics of the low-metallicity gas are unaltered by the presence of metal-bearing molecules (CO, OH and H_2O). Allowing the metal-ions to react with the primordial species has not made a appreciable difference to the metal-ion abundances. From this model we can see that metal-ions are the dominant (metal-based) coolant in a dust-free low-metallicity supernova model.

The results from the 2D shock-cloud interaction are presented in Figures 5.5 - 5.8. The final outputs for density and temperature (Figures 5.5(b) & 5.6(b)) also display that molecular cooling (from CO, OH & H_2O) has made very little difference to the fragmentation and clumping of the cloud. The lowest temperature in the final output has decreased from 71.22 K (metal-ion model) to 71.14 K, which is insignificant. The structure and temperature of the two large clumps remains unaltered. Due to a slight decrease in C^+ cooling due to the formation of molecules, the small

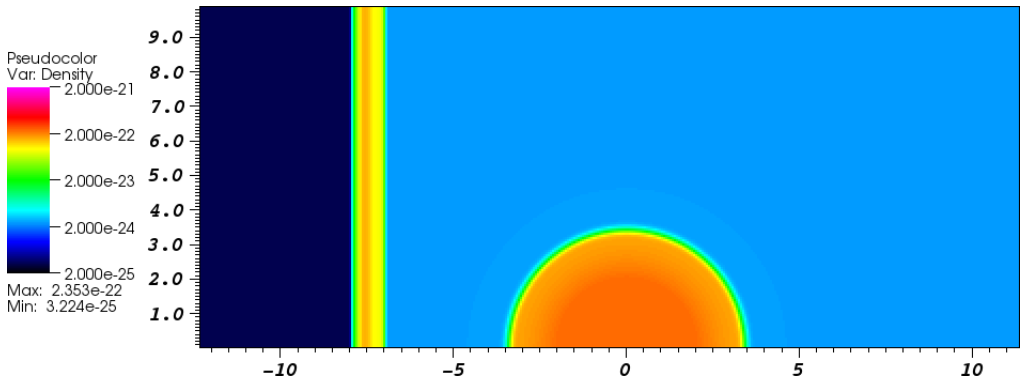

(a) $t = 0$ yr

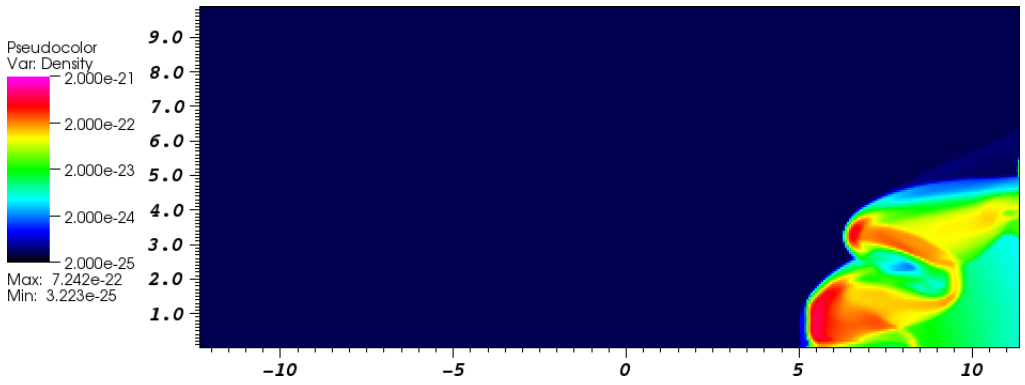

(b) $t = 475,000$ yr

Figure 5.5: 2D metal-molecule model - density of the gas is displayed as the shell collides with the clump to form two smaller dense clumps. The legend displays mass density ($\mathrm{g{\cdot}cm^{-3}}$), which equates to max. $n = 981.6\,\mathrm{cm^{-3}}$ and min. $n = 0.0098\,\mathrm{cm^{-3}}$. [The x and y axis represent the distance from the centre of the clump at t= 0 s (in 10^{18} cm)]

clump present in the top right of the shocked clump in Figure 5.1(f) did not form in this model (Figure 5.5(b)). Overall affect of metal-bearing molecules is negligible in the low density regime ($n \lesssim 10^3\,\mathrm{cm^{-3}}$) of this shock-cloud model.

The fractional abundances of CO, OH and H_2O present at the beginning of the 2D simulation are presented in Figure 5.7 and the final abundances are presented in Figure 5.8. The CO molecule is known as a tracer of GMC in milky way and is the dominant coolant in dense molecular clouds ($n < 10^5\,\mathrm{cm^{-3}}$ T < 100 K) (Neufeld *et al.* 1995). The initial values of CO is displayed in Figure 5.7(a) and is only present within coolest dense gas of the SN shell and has the highest abundance of $\mathrm{x_{CO}} = 10^{-14}$ within the neutral cloud. After 475000 years the shock has passed through the cloud and the abundance has not increased above $\mathrm{x_{CO}} \sim 10^{-12}$ (Figure 5.8(a)), and traces the cooler gas of the shocked cloud. It is not found in the gas interacting with the shock, where it is collisionally

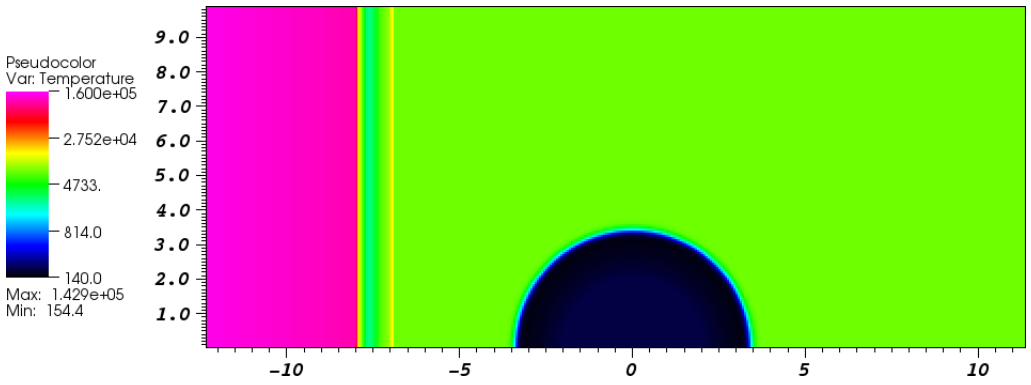

(a) $t = 0$ yr

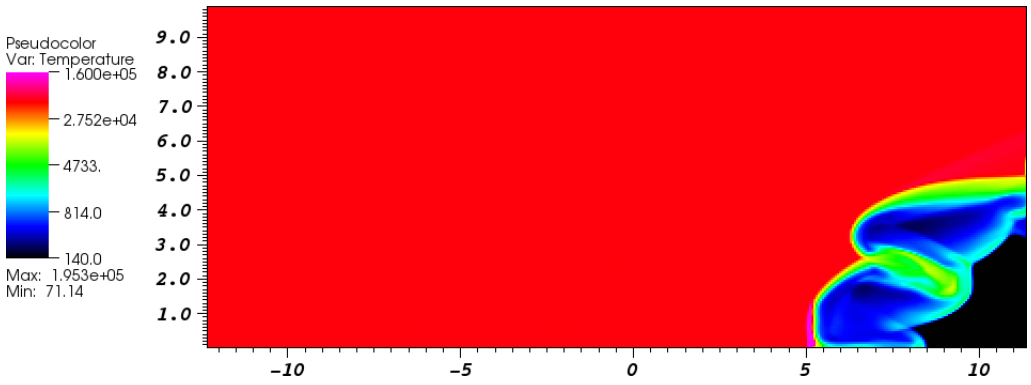

(b) $t = 475,000$ yr

Figure 5.6: Graphs displaying the temperature (K) of the 2D metal-molecule model at the start and end of the simulation. [The x and y axis represent the distance from the centre of the clump at t= 0 s (in 10^{18} cm)]

dissociated.

The OH is the most abundant metal-bearing molecular coolant and is displayed in Figures5.7(b) - 5.8(b). This is consistent with Galactic shock models (Hollenbach & McKee 1979). Initially the OH abundance is $x_{OH} = 10^{-10}$ within the SN shell, which is much higher than CO and H_2O which have fractional abundances $\sim 10^{-15}$. After 475000 years OH has highest values on the boundary of the dense clumps interacting with shock, where the gas temperature is around 2000 K. The water molecule is the is the least abundant of the three molecules (Figures 5.7(c) and 5.8(c)). The shock has slightly increased the amount of H_2O molecules within the clump and is most abundant in warm dense parts of the shocked cloud gas that is not interacting with the shock.

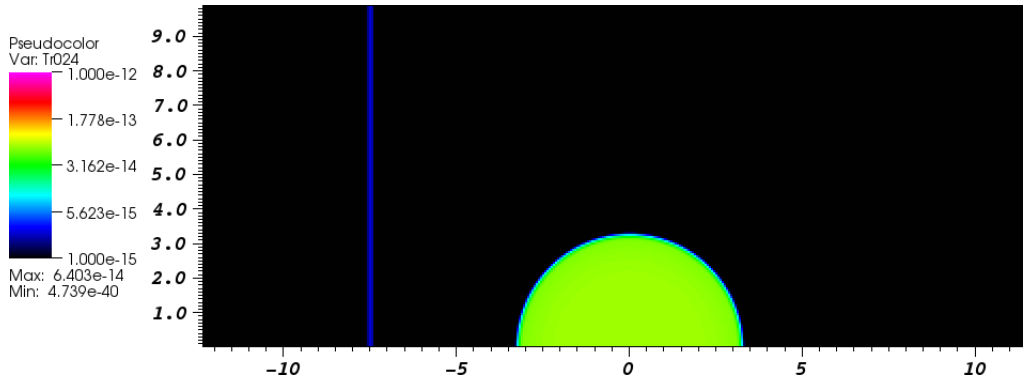

(a) x_{CO}

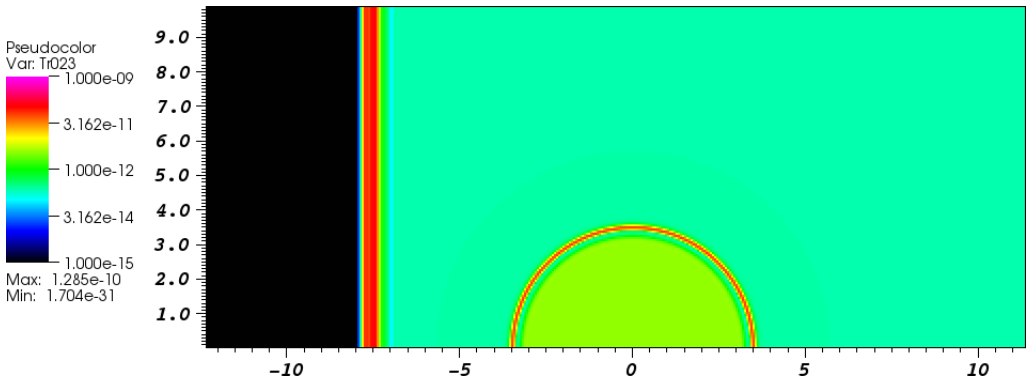

(b) x_{OH}

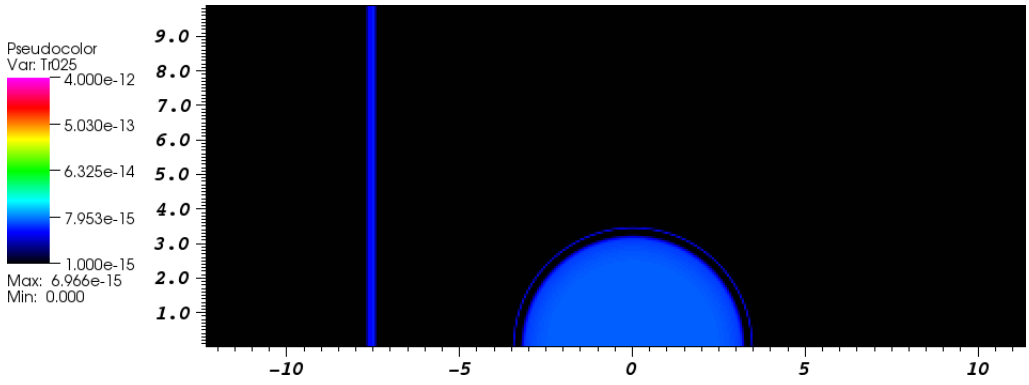

(c) x_{H_2O}

Figure 5.7: 2D metal-molecule model - Fractional abundances of CO, OH and H_2O at t=0 yrs. [The x and y axis represent the distance from the centre of the clump at t= 0 s (in 10^{18} cm)]

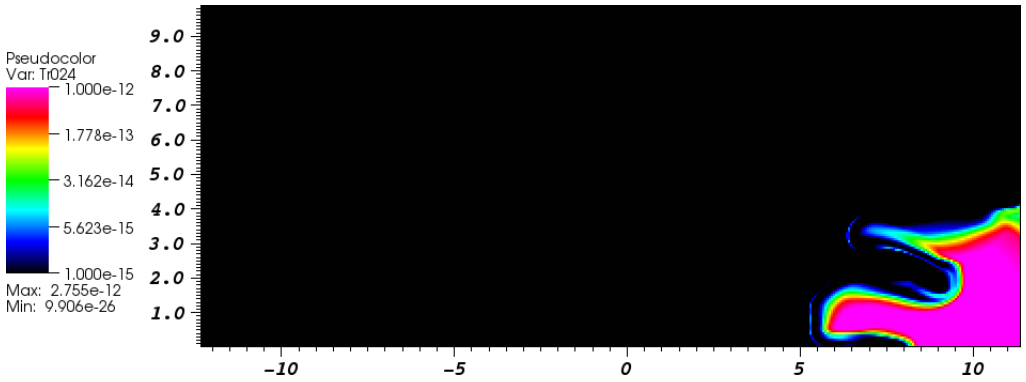

(a) x_{CO}

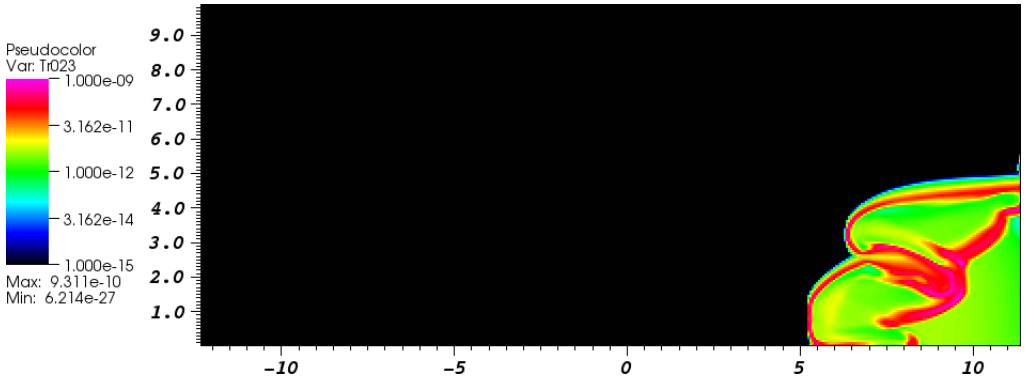

(b) x_{OH}

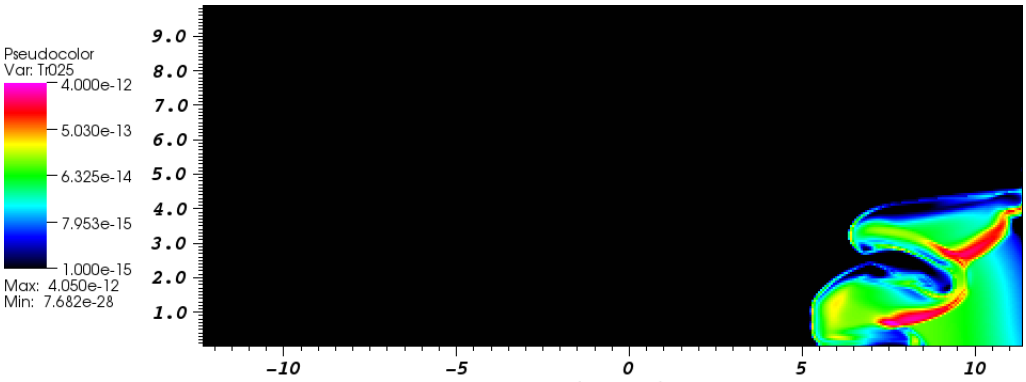

(c) x_{H_2O}

Figure 5.8: 2D metal-molecule model - Fractional abundances of CO, OH and H_2O at $t = 475,000$ yr.[The x and y axis represent the distance from the centre of the clump at t= 0 s (in 10^{18} cm)]

5.3.3 Metal-dust model

Chiaki *et al.* (2013, hereafter C13) study a 1D SN explosion interacting with a uniform density gas of metallicity Z= 10^{-5} $Z_{\odot}$. As mentioned in the §5.1 the non-equilibrium cooling in only introduced below 10^4 K for primordial gas and the metal cooling is calculated assuming collisional ionization equilibrium. In order to ascertain the importance of non-equilibrium cooling for the evolution of the supernova remnant, we have considered the same initial conditions as C13 for the metal-dust model. Hence we study a 10^{51} erg SN explosion in a neutral gas cloud ($x_{H_2} = 10^{-3}$, n= $1\,cm^{-3}$).

The results are presented in Figure 5.9, the upper plot displays the results from C13 model and the lower plot displayed the results from the metal-dust model. The output for the following specific times post- explosion are displayed: (1) $t = 1.0 \times 10^5$, (2) $t = 5.6 \times 10^5$, $t = 3.2 \times 10^6$ and (4) $t = 1.0 \times 10^7$ years. At the first output 10^5 years after the explosion is initiated, the difference between the two models is apparent because the metal-dust model has already formed the radiative shell at $\sim$ 30 pc from the progenitor star. At this point both models have their respective supernova remnants reach the same distance from the progenitor star but the C13 model has not reached the radiative phase.

Therefore the subsequent divergence between the two models is due to C13 not including comprehensive radiative cooling above 10^4 K. Hence their simulation does not capture the formation of SN shell at earlier times. Therefore the C13 shell terminates $\sim$ 20 pc further than the metal-dust model.

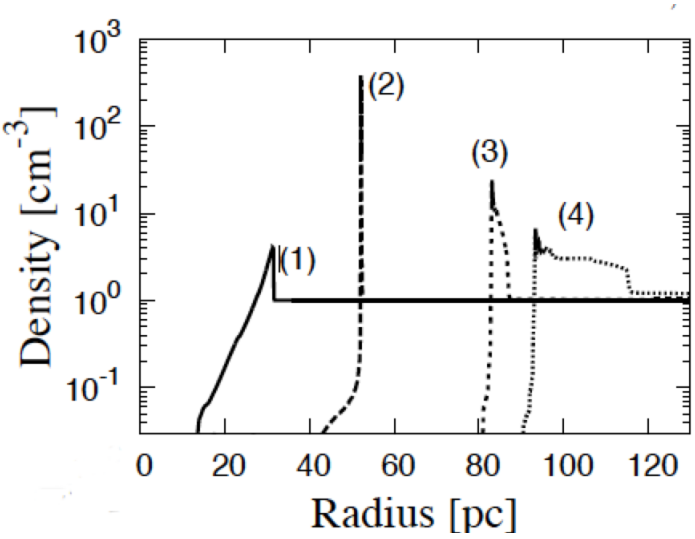

(a)

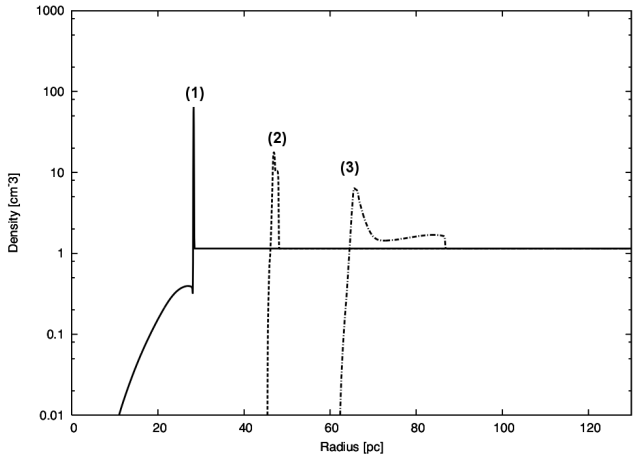

(b)

Figure 5.9: The graphs 1D Sm model with initial conditions described by Chiaki (a) chiaki model and (b) my model.for times (1) $t = 1.0 \times 10^5$, (2) $t = 5.6 \times 10^5$, $t = 3.2 \times 10^6$ and (4) $t = 1.0 \times 10^7$ years.

5.4 Discussion

In the chapter we have extended the basic metal-free microphysics module described in chapter §3 to include metal-ions, metal-bearing molecules and dust. We investigated the effect of metal ions and metal-bearing molecules on the 2D shock-cloud model. We simulate a 1pc cloud interacting with a shock originating from a supernova explosion (10^{52} erg). and is embedded within a $1\,\mathrm{cm}^{-3}$ ionised ambient medium. The cloud is 40 pc from the progenitor star, it has density $n = 100\,\mathrm{cm}^{-3}$ and is embedded in a $1\ \mathrm{cm}^{-3}$ ionised ambient medium. We assume that this environment is situated within a protogalaxy at redshift $z = 10$ and has a metallicity of $10^{-3}\,\mathrm{Z}_{\odot}$. We also investigate the effect of metal ion and dust cooling on 1D SN models.

The results from the 2D metal-ion model (§5.3.1), have shown that including non-LTE metal line cooling for the metallicity Z= 10^{-3} $\mathrm{Z}_{\odot}$ impacts the cooling of the compressed ridge that forms as the SN shell interacts with the clump. This is reflected in the thickness of the high density ridge ~ 0.3 pc thats forms at t$\approx 8 \times 10^{1}2$ s, which is double the radius of the metal-free model. This structure does not fragment as easily as the metal-free model, producing fewer but larger (in radius) pressure contained clumps. The cooling of neutral gas that has been shocked is not as efficient as the metal-free model. Glover & Abel (2008) showed that if a comprehensive cooling function is used, when the gas cools from temperatures $\sim 10^4$ K, it cools to a higher temperature than gas which used a simpler H_2 cooling function. This may be the cause of the higher temperatures of the clumps. To determine whether this decrease in cooling is due to the loss in hydrogen atoms or a more comprehensive cooling function, we must include more metal-line cooling from collisions with atoms in further work.

We found that the molecular cooling (from metal-bearing molecules CO, OH & H_2O) had negligible affect in the density range of out simulations ($n < 10^3\,\mathrm{cm}^{-3}$). However it may become dominant in gas of larger densities, as shown by Schneider *et al.* (2012) for a dust free gas (with metallicities up to Z= 10^{-2} Z$\odot$) of densities $n \sim 10^4 - 10^5\,\mathrm{cm}^{-3}$. The authors also confirm that including Fe and Si cooling in a dust-free low-metallicity gas does not make any difference. The metal-molecule model shows that for low densities $\leq 10^3\,\mathrm{cm}^{-3}$ the cooling is dominated by metal-ion cooling. Incorporating metal-bearing molecules makes a negligible difference in the abundances of the metal-ions compared to the metal-ion model. Hence the cooling from the metal-ion model (where the metal ions and primordial species do not react) is not over-estimated, and this model is a good approximation for a dust-free low-metallicity environment.

The next set of results are obtained from the 1D metal-dust model with metallicity Z= 10^{-5} Z$\odot$. We find that including non-LTE cooling for the full temperature range of the the SN model, captures the formation of the radiative shell at an earlier stage than anticipated by Chiaki *et al.* (2013) allows the shell to form much earlier. This is an important result and in future all SN models should include non-equilibrium chemistry and related radiative cooling. It is known that dust cooling is important at high redshift (Dopcke *et al.* 2011; Cazaux & Spaans 2004) and for future work the 2D shock-cloud model must be extended to include dust cooling. A gas with metallicity Z= 10^{-3} Z$_\odot$ must be considered, and therefore so we can compare to the metal-ion model.

We have assumed that the dust grains have similar properties to Milky Way dust and the number density has been scaled with metallicity. We have very little understanding of dust at high redshift, and even less understanding of dust production/destruction in primordial supernova explosion(Cazaux & Spaans 2004; Cherchneff & Dwek 2010; Schneider *et al.* 2012; Silvia *et al.* 2010). Therefore, it is a good staring point to assume Galactic dust properties, as previous studies have not included dust cooling in high redshift SN models. It would be beneficial to extend the investigation on dust cooling to include the effects of different grain sizes/type, dust-to-gas ratios and grain destruction. SN shocks are known to destroy dust grains, this process has been investigated at high redshift by Nozawa *et al.* (2007), they found that all small grains (i.e. $a = 0.05\,\mu$m) in an ambient medium of $1\,\mathrm{cm}^{-3}$ were completely destroyed by core collapse SNe and large grains $a > 0,2\,\mu$m are ejected into the ISM. Smaller grains ($a \approx 0.0025\,\mu$m) give much more cooling that grains of size $a \approx 0.1\,\mu$m (Montier & Giard 2004) and the dust component observed in the local ISM has distribution of sizes. It will be interesting to model a distribution of sizes for the grains, if smaller grains survived in the dense clump, this would have an effect on its thermal state and hence its fragmentation.

5.5 Conclusions

In the chapter we have extended the basic metal-free microphysics module described in chapter §3 to include metal-ions, metal-bearing molecules and dust. We investigated the effect of metal ions and metal-bearing molecules on the 2D shock-cloud model and the effect of dust cooling on 1D SN models.

Metal-line cooling has been shown to be important in many aspects of protogalaxy modelling (Nagakura *et al.* 2009; Greif *et al.* 2010; Vasiliev *et al.* 2012). We also found that the inclusion

of metal ion cooling make an impact on the shocked gas ($\sim 10^{-3}\,Z_{\odot}$) within this 2D shock-cloud model. Incorporating 'better' coolants at higher temperatures, promotes quicker recombination times. This reduction of electrons translates to a decrease of molecular hydrogen at lower temperatures. Hence we find that the clumps that form from the shock-cloud interaction have higher temperatures than the metal-free model (Chapter §3). This behaviour has also been observed in the Glover & Abel (2008) cooling function; it cooled the gas from 10^4 K to a higher temperature compared to other less comprehensive cooling functions.

Another subtle but significant result from the metal-ion model, was that the way number density is modelled within the simulation can make a difference. Many low-metallicity chemico-dynamic models (e.g. Greif *et al.* 2010) only treat the mass density calculated by the hydrodynamic part of the code as purely the number density of hydrogen nuclei. From Table , it can bee seen that by including the metals in this number density the temperature of the cloud has increased by 8 K. This small increase in temperature of a dynamically stable gas cloud could translate as a big difference in a shock-cloud interaction, due to the highly non-linear state of the system. Therefore this is a subject that requires further investigation.

In agreement with Schneider *et al.* (2012) we found that found molecules have negligible effect on the shock-cloud interaction for the densities $n < 10^3\,\mathrm{cm}^{-3}$. The molecules trace similar environments as they do in the local ISM, i.e. OH traces the shocked gas while CO and H_2O are found in neutral cool gas. Although, the effects of cosmic rays on molecular formation have not been studied in this work, we recommend that this is completed in future work. Our work highlights the importance of metal-ion cooling in these low metallicity environments. Hence models which only include primordial chemistry plus dust cooling (e.g. Omukai *et al.* 2005), may not be realistically capturing the thermal state of the gas (i.e. recombination time). It would be beneficial to refine these models to include metal-ion cooling.

Our final model included both metal-line cooling and dust cooling for the entire temperature range of the SN model. We have compared these result to the model by Chiaki *et al.* (2013) and found that non-equilibrium cooling pays an important role at all temperatures and not just temperatures below 10^4 K. The comprehensive modelling of the radiative cooling results in the SN shell developing at a much earlier time. Therefore early universe SN models should include non-equilibrium chemistry and cooling for all temperatures, to capture the realistic evolution of a SN remnant. This may be as important as incorporating multidimensional simulations.

Given these positive results of the 1D metal-dust model, the chemistry module should be extended to 2D shock-cloud model for gas metallicity of Z= 10^{-5} $Z_{\odot}$. This may give us further insight into the formation of the HMP star SDSS J102915+172927.

CHAPTER 6

IS THERE A COSMIC CARBON-DUST PATHWAY?

Based on paper by Dhanoa & Rawlings (2014)

6.1 Introduction

The observational properties of dust and the physical consequences of its presence in the interstellar medium are extremely well-known and well-documented (Draine 2003). However its composition, structure and size-distribution are still subjects of much discussion. Even though there are no direct samples of interstellar dust, carbonaceous dust deposits found in meteorites give us an indication of what structure and composition we might expect. These grains consist of a core of microcrystalline aromatic moieties surrounded by a crystalline graphite mantle (Bernatowicz *et al.* 2006). Significantly, the precise chemical kinetic pathways leading to the (relatively simple) case of carbon-dust formation are almost entirely speculative.

The recent observations of higher than expected dust masses around high redshift quasars (Dwek *et al.* 2007; Bertoldi *et al.* 2003) and local supernovae (Matsuura *et al.* 2011), has caused a resurgence of interest in the issues of dust formation mechansims and efficiencies. In the local universe, dust is observed mainly in two environments: dense interstellar clouds and circumstellar media. The main sources of interstellar dust are believed to be evolved red giants, novae and supernovae (Dwek 2004; Salpeter 1977; see Tielens 2008 for a review). There are thus two questions that we address in this paper: (i) what is the chemical pathway for the formation of

macromolecular species that leads to the formation of dust nucleation sites?, and (ii) what range of physical parameters determine the viability of these pathways?

For the sake of (relative) simplicity we limit our discussion to the formation of carbon dust in carbon-rich circumstellar environments, making the simplifying assumption that the oxygen is completely locked up in the relatively inert form of CO. In such an environment the C:O $\gtrsim 1$ ratio and is a crucial parameter. However, it should be noted (see below) that this usually-assumed approximation has been challenged by relatively recent observational and modelling efforts (e.g. Andrea *et al.* 1994).

Some of the earliest attempts at modelling carbon dust formation concentrated on novae, some of which are seen to produce very optically thick (carbon) dust shells on timescales of days. Rawlings (1988) developed a proto-PDR model of the chemistry in novae ejecta, and found that molecule formation requires the presence of H_2 and carbon neutrality (CI). The presence of C^+ (and the carbon ionization continuum) inhibits molecule formation. Chemical equilibrium is established very fast (within $\sim$ 10s). Rawlings & Williams (1989), hereafter RW89, extended this and proposed a non-LTE chemical kinetic model of (carbon) dust formation in novae ejectae which proceeds via a limited hydrocarbon chemistry - totally dominated by the photophysics, and requiring all oxygen to be locked up in CO. This latter finding has been challenged - both by the observations that suggest that carbon dust is formed in oxygen rich (O>C) environments (e.g. Andrea *et al.* 1994) - and also models of the chemistry in nova outflows (Pontefract & Rawlings 2004).

In these models C_2 (for which the more significant of the two pre-dissociation bands is shielded against photodissociation in a CI region) is the key building block species, rather than C_2H_2 which is susceptible to photodissociation. As such, nucleation of dust was found to be possible only in a CI region, but requires some source of ionisation to drive the chemistry.

Pontefract & Rawlings (2004) extended the work by RW89 by including oxygen and nitrogen chemistry and updated the photoreaction rates. Surprisingly, they found that the overall chemistry is not as dependent on the photochemistry as earlier studies had suggested and that carbon dust could be formed even when all of the oxygen is not 'locked' in CO. The work highlighted that CN, CO and C_2 are key molecular species in the formation pathways of larger species. Although C_2H_2 was included its chemistry was not closely scrutinised.

More generally, it has been proposed that Polycyclic Aromatic Hydrocarbon molecules (PAHs) are key intermediates in carbon dust formation and act as nucleation sites for dust grains (Cherchneff 2011; Cherchneff *et al.* 1992; Helling *et al.* 1996). This inferred link is due to the the close relationship between the molecular structure of PAHs and the carbon structure of graphite. Also,

observations of the far-IR continuum due to carbon dust are accompanied by strong PAH features (Tielens 2008). However, some caution should be exercised with the interpretation of these features. For example, PAH (and/or hydrogenated amorphous carbon) emission is also detected in some carbon-dust producing novae but in all cases it is only seen well *after* dust formation and in an environment when it would be susceptible to photodissociation. This indicates that - for novae at least - the PAHs are transitory products of dust destruction, rather than intermediates to dust formation (Evans & Rawlings 2008).

Gail & Sedlmayr (1987) proposed chemical mechanisms required to form PAH molecules in stellar winds. The acetylene molecule (C_2H_2) was found to be crucial in the formation pathway. An important contribution came from Frenklach & Feigelson (1989), hereafter (FF89). They investigated a mechanism of PAH formation, using a chemical kinetic approach. The chemistry network was based on soot production in terrestrial hydrocarbon flames, which they applied to astrophysical conditions, i.e. much lower pressure and densities. They confirmed that the complex network of chemical reactions can essentially be described by a sequence of hydrogen abstraction followed by acetylene addition. Cherchneff *et al.* (1992) found the dominant pathway for closure of the first aromatic ring in flames is via the recombination of propargyl.

Acetylene does not possess a permanent dipole moment and so does not have a rotational spectrum observable at radio wavelemgths. It is therefore somewhat elusive; - detections rely on rovibrational transitions, observable in the mid-infrared. For this reason, detections tend to be limited to the warm gas ($\sim 100 - 1000$K) along the lines of sight towards young stellar objects (e.g. Boonman *et al.* 2003). There is also strong evidence for the presence of C_2H_2 in evolved carbon stars within the dust formation region ($1 - 5$ stellar radii); the most well known of which - IRC+10216 - exhibits a forest of C_2H_2 lines in the 11-14μm window (Fonfría *et al.* 2008). Indeed, after H_2 and CO, C_2H_2 is determined to be the most abundant species in the gas - with a fractional abundance of $\sim 8 \times 10^{-5}$ - although this is primarily detected *outside* the dust-formation zone and so is not necessarily associated with the dust-formation process. There may even be some evidence of C_2H_2 freeze-out into icy mantles at larger radii in IRC+10216, and an icy mantle-based origin for interstellar C_2H_2 is strongly suggested by Spitzer observations of the correlation between C_2H_2 and gas-phase CO_2 towards Cepheus A East (Sonnentrucker *et al.* 2007).

Cherchneff *et al.* (1992) addressed the issue of PAH chemistry and dust formation in the carbon-rich envelopes of late AGB stars; driven by stellar pulstations and (strong, density enhancing) shocks. Although extremely dense, the gas is much cooler and not subject to the intense FUV radiation field that is present in a nova, so the chemical model was based on a terrestrial neutral gas

acetylenic-burning soot chemistry. In such environments the carbon budget is largely split between CO and C_2H_2. The chemistry was largely based on well-studied flame chemistries (eg. FF89), expanded and augmented to include free radicals. It was found that C_2H_2 is the key species in macro-molecular growth and (especially) ring closure/cyclization to form aromatic hydrocarbon rings, as well as the polymerization to multiple ring PAHs. The formation of the first aromatic ring is often recognised as the main 'bottleneck' in macro-molecular growth/dust nucleation. In this, as in later studies (e.g. Cherchneff & Cau 1999), ring closure was found to proceed following reactions of two propargyl radicals (C_3H_3) or via a lesser channel involving reaction of acetylene with 1,3 butadiyne (C_4H_2) (e.g. see Figs. 3 & 4 in that paper). In either case C_2H_2 initiates the chemistry. Reaction networks need to include both two-body and three-body reactions, but did not include photoreactions, or an ion-molecule chemistry. Although they were able to identify the presence of a temperature window (900-1100K) in which the formation of PAHs is possible, the formation efficiency is too low - possibly due to the lack of inclusion of the effects of a local UV radiation field and/or an ion-molecule chemistry.

Considering a different class of object Woods *et al.* (2002) modelled the formation of benzene (C_6H_6) in a protoplanetary nebula (CRL618) where the chemistry is characterised by high densities, temperatures and ionization rates - although photoreactions were significantly inhibited throughout the molecule-formation zone due to the assumed presence of dust. This chemistry is somewhat different to the Cherchneff et al. schemes due to the presence of a degree of ionization and an efficient ion-molecule chemistry. However, even in these conditions, C_2H_2 plays a crucial role - mainly through the initiating reaction of

$$HCO^+ + C_2H_2 \rightarrow \text{products...}$$

All of the above models and reaction schemes have made extremely simplistic assumptions about the radiation field and the photoreaction rates; either by only considering the chemistry in low luminosity environments (or external to an optically thick dust-formation zone) - in which case they are ignored, or by simply 'scaling up' interstellar photoreaction rates in a way that does not properly take into account the specific nature of the radiation field and/or the significance of ionization continua. The overall aim of this work is therefore to include an ion-molecule chemistry and a careful re-calculation of the photoreaction rates using local radiation fields and accurate cross-sectional data to re-assess the viability of C_2H_2 formation in a variety of carbon-rich circumstellar environments. As C_2H_2 is fundamental to the formation of PAH molecules, we try to determine if

the amount of C_2H_2 produced in carbon rich AGB and nova environments is enough to seed dust formation. We use a specially adapted chemical network for high temperatures and densities, paying particular attention to a more accurate account of the photochemistry involved in non-interstellar conditions, which (as explained above) previously had been highly over-simplified. We investigate a broad range of dust-forming objects which includes carbon stars with effective temperatures higher than AGB stars (e.g. CH subgiants), AGB stars and novae. By doing this we aim to establish the range of parameter space within which effective C_2H_2 formation is possible. It is worthwhile noting that the presence of C2H2 is a necessary, but not sufficient condition for PAH growth in H-rich circumstellar outflows. Therefor, we will establish a parameter space in which it is possible to form PAH rich outflows.

In section §6.2, we describe the model that was implemented. Section §6.3 specifies the physical and chemical parameters used for the three different carbon rich circumstellar environments that we have modelled. We describe the results and analysis in section §6.4. Finally, in section §6.5 we summarise our results and their implications.

6.2 The Model

The nucleation sites for dust grain formation are formed in the gas phase in a cooling, expanding atmosphere, such as in the outflow from a red giant (Cadwell *et al.* 1994). Therefore if PAHs are the key intermediate molecules to carbonaceous dust they should also be formed in the stellar winds that feed the circumstellar environment. We therefore model the time-dependent chemistry that occurs in an appropriately located gas parcel. This will be the part of the envelope whose temperature lies within the range that is appropriate for dust formation - corresponding to the 'condensation radius' in previous studies (eg. Clayton & Wickramasinghe 1976).

As explained above, the main chemical pathway to form a PAH molecule starts with the polymerization of C_2H_2 (Gail & Sedlmayr 1987) and we therefore identify acetylene as being the key molecule in the formation of larger species, such as PAHs. We investigate the viability of acetylene formation as being the controlling factor in the formation of dust nucleation sites via PAHs as intermediate macro-molecules.

The gas in stellar outflows is dense (n$> 10^9$cm^{-3}) and warm (T > 1000 K), so that (providing the gas is not *too* hot, such that bond-breaking, collisional dissociation reactions can occur), molecules can be formed efficiently and quickly. As the gas expands and its density falls, the chemical reaction rates are quenched. However, the geometrical dilution timescale is typically

Table 6.1: Chemical Species

H, H_2, H^+, H^-, H_2^+, H_3^+
C, C^+, C^-, CO, CO^+, CH, CH^+, CH_2, CH_2^+, CH_3, CH_3^+
CH_4, CH_4^+, C_2, C_2^+, C_2H, C_2H^+, C_2H_2, $C_2H_2^+$
N, N^+, NH, NH^+, NH_2, NH_2^+, NH_3, NH_3^+, NH_4^+, N_2, N_2^+, N_2H^+
O, O^+, O^-, O_2, O_2^+, OH, OH^-, OH^+, H_2O, H_2O^+, H_3O^+
HCO, HCO^+, H_2CO, H_2CO^+, CO_2, CO_2^+
CN, CN^+, CN^-, HCN, HCN^+, HNC, $HCNH^+$
NO, NO^+, HNO, HNO^+, NO_2, NO_2^+, OCN
He, He^+, HeH^+, Na, Na^+, e^-
S, S^+, S^-, HS, HS^+, H_2S, H_2S^+, H_3S^+
CS, CS^+, HCS, HCS^+, H_2CS^+, SO, SO^+, SO_2, SO_2^+, OCS, OCS^+
NS, Si, Si^+, SiH, SiH^+, SiH_2^+, SiO, SiO^+, $SiOH^+$, SiO_2

many orders of magnitude larger than the chemical kinetic timescale (Rawlings 1988) and this is not a critical factor in determining the dust-formation efficiency. Despite the possible presence of shocks etc. - and although the gas is very far from thermal equilibrium, the characteristic timescale of the outflow is much larger than the chemical kinetic timescale. We therefore assume that both the circumstellar environment and the stellar wind are spherically symmetric around the star. We model the time dependent chemistry that would occur during the period of a single shock.

The chemistry is evolved to chemical equilibrium which, as argued above, occurs on a timescale that is very much shorter than that for which changes in the physical conditions occur. In practice, equilibrium was determined from the requirement that the abundances of all species changed by $< 1\%$ on any time step and typically was achieved on timescales of seconds. We have investigated the sensitivity of the equilibrium abundances to the physical conditions. The key free parameters that we have varied are: the total abundances of the elements, the photospheric temperature of the star, the density and the temperature of the gas. Other parameters, such as the dilution factor for the radiation field, are taken to be defined by the observed location of dust formation. The elemental abundances are given in Table 6.3. The cosmic ray ionisation rate is set to $10^{-17}s^{-1}$, which is representative of the assumed galactic background rate (Dalgarno 2006*b*).

6.2.1 The Chemistry

The chemical network includes 1537 reactions between 102 gas-phase species involving 8 elements (H, He, C, N, O, S, Na and Si). These are listed in Table 6.1.

The chemical complexity of the reactants was limited as we only concentrate on the initiating steps in the formation of larger molecular species.

Table 6.2: Main formation and destruction reactions of C_2H_2, rates from Woodall *et al.* (2007*b*)

	Reaction	Reaction rate
1	$CH_2 + CH_2 \rightarrow C_2H_2 + 2H$	$k_1 = 1.80 \times 10^{-10} e^{-400K/T}$
2	$CH_2 + CH_2 \rightarrow C_2H_2 + H_2$	$k_2 = 2.63 \times 10^{-9} e^{-6013K/T}$
3	$H^- + C_2H \rightarrow C_2H_2 + e^-$	$k_3 = 1.00 \times 10^{-9}$
4	$C^- + CH_2 \rightarrow C_2H_2 + e^-$	$k_4 = 5.00 \times 10^{-10}$
5	$C + CH_3 \rightarrow C_2H_2 + e^-$	$k_5 = 1.00 \times 10^{-10}$
6	$C + C_2H_2 \rightarrow C_3H + H$	$k_6 = 1.45 \times 10^{-10} \left(\frac{T}{300}\right)^{-0.12}$
7	$C + C_2H_2 \rightarrow C_3 + H_2$	$k_7 = 1.45 \times 10^{-10} \left(\frac{T}{300}\right)^{-0.12}$
8	$H^+ C_2H_2 \rightarrow C_2H_2^+ + H$	$k_8 = 5.40 \times 10^{-10}$
9	$H + C_2H_2 \rightarrow C_2H + H_2$	$k_9 = 3.80 \times 10^{-10} e^{-\frac{13634}{T}}$
10	$O + C_2H_2 \rightarrow CO + CH_2$	$k_{10} = 8.39 \times 10^{-12} \left(\frac{T}{300}\right)^{1.03} e^{-\frac{1197}{T}}$
11	$O + C_2H_2 \rightarrow C_2H + OH$	$k_{11} = 5.30 \times 10^{-9} e^{-\frac{8520}{T}}$
12	$He^+ + C_2H_2 \rightarrow CH^+ + CH + He$	$k_{12} = 7.70 \times 10^{-10}$
13	$He^+ + C_2H_2 \rightarrow C_2^+ + He + H_2$	$k_{13} = 1.61 \times 10^{-9}$
14	$He^+ + C_2H_2 \rightarrow C_2H^+ + He + H$	$k_{14} = 8.75 \times 10^{-10}$
15	$He^+ + C_2H_2 \rightarrow C_2H_2^+ + He$	$k_{15} = 2.54 \times 10^{-10}$
16	$C^+ + C_2H_2 \rightarrow C_3H^+ + H$	$k_{16} = 2.20 \times 10^{-9}$
17	$S^+ + C_2H_2 \rightarrow HC_2S^+ H$	$k_{17} = 9.50 \times 10^{-10}$
18	$Si^+ + C_2H_2 \rightarrow SiC_2H^+ + H$	$k_{18} = 1.30 \times 10^{-10} \left(\frac{T}{300}\right)^{-0.71} e^{-\frac{29}{T}}$
19	$Si^+ + C_2H_2 \rightarrow SiC_2H_2^+ + photon$	$k_{19} = 2.50 \times 10^{-10}$
20	$Si + C_2H_2 \rightarrow SIC_2 + H_2$	$k_{20} = 1.00 \times 10^{-13} \left(\frac{T}{300}\right)^{-1.00}$

The ratefile is an adapted set of reactions, applicable to high densities, high temperatures and intense radiation fields. Many of the reactions and rate coefficients (k_i) were taken from the UMIST database for Astrochemistry (Woodall *et al.* 2007*b*) where the formulation for the rate coefficients is valid in the operative temperature range. Additional data was taken from databases that are relevant to high temperature/high density environments (e.g. Rawlings *et al.* 1993; Lim *et al.* 2002; Pontefract & Rawlings 2004, etc.). Although the densities are very much larger than those applicable to interstellar studies. We have not included three-body reactions as the main formation reactions (Table 6.2) are not dependent on molecular hydrogen. Reaction types that are included in the chemistry are: charge transfer, ion-molecule, radiative association, neutral exchanges, radiative recombination, dissociative recombination and negative ion reactions. Reactions which are particularly significant in addition to those applicable to interstellar clouds are neutral-neutral reactions, reactions with significant activation energy barriers, and reactions between ro-vibrationally excited species, due to the high temperatures that exist in circumstellar outflows.

The main formation and destruction reactions for C_2H_2 are given in Table 6.2.

6.2.1.1 Photoreactions

In circumstellar environments, irradiated by the central star, the UV radiation field is typically very much stronger and has quite a different spectral shape to that whch pertains in the interstellar medium. It is therefore important that we pay particular attention to the correct evaluation of the photo-reaction rate coefficients: The rates for all photodissociation, photoionisation and photodetachment reactions are calculated *ab initio*.

In these conditions, the key factor in determining the viability of any chemical kinetic pathway that leads to dust-formation is therefore the stability of the intermediates against photodissociation/photoionisation by the stellar radiation field.

The calculation of the photorates by a time-dependent non-interstellar radiation field in an expanding atmosphere is a non-trivial task. There are two components to the calculation of the photoreaction rate-coefficients in the local radiation field:

1. a basic 'photospheric' rate, calculated for the specific photoreaction and radiation field
2. a time-dependent geometrical dilution, due to the expansion of the wind

In earlier models, and for the sake of simplicity, photoreaction rates were calculated by scaling the unshielded interstellar photorates by a ratio of the stellar flux to that of the interstellar radiation field, either by a single scaling factor, or by a value appropriate to a single characteristic wavelength for each reaction in question (Rawlings 1988). In this study we use a more accurate approach that can encompass the variety of situations that we wish to investigate: Photoreactions are calculated by fully integrating the known cross-sections and oscillator strengths (for line transitions) over the specified radiation field. Following van Dischoeck (1988) we treat the contributions to the photodissociation rate arising from continuous absorption and those arising from absorption in discrete transitions as separable. These can be written as

$$k_{pd}^{cont} = \int \sigma(\lambda) I(\lambda)\, d\lambda \,\mathrm{s}^{-1} \tag{6.1}$$

and

$$k_{pd}^{line} = \frac{\pi e^2}{mc^2} \lambda_{ul}^2 f_{ul} \eta_u x_l I(\lambda_{ul})\,\mathrm{s}^{-1} \tag{6.2}$$

respectively, where k is the photoreaction rate coefficient, λ is the wavelength, I_λ is the flux, $\sigma(\lambda)$ is the cross-section for the reaction, f_{ul} is the oscillator strength and the other symbols have

their usual meanings. Photoreaction cross-sectional data and oscillator strengths were taken from a variety of sources (e.g. van Dischoeck 1988; Rawlings *et al.* 1993) as described in Rollins & Rawlings (2012). We assume that the gas is within the carbon-neutral zone (equivalent to being behind the photodissociation region: As was shown in Rawlings (1988), complex chemistries are unsustainable in CII regions). We therefore assume that H_2 and CO are fully self-shielding and that carbon photoionization is effectively suppressed. The lower limit of the integral in equation 1 is therefore set to the ionization threshold for CI (1102Å).

This study is too generalised to consider the radiation fields of individual sources so we instead opt to characterise the radiation field by that of an (appropriately diluted) single temperature black-body (T_{BB}). In addition, as we have investigated a wide range of T_{BB} which may also be time-dependent, we have utilised a parametric fit to the dependence of the photoreaction rates to T_{BB}. Thus, after calculating the photospheric rates for several values of T_{BB} we fit a simple quadratic to the logarithm of the rates:

$$\log(k) = a + b.\log T_{BB} + c.\log(T_{BB})^2 \tag{6.3}$$

where the coefficients a, b and c are specific to each reaction and are defined for a certain temperature range. The ranges used are as specified in Table 6.3.

For the geometrical dilution we assume simple spherical symmetry, in which case, at a distance R from the star, the the dilution factor is given by

$$W = \left(\frac{R_\star}{2R}\right)^2 \quad R \gg R_\star, \tag{6.4}$$

where $R_\star$ is the photospheric radius of the star.

Finally, we include a (small) contribution to the photorate deriving from the local internally generated UV field induced by cosmic ray ionizations (Prasad & Tarafdar 1983; Gredel *et al.* 1989).

6.3 Physical and Chemical Parameters

We have investigated three different carbon-rich (C>O) astrophysical environments. We have studied acetylene formation in the outflows from:

1. Thermally pulsing asymptotic giant branch (AGB) stars,

2. Novae, and

Table 6.3: Physical and chemical parameter ranges for the three different cases being investigated.

	AGB	Nova	Stars of spectral Class G-K
[C/O]	1.5	21	1.5
Density Range (cm^{-3})	10^{11}–10^{14}	10^{11}–10^{14}	10^{11}–10^{14}
Photosphere Temperature (K)	1500–3500	15,000–25,000	3750–6000
Gas Temperature (K)	2000	2000	2000
Dilution Factor	0.111	$5.59x10^{-5}$	0.111
Period of shock (days)	650	100	135

3. G/K-type Carbon stars

The physical conditions are quite different in these three classes of objects, yet they are each known to be prolific sources of carbon dust.

Firstly, we have extended the work of Cherchneff *et al.* (1992), which modelled PAH formation in the post-shock gas in thermally pulsing asymptotic giant branch (AGB) stars. These are well known dust production sites. Including a more complete photochemistry has allowed us to determine more accurately the stability of C_2H_2 in this environment. We have applied our model to examine the viability of PAH formation in the ejecta around novae, some of which (but not all) are also known to be efficient dust-producers. We have also investigated the outflows from stars that are somewhat hotter than AGB stars, so that we can ascertain the possibility of soot chemistries operating in these circumstellar environments. The initial conditions selected for each of these three scenarios are discussed below.

There are considerable variations (and uncertainties) in the observationally inferred elemental abundances for each source type. However, the C:O ratio is a key parameter. This determines the efficiency of the hydrocarbon chemistry and, hence (whatever reaction pathway is followed) the viability of carbon dust formation. To effect the requisite variations in the C:O ratio we have adopted cosmic abundance values for all elements other than carbon; 0.85, 6.0×10^{-5}, 4.6×10^{-4}, 1.4×10^{-5}, 3.5×10^{-5} and 3.2×10^{-5} for He, N, O, S, Na and Si respectively. The abundance of carbon is then varied to give the (observed) C:O ratio as specified in Table 6.3.

6.3.1 Case I: AGB Stars

High carbon-oxygen ratios (> 2) are unlikely in the Galaxy (although common in the Large Magellanic Cloud) and are excluded. Lower ratios of C:O ~ 1.5 are expected for most carbon stars (Bergeat *et al.* 2001). Lambert *et al.* (1986) found slightly subsolar values for the oxygen and

Table 6.4: Table of nova parameters

Nova Parameter	30 days post-outburst
Rate of magnitude decline (optical), $\dot{m}_{\rm V}$	0.03 mag d^{-1}
Luminosity of nova, L_{nova}	31080
Photospheric radius, r_{phot}	25 $R_\odot$ (=$R_{p,0}$)
Photospheric temperature, T_{phot}	20,100 K

nitrogen abundances in AGB stars, but our approximation of using solar abundances is essentially valid. This is consistent with the abundances used by Cherchneff *et al.* (1992) and Cherchneff (2012) to model an AGB star that is similar to the well-known source IRC+10216.

We assume the shocks form at 1.5 stellar radii from the star and the gas has a kinetic temperature of 2000 K with a maximum density of 10^{14} cm^{-3}. The outflows undergo periodic shocks due to stellar pulsations. We model the time-dependent chemistry that would occur in a single shock with a period of 650 days. This follows the physical parameters used by Cherchneff (2012), allowing us to compare our results to distinguish the effects of including a complete photochemistry. In a study of 390 carbon rich stars by Bergeat *et al.* (2001), the highest effective temperature evaluated was 3870 $\pm$ 1080 K. We have therefore investigated photospheric temperatures in the range T=1500-3500K. The initial conditions and parameter ranges that we consequently adopt for AGB outflows are given in Table 6.3.

6.3.2 Case II: NOVAE

It has long been established that dust is sometimes formed, rapidly and efficiently, in nova outflows (e.g. Gallagher 1977). In the most extreme circumstances, a steep decrease in the visual emission occurs, accompanied by a strong rise in thermal infrared emission - as an optically thick dust shell is formed (Clayton & Wickramasinghe 1976). Following Rawlings (1988), we adopt the following relations between the physical parameters:

$$\Delta m_{\rm V} = \dot{m}_{\rm V} \times t_0, \tag{6.5}$$

$$L_{nova} = 1.036 \times 10^6 \times \dot{m}_{\rm V}, \tag{6.6}$$

$$r_{phot} \sim 9.97 \times 10^9 \times L_{nova}, \tag{6.7}$$

$$T_{phot} = 15280 \times 10^{(\frac{\Delta m_{\rm V}}{7.5})}, \tag{6.8}$$

where $\dot{m}_V$ is the rate of magnitude decline in the optical, r_{phot} is the initial photospheric radius, L_{nova} is the nova luminosity and t_0 is the number of days post outburst.

The values for the rate of visual decline from maximum ($\dot{m}_v = 0.03$ mag d^{-1}) and time at start of calculation (t_0= 30 days post outburst) were adopted following Rawlings & Williams (1989). Novae can be classed by the time taken for a nova to diminish by 2 magnitudes below maximum visual brightness. Generally, 'slower' novae (i.e. those with smaller values of $\dot{m}_v$) are more effective at producing optically thick shells of carbon dust. Parameters for a typical dust-producing nova are given in Table 5 and are used in our model. The parameter range investigated and initial conditions are given in the Table 6.4. The fractional abundance of carbon is much higher than in the case of AGB stars (Rawlings & Williams 1989). This is due to the thermonuclear processing of the gas and dredge-up of white dwarf material that occurs following the thermonuclear runaway that drives the nova outburst.

6.3.3 Case III: Carbon Stars in Spectral Class G-K

We investigate stars with photospheric temperatures in the range 3750–6000K. Low mass main sequence stars are not likely to have a high C:O ratio. However, CH subgiants are low luminosity peculiar giants, which have a high C:O ratio in their atmosphere as a result of mass transfer from an evolved companion (Smith *et al.* 1993). The upper limit of C:O observed in these stars is 1.5 (Luck & Bond 1982). The parameter ranges chosen to represent these objects are given in Table 6.3. We have optimised the parameters for dust production by only considering the highest values possible for the C:O ratio and the gas density. The maximum period of these pulsating stars are 135 days (Good 2003).

6.4 Results

C_2H_2 formation is a necessary, but not sufficient, criterion for carbon dust formation via PAH chemistry in hydrogen-rich environments. Therefore we need to establish the conditions needed for a positive result, i.e. the minimum fractional abundance of C_2H_2 that will explain the requisite abundance of dust nucleation sites. To do this, we follow Rawlings & Williams (1989); where the number of grains is equated to the number of nucleation sites. Considering the case of a nova, the number of grains, N_g, inferred from infrared observations is $\sim 7 \times 10^{38}$ (Clayton & Wickramasinghe 1976). The dust shell condenses at a radius $r_c \sim 8 \times 10^{14}$ cm, and has a typical thickness of $\sim r_c/10$. The shell volume is therefore $V \sim 6 \times 10^{44}\,\mathrm{cm}^3$, implying a number density

of grains of $\sim 10^{-6}$ cm^{-3}. Note that this is a lower limit, subject to the ejecta configuration. The gas density is $\sim 10^{9}$ cm^{-3}, hence the minimum fractional abundance of nucleation sites needed is 10^{-15}. On the assumption that each C_2H_2 molecule is efficiently converted into a nucleation site (i.e. that there are no kinetic bottlenecks in the formation of larger molecules), we can very crudely adopt this value as the threshold for the minimum fractional abundance of acetylene which can promote a PAH-driven dust formation pathway. Although this criteria is derived from a gas density that is lower than the range we explore in this work, we apply it as a lower bound on the amount nucleation sites we expect within our parameter space. We understand this is a very crude assumption, as C2H2 rich environments may not always translate to efficient PAH formation. However, this acts as a primary filter allowing us to establish which environments which will definitely not be effective in forming PAHs.

Results from our models are shown in Figures 6.1-6.3 as contour plots of the equilibrium abundance of C_2H_2 as a function of density and photospheric temperature. We discuss the results for the three cases in sections §6.4.1 - §6.4.3.

6.4.1 Case I: AGB

The results for AGB winds are presented in Figure 6.1. The upper figure shows that the C_2H_2 abundance is not strongly sensitive to the density. There is, however, a strong dependence on the photospheric temperature. For photospheric temperatures below ~2500K, C_2H_2 can be produced with the requisite efficiency for any density within the range explored ($\sim 10^{11} - 10^{14}$cm^{-3}). The lack of sensitivity to density implies that *if* C_2H_2 leads to PAH formation, then the production of dust will not be critically limited to the geometrical dilution of the wind. For comparison, the lower plot in Figure 6.1 displayed the results for the same gas temperature and density range, but does not include the effects from the stellar radiation field. The photorates from the interstellar radiation field are included. We can see that even at low photospheric temperatures ($T_{eff} < 2500$ K), the radiation field from the star plays a key role by reducing the amount of acetylene that is present. Only at high densities $n \gtrsim 10^{13}$ cm^{-3} within this range is the gas moderately shielded. Therefore models such as Cherchneff (2012) which exclude ion-molecule chemistry and a radiation field, should be extended to investigate such effects. As this the radiation field could reduce C_2H_2 abundance by a factor of $\times 10^2 - 10^4$ within gas at densities $n < 10^{13}$ cm^{-3}.

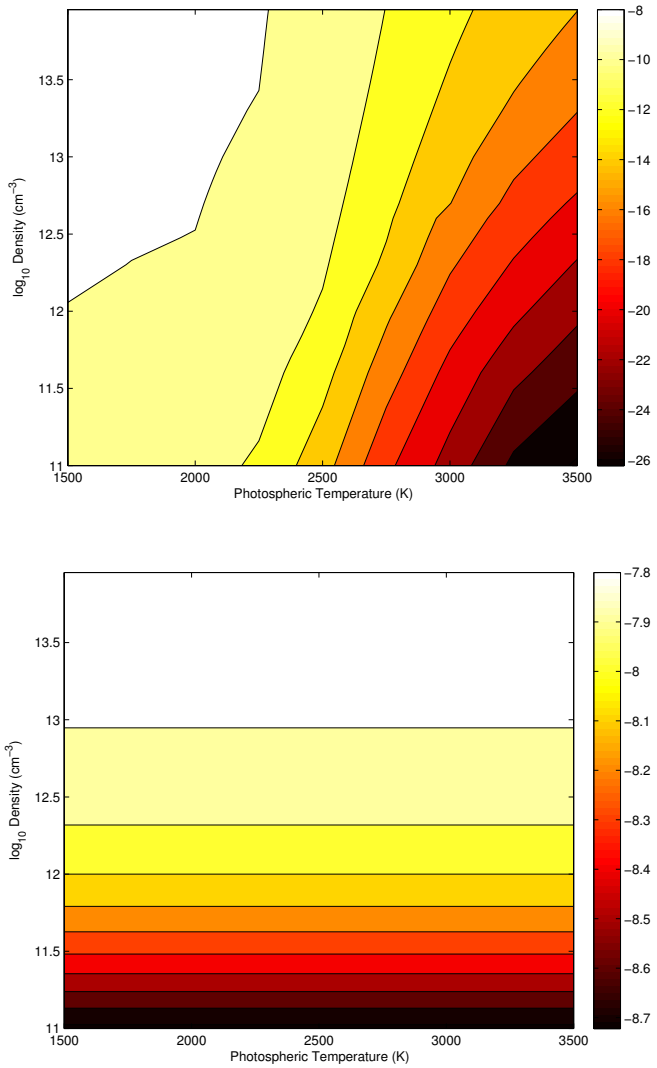

Figure 6.1: The upper contour plot shows results from a model which includes photorates from the both the stellar radiation filed and the interstellar radiation; the lower plot displays the results from a model which only includes photorates from the interstellar radiation field. Both legends display the logarithm of the fractional abundance of C_2H_2, in the circumstellar envelope of a carbon-rich AGB star after 650 days. The density and photospheric temperature are treated as free parameters. All other parameters are fixed and given values as specified in Table 6.3.

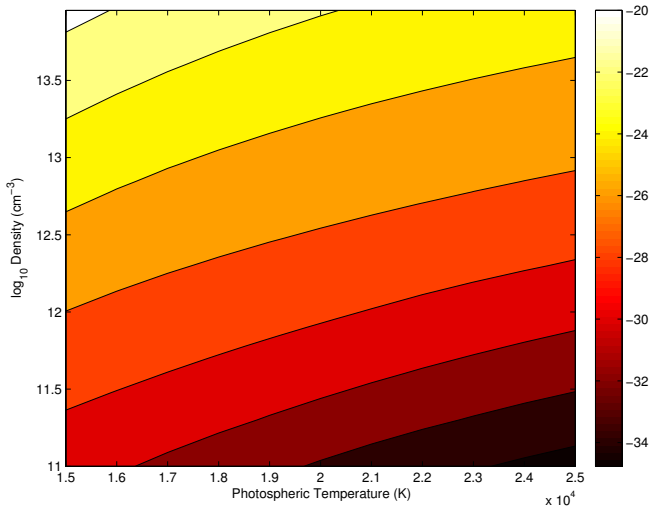

Figure 6.2: Contour plot showing the logarithm of the fractional abundance of C_2H_2 in the ejecta from a nova after 100 days. The density and photospheric temperature are treated as free parameters. All other parameters are fixed and given values as specified in Table 6.3.

6.4.2 Case II: Nova

The results for nova outflows are presented in Figure 6.2 and show the opposite trends what was found for AGB winds; there is a stronger dependence on density, compared to a weak dependence on photospheric temperature. Despite the high abundance of carbon in novae (Starrfield *et al.* 2000), the photospheric temperatures are ten times higher than for AGB stars and, even after significant geometrical dilution is taken into account, C_2H_2 is highly susceptible to photodissociation and never attains appreciable abundances. This is a strongly negative result and supports the findings of previous studies (e.g. Rawlings & Williams 1989) - C_2H_2 can not be produced in irradiated nova environments at abundance levels sufficient to seed dust formation via PAH chemistry.

6.4.3 Case III: Stars in Spectral Class G-K

Results for the circumstellar environment of carbon-rich stars with photospheric temperatures of 3750–6000K are presented in Figure 6.3. The critical fractional abundance of C_2H_2 is not reached. However, for the lowest photospheric temperatures (T<4400 K) and highest densities (n$>10^{13}$ cm^{-3}) the abundance is closer to the threshold than was the case for the nova outflows. We can conclude that, whilst the spherically symmetric model produces a negative result.

However, unlike the situation with AGB outflows, this result is not robust to density variations so, if the clumps were to dissipate within the temperature window for PAH formation then the

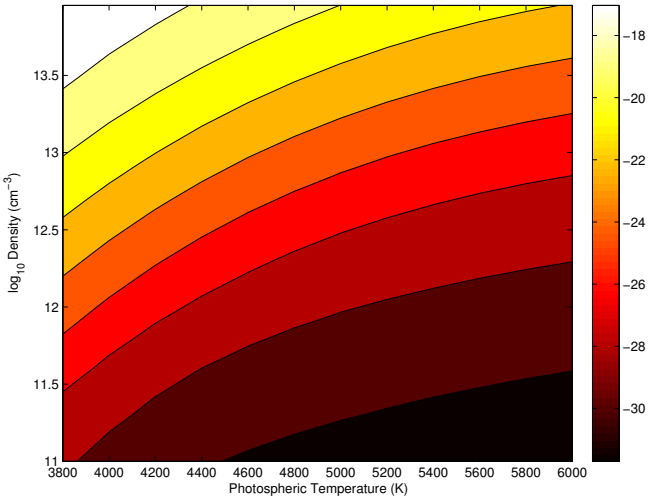

Figure 6.3: Contour plot showing the logarithm of the fractional abundance of C_2H_2 after 135 days in the circumstellar environment of a star with spectral class G-K. The density and photospheric temperature are treated as free parameters. All other parameters are fixed and given values as specified in Table 6.3.

C_2H_2 abundance (and dust formation efficiency) would be strongly diminished.

6.5 Conclusions

We have used a simple model of the time-dependent chemistry of several different astrophysical dust forming environments to consider the stability of acetylene (C_2H_2). In previous studies of dust formation, based on terrestrial flame chemistries, this molecule is a precursor to PAH formation and so its presence at appreciable abundance levels can be used to establish the viability of PAH formation and, by inference, dust formation based on PAH condensation chemistry. However, C_2H_2 is highly susceptible to photodissociation by stellar ultraviolet. The novel approach in this study is that we have carefully calculated the photodissociation rates for the molecular species involved in the C_2H_2 chemistry, subject to the local radiation field. Previous studies had made major simplifying assumptions in this respect.

In each case we have investigated the dependence of the C_2H_2 abundance as a function of gas density and photospheric temperature. In general, we find that the inclusion of accurate photorates significantly restricts the parameter space within which efficient C_2H_2 formation (and hence, presumably, PAH formation) can occur.

In the case of the winds driven by thermally pulsing AGB stars, we find that - as in previous studies - C_2H_2 can be formed very efficiently indeed and that a PAH chemistry is therefore at least a viable pathway for carbon dust formation in these environments. This is an interesting results as some previous studies (which have not included photochemistry in their modelling) have not been so successful at producing C_2H_2 (e.g. Cherchneff *et al.* 1992; Helling *et al.* 1996). However, we find that this positive result only holds for photospheric temperatures that are $<$2500 K. There are dust-producing carbon AGB stars with photospheric temperatures $\sim$ 3500K (e.g. Eglītis & Eglīte 1995). If we were to include a more accurate physical model of the outflows, including shocks and clumping, a PAH chemistry may also be applicable in these objects. For example studies such as Cherchneff (2012) can reach C_2H_2 fractional abundances of 10^{-4} including shock chemistry and neglecting a UV field. Our studies show that photoreactions that occur in AGB outflows can also have a strong effect on the chemistry, and therefore shock models of these outflows need to include these effects.

As compared to the dust-forming environment of AGB stars, the ejecta of novae are subject to a much stronger radiation field with a significantly higher black-body temperature. The photodissociation rates for unshielded molecular species, such as C_2H_2, are very much larger than in the other sources considered in this study (e.g. Rawlings & Williams 1989). As a result C_2H_2 can never attain significant abundances. Of course, other factors should be taken into account - such as possible variations in the elemental abundances in the ejecta - but the extreme clumping required is incompatible with the observed spherical coverage of the optically thick dust shell in these objects. In this case, it seems that other (non PAH-based) formation channels must be operating - involving species that can survive the intense radiation field (e.g. C_2, which is partly shielded by the carbon ionization continuum Rawlings & Williams (1989)).

Finally, CH subgiants have physical characteristics that are closer to Main Sequence stars than stars in the Giant phase. They have lower luminosities than equivalent stars on the Main Sequence and are known to be chemically peculiar (Smith *et al.* 1993), having a carbon over-abundance. The winds from these stars are not expected to have the same shock-generated density enhancements as in the AGB outflows. Thus, even with the extreme parameters we have chosen, we still obtain a negative result within the inner wind. Again, an environment that is conducive to C_2H_2-PAH chemistry may exist in the outer winds if significant clumping occurs, but it would seem that alternative dust formation pathways are more likely in these environments.

In summary, we find that C_2H_2 (and PAH) formation is at least viable in AGB outflows, but is

only possible in the winds of CH subgiants if significant clumping is present in outer winds, and is not possible at all in nova winds. It is evident that though the physical parameters of the gas are similar in all three cases - the spectrum of the radiation field has a significant effect on acetylene production. Therefore, on the basis of these studies, it is evident that the formation pathway for (carbon) dust cannot be the same in all environments; in particular, the modified flame-PAH chemistries that provide a plausible formation channel in the dust-rich winds of thermally pulsing AGB stars cannot be applied to environments such as novae. It would therefore seem that multiple (and, as yet, largely undefined) pathways for the kinetic formation of carbon dust exist.

CHAPTER 7

CONCLUDING REMARKS AND PROPOSAL FOR FUTURE WORK

The coupling of non-equilibrium chemistry and cooling to a multidimensional hydrodynamic code, is required to accurately model low-metallicity supernova shocks. The work presented in this thesis highlights the need to include the all relevant physical processes that affect the microphysics of the gas.

In Chapter 2 we first try to understand the chemistry that would occur in a metal-free cloud that has been mixed with ejecta from a single supernova. We investigate the chemical evolution from three different SN yields, in both a stable cloud and a cloud undergoing gravitational collapse. For the range of initial conditions we investigated for a stable cloud, it has been shown that if the cloud density is n$< 100\,\mathrm{cm}^{-3}$, CO and H_2O are the most abundant tracers. When it is possible to observe molecules at redshift $z > 10$, these would be most observable as they can reach fractional abundances above 10^{-12}. If the cloud being observed has only been seeded by a single supernova, these molecular tracers would not be useful to constrain the progenitor mass of the star that underwent the supernova explosion. The chemistry occurring in low-metallicity clouds is not dependent on H_2 and is driven by atomic reactions. The molecular tracer that could constrain the progenitor mass is NO, though it is does not reach abundances that could be observable. Nitrogen is an element that differs significantly in the SN yield from the three different progenitor masses. This is subject to the accuracy of these computational SN yields. The other molecular tracers have abundances that are very low and so have very little chance of being observed. For the formation of

the molecule CO the most advantageous environment is: high density, high temperature, a high abundance of dust grains, a low ionisation rate from cosmic rays and shielded from UV radiation.

We also considered gas that may undergo collapse, which reached a maximum density of $10^7\,\mathrm{cm}^{-3}$ and the temperature remained constant at 100 K. The increase in density causes all the molecular tracers to increase in abundance. The molecules CO and H_2O have a significant increase in their abundances and would be the most likely to be observed. The inclusion of cosmic rays has a small effect on molecules that rely on neutral-neutral reactions but a significant effect on NH_3 and HCO^+, which depend on the ionisation fraction of the cloud. Neither of these molecules could be observed. The best molecular tracer of progenitor mass in this case is CS which has a fractional abundance above 10^{-12} for all three cases, and the difference in sulphur abundance between the three SN yields is significant.

The second infall model we consider reaches a maximum density of $10^{10}\,\mathrm{cm}^{-3}$ and has the associated temperature increase to 1000 K to represent the environment of a hot core. The ionisation fraction becomes very small and the molecular fraction of the gas increases greatly. The fractional abundance of H_2 becomes 0.01 and the nearly all of the carbon and nitrogen atoms are 'locked up' in CO and NO. The cosmic ray ionisation rate has very little effect on these molecules. In conclusion CO and H_2O have large enough abundances in high density gas ($n > 10^7$ cm^{-3}) to be observed. Theoretically, at late times NO is the best tracer of progenitor mass as for two cases (150 & 200 $M_\odot$) the abundances are observable. However for the 80 M$\odot$ case is the abundance of NO only reaches $\sim 10^{-14}$. Other molecules have very small abundances in this environment. Hence cooler dense gas such as described in the previous infall case with constant temperature is a favourable environment to distinguish the molecular tracers of progenitor mass.

We go on to couple a metal-free chemistry to a hydrodynamics code in Chapter 3 and investigate the shock-driven fragmentation of a metal-free clump (13 $M_\odot$) that interacts with a supernova shock at redshift $z = 10$. A microphysics module was developed so the non-equilibrium chemistry and associated cooling that occurs at all temperatures can be followed. Our model has improved upon these studies by modelling a multiphase medium with multidimensional simulations. We once the shock passes through the cloud in fragments into small dense clumps. The largest clump has mass of $\sim$0.3 $M_\odot$. However, these clumps are not gravitationally bound and are unlikely to become star forming sites. In order to ascertain the dominant processes that affect the chemistry and hence thermal state of the gas, we explored the affect of cosmic rays, deuterium chemistry,

CMB ionisation and H_2 heating. For the density range of our simulations $n < 10^3$, we find the cosmic ray ionisations can make quit a difference to the mass of the clumps. X-rays were not considered in this work but are recommended for for future work.

In Chapter 4 we present a self consistent metal-free SN model which investigates the fragmentation of interstellar clumps. To obtain the initial conditions of the SN model we simulate the formation of a HII region around a 40 $M_\odot$ star in a number of gas clouds with differing density profiles. As the explosion mechanism for this star is not well understood, we investigate a range of explosion energies and their impact on compression and fragmentation of the clump. We wanted to constrain the environment which is favourable to form dense clumps which may produce low-mass stars ($< 1\,M_\odot$). We argue that dense clumps that compress when interacting with a shock could form HMP stars similar to SDSS J102915+172927, as these clumps are expected to accrete less of the surrounding metal-rich material (Reach *et al.* 2005).

We have investigated a hypernova interacting with a dense clump ($n = 100$ cm^{-3}, $r = 1$ pc) embedded in a 10 cm^{-3} ambient cloud and is 40 pc from the progenitor star. We followed the evolution of the supernova remnant and its interaction with the surrounding ionised and neutral medium. When the radiative shell interacts with the metal-free clump, the clumps reaches a maximum of density ~ 78000 cm^{-3}. This is a $10^{2.89}$ density enhancement and is consistent with Galactic shock-cloud models considering solar metallicity gas with equilibrium cooling functions. The clump undergoes a reduction in Jeans mass from 10^5 $M_\odot$ to 10^3 $M_\odot$, but does not become gravitationally unstable. Further work is required to ascertain the effects of X-rays and UV radiation on the clump during the supernova phase.

In this chapter we have shown that an appreciable Jean mass reduction of a small dense clump is achieved and the density enhancement comparable to Galactic studies, by including non-equilibrium metal-free radiative cooling. Further refinement of this model by including low-metallicity chemistry and thermal models plus positive feedback effects from X-rays and UV radiation, may cause a further reduction in Jeans mass. Galactic models should be extended to include non-equilibrium cooling, as this work has shown that it is the dominant process in shock-cloud interactions.

In Chapter 5 we go onto investigate metal line cooling and cooling from CO, OH and H_2O. As our aim was to determine the affect of chemistry and cooling from different metal models, we implement the toy model from Chapter 3 , with a gas of metallicity Z= 10^{-3} $Z_\odot$. This is a much

higher metallicity than the star found by Caffau *et al.* (2011) but it gave us the opportunity to investigate the affect of metal line cooling compared to including molecular cooling as well, as the difference between the two models would be increased at this metallicity. We found that metal line cooling allows much larger but less dense clumps to form, due to quicker recombination times, there is a reduction in free electrons at lower temperatures and therefore a reduction in H_2. We found that the molecular cooling (from CO, OH & H_2O) had negligible affect in the density range of out simulations ($n < 10^3\,\mathrm{cm}^{-3}$).

We also explored a 1D SN model which included dust cooling and focused on the evolution of a SN shell with metallicity Z= 10^{-5} $Z_\odot$. When we compared our results with Chiaki *et al.* (2013), we found that dust and metal-non-LTE cooling causes the formation of the SN shell to occur at much earlier times. Given these positive results, the metal-dust model should be extended to to 2D shock-cloud model for a gas of metallicity of Z= 10^{-5} $Z_\odot$. If this is done with with cosmological initial conditions, we may gain further insight into the formation of the HMP star SDSS J102915+172927. The explosion of stars within the first galaxies is a complex system to model with many important unconstrained parameters; for example the spectrum of cosmic rays present, X-ray and UV radiation fields. The nature and production of dust at high redshift is also poorly constrained, it would recommended to extend the dust model by exploring different sizes of dust grains and possible destruction mechanisms.

Even though the physical properties of dust in the local ISM is well constrained, the formation pathways are still under discussion. In Chapter 6 we have carried out an investigation of the chemical evolution of gas in different carbon-rich circumstellar environments. We pay careful attention to the accurate calculation of the molecular photoreaction rate coefficients to ascertain whether there is a universal formation mechanism for carbon dust in strongly irradiated astrophysical environments. A large number of possible chemical channels may exist for the formation of PAHs, so we have concentrated on the viability of the formation of the smallest building block species, C_2H_2, in a variety of carbon-rich stellar outflows. We find that C_2H_2 (and PAH) formation is viable in AGB outflows, and is not possible at all in nova winds and CH subgiants. Therefore, on the basis of these studies, it is evident that the formation pathway for (carbon) dust cannot be the same in all environments; in particular, the modified flame- PAH chemistries that provide a plausible formation channel in the dust-rich winds of thermally pulsing AGB stars cannot be applied to environments such as novae. It would therefore seem that multiple pathways for the kinetic formation of carbon dust exist.

APPENDIX A

CHEMISTRY NETWORK

All the molecular reaction rates that have been adapted for the temperature range ($10 - 10^{12}$ K) have been divided into two catorgories: i) Formation rates (displayed in Tables A.1 & A.4) and ii) Destruction rates (displayed in Table s A.2 & A.3).

The destruction rates are extrapolated above their valid temperature range. If there is a maximum value after which the rate decreases (T_{ex}), this maximum value is kept constant for all higher temperatures ($T > T_{ex}$). All the destruction rates, with the corresponding maximum extrapolation temperatures and temperatures ranges are displayed in TableA.2.

If the formation rates are valid to a temperature below 41,000 K the value at upper tempraturature range is kept constant until 41,000K. After this point all rates (K) are treated in either of the two ways:

$$K_1 = k \times \exp\left(1.0 - \frac{\mathrm{T}}{41000.0}\right) \text{ or } K_2 = k \times \exp\left(10 \times \left(1.0 - \frac{\mathrm{T}}{41000.0}\right)\right)$$

where k is the value of the rate at 41000K. The details of how each reaction is cut-off is fund in Table A.1.

Reaction Number	Valid Temperature Range (K)	Below Minimum Temperature	Above Maximum Temperature	Cut off Type T >41000K
R16	S:10 – 32000	-	C	CT2
R17	16 – 100	C	E	CT
R18	S:10 – 41000	-	-	CT2
R29	10 – 41000	-	-	CT
R30	10 – 41000	-	-	CT
R33	10 – 41000	-	-	CT
R34	10 – 41000	-	-	CT
R35	10 – 41000	-	-	CT
R36	S:10 – 41000	-	-	CT
R53	10 – 10000	-	C	CT
R54	10 – 10000	-	C	CT
R55	10 – 10000	-	C	CT
R56	10 – 10000	-	C	CT
R57	10 – 10000	-	C	CT
R58	10 – 10000	-	C	CT
R59	10 – 10000	-	C	CT
R60	10 – 10000	-	C	CT
R61	10 – 10000	-	C	CT
R61	10 – 10000	-	C	CT
R63	10 – 10000	-	C	CT
R64	10 – 10000	-	C	CT
R65	10 – 10000	-	C	CT
R66	10 – 10000	-	C	CT
R67	10 – 10000	-	C	CT
R68	10 – 10000	-	C	CT

Table A.1: Molecular reactions that are cut-off at 41000 K: E= rate extrapolated; C= max/min value kept constant and extended; - = Not Applicable; S= switching between different reaction rates within temperature range; CT2= $k \exp\left(10.0 \times (1.0 - T/4.1e4)\right)$ and CT= $k \exp\left(1.0 - T/4.1e4\right)$ are exponential cut-off and k is the value of the reaction rate at 41000 K

Reaction Number	Valid Temperature Range of Rate (K)	Below Range	Above Range	Maximum Extrapolation Temperature T_{ex} (K)
M48	10 – 41000	E	E	1.0E12
M55	10 – 41000	E	E	1.0E12
M62	10 – 300	E	E	1.0E12
M63	10 – 1000	E	E	1.0E12
M64	10 – 1000	E	E	1.0E12
M65	10 – 1000	E	E	1.0E12

Reaction Number	Valid Temperature Range of Rate (K)	Below Range	Above Range	Maximum Extrapolation Temperature T_{ex} (K)
M66	10 – 1000	E	E	1.0E12
M67	10 – 300	E	E	1.0E12
M68	10 – 300	E	E	1.0E12
M69	2000 - 10000	E	E	1.0E12
M70	2000 - 10000	E	E	1.0E12
M71	1763 - 41000	E	E	1.0E12
M72	1763 - 41000	E	E	1.0E12
M73	1340 - 41000	E	E	1.0E12
M74	1743 - 41000	E	E	1.0E12
M75	10 – 41000	E	E	1.0E12
M76	10 – 41000	E	E	1.0E12
M77	10 - 41000	E	E	1.0E12
M78	10 – 41000	E	E	1.0E12
M79	10 – 41000	E	E	1.0E12
M87	10 – 41000	E	E	1.0E12
M88	10 – 41000	E	E	1.0E12
M89	10 – 41000	E	E	1.0E12
M91	3400 –41000	E	E	1.0E8
M92	3400 –41000	E	E	1.0E8
M93	3400 –41000	E	E	1.0E8
M94	3400 –41000	E	E	1.0E8
M95	3400 –41000	E	E	1.0E8
M96	3400 –41000	E	E	1.0E8
M97	3400 –41000	E	E	1.0E8
M98	3400 –41000	E	E	1.0E8
M99	3400 –41000	E	E	1.0E8

Reaction Number	Valid Temperature Range of Rate (K)	Below Range	Above Range	Maximum Extrapolation Temperature T_{ex} (K)

Table A.3: Molecular reactions adapted to maximum temperature (10^{12} K): E= rate is extrapolated to a maximum Extrapolation Temperature (T_{ex}) and then extended as a constant after that temperature; C= max/min value kept constant; - = Not Applicable; S= switching within temperature range

Reaction Number	Valid Temperature Range of Rate (K)	Below Range	Above Range	Maximum Extrapolation Temperature T_{ex} (K)
R07	1833 – 41000	E	E	1.0E12
R08	10 – 10000	-	C	-
R09	10 – 10000	-	C	-
R10	2803 – 41000	E	E	1.0E7
R11	10 – 41000	-	E	1.0E5
R12	100 – 300	E	E	1.0E8
R13	3400 –41000	E	E	1.0E8
R14	3400 –41000	E	E	1.0E8
R15	3400 –41000	E	E	1.0E8
R19	10 – 300	-	E	1.0E12
R20	10 – 300	-	E	1.0E12
R21	10 – 1000	-	E	1.0E12
R22	10 – 1000	-	E	1.0E12
R23	10 – 10000	-	C	-
R24	S:10 – 41000	-	C	-
R25	10 – 300	-	E	1.0E12
R26	10 – 300	-	E	1.0E4
R27	10 – 300	-	E	1.0E12
R28	10 – 300	-	E	1.0e12
R31	10 – 300	-	E	1.0e12
R32	10 – 41000	-	E	1.0e12
R45	10 – 200000	-	C	-
R46	10 – 200000	-	C	-
R47	10 – 10000	-	C	-
R48	10 – 10000	-	C	-
R49	3400 –41000	E	E	1.0E8
R50	3400 –41000	E	E	1.0E8
R51	1833 – 41000	E	E	5.5E4
R52	2803 – 41000	E	E	1.0E7

Table A.2: Molecular reactions adapted to maximum temperature (10^{12} K): E= rate is extrapolated to a maximum Extrapolation Temperature (T_{ex}) and then extended as a constant after that temperature; C= max/min value kept constant; - = Not Applicable; S= switching within temperature range

Reaction Number	Valid Temperature Range (K)	Below Minimum Temperature	Above Maximum Temperature	Cut off Type T >41000K
M29	10 – 41000	-	-	CT
M30	10 – 41000	-	-	CT
M31	10 – 41000	-	-	CT
M32	10 – 41000	-	-	CT
M33	10 – 41000	-	-	CT
M34	10 – 41000	-	-	CT
M35	10 – 41000	-	-	CT
M36	10 – 41000	-	-	CT
M37	10 – 41000	-	-	CT
M38	10 – 41000	-	-	CT
M39	10 – 41000	-	-	CT
M40	10 – 41000	-	-	CT
M41	10 – 41000	-	-	CT
M42	10 – 41000	-	-	CT
M43	10 – 41000	-	-	CT
M44	10 – 41000	-	-	CT
M45	10 – 41000	-	-	CT
M46	10 – 41000	-	-	CT
M47	10 – 41000	-	-	CT
M49	10 – 41000	-	-	CT
M50	10 – 41000	-	-	CT
M51	10 – 41000	-	-	CT
M52	10 – 41000	-	-	CT
M53	10 – 41000	-	-	CT
M54	10 – 41000	-	-	CT
M56	10 – 41000	-	-	CT
M57	10 – 41000	-	-	CT
M58	10 – 41000	-	-	CT
M59	10 – 41000	-	-	CT
M60	10 – 41000	-	-	CT

Reaction Number	Valid Temperature Range (K)	Below Minimum Temperature	Above Maximum Temperature	Cut off Type T >41000K
M61	10 – 41000	-	-	CT
M80	10 – 41000	-	-	CT
M81	10 – 41000	-	-	CT
M82	10 – 41000	-	-	CT
M83	10 – 41000	-	-	CT
M84	10 – 41000	-	-	CT
M85	10 – 41000	-	-	CT
M86	10 – 41000	-	-	CT
M90	10 – 41000	-	-	CT

Table A.4: Molecular reactions that are cut-off at 41000 K: E= rate extrapolated; C= max/min value kept constant and extended; - = Not Applicable; S= switching between different reaction rates within temperature range; CT2= $k \exp\left(10.0 \times (1.0 - T/4.1e4)\right)$ and CT= $k \exp\left(1.0 - T/4.1e4\right)$ are exponential cut-off and k is the value of the reaction rate at 41000 K

Bibliography

Abel, T., Anninos, P., Zhang, Y. & Norman, M. L., 1997, *New Astronomy*, **2**, 181

Abel, T., Bryan, G. L. & Norman, M. L., 2002, *Science*, **295**, 93

Abel, T., Wise, J. H. & Bryan, G. L., 2007, ApJ, **659**, L87

Ahn, K. & Shapiro, P. R., 2007, MNRAS, **375**, 881

Andrea, J., Drechsel, H. & Starrfield, S., 1994, A&A, **291**, 869

Aoki, W., Frebel, A., Christlieb, N., Norris, J. E., Beers, T. C., Minezaki, T., Barklem, P. S., Honda, S., Takada-Hidai, M. & et al., 2006, in S. Kubono, W. Aoki, T. Kajino, T. Motobayashi & K. Nomoto (eds.), *Origin of Matter and Evolution of Galaxies*, volume 847 of *American Institute of Physics Conference Series*, pp. 53–58

Arzoumanian, D., André, P., Didelon, P., Könyves, V., Schneider, N., Men'shchikov, A., Sousbie, T., Zavagno, A., Bontemps, S., di Francesco, J., Griffin, M. & et al., 2011, A&A, **529**, L6

Asplund, M., Grevesse, N., Sauval, A. J. & Scott, P., 2009, ARA&A, **47**, 481

Badnell, N. R., 2006, ApJS, **167**, 334

Ballesteros-Paredes, J., Klessen, R. S., Mac Low, M.-M. & Vazquez-Semadeni, E., 2007, *Protostars and Planets V*, 63

Bayet, E., Davis, T. A., Bell, T. A. & Viti, S., 2012, MNRAS, **424**, 2646

Bayet, E., Viti, S., Williams, D. A. & Rawlings, J. M. C., 2008, ApJ, **676**, 978

Beers, T. C. & Christlieb, N., 2005, ARA&A, **43**, 531

Beers, T. C., Preston, G. W. & Shectman, S. A., 1992, AJ, **103**, 1987

Bergeat, J., Knapik, A. & Rutily, B., 2001, A&A, **369**, 178

Bernatowicz, T. J., Croat, T. K. & Daulton, T. L., 2006, *Origin and Evolution of Carbonaceous Presolar Grains in Stellar Environments*, pp. 109–126

Bertoldi, F., Carilli, C. L., Cox, P., Fan, X., Strauss, M. A., Beelen, A., Omont, A. & Zylka, R., 2003, A&A, **406**, L55

Bertoldi, F. & McKee, C. F., 1990, ApJ, **354**, 529

Blondin, J. M. & Ellison, D. C., 2001, ApJ, **560**, 244

Boonman, A. M. S., van Dishoeck, E. F., Lahuis, F., Doty, S. D., Wright, C. M. & Rosenthal, D., 2003, A&A, **399**, 1047

Boss, A. P., 1995, ApJ, **439**, 224

Boss, A. P. & Keiser, S. A., 2010, ApJ, **717**, L1

Bromm, V., Coppi, P. S. & Larson, R. B., 2002, ApJ, **564**, 23

Bromm, V., Ferrara, A., Coppi, P. S. & Larson, R. B., 2001, MNRAS, **328**, 969

Bromm, V. & Larson, R. B., 2004, ARA&A, **42**, 79

Bromm, V. & Loeb, A., 2003, Nature, **425**, 812

Bromm, V. & Yoshida, N., 2011, ARA&A, **49**, 373

Bromm, V., Yoshida, N., Hernquist, L. & McKee, C. F., 2009, Nature, **459**, 49

Cadwell, B. J., Wang, H., Feigelson, E. D. & Frenklach, M., 1994, ApJ, **429**, 285

Caffau, E., Bonifacio, P., François, P., Sbordone, L., Monaco, L., Spite, M., Spite, F., Ludwig, H.-G., Cayrel, R., Zaggia, S., Hammer, F., Randich, S., Molaro, P. & Hill, V., 2011, Nature, **477**, 67

Caffau, E., Bonifacio, P., François, P., Spite, M., Spite, F., Zaggia, S., Ludwig, H.-G., Steffen, M., Mashonkina, L., Monaco, L., Sbordone, L., Molaro, P., Cayrel, R., Plez, B., Hill, V., Hammer, F. & Randich, S., 2012, A&A, **542**, A51

Cazaux, S. & Spaans, M., 2004, ApJ, **611**, 40

Ceccarelli, C., Hily-Blant, P., Montmerle, T., Dubus, G., Gallant, Y. & Fiasson, A., 2011, ApJ, **740**, L4

Cen, R. & Riquelme, M. A., 2008, ApJ, **674**, 644

Cherchneff, I., 2009, in T. Henning, E. Grün & J. Steinacker (eds.), *Cosmic Dust - Near and Far*, volume 414 of *Astronomical Society of the Pacific Conference Series*, p. 36

Cherchneff, I., 2011, in C. Joblin & A. G. G. M. Tielens (eds.), *EAS Publications Series*, volume 46 of *EAS Publications Series*, pp. 177–189

Cherchneff, I., 2012, A&A, **545**, A12

Cherchneff, I., Barker, J. R. & Tielens, A. G. G. M., 1992, ApJ, **401**, 269

Cherchneff, I. & Cau, P., 1999, in T. Le Bertre, A. Lebre & C. Waelkens (eds.), *Asymptotic Giant Branch Stars*, volume 191 of *IAU Symposium*, p. 251

Cherchneff, I. & Dwek, E., 2009, ApJ, **703**, 642

Cherchneff, I. & Dwek, E., 2010, ApJ, **713**, 1

Cherchneff, I. & Lilly, S., 2008, ApJ, **683**, L123

Chevalier, R. A., 1999, ApJ, **511**, 798

Chiaki, G., Yoshida, N. & Kitayama, T., 2013, ApJ, **762**, 50

Chieffi, A. & Limongi, M., 2002, ApJ, **577**, 281

Christlieb, N., Bessell, M. S., Beers, T. C., Gustafsson, B., Korn, A., Barklem, P. S., Karlsson, T., Mizuno-Wiedner, M. & Rossi, S., 2002, Nature, **419**, 904

Clayton, D. D. & Wickramasinghe, N. C., 1976, Ap&SS, **42**, 463

Coc, A., Angulo, C., Vangioni-Flam, E., Descouvemont, P. & Adahchour, A., 2005, *Nuclear Physics A*, **752**, 522

Dale, J. E., Ercolano, B. & Bonnell, I. A., 2012, MNRAS, **427**, 2852

Dalgarno, A., 2006*a*, *Proceedings of the National Academy of Science*, **103**, 12269

Dalgarno, A., 2006*b*, *Proceedings of the National Academy of Science*, **103**, 12269

Dekel, A. & Birnboim, Y., 2006, MNRAS, **368**, 2

Dijkstra, M., Haiman, Z. & Spaans, M., 2006, ApJ, **649**, 14

Dopcke, G., Glover, S. C. O., Clark, P. C. & Klessen, R. S., 2011, ApJ, **729**, L3

Dorfi, E. A., 1991, A&A, **251**, 597

Dorfi, E. A., 2000, Ap&SS, **272**, 227

Dove, J. E., Rusk, A. C. M., Cribb, P. H. & Martin, P. G., 1987, ApJ, **318**, 379

Draine, B. T., 1978, ApJS, **36**, 595

Draine, B. T., 2003, ARA&A, **41**, 241

Draine, B. T., 2011, *Physics of the Interstellar and Intergalactic Medium*

Dwek, E., 1987, ApJ, **322**, 812

Dwek, E., 2004, ApJ, **607**, 848

Dwek, E. & Arendt, R. G., 1992, ARA&A, **30**, 11

Dwek, E. & Cherchneff, I., 2010, in D. J. Whalen, V. Bromm & N. Yoshida (eds.), *American Institute of Physics Conference Series*, volume 1294 of *American Institute of Physics Conference Series*, pp. 142–147

Dwek, E., Galliano, F. & Jones, A. P., 2007, ApJ, **662**, 927

Dwek, E. & Werner, M. W., 1981, ApJ, **248**, 138

Eglītis, I. & Eglīte, M., 1995, Ap&SS, **229**, 63

Ekström, S., Meynet, G., Chiappini, C., Hirschi, R. & Maeder, A., 2008, A&A, **489**, 685

Elmegreen, B. G., 1998, in C. E. Woodward, J. M. Shull & H. A. Thronson, Jr. (eds.), *Origins*, volume 148 of *Astronomical Society of the Pacific Conference Series*, p. 150

Evans, A. & Rawlings, J. M. C., 2008, in M. B. . A. Evans (ed.), *Classical Novae, 2nd Edition. Edited by M.F. Bode and A. Evans. Cambridge Astrophysics Series, No. 43, Cambridge: Cambridge University Press, 2008.*, p. 308

Falle, S. A. E. G., Komissarov, S. S. & Joarder, P., 1998, MNRAS, **297**, 265

Fang, T. & Cen, R., 2004, ApJ, **616**, L87

Fatuzzo, M., Adams, F. C. & Melia, F., 2006, ApJ, **653**, L49

Ferrara, A., 1998, ApJ, **499**, L17

Flower, D., 2007, *Molecular Collisions in the Interstellar Medium*

Fonfría, J. P., Cernicharo, J., Richter, M. J. & Lacy, J. H., 2008, ApJ, **673**, 445

Foster, P. N. & Boss, A. P., 1996, ApJ, **468**, 784

Foster, P. N. & Boss, A. P., 1997, ApJ, **489**, 346

Frebel, A., 2010, *Astronomische Nachrichten*, **331**, 474

Frebel, A., Aoki, W., Christlieb, N., Ando, H., Asplund, M., Barklem, P. S., Beers, T. C., Eriksson, K. & et al., 2005, in V. Hill, P. Francois & F. Primas (eds.), *From Lithium to Uranium: Elemental Tracers of Early Cosmic Evolution*, volume 228 of *IAU Symposium*, pp. 207–212

Frebel, A., Johnson, J. L. & Bromm, V., 2007, MNRAS, **380**, L40

Frenklach, M. & Feigelson, E. D., 1989, ApJ, **341**, 372

Fryer, C. L., Belczynski, K., Wiktorowicz, G., Dominik, M., Kalogera, V. & Holz, D. E., 2012, ApJ, **749**, 91

Fukugita, M. & Kawasaki, M., 1994, MNRAS, **269**, 563

Gail, H. & Sedlmayr, E., 1987, in G. E. Morfill & M. Scholer (ed.), *NATO ASIC Proc. 210: Physical Processes in Interstellar Clouds*, pp. 275–303

Gall, C., Hjorth, J. & Andersen, A. C., 2011, A&A Rev., **19**, 43

Gallagher, J. S., 1977, AJ, **82**, 209

Galli, D. & Palla, F., 1998, A&A, **335**, 403

Gardner, J. P., Mather, J. C., Clampin, M., Doyon, R., Greenhouse, M. A., Hammel, H. B., Hutchings, J. B., Jakobsen, P., Lilly, S. J., Long, K. S. & et al., 2006, Space Sci. Rev., **123**, 485

Glassgold, A. E. & Langer, W. D., 1973, ApJ, **179**, L147

Glover, S., 2005, Space Sci. Rev., **117**, 445

Glover, S., Savin, D. W. & Jappsen, A.-K., 2005, in *IAU Symposium*, volume 235 of *IAU Symposium*, p. 319P

Glover, S. C. O. & Abel, T., 2008, MNRAS, **388**, 1627

Glover, S. C. O. & Jappsen, A.-K., 2007, ApJ, **666**, 1

Glover, S. C. O. & Savin, D. W., 2009, MNRAS, **393**, 911

Goldsmith, P. F. & Langer, W. D., 1978, ApJ, **222**, 881

Good, G. A., 2003, *Observing Variable Stars*

Gould, R. J. & Salpeter, E. E., 1963, ApJ, **138**, 393

Gredel, R., Lepp, S., Dalgarno, A. & Herbst, E., 1989, ApJ, **347**, 289

Greif, T. H., Glover, S. C. O., Bromm, V. & Klessen, R. S., 2010, ApJ, **716**, 510

Greif, T. H., Johnson, J. L., Klessen, R. S. & Bromm, V., 2008, MNRAS, **387**, 1021

Greif, T. H., Springel, V., White, S. D. M., Glover, S. C. O., Clark, P. C., Smith, R. J., Klessen, R. S. & Bromm, V., 2011, ApJ, **737**, 75

Haiman, Z., Rees, M. J. & Loeb, A., 1997, ApJ, **476**, 458

Haiman, Z., Thoul, A. A. & Loeb, A., 1996, ApJ, **464**, 523

Hasegawa, K., Umemura, M. & Susa, H., 2009, MNRAS, **395**, 1280

Heger, A. & Woosley, S. E., 2002, ApJ, **567**, 532

Heger, A. & Woosley, S. E., 2010, ApJ, **724**, 341

Helling, C., Jorgensen, U. G., Plez, B. & Johnson, H. R., 1996, A&A, **315**, 194

Hennebelle, P. & Chabrier, G., 2009, ApJ, **702**, 1428

Herbst, E., 1993, in T. J. Millar & D. A. Williams (eds.), *Dust and Chemistry in Astronomy*, p. 183

Hewitt, J. W., Rho, J., Andersen, M. & Reach, W. T., 2009, ApJ, **694**, 1266

Hollenbach, D. & McKee, C. F., 1979, ApJS, **41**, 555

Hollenbach, D. & McKee, C. F., 1989, ApJ, **342**, 306

Hummer, D. G., 1994, MNRAS, **268**, 109

Indriolo, N., Blake, G. A., Goto, M., Usuda, T., Oka, T., Geballe, T. R., Fields, B. D. & McCall, B. J., 2010, ApJ, **724**, 1357

Indriolo, N., Geballe, T. R., Oka, T. & McCall, B. J., 2007, ApJ, **671**, 1736

Jappsen, A.-K., Glover, S. C. O., Klessen, R. S., Mac Low, M.-M. & Kitsionas, S., 2006, in *IAU Joint Discussion*, volume 7 of *IAU Joint Discussion*

Jappsen, A.-K., Klessen, R. S., Glover, S. C. O. & Mac Low, M.-M., 2009, ApJ, **696**, 1065

Jappsen, A.-K., Klessen, R. S., Larson, R. B., Li, Y. & Mac Low, M.-M., 2005, A&A, **435**, 611

Jasche, J., Ciardi, B. & Enßlin, T. A., 2007, MNRAS, **380**, 417

Joggerst, C. C., Almgren, A., Bell, J., Heger, A., Whalen, D. & Woosley, S. E., 2010, ApJ, **709**, 11

Joggerst, C. C., Woosley, S. E. & Heger, A., 2009, ApJ, **693**, 1780

Johansson, E. P. G. & Ziegler, U., 2013, ApJ, **766**, 45

Johnson, J. L., Greif, T. H. & Bromm, V., 2007, ApJ, **665**, 85

Johnston, S., Taylor, R., Bailes, M., Bartel, N., Baugh, C., Bietenholz, M., Blake, C., Braun, R. & et al., 2008, *Experimental Astronomy*, **22**, 151

Jun, B.-I., Jones, T. W. & Norman, M. L., 1996, ApJ, **468**, L59

Kaufman, M. J. & Neufeld, D. A., 1996, ApJ, **456**, 611

Kawachi, T. & Hanawa, T., 1998, PASJ, **50**, 577

Kitayama, T. & Yoshida, N., 2005, ApJ, **630**, 675

Kitayama, T., Yoshida, N., Susa, H. & Umemura, M., 2004, ApJ, **613**, 631

Klein, R. I., McKee, C. F. & Colella, P., 1994, ApJ, **420**, 213

Klessen, R. S. & Burkert, A., 2000, ApJS, **128**, 287

Klessen, R. S., Glover, S. C. O. & Clark, P. C., 2012, MNRAS, **421**, 3217

Lambert, D. L., Gustafsson, B., Eriksson, K. & Hinkle, K. H., 1986, ApJS, **62**, 373

Larson, R. B., 1985, MNRAS, **214**, 379

Larson, R. B., 2005, MNRAS, **359**, 211

Leão, M. R. M., de Gouveia Dal Pino, E. M., Falceta-Gonçalves, D., Melioli, C. & Geraissate, F. G., 2009, MNRAS, **394**, 157

Li, Y., Klessen, R. S. & Mac Low, M.-M., 2003, ApJ, **592**, 975

Lim, A. J., Raga, A. C., Rawlings, J. M. C. & Williams, D. A., 2002, MNRAS, **335**, 817

Lipovka, A., Núñez-López, R. & Avila-Reese, V., 2005, MNRAS, **361**, 850

Luck, R. E. & Bond, H. E., 1982, ApJ, **259**, 792

Mac Low, M.-M. & Klessen, R. S., 2004, *Reviews of Modern Physics*, **76**, 125

Machida, M. N., Tomisaka, K., Nakamura, F. & Fujimoto, M. Y., 2005, ApJ, **622**, 39

Mackey, J., Bromm, V. & Hernquist, L., 2003, ApJ, **586**, 1

Mackey, J. & Lim, A. J., 2010, MNRAS, **403**, 714

Martin, P. G., Schwarz, D. H. & Mandy, M. E., 1996, ApJ, **461**, 265

Matsuura, M., Dwek, E., Meixner, M., Otsuka, M., Babler, B., Barlow, M. J., Roman-Duval, J., Engelbracht, C., Sandstrom, K., Lakićević, M. & et al., 2011, *Science*, **333**, 1258

McKee, C. F. & Ostriker, E. C., 2007, ARA&A, **45**, 565

Melioli, C., de Gouveia Dal Pino, E. M., de La Reza, R. & Raga, A., 2006, MNRAS, **373**, 811

Miyake, S. & Stancil, P. C., 2007, in *American Astronomical Society Meeting Abstracts*, volume 39 of *Bulletin of the American Astronomical Society*, p. 139

Montier, L. A. & Giard, M., 2004, A&A, **417**, 401

Morlino, G. & Caprioli, D., 2012, A&A, **538**, A81

Nagakura, T., Hosokawa, T. & Omukai, K., 2009, MNRAS, **399**, 2183

Nagakura, T. & Omukai, K., 2005, MNRAS, **364**, 1378

Nakamura, F., McKee, C. F., Klein, R. I. & Fisher, R. T., 2006, ApJS, **164**, 477

Nakamura, F. & Umemura, M., 2002, ApJ, **569**, 549

Neufeld, D. A., Lepp, S. & Melnick, G. J., 1995, ApJS, **100**, 132

Nozawa, T., Kozasa, T., Habe, A., Dwek, E., Umeda, H., Tominaga, N., Maeda, K. & Nomoto, K., 2007, ApJ, **666**, 955

Omukai, K., 2010, in N. Kawai & S. Nagataki (eds.), *American Institute of Physics Conference Series*, volume 1279 of *American Institute of Physics Conference Series*, pp. 110–115

Omukai, K., Tsuribe, T., Schneider, R. & Ferrara, A., 2005, ApJ, **626**, 627

O'Shea, B. W., Abel, T., Whalen, D. & Norman, M. L., 2005, ApJ, **628**, L5

Panagia, N., 2005, *Nuovo Cimento B Serie*, **120**, 667

Patnaude, D. J., Fesen, R. A., Raymond, J. C., Levenson, N. A., Graham, J. R. & Wallace, D. J., 2002, AJ, **124**, 2118

Peebles, P. J. E., 1971, *Physical cosmology*

Phillips, J. P. & Marquez-Lugo, R. A., 2010, MNRAS, **409**, 701

Pontefract, M. & Rawlings, J. M. C., 2004, MNRAS, **347**, 1294

Prasad, S. S. & Tarafdar, S. P., 1983, ApJ, **267**, 603

Preibisch, T., Brown, A. G. A., Bridges, T., Guenther, E. & Zinnecker, H., 2002, AJ, **124**, 404

Raga, A. C., Cantó, J., Rodríguez, L. F. & Velázquez, P. F., 2012, MNRAS, **424**, 2522

Raga, A. C., de Gouveia Dal Pino, E. M., Noriega-Crespo, A., Mininni, P. D. & Velázquez, P. F., 2002, A&A, **392**, 267

Raga, A. C., Mellema, G. & Lundqvist, P., 1997, ApJS, **109**, 517

Rawlings, J. M. C., 1988, MNRAS, **232**, 507

Rawlings, J. M. C., Drew, J. E. & Barlow, M. J., 1993, MNRAS, **265**, 968

Rawlings, J. M. C., Hartquist, T. W., Menten, K. M. & Williams, D. A., 1992, MNRAS, **255**, 471

Rawlings, J. M. C. & Williams, D. A., 1989, MNRAS, **240**, 729

Reach, W. T., Rho, J. & Jarrett, T. H., 2005, ApJ, **618**, 297

Reach, W. T., Rho, J., Jarrett, T. H. & Lagage, P.-O., 2002, ApJ, **564**, 302

Rho, J. & Reach, W., 2003, in J. Arthur & W. J. Henney (eds.), *Revista Mexicana de Astronomia y Astrofisica Conference Series*, volume 15 of *Revista Mexicana de Astronomia y Astrofisica, vol. 27*, pp. 263–266

Rollins, R. P. & Rawlings, J. M. C., 2012, MNRAS, **427**, 2328

Salpeter, E. E., 1977, ARA&A, **15**, 267

Salvaterra, R., Ferrara, A. & Schneider, R., 2004, *New Astronomy*, **10**, 113

Sánchez-Salcedo, F. J., Vázquez-Semadeni, E. & Gazol, A., 2002, ApJ, **577**, 768

Santoro, F. & Shull, J. M., 2006, ApJ, **643**, 26

Savin, D. W., 2002, ApJ, **566**, 599

Schaerer, D., 2002, A&A, **382**, 28

Schneider, R., Ferrara, A., Natarajan, P. & Omukai, K., 2002, ApJ, **571**, 30

Schneider, R., Omukai, K., Bianchi, S. & Valiante, R., 2012, MNRAS, **419**, 1566

Schörck, T., Christlieb, N., Cohen, J. G., Beers, T. C., Shectman, S., Thompson, I., McWilliam, A., Bessell, M. S., Norris, J. E., Meléndez, J. & et al., 2009, A&A, **507**, 817

Sedov, L. I., 1946, *Journal of Applied Mathematics and Mechanics*, **10**, 241

Shapiro, P. R. & Kang, H., 1987, ApJ, **318**, 32

Shigeyama, T. & Tsujimoto, T., 1998, ApJ, **507**, L135

Shu, F. H., 1977, ApJ, **214**, 488

Silvia, D. W., Smith, B. D. & Shull, J. M., 2010, ApJ, **715**, 1575

Slyz, A. D., Devriendt, J. E. G., Bryan, G. & Silk, J., 2005, MNRAS, **356**, 737

Smith, R. J., Glover, S. C. O., Bonnell, I. A., Clark, P. C. & Klessen, R. S., 2011, MNRAS, **411**, 1354

Smith, V. V., Coleman, H. & Lambert, D. L., 1993, ApJ, **417**, 287

Sonnentrucker, P., González-Alfonso, E. & Neufeld, D. A., 2007, ApJ, **671**, L37

Spergel, D. N., Bean, R., Doré, O., Nolta, M. R., Bennett, C. L., Dunkley, J., Hinshaw, G., Jarosik, N. & et al., 2007, ApJS, **170**, 377

Stacy, A. & Bromm, V., 2007, MNRAS, **382**, 229

Stacy, A., Greif, T. H. & Bromm, V., 2010, MNRAS, **403**, 45

Starrfield, S., Truran, J. W. & Sparks, W. M., 2000, *New Astronomy Review*, **44**, 81

Susa, H., 2008, ApJ, **684**, 226

Sutherland, R. S. & Dopita, M. A., 1993, ApJS, **88**, 253

Swordy, S. P., 2001, Space Sci. Rev., **99**, 85

Taylor, G. I., 1950, *Proceedings of the Royal Society A*, **201**, 159

Tegmark, M., Silk, J., Rees, M. J., Blanchard, A., Abel, T. & Palla, F., 1997, ApJ, **474**, 1

Tenorio-Tagle, G., 1996, AJ, **111**, 1641

Tielens, A. G. G. M., 2008, ARA&A, **46**, 289

Tominaga, N., 2009, ApJ, **690**, 526

Tsuribe, T. & Omukai, K., 2006, ApJ, **642**, L61

Tsuribe, T. & Omukai, K., 2008, ApJ, **676**, L45

Turk, M. J., Abel, T. & O'Shea, B., 2009, *Science*, **325**, 601

Umeda, H. & Nomoto, K., 2002, ApJ, **565**, 385

Vaidya, B., Hartquist, T. W. & Falle, S. A. E. G., 2013, MNRAS, **433**, 1258

van Dischoeck, E., 1988, in T. J. Millar & D. A. Williams (eds.), *Rate Coefficients in Astrochemistry*, volume 146 of *Astrophysics and Space Science Library*

Vanhala, H. A. T. & Cameron, A. G. W., 1998, ApJ, **508**, 291

Vasiliev, E. O., Vorobyov, E. I., Matvienko, E. E., Razoumov, A. O. & Shchekinov, Y. A., 2012, *Astronomy Reports*, **56**, 895

Vasiliev, E. O., Vorobyov, E. I. & Shchekinov, Y. A., 2008, A&A, **489**, 505

Verner, D. A. & Ferland, G. J., 1996, ApJS, **103**, 467

Vishniac, E. T., 1983, ApJ, **274**, 152

Voronov, G. S., 1997, *Atomic Data and Nuclear Data Tables*, **65**, 1

Walmsley, M., 1991, in E. Falgarone, F. Boulanger & G. Duvert (eds.), *Fragmentation of Molecular Clouds and Star Formation*, volume 147 of *IAU Symposium*, p. 161

Wang, C.-Y. & Chevalier, R. A., 2001, ApJ, **549**, 1119

Watson, W. D. & Salpeter, E. E., 1972, ApJ, **174**, 321

Whalen, D., Abel, T. & Norman, M. L., 2004, ApJ, **610**, 14

Whalen, D. & Norman, M. L., 2008, ApJ, **673**, 664

Wise, J. H. & Abel, T., 2007, ApJ, **665**, 899

Wise, J. H. & Abel, T., 2008, ApJ, **685**, 40

Wise, J. H., Abel, T., Turk, M. J., Norman, M. L. & Smith, B. D., 2012, MNRAS, **427**, 311

Woodall, J., Agúndez, M., Markwick-Kemper, A. J. & Millar, T. J., 2007*a*, A&A, **466**, 1197

Woodall, J., Agúndez, M., Markwick-Kemper, A. J. & Millar, T. J., 2007*b*, A&A, **466**, 1197

Woods, P. M., Millar, T. J., Zijlstra, A. A. & Herbst, E., 2002, ApJ, **574**, L167

Woodward, P. R., 1976, ApJ, **207**, 484

Yoshida, N., Abel, T., Hernquist, L. & Sugiyama, N., 2003, ApJ, **592**, 645

Yoshida, N., Oh, S. P., Kitayama, T. & Hernquist, L., 2007, ApJ, **663**, 687

Yoshida, N., Omukai, K., Hernquist, L. & Abel, T., 2006, ApJ, **652**, 6

Zhang, W., Woosley, S. E. & Heger, A., 2008, ApJ, **679**, 639

ACKNOWLEDGEMENTS

I would like to thank Jonathan Rawlings for taking me on as a PhD student - otherwise I would be stuck outside the world of astrophysics. I always have enjoyed his dry, sometimes off beat sense of humour. He has always given me the freedom to research whatever I like, and this has been invaluable. Also I would like to thank my examiners, Prof Serena Viti and Prof Anthony Whitworth, for being gracious and understanding throughout my viva.

There are two people without whom this thesis would never have been completed: Jeremy Yates and Jonathan Mackey. When Jeremy heard my project idea, and he lead me to the right code and the right collaborator. Throughout the project he has been a mentor, guide and inspiration (yes inspiration is not an overstatement anyone who has seen him function as DiRAC director knows what I am saying). He never gave up on me and never let me down. He even read my chapters at the last minute, while on holiday. It is with his support and encouragement that I was able to carry on and finish this thesis. I know I am not the first person to be so grateful for Jeremys help, and I know I will not be the last.

Jonathan Mackey has been a wonderful collaborator, always supportive and helpful. He had the perfect balance between giving me guidance in terms of methods, tests, etc and allowing me complete control of the direction of the project. He is a rigorous, dedicated and adept scientist, who has been generous with his time, expertise and compassion. I will always be indebted to him. He was even kind enough to offer to read/correct my thesis. On the topic of pages covered in red ink I must thank Thomas Bisbas and Paul Woods. Anyone who has seen how badly I write knows that this is no small task!

When I first started my PhD I used to read peoples thesis acknowledgements and I thought there was an unnecessary amount of gushing over support from partners or friends. Now at the end of my PhD, I dont think that you can say enough. The support I have received from friends has been invaluable. If anything has tested my strength, resolve and mental stamina, it has been this PhD. In my darkest hours it is been these special people that have given me a soft sacred spot to be vulnerable; then they wiped my tears and reminded me that I have a backbone and that anything is possible if I keep going. I am going to name all these special people in one go as each one is equally treasured and equally important: Barney, Emily, Christiano, Farah, Helen, Maureen, Patrick, Silvia and Stephanie. I love you all you are my chicas for life! These people never tried to change me into another person but they helped me to be the best version of myself.

There is another special person that deserves acknowledgement and that is my mother. In truth without her taking me in when my funding ran out, this would not be possible. She has spoiled me rotten with good indian food and warm tea on demand (accompanied by ‘when will this be over). There is nothing as special as family and nothing as unique as a punjabi one.

I have had a brilliant time at UCL -it is warm, vibrant and lively group. G18 has been my mecca :) There is no way to translate the weird , quirky fun we have had.